

NANOMATERIALS IN TWO DIMENSIONS

Mechanistic Insights into the Formation and Synthesis of Superlattices and Nanosheets

Maaïke van der Sluijs

Nanomaterials in Two Dimensions

Mechanistic Insights into the Formation and Synthesis of
Superlattices and Nanosheets

PhD thesis, Utrecht University
Nanomaterials in Two Dimensions
Maaïke M. van der Sluijs, 2024

ISBN: 978-90-393-7694-2
Printed by Ridderprint

Cover: Inspired by The Storied Life of A.J. Fikry by Abacus and work by Aleksandra Jovanic

Nanomaterials in Two Dimensions

Mechanistic Insights into the Formation and Synthesis of
Superlattices and Nanosheets

Nanomaterialen in twee dimensies

Mechanistische inzichten in de vorming en synthese van superstructuren en nanoplaatjes

(met een samenvatting in het Nederlands)

Proefschrift

ter verkrijging van de graad van doctor aan de
Universiteit Utrecht
op gezag van de
rector magnificus, prof. dr. H.R.B.M. Kummeling,
ingevolge het besluit van het College voor Promoties
in het openbaar te verdedigen op

woensdag 19 juni 2024 des middags te 12.15 uur

door

Maike Marina van der Sluijs

geboren op 2 maart 1990
te Utrecht

Promotor:

Prof. dr. D.A.M. Vanmaekelbergh

Beoordelingscommissie:

Prof. dr. P.C.A. Bruijninx

Prof. dr. M. Dijkstra

Prof. dr. A.J. Houtepen

Prof. dr. W.K. Kegel

Dr. F.T. Rabouw

Dit proefschrift werd mogelijk gemaakt met financiële ondersteuning van de Europese onderzoeksraad (Horizon 2020 “First Step”, 692691).

Table of contents

Chapter 1	Introduction	1
Chapter 2	Theoretical Background	5
Chapter 3	Oriented Attachment: From Natural Crystal Growth to a Materials Engineering Tool	27
Chapter 4	From PbSe Nanocrystals to Honeycomb Superlattices	55
Chapter 5	The Increasing Crystallinity in the Self-Templated Growth of Ultrathin PbS Nanosheets	91
Chapter 6	Cation Exchange and Spontaneous Crystal Repair Resulting in Ultrathin, Planar CdS Nanosheets	125
	Appendices	
	Samenvatting in het Nederlands	154
	List of Publications	168
	About the author	169



CHAPTER 1

Introduction



Whether you like it or not, science is a fundamental part of our everyday life. It is one of the driving forces in the progress of mankind and should not be taken lightly but in everyday situations we also casually apply scientific thinking. When we run into a problem, we intuitively start to figure out the cause and run through possible solutions. If we fail to resolve the issue, we go back to the drawing board and try again. Thus, we all apply some form of rational thinking in our everyday lives. At its core, science can be considered as the formalization of this instinctive problem solving, with the recording of the observations being a notable difference: “Remember kids, the only difference between screwing around and science is writing it down”.¹ However, scientific reality is often very counter-intuitive and scientific questions are generally more complicated,² more *fundamental*,³ and sometimes occurring on such a small scale that they are not visible by eye.

The nanoscale, nanotechnology and top-down versus bottom-up

Table salt is an everyday example of a crystal (sodium chloride, NaCl), its crystalline white flakes do not only enhance the flavours in our food but also adhere to the scientific definition of a crystal. Crystals consist of periodically arranged atoms over large ranges. Thus, a crystal can be reduced to the building block that repeats throughout the structure: the unit cell and translation vectors. As the crystals become very small, smaller than 100 nanometer (nano being 0.000000001 or 10^{-9} meter) the properties of the crystalline material can be influenced by the size of the crystal. For comparison, a strand of DNA is 2.5 nm wide, a human red blood cell has an average diameter of 7500 nm (0.0000075 or 7.5×10^{-6} meter) and a DVD is 1200000 nm thick (0.0012 or 1.2×10^{-3} meter). An extensive subfield of the nanosciences consists of the study and optimization of colloidal self-standing nanocrystals with the aim to use them in nanotechnology. Technological application on a small scale, nanotechnology, emerged as a concept in culture and science as early as 1956.⁴⁻⁷ But it has taken until the last few decades before nanotechnology began to impact our everyday lives. At the moment, nanoparticles are used in applications such as sunscreen, band-aids, TV screens and in medical diagnosis. Even the 2023 Nobel Prize in Chemistry was awarded to three scientists, Louis Brus, Alexei Ekimov and Mounji Bawendi, for “the discovery and development of quantum dots”.^{8,9}

Many of the components used in computers, smart phones and televisions are produced with advanced techniques to create smaller and smaller electronics. Often, these small electronics are prepared with a top-down approach. For example, a big silicon crystal is etched and electrically contacted to create tiny transistors. However, nature has used a bottom-up approach that, on a cosmological timescale, has resulted in amazing functionalities. We as humans are a larger system, built up from individual components in which for example our DNA serves as an encrypted chemical code. A code that is reproducibly used by enzymes to build up incredibly complex and fully functional structures such as proteins. Applying a bottom-up approach to the production of materials would be a tuneable and versatile addition for the engineering of suitable small electronics.

In this thesis, we discuss the synthesis and characterization of colloidal nanocrystals, which are nanocrystals dispersed in a solution. All nanocrystals studied here consist of semiconductors, e.g. materials that have the Fermi-level positioned in a band gap between the valence and conduction band and hence, can be switched on and off electronically. In addition their opto-electronic properties are influenced by their size. The nanocrystals discussed in this thesis consist of lead- or cadmium- chalcogenide units (PbX, CdX, X=Se, S). These nanocrystals are

interesting for many novel applications, ranging from IR photodetectors to solar cells. Here, we studied the nanocrystals as self-standing objects but also used a bottom-up approach to form larger hierarchical 2-dimensional superstructures from nanocrystals. With a solvent evaporation method, the nanocrystals were allowed to self-assemble at a liquid interface driven by certain interactions between the nanocrystals. Then, the nanocrystals begin to align their crystal structures and eventually grow together to form one crystal i.e. a crystal of nanocrystals in which the atomic planes are aligned with each other. We should remark here that our control of the process and the reproducibility does not (yet) come close to the achievements in nature.

In addition, we studied the intriguing formation of very thin but extended PbS nanosheets. The surprisingly rectangular nanosheets were shown to have a deformed orthorhombic PbS crystal structure with the incorporation of some defects. By studying the reaction intermediates at lower temperatures we observed the evolution of pseudo-crystalline templates toward mature, crystalline PbS nanosheets. With these observations we were able to propose a reaction mechanism. In addition, we monitored the chemical transformation of the PbS nanosheets into CdS nanosheets of the same dimensions by Cd-for-Pb cation exchange. We observed that, in the early stages of the exchange, the nanosheets show large in-sheet voids that repair spontaneously upon further exchange and annealing, resulting in ultrathin, planar, and crystalline CdS nanosheets.

Scope of the thesis

In [chapter 2](#), I briefly present the background necessary to understand the concepts and terminology used in the rest of the thesis. Specifically, I discuss the implicit presence and usage of nanocrystals in history and then go into how we understand nanocrystals currently. First, I discuss the inorganic core of the nanocrystals and the influence of dimensionality on the luminescent properties. Then, I briefly discuss the post-synthetic process of cation exchange with which the crystalline core of the nanocrystals can be tailored further. From there, I give some insight into our understanding of the surface chemistry of nanocrystals in general and specifically the organic ligand layer which stabilizes the nanocrystals in dispersion. I briefly discuss a classification method with which the binding of ligands to the surface, and surface tailoring via ligand exchange can be understood. I go on to discuss the interactions between ligand-stabilized nanocrystals in an organic apolar dispersion, specifically looking at the interactions between nanocrystals which play a role during self-assembly. Finally, I present a short introduction on oriented attachment at a liquid interface to introduce [chapter 3](#).

In [chapter 3](#), I discuss the literature on oriented attachment up until 2020, based on our review paper published on the subject. I discuss the different types of stabilization for nanocrystals in dispersion, followed by the general history of oriented attachment. Specifically, I focus on oriented attachment in the PbX (X = S, Se, Te) and CdX family (X = S, Se, Te). Finally, there is a discussion on the current state of the in situ study of oriented attachment with X-ray scattering methods and the additional insight to be gained from molecular dynamics simulations to model the nanocrystal assembly and orientation at an interface.

In [chapter 4](#), I present a study of the formation of honeycomb superlattices fashioned from PbSe nanocrystals by self-assembly and oriented attachment. Initially, I discuss how to avoid perturbation of the superlattice prior to characterisation by drying the structure in vacuum as soon as possible. Then, I studied the influence of the reactivity of the liquid substrate on the formation process and the final stages of alignment and attachment of the PbSe nanocrystals.

The self-assembly pathway was then further investigated by varying the repulsion potentials between the nanocrystals in coarse-grained molecular dynamics simulations.

In **chapter 5**, I discuss our study of the synthesis and growth mechanism for 2D PbS nanosheets. With atomically resolved TEM techniques we elucidate the structure of the nanosheets and study the crystallinity of the nanosheets during the growth (synthesis). The ex situ analysis allowed us to propose a reaction mechanism for the growth of these nanosheets. Finally, we apply this knowledge to improve the crystallinity of the synthesized PbS sheets.

In **chapter 6**, I show a post-synthetic Cd-for-Pb cation exchange starting with PbS nanosheets, in order to obtain CdS nanosheets. With ex situ TEM analysis we studied the cation exchange in time: Early on, the nanosheets show significant damage; but over time the damage is repaired and the completely exchanged CdS nanosheets even show (trap) luminescence.

References

- [1] Mythbusters. In Bouncing Bullet, 2012; Vol. 10.
- [2] van der Sluijs, M. M. De Categorisering van Science Plays: Een Toetsend Onderzoek aan de Hand van de Jeugdvoorstelling Het Verhaal van de Getallen. Bachelor, 2015.
- [3] Andrei Petukhov, who has stressed in many presentations that we do fundamental science.
- [4] Clarke, A. C. The Next Tenants. In Tales from the White Hart, Ballantine Books, 1956.
- [5] Feynman, R. There is Plenty of Room at the Bottom. 1959.
- [6] Silverberg, R. How it Was When the Past Went Away. In Three for Tomorrow, Meredith Press, 1969.
- [7] Taniguchi, N. On the Basic Concept of Nanotechnology. 1974.
- [8] Nanoscience. Nobel Prize Outreach, 2023. www.nobelprize.org/prizes/chemistry/2023/advanced-information
- [9] Vanmaekelbergh, D. Colloïdale Quantumdots, Kristalzaden voor de Nanowetenschap. Nederlands Tijdschrift voor Natuurkunde 2024, 90 (1), 14-18.

CHAPTER 2

Theoretical Background



Here, we provide some of the foundational knowledge to comprehend the concepts and terminology used in the rest of this thesis. Initially we discuss the nature of light and how it gives colour to objects in our everyday life. Then we delve into the presence and empirical craftsmanship allowing the utilization of nanotechnology throughout history, before we continue to our contemporary scientific understanding of nanocrystals (NCs). First, we explore the crystalline inorganic core of NCs, emphasizing the impact their size and shape have on specifically their luminescent properties. Then, we discuss the post-synthetic process of cation exchange, by which the NC core can be tailored further towards NCs with shapes and compositions not accessible via direct synthesis.

Subsequently, we focus on the broader understanding of the NCs surface chemistry, specifically the surface pacifying organic ligand layer. This ligand layer can stabilize the NCs in dispersion and generally determines the interaction of the NCs with the environment and other NCs. We briefly discuss a classification method which categorizes ligands by the number of electrons they contribute to the bond formed with the surface atom and how this knowledge can be applied when tailoring the ligand shell with ligand exchange. We also discuss the interactions between ligand-stabilized NCs, specifically during self-assembly of these NCs. Finally, we introduce oriented attachment, a method with which larger (thin) superstructures or superlattices can be formed from directly connected NCs.

2.1. What is light?

The electromagnetic spectrum organizes photons, particles of light, based on their energy or wavelength i.e. energy that travels as particles or waves and spreads out as it goes.¹ In **Figure 2.1** we show the electromagnetic spectrum schematically. Visible light, i.e. the part that the human eye is sensitive to, only covers a small part of this spectrum. While we see this light as white, it is actually a combination of colours and wavelengths between 380 nm (violet) and 660 nm (red). Once the light is diffracted or refracted, for example through a prism, by raindrops or on the back of a DVD, we can distinguish the separate colours of the rainbow present in the white light.

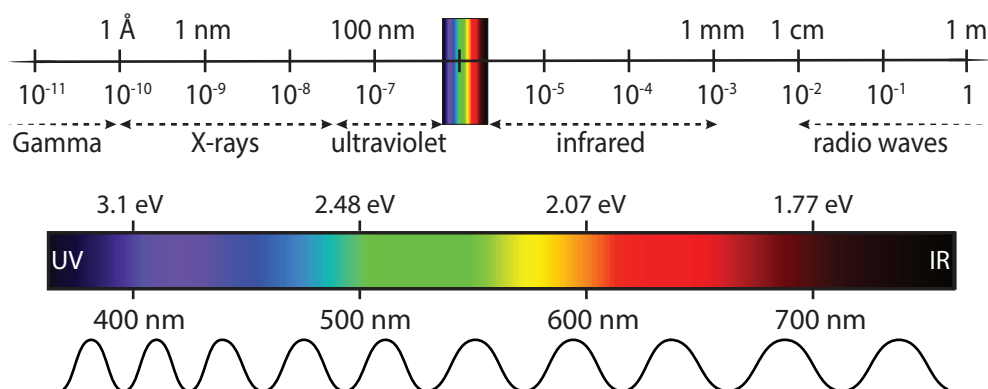


Figure 2.1 Schematic overview of the electromagnetic spectrum which ranges from waves on a meter scale to waves on angstrom scale. A human's eyes are only sensitive to the visible light between 380 (high energy) and 760 nm (low energy).

The colour of an object comes from the spectral parts of visible light that it absorbs and reflects. For example, an object is perceived as black when it absorbs photons from the entire visible spectrum, but when it reflects photons across the entire spectrum it is perceived as white. Varying mixes of absorbed and reflected light then give rise to any colour in between. Whether or not a material will absorb a photon is determined by the energy difference between the ground state of the material and the excited states, commonly referred to as the bandgap energy. Photons with an energy lower than the bandgap are either reflected or transmitted, while those with an energy equal to or higher than the band gap are absorbed. Just below the visible light, at a lower energy (on the right of [Figure 2.1](#)), lies the infrared region (IR), while at a slightly higher energy we have the ultraviolet region (UV). Human eyes are less (or not at all) sensitive in these areas, but many animals are still able to see one or the other (goldfish are in fact sensitive to both)² and we commonly still refer to these areas as light. For many applications, such as medical imaging, sterilisation and night-vision suitable UV/IR sensitive materials are required. In this field, semiconductor nanomaterials have become a rapidly growing class of candidates, especially due to their small size, low production cost and tunability.

2.2 The inadvertent historical presence of nanocrystals

In our daily lives, the properties of materials are independent from the size of the object. A sheet of paper for example, does not change colour if it is cut into smaller pieces. But, when materials become small enough, their properties can become size-dependent and be very different from their macroscopic (bulk) counterparts. These so-called nanomaterials have at least one dimension smaller than 100 nanometer. One nanometer is 0.00000001 or 10^{-9} meter, for comparison a human red blood cell has an average diameter of 7500 nm (0.0000075 or 7.5×10^{-6} meter) and a DVD is 600.000 nm thick (0.0006 or 6×10^{-4} meter). While the concept of technology on a small scale first emerged in science fiction literature,^{3,4} its scientific origin is associated with two speeches. The first a speech by Richard Feynman in 1959 (*There is plenty of room at the bottom*),⁵ and the second a speech by Norio Taniguchi 15 years later (*On the basic concept of nanotechnology*).⁶ These lectures galvanized a scientific focus on the nanoscale and then during the 1990s, funding by various scientific institutions further encouraged the connection between nanotechnology and future applications.⁷⁻⁹ Over the last 30 years, research into nanomaterials has drastically increased, and nanocrystals are currently exploited in a growing number of commercial applications. For example, nanomaterials are used in television screens, sunscreen and protective coatings.¹⁰ Still, the association between “nano” and the future remains strong in the public mind. Nanotechnology is predicted to further shape our future, expected to play a pivotal role in the generation of devices in electronics, medicine, photonics, textiles and catalysis or more.¹¹

Despite the futuristic connotations of nanomaterials, they have a long history of being used and adapted precisely because of their tunability, but without the basic physical-chemical understanding of the system. The study of historical objects has shown that nanoparticles were used, and their production (empirically) mastered long ago. As early as the Bronze age (approximately 3300 to 1200 Before the Common Era, BCE), silica melts were enriched with metallic colorants (such as Cu, Co, Fe, Mo and Ag) to make coloured glass. In highly reducing atmospheres the metal oxides were reduced to nanocrystals (NCs) which coloured the glass. The Assyrians developed a recipe for the incorporation of gold in glass (a ruby red colour) in 700 BC,¹² but the technique was mastered by the Romans. A beautiful example is the dichroic Lycurgus

cup (4th century Common Era, CE) which looks green in reflection, but red in transmission. These techniques continued to evolve and by the 12th century the observable properties and colours were so well-controlled that large glass-stained windows could adorn cathedrals.

So far, we discussed historic examples of metallic NCs, but one of the earliest examples of semiconductor NCs is of lead sulphide galena as hair-dye (PbS). In Greco-Roman times (8th century BCE to 5th century CE) lead oxide in an alkaline environment could react with the sulphur-based amino acids of keratin in hair. The formed PbS NCs blacken the hair but keep it soft and pliable. As early as 2000 BCE and occasionally throughout history, it was suggested that lead can be toxic, but its many symptoms were not yet well defined and its toxicity may have played a role in the decline of several civilisations including the Roman empire.¹³ The important properties of lead, like its softness, malleability, ductility, resistance to corrosion and abundance made it a material used extensively. The many applications have ranged from an artificial taste enhancer in wine, to make-up for lightening the skin, a drying agent in paint and off course in plumbing. We now understand that lead is highly toxic, but it took until the 20th century before legislation restricting its use was enacted.¹⁴ However, the many applications and its non-biodegradable nature means that the lead will never fully disappear from our environment.

For centuries, NCs were used and manipulated without the scientific understanding of the basic physical-chemical properties of the system. It was not until the 19th century that chemist and physicist Michael Faraday suggested that the colour of Au colloids was linked to the size of the dispersed objects (read NCs). In 1857 he was etching thin gold microscopy samples and accidentally prepared a red coloured gold dispersion (a dispersion that is still stable over a 150 years later). When shining a beam of light through the dispersion, he observed a well-defined cone. It led him to the conclusion that “finely-divided gold” could be the origin of the red colour. When adding salt, the colour of the dispersion turned blue and although he was unable to explain why, he suggested that “a mere variation in the size of its particles gave rise to a variety of colours”.

It took until 1898 (31 years after Faraday’s death) before the colloidal nature of gold in red coloured glass was proven with the slit ultramicroscope.¹⁵ The development of advanced optical microscopy and spectroscopy techniques proved to be very important to the modern nanomaterials field. Eventually the slit ultramicroscope earned Zsigmondy the 1925 Nobel Prize in chemistry and its development led directly to two more Nobel prizes.¹⁶ For the development of these advanced techniques, the preparation of high-quality transparent and coloured glass was essential. The optical properties of so-called “schott-glasses” containing CdS and CdSe were studied extensively.¹⁷ In particular, scientists were tuning the absorption and emission edge by varying the preparation temperature of the glasses.^{18,19} Quickly, these studies were expanded and NCs of very different compositions, in varying matrices or as colloids were characterized, showing similar optical properties.¹¹

These studies formed the basis for the work of Alexey Ekimov (a Russian) and Louis Brus (an American). Separated by the Iron Curtain, they independently and intentionally synthesized and studied semiconductor nanocrystals.²⁰ They both correctly attributed the observed size-dependent properties to the quantum confinement effect. Ekimov studied copper chloride NCs in glass. When heating the glass, the NCs grew bigger and the optical absorption shifted to longer wavelengths and lower energy.^{21,22} At the same time, Brus worked on CdS NCs dispersed in water. Over time, the absorption spectra of these dispersions shifted to lower energy

something which he suspected was a size effect.²³ It was not until 1984 that Brus learned of Ekimov's publications and despite some early contact, collaborations between Ekimov and Alexander Efros started in earnest after the fall of the Iron Curtain. Together, they connected the empirical evidence on size effects with scientific understanding of the underlying process. They ascribed the size-dependent optical properties of semiconductor NCs to confinement of the exciton in a NC smaller than the exciton Bohr radius, the "quantum size effect".^{24,25}

The aqueous dispersions of NCs suffered from polydispersity, i.e. the nanocrystals varied in size and shape and the light-emission upon photo-excitation was poor. It inhibited both their characterization and potential for applications. Then, in 1993 Mounghi Bawendi, David Norris and Chris Murray published a new method for NC synthesis. This so-called hot-injection synthesis, primarily developed by Murray and Bawendi, starts with the quick injection of organometallic precursors in a high-temperature solvent. The injection abruptly supersaturates the solvent with precursors, which initiates nucleation. These nuclei then continue to grow slowly as functional organic ligands bind to the surface atoms. The ligands provide colloidal stability and passivate uncoordinated orbitals, thereby improving the optical properties. The synthesis method formed macroscopic quantities of well passivated NCs with a good size dispersion controlled by the temperature of the reaction. This adaptable, reproducible and precise benchtop synthesis further inspired the rapidly growing nanoscience field. Over the next 30 years, the basic principle of the synthesis was extended to a plethora of other semiconductors and NC shapes.²⁶⁻²⁹

These three scientists, Louis Brus, Alexei Ekimov and Mounghi Bawendi, were recently awarded the Nobel Prize in Chemistry for "the discovery and development of quantum dots". However, if the Nobel Prize was not limited to three (living) winners, the list of laureates could have been much longer.

2.3 Nanomaterials and their properties

A crystal is a solid material that has long-range order, or more precisely, it is build up from periodically arranged atoms, ions or molecules. There are many geometric structures possible, but the entire structure of a crystal can always be described by the unit cell, an identical unit which is repeated throughout the crystal.³⁰ Energy is required to cut a crystal, as it cost energy to break the bonds between the atoms in the crystal lattice and to form new surfaces. The surfaces of crystals in the ≤ 100 nm size are known as crystal facets, small-area specific crystal surfaces. Depending on the direction in which the unit cell is cut, a variety of facets can form. The type of facet that is exposed has a big impact on the overall chemical and physical properties of these crystals. By the adsorption of molecules onto the surface, the relative stability of the facet can be altered significantly.³¹

Nanocrystals, particularly colloidal nanocrystals, consist of an inorganic crystalline core with surface facets that are covered by an (organic) layer of ligands (**Figure 2.2a**). As a chemist, we apply the principles of inorganic chemistry to design the core of a NC: those of organometallic and coordination chemistry to address the NC surface-ligand interaction,³² and those of physical and organic chemistry to understand the ligand-solvent interaction.³³ As such, we should keep in mind that colloidal NCs are *hybrid* particles, of which the overall properties are determined by the mutual interaction of the inorganic core with the ligands. The interesting optoelectronic properties predominantly originate from the size and shape of the inorganic core.

The (soft) ligand layer around the core dictates the interaction of the nanocrystals with the environment. When the ligands have a favourable interaction with the surrounding solvent they maximize their interaction by sticking out from the surface like a hedgehog. However, if the ligand-solvent interaction is unfavourable the ligands stick to each other and destabilize the nanocrystal dispersion (**Figure 2.2a**). We will discuss the properties of the ligand layer in more detail in **section 2.3.3**.

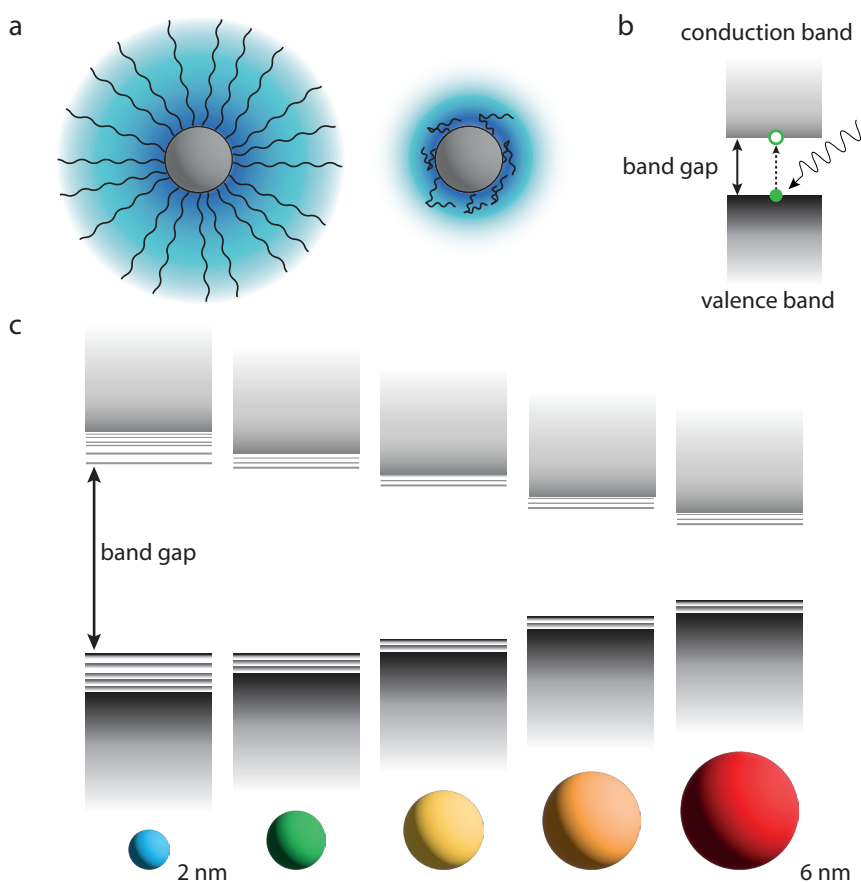


Figure 2.2 (a) Schematic representation of colloidal NCs when dispersed in a favourable and unfavourable solvent. (b) Schematic representation of the band structure of a bulk semiconductor material. (c) Schematic representation of the quantum confinement effects: the bandgap of the semiconductor material increases with decreasing size, and discrete energy levels arise at the band-edges. Note that the energy difference between the band-edge levels also increases with decreasing size.

2.3.1 The crystalline inorganic core

The colloidal NCs studied here all consist of binary II–VI semiconductors (e.g., CdS, PbSe, PbS). In bulk, these materials, like all solids, consist of a large number of closely packed atoms (more than $\sim 10^7$ atoms). When atoms bind together the wavefunctions of the valence electrons overlap and the atomic energy levels split into bonding and non-bonding molecular energy levels. In macroscopic solids the large number of atoms obscures the energy levels of the individual atoms. Instead, two energy bands with a quasi-continuous density of states are formed. The valence band (VB) is the highest energy band still occupied by electrons, while the conduction band (CB) is the highest empty band (**Figure 2.2b**). These two bands are separated by a material-dependent gap, the band gap (E_g) an area with no available energy states.³⁴ The presence of electrons in the CB determines whether a material can conduct electricity. When there are no electrons in the CB, the electrical conductance is very low, making the material an insulator, but as soon as there are electrons in the CB the material can conduct. In between these two extremes are the semiconductors, their band gap is small enough for electrons to be promoted from the VB to the CB by external energy input. As such, insulators can also be transformed into semiconductors by addition of impurity dopant atoms, these introduce energy states in the band gap from which electrons can be thermally excited into the CB.³⁵ For example, thermal energy (heat), or light (photons) with an energy at least equal to the band gap can excite these electrons to the CB (**Figure 2.2b**). An excited electron (e^-), leaves a hole (h^+) behind in the VB, and together they form an electron-hole pair, an ‘exciton’. When the electron and hole recombine, it can result in the emission of a photon with the precise energy of the band gap but non-radiative pathways are possible as well.

As semiconductors become smaller than ~ 100 nm (consisting of less than $\sim 10^7$ atoms), their physical and chemical properties become size-dependent. Two fundamental nanoscale effects are the cause of this, the first being the increase in the number of atoms at the surface relative to the internal atoms. Atoms at the surface have fewer neighbouring atoms than the inner particles and thus they have unsaturated chemical bonds (“dangling orbitals”). The second effect is spatial confinement, as the NCs become smaller than ~ 100 nm, the number of atoms in the particle decreases (to 10^6 or even fewer atoms). Thus, less atomic orbitals are available to form the band structure while the nanocrystals approach the exciton Bohr radius (a_0). This material dependent length scale describes the spatial expansion of the excitons in the solid and ranges from ~ 2 to 50 nm. In bulk material the excitons have a natural size decided by the kinetic energy of the carriers and their attraction, but in NCs they become confined. Thus, the band gap increases while the continuous spectrum of electronic states becomes discrete.³⁶ In addition, confinement is also influenced by the shape of the nanocrystal, a sphere induces quantum confinement in 3 dimensions. However, in a rod the excitons are confined in only two dimensions. Nanosheets or nanoplatelets allow confinement to even be brought down to atomic level control, one atom layer less and the confinement increases significantly.

The size-dependence of the NC band-gap allows the direct tuning with high quality control of the optical properties of the semiconductor NCs through a wide range of wavelengths.³⁷ However, the spectral region in which the NCs can be tuned is largely influenced by the exciton Bohr radius of the material. For example, NCs made from cadmium selenide (CdSe) have been studied extensively, partially due to their beautiful emitting colours. The bulk band gap of CdSe is 1.74 eV (712 nm), and all light with a higher energy than the band gap is absorbed while the red light is reflected. Thus, the colour of bulk CdSe is red. The exciton Bohr radius

is only 6 nm,³⁶ meaning that CdSe NCs of ~ 12 nm begin to show quantum confinement. To excite the electrons from the VB to the CB, photons with higher energy than the band gap are necessary, shifting the absorption onset to higher energy (lower wavelength). After excitation, the excited electron can emit a photon, with the precise energy of the band gap, to return to the VB ground state (**Figure 2.2b**). We schematically show the size-dependence of the band gap for CdSe NCs from 2 to 6 nm in **Figure 2.2c**. There, the colour of the NCs represents the colour upon emission, i.e., the luminescence colour. However, when observing a dilution of CdSe NCs in daylight (**Figure 2.3a**), the colour is less clear than under UV-excitation where we do observe the beautiful colours of the emitted photons (**Figure 2.3b**).

By contrast, lead selenide (PbSe), has a much smaller bulk bandgap of 0.27 eV (4592 nm) and an exciton Bohr radius of 46 nm.³⁸ Thus, the absorption spectrum of all PbSe NCs lies outside of the visible range, all visible light is absorbed and the dispersion appears black. (**Figure 2.3b**) However, the principle is the same and the optical properties of PbSe can be tuned in the IR in a similar fashion as for CdSe.

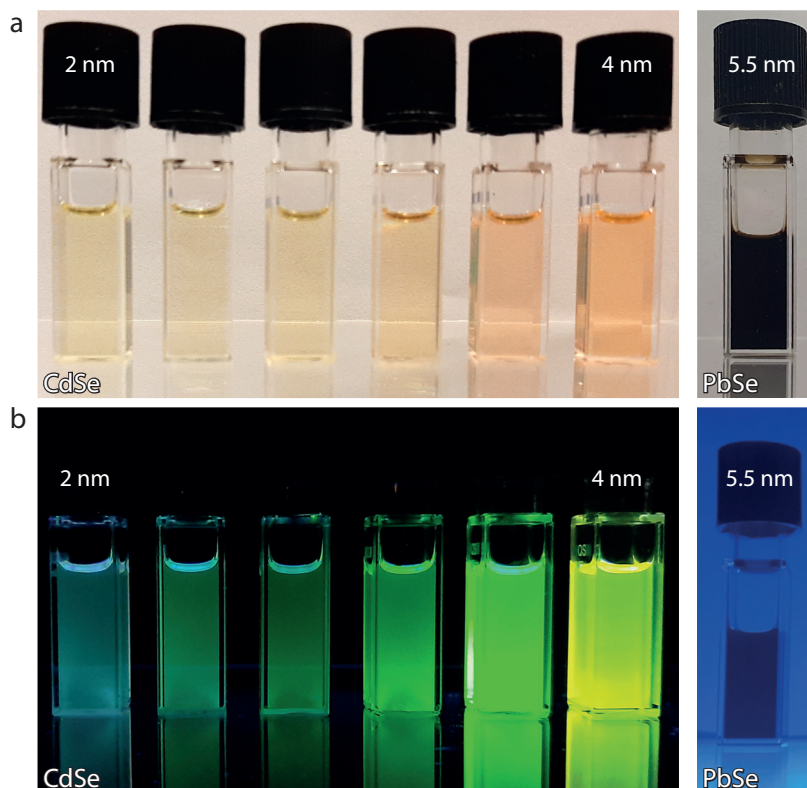


Figure 2.3 (a) Pictures of CdSe and PbSe NC dispersions in daylight and under excitation with a UV-lamp (b). While CdSe shows a nice variety of colours, the band gap of PbSe NCs lies in the near-infrared resulting in a black dispersion under both conditions. Figure prepared with input from Relinde Moes and Elleke van Harten.

2.3.2 Cation exchange in colloidal nanocrystals

After synthesis, the crystalline core of the colloidal NCs can be further customised with post-synthetic treatments, one of which is a cation exchange reactions. All colloidal NCs studied here consist of large anions (S^{2-} , Se^{2-}) and smaller cations (Pb^{2+} , Cd^{2+}). In **Figure 2.4** on the left we show a schematic depiction of a PbSe NC synthesized by wet-chemical synthesis. In a cation exchange reaction, the cations of the parent NCs are substituted by a new cation. Thus, NCs with an AX composition (A being the cation, X being the anion) can be (partially) exchanged into BX NCs. During these reactions the anion sublattice is not significantly altered or distorted. It can function as a structural framework while the exchange occurs, even when degree and rate of cation exchange is high.³⁹ We note here that anion exchange is also possible, but due to the larger size and lower diffusivity of these ions that exchange is more challenging in a controlled manner.⁴⁰⁻⁴⁴

In a cation exchange reaction, the parent NCs can be either completely exchanged (BX),^{45,46} partially exchanged ($A_{1-y}B_yX$) or can form heterostructures (AX/BX) with atomically sharp interfaces and band gap offsets.⁴⁷⁻⁴⁹ Remarkably, the size, shape and crystal structure of the “parent” NCs is preserved in these reactions due to the stable anion framework. Consequently, cation exchange reactions were developed into a powerful post-synthetic tool with which to obtain colloidal quantum materials that are unattainable or challenging to achieve by direct synthesis. The anion network is not significantly altered or distorted, allowing it to function as a structural framework whilst the exchange occurs, even in cases where the degree of cation exchange is high and the process rapid.

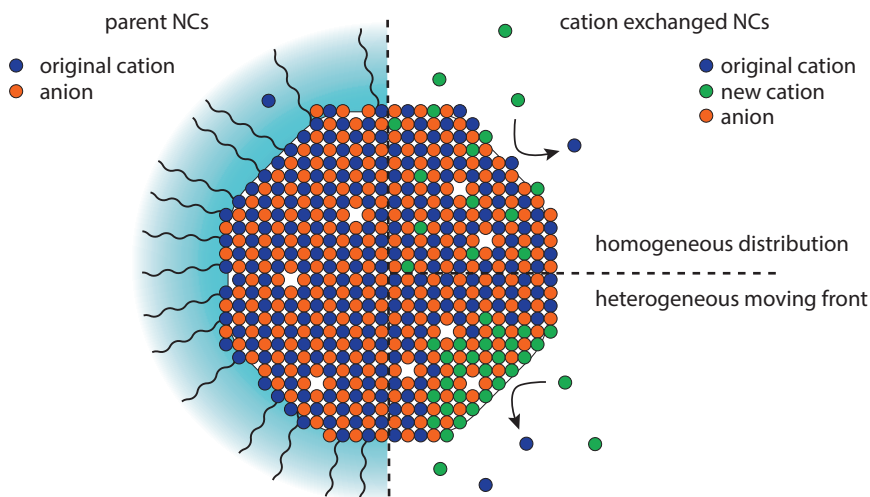


Figure 2.4 Schematic depiction of the parent NCs as synthesized (left), including ligand layer and inorganic crystalline core consisting of cations (blue) and anions (orange). The number of defects or missing ions in the image, is just to point out that any crystal will contain defects. On the right the schematic depiction of cation exchange in the parent NCs. The upper scheme displays a homogeneous distribution while the lower scheme shows a heterogeneous moving front. Figure adapted from Maarten Bransen.

In bulk crystals, long-range solid-state ion diffusion is required; then for cation exchange high temperatures and pressures are necessary (above 600 °C).⁴³ In contrast the short distances and abundance of facet/solvent interfaces of NCs makes ion diffusion (solid-state-ion diffusion) significantly easier. As such, relatively low temperatures and short reaction times (minutes to hours) are enough to achieve cation exchange. Some exchange reactions can even happen at room temperature and with stoichiometric amounts of the replacing cation (e.g. Cd²⁺ for Ag⁺ exchange in CdS NCs), but others still require higher temperatures and large excesses of the replacing cation (e.g. Pb²⁺ for Cd²⁺).³⁷

Understanding cation exchange requires consideration of the chemical equilibrium (thermodynamics) and all factors that determine the rates of cation exchange (kinetics). In the cation exchange procedure, the new cation precursor is added to a dispersion of parent NCs and the overall free energy of the reaction will determine if the exchange will proceed. This free energy of the reaction depends for example on the nature of the incoming and outgoing cations, their relative stabilities in the NCs and in solution and the overall stability of the NCs before and after exchange. Then, a chain of inherently linked elementary kinetic and thermodynamic steps have to proceed collectively for the exchange to occur.^{37,39,43,50,51} The rate at which the new cations diffuse into the parent NCs and displace the parent cations also depends on many factors: for example whether the cation can diffuse through interstitial sites, if vacancies are present (even on the surface)⁵² and if the NCs contain defects such as dislocations, stacking faults, and possible grain boundaries.^{51,53,54}

As the cations are exchanged in a NC, the area between the old and the new crystal structure, the reaction zone, is where significant structural distortions occur, where vacancies and sometimes defects form. If a NC is significantly larger than the reaction zone, only a portion of the NC at a time will experience invasive structural distortions, but a smaller NC will be completely distorted.⁴³ By studying cation exchange in anisotropic NCs, such as rectangular nano-sheets, the reaction front can be followed with respect to the crystal structure.^{55,56} The study of Cd-for-Pb exchange in anisotropic PbSe NCs by Casavola et al., allowed her to propose a plausible mechanism by which the cation exchange occurs. It was stated that the solid diffusion of Cd, Pb atoms within the nanostructure takes place through vacancy-assisted migration in the cation sublattice. It presumes that a vacancy is present at the surface, which then diffuses to the AX/BX interface. This diffusion means that B ions jump into the vacancy while also leaving a vacancy behind, an A ion can jump into the new vacancy and leave the AX core. Cascading vacancy-assisted jumps can allow the A ion to reach the surface, after which it is exchanged for a B ion and continues on into the solvent, usually assisted by a coordinating ligand.⁴⁵

There are two ways in which the new cations can spread through the parent NCs. For instance, the new cations could spread homogeneously (a uniform distribution, **Figure 2.4** right top); a type of exchange which has for instance been observed for impurity doping with magnetic cations.⁵⁷⁻⁵⁹ Or, a BX phase could replace the AX phase and form heterointerfaces (**Figure 2.4** right bottom).^{45,56,60} Usually, these interfaces form when the reactivity of the facets varies over the structure,^{61,62} or when the AX and BX lattice structures are different, e.g. rock salt PbSe versus zinc blende CdSe in Pb for Cd exchange.^{51,63-65} In **chapter 6**, we monitor the Cd-for-Pb exchange of PbS NSs. The 2D nature of these sheets allowed us to follow the cation exchange in a specific orientation by ex situ techniques.

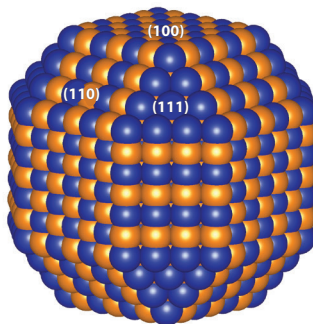
2.3.3 The organic ligand shell

Having discussed the inorganic crystalline core of the NCs, we now continue to the (organic) outer layer or “shell” of colloidal NCs (**Figure 2.5a**). Both parts can be changed separately, but their mutual interaction dictates the overall properties of the NC.³⁷ The ligand shell electronically passivates the unsaturated atoms on the surface facets of the NCs and determines the molecular interaction of the NCs with the surrounding medium. The organic surfactant molecules (i.e. ligands) are amphiphilic. They have a polar head group and a non-polar hydrocarbon tail. Ligands can form coordinating bonds between the metal ions at the surface of the NC and the unshared electrons of the electron donating atoms (such as N, O, S, P) in the polar head group. In this manner, the polar head passivates the surface and the apolar hydrocarbon tail interacts with the solvent surrounding the colloidal NCs. These tails have a favourable interaction with an apolar solvent and will extend fully to increase their contact area. Thus, they provide the NCs with colloidal stability by forming a mohawk/bristle and forming aggregates.^{66,67} However, with a polar solvent the tails interact unfavourably and preferentially attract other ligands from adjacent NCs destabilizing the colloidal NC dispersion (**Figure 2.2a**).

During the synthesis of colloidal NCs the ligands play an important role. Bulk crystals crystallize predominantly in the thermodynamically stable phase. In the case of nanocrystals, the surface stabilizing ligands can lower the surface energy of specific facets. Colloidal NCs are synthesized with a (metastable) crystal structure and overall shape influenced by the ligands. When a strong bond forms between the ligands and a facet, the growth rate on that facet will decrease, while weaker bonds can result in unstable growth. For example, the rock salt PbSe NCs shape is directly influenced by ligands. For the uncapped facets of this cubic crystal structure the (calculated) surface energy varies greatly. The nonpolar (100) facets have a low surface energy of 0.184 J m^{-2} , while the surface energy of the (110) and (111) facets are respectively 73 and 78% higher (**Table 2.1**).⁶⁸ A PbSe NC without ligands would have a cubic shape consisting of only {100} facets (**Figure 2.5b**) to minimize the overall surface energy.

Table 2.1 Overview of the calculated surface energies of a rock salt PbSe NC,⁶⁸ with a schematic depiction of such a PbSe NC below.

Facet	Number of facets on a NC	Calculated surface energy	Surface energy increase	Type	Atoms
(100)	6	0.184 J m^{-2}	-	nonpolar	Pb / Se
(110)	8	0.318 J m^{-2}	73%	nonpolar	Pb / Se
(111)	8	0.328 J m^{-2}	83%	reconstructed	Pb



In practice, the higher energy {110} and {111} facets are stabilized by ligands, resulting in NCs shaped like a truncated cube-octahedral (**Figure 2.5c**). After synthesis, large surface reconstructions can occur and the ligand density can vary, effectively varying the facet-size. When the NCs have a high ligand density, the high surface energy facets are stabilized, while a lower ligand density results in the prominence of the low energy {100} facets (**Figure 2.5d** and **e**).⁶⁹ In general, it is good to keep in mind that for a PbSe NC with a diameter of about 6.5 ± 0.3 nm and an average of 505 oleate ligands per NC, the lower and upper limit for the coverage per facet becomes $3.7\text{--}5.0$ nm⁻² for {111}, $2.0\text{--}4.3$ nm⁻² for {110}, and $0\text{--}1.0$ nm⁻² for {100}.⁷⁰ Thus, we can consider the {100} facets to be “reactive” as they both have a lower ligand density and form weaker ligand bonds.

A bond between a ligand and a surface atom can sound like something very definite, but NMR analysis has shown that the surfactant molecules bind to- and dissociate from the surface reversibly, on a bond-strength dependent timescale.^{71,72} Weaker ligands, such as amines, interact with the surface at faster rates (≥ 0.05 ms⁻¹), while ligands that form stronger bonds stay longer on the surface (s⁻¹ range).³⁷ Thus, over time the number of ligands bound to the NC surface fluctuates significantly. Consequently, NCs cannot be defined as systems with a single chemical formula, instead we should consider them as dynamic structures with batch-to-batch variations, an inconstant ligand shell and compositions and shapes that are ligand concentration-dependent. Working with colloidal NCs in a controlled manner can thus be a challenge, especially over long periods of time.

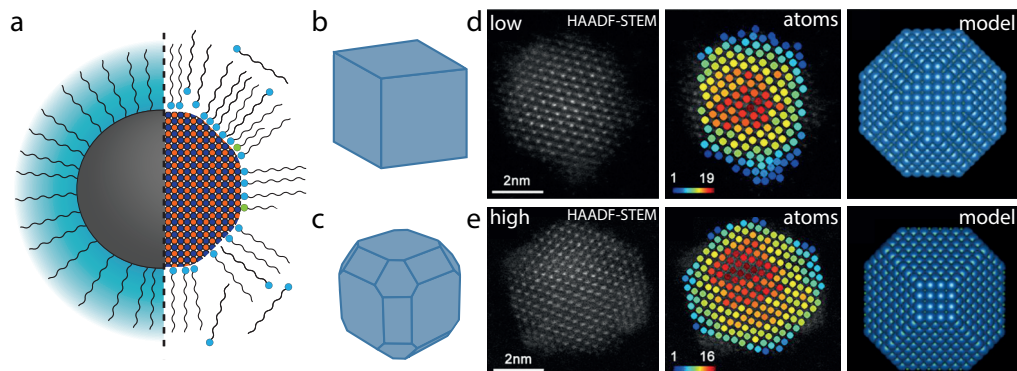


Figure 2.5 (a) A schematic and more detailed image of a colloidal NC, with amphiphilic organic molecules which bind to the crystal facets of the NC. Image adapted from Maarten Bransen. (b) Schematic model of a rock salt PbSe NC with minimized surface energy, a cube of only {100} facets. In the presence of ligands (c), the higher energy {110} and {111} facets are stabilized forming a truncated cube-octahedral. In (d) and (e) we show an HAADF-STEM study of PbSe NCs with an atom counting technique for a low and high-ligand density NC, reproduced from a paper by Peters et al.⁶⁹ The intensities of the columns in the HAADF-STEM image are integrated and the numbers of lead atoms in that row are counted and color-coded in the middle image, blue is only 1 atom but red is 16 or 19 atoms. The right panel shows the proposed model for the fitted data of multiple NCs characterized in this way. Notice the increased size of the {111} facets for the oleate-saturated NCs.

2.3.4 Ligand classification

In semiconductor NCs the surface can consist of both the metal cations and the non-metal anions. Both ions can form bonds with ligands, but the number of options for anions (e.g., S, Se, Te, P) is quite limited (typically alkyl phosphines such as trioctylphosphine are used). There are many more options for ligand head groups that bind to the metal cations (e.g., Cd, Pb, Zn), such as organic alkylamines (R-NH₂), fatty acids (R-COOH), or alkylthiols (R-SH) and even fully inorganic molecules or ions such as S²⁻ or OH⁻ were shown to work as surfactants.³⁷

The Covalent Bonds Classification (CBC) method is a way to categorize ligands by the three possible bond modes defined and depicted schematically in **Figure 2.6**. Classification is done based on the number of electrons the neutral ligand contributes to the bond that is formed with the valence shell of the surface metal cation (M).⁷³ A ligand can contribute either two (L-type), one (X-type) or zero (Z-type) electrons to the ligand-metal-bond (**Figure 2.6**). In a chemical sense, the L-type ligands (2-electron donors) are actually Lewis bases and Z-type ligands (0-electron donors) are Lewis acids. These ligands form dative bonds with L-type donors or Z-type acceptors. X-type ligands (1-electron donors) are radicals, which can form a normal covalent bond with other X-type ligands.⁷⁴ Electrostatic and covalent contributions determine the strength of Lewis acid and base interactions. Smaller and/or more charged metal ions (i.e. hard Lewis bases) will form stronger bonds with donors capable of strong electrostatic interactions (i.e. hard Lewis bases). Conversely, larger and/or less charged metal ions (i.e. soft Lewis acids) will favour larger and more polarisable ligands (i.e. soft Lewis bases).

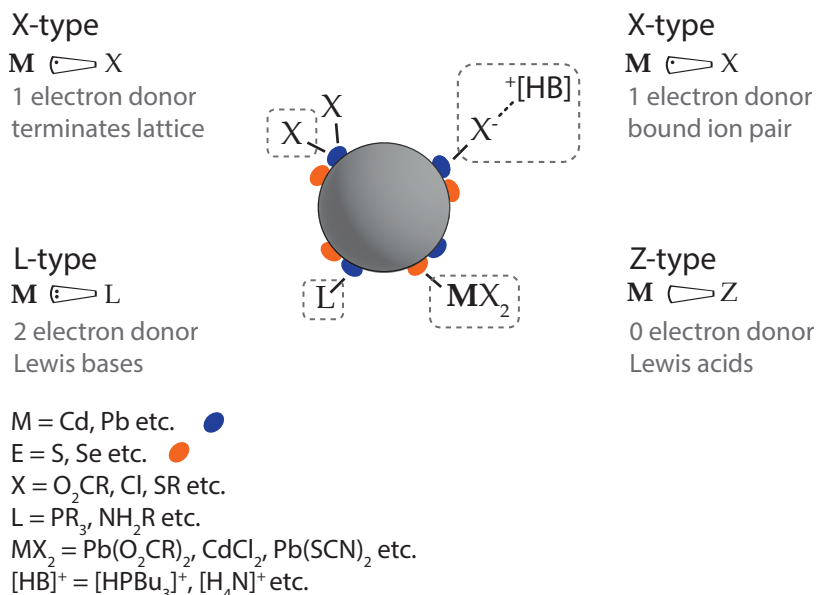


Figure 2.6 Nanocrystal ligand binding motifs as defined by the Covalent Bond Classification method.⁷³ A ligand can contribute either two (L-type), one (X-type) or zero (Z-type) electrons to the ligand-metal-bond. The X-type ligands can either terminate the crystal lattice or bind as an ion pair. In a chemical sense, the L-type ligands (2-electron donors) are actually Lewis bases, Z-type ligands (0-electron donors) are Lewis acids and X-type ligands are radicals. Schematic picture adapted from reference 32.

Post-synthetically, the original ligand shell can be exchanged but the bond strength of the native ligands largely determines the success of these treatments. The stoichiometry of semiconductor NCs and the composition of their facets greatly influences the NC ligand shell. Often, the synthesized NCs have cation rich facets,⁷⁵ which are passivated by anionic X-type ligands such as oleates.^{71,76} However, we should note again that it is not the ligand that is classified with CBC but the binding mode. Thus, oleic acid/oleate could also bind in an LX or a L_2 mode,⁷⁷ or NCs could even be rethought as a stoichiometric inorganic core which is stabilized by adsorbed lead oleate Z-type ligands. Unfortunately, solution NMR does not provide the necessary level of detail to distinguish these types of binding. Ligands weakly bonded with the surface atoms are easily replaced by stronger ligands (e.g. amines by thiols). When replacing ligands with a comparable binding strength (i.e. the same functional head group) or a weaker ligand (e.g. fatty acids by amines) a large excess of the new ligand is needed.³⁷ Keeping the CBC characterization in mind, X-type, L-type and Z-type ligands can all be exchanged by different ligands of the same type (Figure 2.7 top). Although the Z-type displacement can be promoted by an L-type ligand binding to the surface (Figure 2.7 bottom).

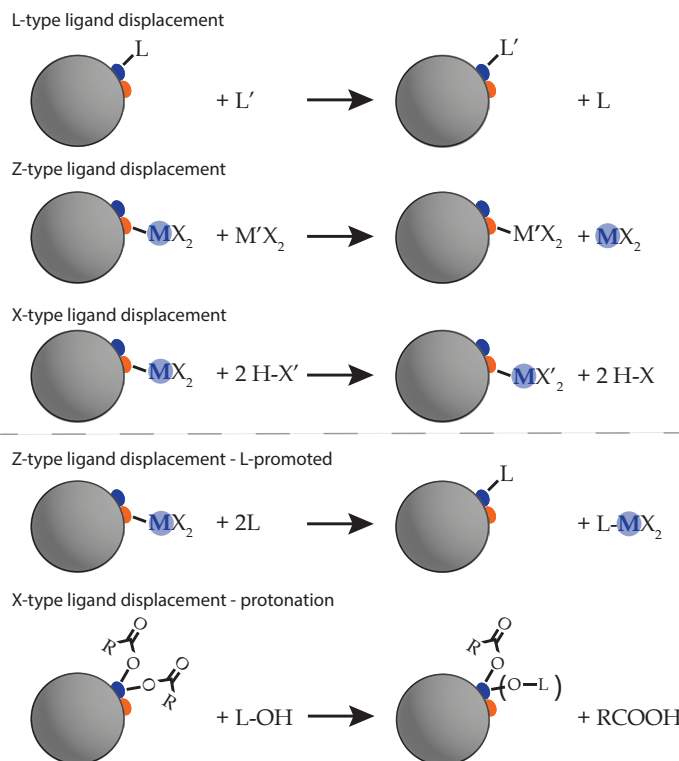


Figure 2.7 Ligand exchanges of L-, Z- and X-type with the same type of ligand (top). For Z-type also L-type promoted exchange is possible where the Z-type ligand is displaced and binds to an L-type to form a complex, as the other L-type ligand binds to the surface. X-type ligands such as oleates on PbSe NCs, need protonation before being displaced. For example, a simple alcohol could provide the proton necessary for the oleic acid to leave the surface of the NCs. There is however discussion as to whether the alkoxide then binds to the surface as an L-type ligand. Adapted from reference 71.

When NC dispersions were mixed with aprotic solvents (such as acetonitrile) no ligands were displaced, but when mixed with short-chain alcohols such as methanol roughly ~10% of the native X-type ligands was released as oleic acid.⁷⁸ It indicates the necessity for a proton transfer when displacing X-type ligands such as oleates on PbSe NCs. The short-chain alcohols can protonate the carboxylates (add a proton to a molecule or ion to form a conjugate acid) with their hydroxide group (Figure 2.7 bottom). There is however a difference in opinion as to whether an alkoxide then binds to the surface as an L-type ligand,^{75,76,78} or not.^{70,71}

2.3.5 Self-assembly and oriented attachment

The development of modern electronics in the middle of the 20th century has changed the course of human society. In these devices, semiconductor crystals, typically silicon, are used to build high-performance electronic circuits, solar cells, and light detectors. Typically, these structures are fabricated with the top-down approach: you start with a bigger structure from which you slowly remove pieces until you end up with the size and shape that you want, like cutting a statue out of marble. However, for the development of flexible or curved electronic devices, this production process can be challenging. An interesting and necessary advancement has been the development of bottom-up fabrication processes. Then, the device components are (self)assembled from (nanoscale) components, like a prefab building or a Lego set. For instance, colloidal semiconductor NCs can be (self-)assembled into thin-films and incorporated in devices. Fabricating device components with a bottom-up approach expands the possibilities for making high-performance and flexible devices with low-temperature, large area, solution-based methods. At the same time, the individual building blocks, the NCs, can be tuned individually by their size and shape, or by forming heterostructures with cation exchange. The fabrication method introduces the tools and freedom to tune the electronic materials with properties not available in traditional bulk semiconductors,⁸⁰ but it is still bound to the same physical-chemical challenges.

Until now, we have discussed NCs in dispersion i.e. stabilized in a solvent by their ligand shell. However, when incorporating NCs in electronic and opto-electronic devices these dispersions are processed into thin-films. For this, a NC dispersion can be dropcasted, spin-coated or printed onto a support; when the solvent evaporates, the NCs form a thin-film aggregate (Figure 2.8). The structure of these aggregates is dependent upon the size and shape uniformity of the individual NCs, on the solvent of the colloidal NC dispersion and on the rate at which the solvent evaporates. When the solvent evaporates quickly, and the NCs all differ in size and shape, they tend to form thin-films that are poorly ordered and glassy solids. On the other hand, the slow evaporation of a NC dispersion with a small size and shape distribution can result in thin-films with long-range order; superlattices.^{80,81} The resulting superstructures can be seen as a framework of hard spheres forming a face-centered-cubic structure (fcc). In contrast, when dispersed in a less ideal solvent the ligands become less extended and some NC attraction begins to influence the self-assembly. Then, the interactions become more soft-sphere-like, and the resulting structures are body-centered tetragonal (bct) or even body-centered cubic (bcc).^{82,83}

Whether these thin-films are amorphous/glassy or ordered, they can be incorporated in devices. However, as the NCs in dispersion (building blocks for the aggregates) consist of both the NC core and ligand layer, the organic ligands are part of the thin-films. When conducting electricity, the ligands in the thin-films form a barrier for the charge carriers. In these thin-films,

the NCs have only weak quantum mechanical coupling and maintain their own localized band structure.⁸⁴ The conducting electrons can only move through the thin-film by hopping from one NC to the next, either by quantum mechanical tunnelling or classic over the barrier “jumping”. Generally, these thin-films have carrier mobilities substantially below $1 \text{ cm}^2/(\text{V s})$.⁸⁵⁻⁸⁷ It limits the implementation of these NC thin-films in applications such as solar cells, photodetectors and field effect transistors.

By exchanging the native long organic ligands with shorter ligands or compact inorganic compounds, the NCs can get closer which reduces the potential barrier between the NCs (**Figure 2.8**). Then, the localized electronic states of the individual NCs can begin to overlap and couple with neighbouring NCs, forming new band structures which depend on the geometric arrangement of the NCs. This ligand tailoring can improve the carrier mobilities substantially, up to $1\text{--}20 \text{ cm}^2/(\text{V s})$.⁸⁸⁻⁹² In principle, eliminating the separation between the NCs could improve the mobility even further. Then the building blocks of the thin-film only consist of the inorganic NC cores, without the insulating ligand layer hindering carrier movement.

The oriented attachment process is an intriguing non-classical crystal growth mechanism, which has been observed in natural biological conditions and is assumed to be important for biomineral formation.⁹³⁻⁹⁵ There, charge-stabilized crystals in a polar liquid slowly become destabilized, allowing the attractions between crystal facets of neighbouring crystals to become dominant in the system. Thus, the dispersed crystals begin to orient these facets towards each other and move closer. When the crystal facets connect directly via covalent bonds, they form a larger crystal for which the overall surface energy is reduced in the spontaneous thermodynamic process. Elimination of two high-energy facets will result in the largest energy reduction.

In a lab environment, oriented attachment has been used to couple self-assembled ordered superstructures of NCs and form 2 and 3 dimensional superlattices with atomic alignment. In addition to an ordered structure of NCs, the formed superlattices also contain a periodic structure of nanopores (**Figure 2.8**). In practice, self-assembly and oriented attachment of lead-chalcogenide NCs (PbSe, PbS and PbTe), has been the system predominantly studied.^{82,83,96-107} These cube-octahedral NCs with a rock salt crystal structure have six chemically identical stoichiometric {100} crystal facets, eight nonstoichiometric {110} and eight nonstoichiometric {111} facets. Typically, the NC dispersion is dropcasted on top of an immiscible liquid such as ethylene glycol. As the solvent slowly evaporates, the NCs self-assemble into a structure on top of the liquid substrate. After self-assembly took place, oriented attachment can be initiated by increasing the facet-facet attraction, for example by ligand exchange with a smaller surface-active species or by desorption of the ligands from a specific facet. In the case of PbSe NCs, the low surface-energy {100} facets bind ligands weakly and in lower numbers than the other facets, meaning these facets will lose their absorbed ligands fastest.^{68,70} Once the stoichiometric {100} facets are bare, they can form irreversible epitaxial bonds with neighbouring NCs. Ideally, a crystalline neck is formed between the NCs,^{108,109} meaning that coupling of the NCs is only limited by the width of the neck formed between the NCs in the superlattice.^{110,111}

When fully controlled, oriented attachment can result in single crystals with a second periodicity on the nanoscale that cannot be achieved in any other way! Specific geometries, such as square (also with a square periodicity of voids) and honeycomb (hexagonal periodicity of voids) can be achieved during NC assembly followed by oriented attachment. The electronic band structure of square and honeycomb superlattices was different from the simple 2D sheets

or quantum wells prepared by oriented attachment.^{112,113} Specifically, honeycomb superlattices combine a conventional semiconductor band gap, but the electron conduction bands (hole valence bands) show Dirac-type bands, like those of graphene!^{114,115} Controlling oriented attachment has been an enormous challenge, and only a few research groups (and PhD candidates) have had the courage and perseverance for a research direction in this field. Basically, the larger bodies of literature on oriented attachment of lead chalcogenides can roughly be counted on two hands, amongst others the research groups of Daniel Vanmaekelbergh, Matt Law, Tobias Hanrath, Zeger Hens, Paul Alivisatos and William Tisdale have significantly contributed to our understanding of the self-assembly and oriented attachment of PbX superlattices in 2 and 3 dimensions.^{82,83,96-103,108,111,116,117} In **chapter 3**, I present a short overview of the field up until 2020. In general, separation of the self-assembly, alignment and attachment steps was shown to be advantageous for the formation of long-range ordered superlattices. Then, in **chapter 4** we discuss our results in understanding the oriented attachment of a monolayer of NCs dropcasted onto a liquid interface. There, we elucidate the drastic influence of the solvent-mediated repulsion during self-assembly on the geometry and quality of the formed 2D superlattices. If facet attractions occur too early, small domains with square and linear attachments break the long-range order in an irreversible way. But at a high solvent vapor pressure during self-assembly, a relatively open hexagonal double layer can stabilize as solvent molecules remain in between the ligands allowing the NCs to act more like “hard spheres”. When ligands are removed during this organization, NCs will align under the influence of attractive (100)/(100) attractions and finally attach irreversibly to form a honeycomb superstructure.

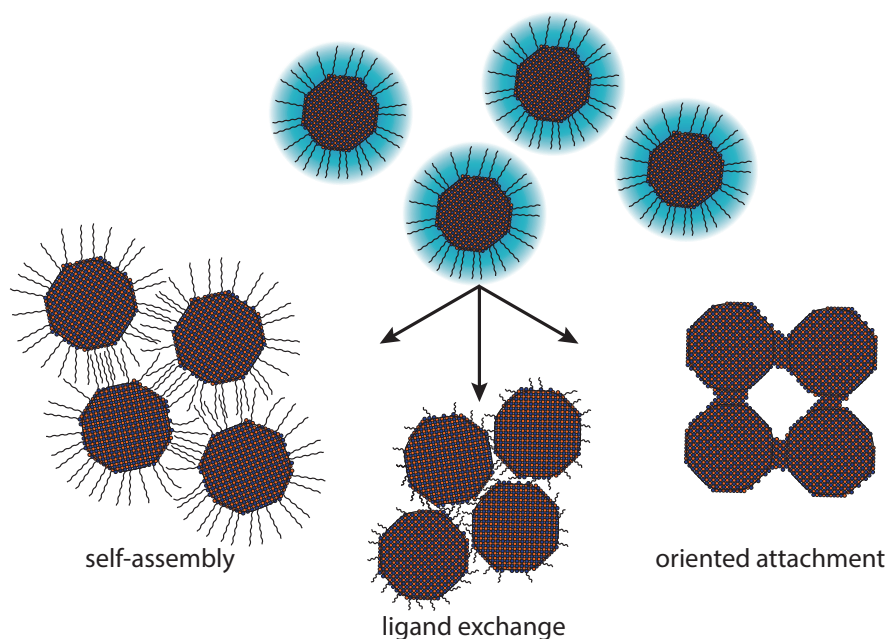


Figure 2.8 Overview of how colloidal NC dispersions can organize into ordered NC superstructures. When self-assembled and ligand exchanged the building blocks consist of the inorganic core and ligand layers whereas oriented attachment forms epitaxial connections between the NCs.

References

- [1] *Electromagnetic (EM) Spectrum*. UCAR Center for Education, **2023**. www.sciencedirect.com/learning-zone/earth-system/electromagnetic-spectrum
- [2] Palacios, A. G.; Varela, F. J.; Srivastava, R.; Goldsmith, T. H. Spectral Sensitivity of Cones in the Goldfish, *Carassius Auratus*. *Vision Research* **1998**, *38* (14), 2135-2146. DOI: 10.1016/s0042-6989(97)00411-2.
- [3] Clarke, A. C. The Next Tenants. In *Tales from the White Hart*, Ballantine Books, 1956.
- [4] Silverberg, R. How it Was When the Past Went Away. In *Three for Tomorrow*, Meredith Press, 1969.
- [5] Feynman, R. There is Plenty of Room at the Bottom. In 1959.
- [6] Taniguchi, N. On the Basic Concept of Nanotechnology. In 1974.
- [7] McCray, W. P. Will Small be Beautiful? Making Policies for our Nanotech Future. *History and Technology* **2005**, *21* (2), 177-203. DOI: 10.1080/07341510500103735.
- [8] Faber, B. Popularizing Nanoscience: The Public Rhetoric of Nanotechnology, 1986–1999. *Technical Communication Quarterly* **2006**, *15* (2), 141-169. DOI: 10.1207/s15427625tcq1502_2.
- [9] Toumey, C. The Literature of Promises. *Nature Nanotechnology* **2008**, *3* (4), 180-181. DOI: 10.1038/nnano.2008.74.
- [10] *Nanotechnology Products Database*. www.product.statnano.com
- [11] Montanarella, F.; Kovalenko, M. V. Three Millennia of Nanocrystals. *ACS Nano* **2022**, *16* (4), 5085-5102. DOI: 10.1021/acsnano.1c11159.
- [12] Thompson, R. C. *On the Chemistry of the Ancient Assyrians*; Luzar & Co, 1925.
- [13] Riva, M. A.; Lafranco, A.; D'Orso, M. I.; Cesana, G. Lead Poisoning: Historical Aspects of a Paradigmatic "Occupational and Environmental Disease". *Safety and Health at Work* **2012**, *3* (1), 11-16. DOI: 10.5491/SHAW.2012.3.1.11.
- [14] Needleman, H. L. History of Lead Poisoning in the World. At International Conference on Lead Poisoning Prevention and Treatment, Bangalore; 1999.
- [15] Zsigmondy, R. Ueber Wässrige Lösungen Metallischen Goldes. *Justus Liebig's Annalen der Chemie* **1898**, *301* (1), 29-54. DOI: 10.1002/jlac.18983010104.
- [16] Mappes, T.; Jahr, N.; Csaki, A.; Vogler, N.; Popp, J.; Fritzsche, W. The Invention of Immersion Ultramicroscopy in 1912 - The Birth of Nanotechnology? *Angew. Chem. Int. Ed.* **2012**, *51* (45), 11208-11212. DOI: 10.1002/anie.201204688.
- [17] Hartmann, P.; Jedamzik, R.; Reichel, S.; Schreder, B. Optical Glass and Glass Ceramic Historical Aspects and Recent Developments: a Schott View. *Appl. Opt.* **2010**, *49* (16). DOI: 10.1364/ao.49.00d157.
- [18] Jaekel, G. Some Modern Absorption Glasses. *Z. Tech. Phys.* **1926**, *7*, 301-304.
- [19] Rooksby, H. P. The Colour of Selenium Ruby Glasses. *J. Soc. Glass Technology* **1932**, *16*, 171-181.
- [20] Efros, A. L.; Brus, L. E. Nanocrystal Quantum Dots: From Discovery to Modern Development. *ACS Nano* **2021**, *15* (4), 6192-6210. DOI: 10.1021/acsnano.1c01399.
- [21] Ekimov, A. I., A. A. Onushchenko, and V. A. Tsekhomskii. Exciton Absorption by Copper Chloride Crystals in a Glassy Matrix. *Fiz. Khim. Stekla* **1980**, *6*, 511-512.
- [22] Ekimov, A. I. Quantum Size Effect in Three-Dimensional Microscopic Semiconductor Crystals. *JETP Letters* **1981**, *34* (6), 345-349.
- [23] Rossetti, R.; Nakahara, S.; Brus, L. E. Quantum Size Effects in the Redox Potentials, Resonance Raman Spectra, and Electronic Spectra of CdS Crystallites in Aqueous Solution. *J. Chem. Phys.* **1983**, *79* (2), 1086-1088. DOI: 10.1063/1.445834.
- [24] Efros, A. L.; Efros, A. L. Interband Absorption of Light in a Semiconductor Sphere. *Sov. Phys. Semicond.* **1982**, *16* (7), 772-775.
- [25] Ekimov. Optics of Zero Dimensional Semiconductor Systems. *Acta Physica Polonica* **1991**, *79* (1).
- [26] Ithurria, S.; Dubertret, B. Quasi 2D Colloidal CdSe Platelets with Thicknesses Controlled at the Atomic Level. *J. Am. Chem. Soc.* **2008**, *130* (49), 16504-16505. DOI: 10.1021/ja807724e.
- [27] Berends, A. C.; de Mello Donega, C. Ultrathin One- and Two-Dimensional Colloidal Semiconductor Nanocrystals: Pushing Quantum Confinement to the Limit. *J. Phys. Chem. Lett.* **2017**, *8* (17), 4077-4090. DOI: 10.1021/acs.jpcl.7b01640.
- [28] Berends, A. C.; Mangnus, M. J. J.; Xia, C.; Rabouw, F. T.; de Mello Donega, C. Optoelectronic Properties of Ternary I-III-VI₂ Semiconductor Nanocrystals: Bright Prospects with Elusive Origins. *J. Phys. Chem. Lett.* **2019**, *10*, 1600-1616. DOI: 10.1021/acs.jpcl.8b03653.

- [29] Diroll, B. T.; Guzelurk, B.; Po, H.; Dabard, C.; Fu, N.; Makke, L.; Lhuillier, E.; Ithurria, S. 2D II-VI Semiconductor Nanoplatelets: From Material Synthesis to Optoelectronic Integration. *Chem. Rev.* **2023**, *123* (7), 3543-3624. DOI: 10.1021/acs.chemrev.2c00436.
- [30] Atkins, P. W.; Overton, T. L.; Rourke, J. P.; Weller, M. T.; Armstrong, F. A. *Shriver and Atkins' Inorganic Chemistry*; Oxford University Press, 2010.
- [31] Houtepen, A. J.; Koole, R.; Vanmaekelbergh, D.; Meeldijk, J.; Hickey, S. G. The Hidden Role of Acetate in the PbSe Nanocrystal Synthesis. *J. Am. Chem. Soc.* **2006**, *128* (21), 6792-6793. DOI: 10.1021/ja061644v.
- [32] Owen, J. S. The Coordination Chemistry of Nanocrystal Surfaces. *Science* **2015**, *347* (6222), 615-616. DOI: 10.1126/science.1259924.
- [33] Mourdikoudis, S.; Liz-Marzán, L. M. Oleylamine in Nanoparticle Synthesis. *Chem. Mater.* **2013**, *25* (9), 1465-1476. DOI: 10.1021/cm4000476.
- [34] Filler, M. Semiconductors, Principles. In *Encyclopedia of Applied Electrochemistry*, Ota, K. I., Kreysa, G., & Savinell, R. F. Ed.; Springer, 2014; pp 1953-1958.
- [35] Zunger, A.; Malyi, O. I. Understanding Doping of Quantum Materials. *Chem. Rev.* **2021**, *121* (5), 3031-3060. DOI: 10.1021/acs.chemrev.0c00608.
- [36] Wise, F. W. Lead Salt Quantum Dots: the Limit of Strong Quantum Confinement. *Acc. Chem. Res.* **2000**, *33* (11), 773-780. DOI: 10.1021/ar970220q.
- [37] de Mello Donegá, C. *Nanoparticles: Workhorses of Nanoscience*; 2014. DOI: 10.1007/978-3-662-44823-6.
- [38] Murphy, J. E.; Beard, M. C.; Norman, A. G.; Ahrenkiel, S. P.; Johnson, J. C.; Yu, P.; Micic, O. I.; Ellingson, R. J.; Nozik, A. J. PbTe Colloidal Nanocrystals: Synthesis, Characterization, and Multiple Exciton Generation. *J. Am. Chem. Soc.* **2006**, *128* (10), 3241-3247. DOI: 10.1021/ja0574973.
- [39] Gupta, S.; Kershaw, S. V.; Rogach, A. L. 25th Anniversary Article: Ion Exchange in Colloidal Nanocrystals. *Adv. Mater.* **2013**, *25* (48), 6923-6943. DOI: 10.1002/adma.201302400.
- [40] Yin, Y.; Rioux, R. M.; Erdonmez, C. K.; Hughes, S.; Somorjai, G. A.; Alivisatos, A. P. Formation of Hollow Nanocrystals Through the Nanoscale Kirkendall Effect. *Science* **2004**, *304* (5671), 711-714. DOI: 10.1126/science.1096566.
- [41] Jain, P. K.; Amirav, L.; Aloni, S.; Alivisatos, A. P. Nanoheterostructure Cation Exchange: Anionic Framework Conservation. *J. Am. Chem. Soc.* **2010**, *132* (29), 9997-9999. DOI: 10.1021/ja104126u.
- [42] Saruyama, M.; So, Y. G.; Kimoto, K.; Taguchi, S.; Kanemitsu, Y.; Teranishi, T. Spontaneous Formation of Wurtzite-CdS/Zinc Blende-CdTe Heterodimers Through a Partial Anion Exchange Reaction. *J. Am. Chem. Soc.* **2011**, *133* (44), 17598-17601. DOI: 10.1021/ja2078224.
- [43] Beberwyck, B. J.; Surendranath, Y.; Alivisatos, A. P. Cation Exchange: A Versatile Tool for Nanomaterials Synthesis. *J. Phys. Chem. C* **2013**, *117* (39), 19759-19770. DOI: 10.1021/jp405989z.
- [44] Saruyama, M.; Sato, R.; Teranishi, T. Transformations of Ionic Nanocrystals via Full and Partial Ion Exchange Reactions. *Acc. Chem. Res.* **2021**, *54* (4), 765-775. DOI: 10.1021/acs.accounts.0c00701.
- [45] Casavola, M.; van Huis, M. A.; Bals, S.; Lambert, K.; Hens, Z.; Vanmaekelbergh, D. Anisotropic Cation Exchange in PbSe/CdSe Core/Shell Nanocrystals of Different Geometry. *Chem. Mater.* **2011**, *24* (2), 294-302. DOI: 10.1021/cm202796s.
- [46] Galle, T.; Khoshkhoo, M. S.; Martin-Garcia, B.; Meerbach, C.; Sayevich, V.; Koitzsch, A.; Lesnyak, V.; Eychmuller, A. Colloidal PbSe Nanoplatelets of Varied Thickness with Tunable Optical Properties. *Chem. Mater.* **2019**, *31* (10), 3803-3811. DOI: 10.1021/acs.chemmater.9b01330.
- [47] Pietryga, J. M.; Werder, D. J.; Williams, D. J.; Casson, J. L.; Schaller, R. D.; Klimov, V. I.; Hollingsworth, J. A. Utilizing the Lability of Lead Selenide to Produce Heterostructured Nanocrystals with Bright, Stable Infrared Emission. *J. Am. Chem. Soc.* **2008**, *130* (14), 4879-4885. DOI: 10.1021/ja710437r.
- [48] Costi, R.; Saunders, A. E.; Banin, U. Colloidal Hybrid Nanostructures: a New Type of Functional Materials. *Angew. Chem. Int. Ed.* **2010**, *49* (29), 4878-4897. DOI: 10.1002/anie.200906010.
- [49] de Mello Donegá, C. Synthesis and Properties of Colloidal Heteronanocrystals. *Chem. Soc. Rev.* **2011**, *40* (3), 1512-1546. DOI: 10.1039/c0cs00055h.
- [50] Rivest, J. B.; Jain, P. K. Cation Exchange on the Nanoscale: An Emerging Technique for new Material Synthesis, Device Fabrication, and Chemical Sensing. *Chem. Soc. Rev.* **2013**, *42* (1), 89-96. DOI: 10.1039/c2cs35241a.
- [51] De Trizio, L.; Manna, L. Forging Colloidal Nanostructures via Cation Exchange Reactions. *Chem. Rev.* **2016**, *116* (18), 10852-10887. DOI: 10.1021/acs.chemrev.5b00739.
- [52] Justo, Y.; Sagar, L. K.; Flamee, S.; Zhao, Q.; Vantomme, A.; Hens, Z. Less Is More. Cation Exchange and the Chemistry of the Nanocrystal Surface. *ACS Nano* **2014**, *8* (8), 7948-7957. DOI: 10.1021/nn5037812.
- [53] Justo, Y.; Goris, B.; Kamal, J. S.; Geiregat, P.; Bals, S.; Hens, Z. Multiple Dot-in-Rod PbS/CdS Heterostructures with High Photoluminescence Quantum Yield in the Near-Infrared. *J. Am. Chem. Soc.* **2012**, *134* (12), 5484-5487. DOI: 10.1021/ja300337d.

- [54] Lesnyak, V.; Brescia, R.; Messina, G. C.; Manna, L. Cu Vacancies Boost Cation Exchange Reactions in Copper Selenide Nanocrystals. *J. Am. Chem. Soc.* **2015**, *137* (29), 9315-9323. DOI: 10.1021/jacs.5b03868.
- [55] Miszta, K.; Dorfs, D.; Genovese, A.; Kim, M. R.; Manna, L. Cation Exchange Reactions in Colloidal Branched Nanocrystals. *ACS Nano* **2011**, *5* (9), 7176-7183. DOI: 10.1021/nn201988w.
- [56] Salzmann, B. B. V.; Wit, J.; Li, C.; Arenas-Esteban, D.; Bals, S.; Meijerink, A.; Vanmaekelbergh, D. Two-Dimensional CdSe-PbSe Heterostructures and PbSe Nanoplatelets: Formation, Atomic Structure, and Optical Properties. *J. Phys. Chem. C* **2022**, *126* (3), 1513-1522. DOI: 10.1021/acs.jpcc.1c09412.
- [57] Sahu, A.; Kang, M. S.; Kompch, A.; Notthoff, C.; Wills, A. W.; Deng, D.; Winterer, M.; Frisbie, C. D.; Norris, D. J. Electronic Impurity Doping in CdSe Nanocrystals. *Nano Lett.* **2012**, *12* (5), 2587-2594. DOI: 10.1021/nl300880g.
- [58] Vlaskin, V. A.; Barrows, C. J.; Erickson, C. S.; Gamelin, D. R. Nanocrystal Diffusion Doping. *J. Am. Chem. Soc.* **2013**, *135* (38), 14380-14389. DOI: 10.1021/ja4072207.
- [59] Barrows, C. J.; Chakraborty, P.; Kornowske, L. M.; Gamelin, D. R. Tuning Equilibrium Compositions in Colloidal Cd_{1-x}Mn_xSe Nanocrystals Using Diffusion Doping and Cation Exchange. *ACS Nano* **2016**, *10* (1), 910-918. DOI: 10.1021/acsnano.5b07389.
- [60] Zhang, J.; Chernomordik, B. D.; Crisp, R. W.; Kroupa, D. M.; Luther, J. M.; Miller, E. M.; Gao, J.; Beard, M. C. Preparation of Cd/Pb Chalcogenide Heterostructured Janus Particles via Controllable Cation Exchange. *ACS Nano* **2015**, *9* (7), 7151-7163. DOI: 10.1021/acsnano.5b01859.
- [61] Sadtler, B.; Demchenko, D. O.; Zheng, H.; Hughes, S. M.; Merkle, M. G.; Dahmen, U.; Wang, L. W.; Alivisatos, A. P. Selective Facet Reactivity During Cation Exchange in Cadmium Sulfide Nanorods. *J. Am. Chem. Soc.* **2009**, *131* (14), 5285-5293. DOI: 10.1021/ja809854q.
- [62] Hewavitharana, I. K.; Brock, S. L. When Ligand Exchange Leads to Ion Exchange: Nanocrystal Facets Dictate the Outcome. *ACS Nano* **2017**, *11* (11), 11217-11224. DOI: 10.1021/acsnano.7b05534.
- [63] Son, D. H.; Hughes, S. M.; Yin, Y.; Paul Alivisatos, A. Cation Exchange Reactions in Ionic Nanocrystals. *Science* **2004**, *306* (5698), 1009-1012. DOI: 10.1126/science.1103755.
- [64] Bals, S.; Casavola, M.; van Huis, M. A.; Van Aert, S.; Batenburg, K. J.; Van Tendeloo, G.; Vanmaekelbergh, D. Three-Dimensional Atomic Imaging of Colloidal Core-Shell Nanocrystals. *Nano Lett.* **2011**, *11* (8), 3420-3424. DOI: 10.1021/nl201826e.
- [65] Jia, G.; Pang, Y.; Ning, J.; Banin, U.; Ji, B. Heavy-Metal-Free Colloidal Semiconductor Nanorods: Recent Advances and Future Perspectives. *Adv. Mater.* **2019**, *31* (25), e1900781. DOI: 10.1002/adma.201900781.
- [66] Atkins, P. W.; de Paula, J.; Keeler, J. *Physical Chemistry*; Oxford University Press, 2014.
- [67] Heuer-Jungemann, A.; Feliu, N.; Bakaimi, I.; Hamaly, M.; Alkilany, A.; Chakraborty, I.; Masood, A.; Casula, M. F.; Kostopoulou, A.; Oh, E.; et al. The Role of Ligands in the Chemical Synthesis and Applications of Inorganic Nanoparticles. *Chem. Rev.* **2019**. DOI: 10.1021/acs.chemrev.8b00733.
- [68] Fang, C.; van Huis, M. A.; Vanmaekelbergh, D.; Zandbergen, H. W. Energetics of Polar and Nonpolar Facets of PbSe Nanocrystals from Theory and Experiment. *ACS Nano* **2010**, *4* (1), 211-218. DOI: 10.1021/nn9013406.
- [69] Peters, J. L.; van den Bos, K. H. W.; Van Aert, S.; Goris, B.; Bals, S.; Vanmaekelbergh, D. Ligand-Induced Shape Transformation of PbSe Nanocrystals. *Chem. Mater.* **2017**, *29* (9), 4122-4128. DOI: 10.1021/acs.chemmater.7b01103.
- [70] Abelson, A.; Qian, C.; Salk, T.; Luan, Z.; Fu, K.; Zheng, J. G.; Wardini, J. L.; Law, M. Collective Topo-Epitaxy in the Self-Assembly of a 3D Quantum Dot Superlattice. *Nat. Mater.* **2020**, *19* (1), 49-55. DOI: 10.1038/s41563-019-0485-2.
- [71] Anderson, N. C.; Hendricks, M. P.; Choi, J. J.; Owen, J. S. Ligand Exchange and the Stoichiometry of Metal Chalcogenide Nanocrystals: Spectroscopic Observation of Facile Metal-Carboxylate Displacement and Binding. *J. Am. Chem. Soc.* **2013**, *135* (49), 18536-18548. DOI: 10.1021/ja4086758.
- [72] Moreels, I.; Justo, Y.; De Geyter, B.; Haustraete, K.; Martins, J. C.; Hens, Z. Size-Tunable, Bright, and Stable PbS Quantum Dots: a Surface Chemistry Study. *ACS Nano* **2011**, *5* (3), 2004-2012. DOI: 10.1021/nn103050w.
- [73] Green, M. L. H. A New Approach to the Formal Classification of Covalent Compounds of the Elements. *J. Organomet. Chem.* **1995**, *500* (1-2), 127-148. DOI: 10.1016/0022-328x(95)00508-N.
- [74] Green, M. L. H.; Parkin, G. Application of the Covalent Bond Classification Method for the Teaching of Inorganic Chemistry. *J. Chem. Educ.* **2014**, *91* (6), 807-816. DOI: 10.1021/ed400504f.
- [75] Moreels, I.; Fritzing, B.; Martins, J. C.; Hens, Z. Surface Chemistry of Colloidal PbSe Nanocrystals. *J. Am. Chem. Soc.* **2008**, *130* (45), 15081-15086. DOI: 10.1021/ja803994m.
- [76] Fritzing, B.; Capek, R. K.; Lambert, K.; Martins, J. C.; Hens, Z. Utilizing Self-Exchange to Address the Binding of Carboxylic Acid Ligands to CdSe Quantum Dots. *J. Am. Chem. Soc.* **2010**, *132* (29), 10195-10201. DOI: 10.1021/ja104351q.
- [77] De Roo, J. The Surface Chemistry of Colloidal Nanocrystals Capped by Organic Ligands. *Chem. Mater.* **2023**, *35* (10), 3781-3792. DOI: 10.1021/acs.chemmater.3c00638.

- [78] Hassinen, A.; Moreels, I.; De Nolf, K.; Smet, P. F.; Martins, J. C.; Hens, Z. Short-Chain Alcohols Strip X-Type Ligands and Quench the Luminescence of PbSe and CdSe Quantum Dots, Acetonitrile Does Not. *J. Am. Chem. Soc.* **2012**, *134* (51), 20705-20712. DOI: 10.1021/ja308861d.
- [79] Gomes, R.; Hassinen, A.; Szczygiel, A.; Zhao, Q.; Vantomme, A.; Martins, J. C.; Hens, Z. Binding of Phosphonic Acids to CdSe Quantum Dots: A Solution NMR Study. *J. Phys. Chem. Lett.* **2011**, *2* (3), 145-152. DOI: 10.1021/jz1016729.
- [80] Kagan, C. R.; Lifshitz, E.; Sargent, E. H.; Talapin, D. V. Building Devices from Colloidal Quantum Dots. *Science* **2016**, *353* (6302). DOI: 10.1126/science.aac5523.
- [81] Murray, C. B.; Kagan, C. R.; Bawendi, M. G. Self-Organization of CdSe Nanocrystallites into Three-Dimensional Quantum Dot Superlattices. *Science* **1995**, *270* (5240), 1335-1338. DOI: 10.1126/science.270.5240.1335.
- [82] Bian, K.; Choi, J. J.; Kaushik, A.; Clancy, P.; Smilgies, D. M.; Hanrath, T. Shape-Anisotropy Driven Symmetry Transformations in Nanocrystal Superlattice Polymorphs. *ACS Nano* **2011**, *5* (4), 2815-2823. DOI: 10.1021/nn103303q.
- [83] Choi, J. J.; Bealing, C. R.; Bian, K.; Hughes, K. J.; Zhang, W.; Smilgies, D. M.; Hennig, R. G.; Engstrom, J. R.; Hanrath, T. Controlling Nanocrystal Superlattice Symmetry and Shape-Anisotropic Interactions Through Variable Ligand Surface Coverage. *J. Am. Chem. Soc.* **2011**, *133* (9), 3131-3138. DOI: 10.1021/ja110454b.
- [84] Araujo, J. J.; Brozek, C. K.; Kroupa, D.; Gamelin, D. R. Degenerately n-Doped Colloidal PbSe Quantum Dots: Band Assignments and Electrostatic Effects. *Nano Lett.* **2018**, *18*, 3893-3900. DOI: 10.1021/acs.nanolett.8b01235.
- [85] Roest, A. L.; Houtepen, A. J.; Kelly, J. J.; Vanmaekelbergh, D. Electron-Conducting Quantum-Dot Solids with Ionic Charge Compensation. *Faraday Discuss.* **2004**, *125*, 55-62. DOI: 10.1039/b302839a.
- [86] Chandler, R. E.; Houtepen, A. J.; Nelson, J.; Vanmaekelbergh, D. Electron Transport in Quantum Dot Solids: Monte Carlo Simulations of the Effects of Shell Filling, Coulomb Repulsions, and Site Disorder. *Phys. Rev. B* **2007**, *75* (8). DOI: 10.1103/PhysRevB.75.085325.
- [87] Houtepen, A. J.; Kockmann, D.; Vanmaekelbergh, D. Reappraisal of Variable-Range Hopping in Quantum-Dot Solids. *Nano Lett.* **2008**, *8* (10), 3516-3520. DOI: 10.1021/nl8020347.
- [88] Yu, D.; Wang, C.; Guyot-Sionnest, P. n-Type Conducting CdSe Nanocrystal Solids. *Science* **2003**, *300* (5623), 1277-1280. DOI: 10.1126/science.1084424.
- [89] Lee, J.-S.; Kovalenko, M. V.; Huang, J.; Chung, D. S.; Talapin, D. V. Band-Like Transport, High Electron Mobility and High Photoconductivity in All-Inorganic Nanocrystal Arrays. *Nature Nanotechnology* **2011**, *6* (6), 348-352. DOI: 10.1038/nnano.2011.46.
- [90] Oh, S. J.; Wang, Z.; Berry, N. E.; Choi, J. H.; Zhao, T.; Gauling, E. A.; Paik, T.; Lai, Y.; Murray, C. B.; Kagan, C. R. Engineering Charge Injection and Charge Transport for High Performance PbSe Nanocrystal Thin Film Devices and Circuits. *Nano Lett.* **2014**, *14* (11), 6210-6216. DOI: 10.1021/nl502491d.
- [91] Sandeep, C. S.; Azpiroz, J. M.; Evers, W. H.; Boehme, S. C.; Moreels, I.; Kinge, S.; Siebbeles, L. D.; Infante, I.; Houtepen, A. J. Epitaxially Connected PbSe Quantum-Dot Films: Controlled Neck Formation and Optoelectronic Properties. *ACS Nano* **2014**, *8* (11), 11499-11511. DOI: 10.1021/nn504679k.
- [92] Lan, X. Z.; Chen, M. L.; Hudson, M. H.; Kamysbayev, V.; Wang, Y. Y.; Guyot-Sionnest, P.; Talapin, D. V. Quantum Dot Solids Showing State-Resolved Band-Like Transport. *Nat. Mater.* **2020**, *19* (3), 323-329. DOI: 10.1038/s41563-019-0582-2.
- [93] Alivisatos, A. P. Biomineralization. Naturally Aligned Nanocrystals. *Science* **2000**, *289* (5480), 736-737. DOI: 10.1126/science.289.5480.736.
- [94] Niederberger, M.; Colfen, H. Oriented Attachment and Mesocrystals: Non-Classical Crystallization Mechanisms Based on Nanoparticle Assembly. *Phys. Chem. Chem. Phys.* **2006**, *8* (28), 3271-3287. DOI: 10.1039/b604589h.
- [95] Chen, J. D.; Wang, Y. J.; Wei, K.; Zhang, S. H.; Shi, X. T. Self-Organization of Hydroxyapatite Nanorods Through Oriented Attachment. *Biomaterials* **2007**, *28* (14), 2275-2280. DOI: 10.1016/j.biomaterials.2007.01.033.
- [96] Evers, W. H.; De Nijs, B.; Filion, L.; Castillo, S.; Dijkstra, M.; Vanmaekelbergh, D. Entropy-Driven Formation of Binary Semiconductor-Nanocrystal Superlattices. *Nano Lett.* **2010**, *10* (10), 4235-4241. DOI: 10.1021/nl102705p.
- [97] Choi, J. J.; Bian, K.; Baumgardner, W. J.; Smilgies, D. M.; Hanrath, T. Interface-Induced Nucleation, Orientational Alignment and Symmetry Transformations in Nanocube Superlattices. *Nano Lett.* **2012**, *12* (9), 4791-4798. DOI: 10.1021/nl3026289.
- [98] Evers, W. H.; Goris, B.; Bals, S.; Casavola, M.; de Graaf, J.; van Roij, R.; Dijkstra, M.; Vanmaekelbergh, D. Low-Dimensional Semiconductor Superlattices Formed by Geometric Control over Nanocrystal Attachment. *Nano Lett.* **2013**, *13* (6), 2317-2323. DOI: 10.1021/nl303322k.
- [99] Walravens, W.; De Roo, J.; Drijvers, E.; Ten Brinck, S.; Solano, E.; Dendooven, J.; Detavernier, C.; Infante, I.; Hens, Z. Chemically Triggered Formation of Two-Dimensional Epitaxial Quantum Dot Superlattices. *ACS Nano* **2016**, *10* (7), 6861-6870. DOI: 10.1021/acsnano.6b02562.

- [100] Weidman, M. C.; Smilgies, D. M.; Tisdale, W. A. Kinetics of the Self-Assembly of Nanocrystal Superlattices Measured by Real-Time In Situ X-Ray Scattering. *Nat. Mater.* **2016**, *15* (7), 775-781. DOI: 10.1038/nmat4600.
- [101] Ondry, J. C.; Hauwiler, M. R.; Alivisatos, A. P. Dynamics and Removal Pathway of Edge Dislocations in Imperfectly Attached PbTe Nanocrystal Pairs: Toward Design Rules for Oriented Attachment. *ACS Nano* **2018**, *12* (4), 3178-3189. DOI: 10.1021/acsnano.8b00638.
- [102] van Overbeek, C.; Peters, J. L.; van Rossum, S. A. P.; Smits, M.; van Huis, M. A.; Vanmaekelbergh, D. Interfacial Self-Assembly and Oriented Attachment in the Family of PbX (X = S, Se, Te) Nanocrystals. *J. Phys. Chem. C* **2018**, *122* (23), 12464-12473. DOI: 10.1021/acs.jpcc.8b01876.
- [103] McCray, A. R. C.; Savitzky, B. H.; Whitham, K.; Hanrath, T.; Kourkoutis, L. F. Orientational Disorder in Epitaxially Connected Quantum Dot Solids. *ACS Nano* **2019**. DOI: 10.1021/acsnano.9b04951.
- [104] Cimada da Silva, J.; Balazs, D. M.; Dunbar, T. A.; Hanrath, T. Fundamental Processes and Practical Considerations of Lead Chalcogenide Mesocrystals Formed via Self-Assembly and Directed Attachment of Nanocrystals at a Fluid Interface. *Chem. Mater.* **2021**. DOI: 10.1021/acs.chemmater.1c02910.
- [105] van der Sluijs, M. M.; Sanders, D.; Jansen, K. J.; Soligno, G.; Vanmaekelbergh, D.; Peters, J. L. On the Formation of Honeycomb Superlattices from PbSe Quantum Dots: The Role of Solvent-Mediated Repulsion and Facet-to-Facet Attraction in NC Self-Assembly and Alignment. *J. Phys. Chem. C* **2022**. DOI: 10.1021/acs.jpcc.1c07430.
- [106] Hoglund, E. R.; Kim, G.; Kavrik, M. S.; Law, M.; Hachtel, J. A. Structural and Temperature Dependence of Emergent Electronic States in PbSe Quantum Dot Superlattices. *Microsc. Microanal.* **2023**, *29*, 361. DOI: 10.1093/micmic/ozad067.168.
- [107] Pinna, J.; Mehrabi Koushki, R.; Gavhane, D. S.; Ahmadi, M.; Mutalik, S.; Zohaib, M.; Protesescu, L.; Kooi, B. J.; Portale, G.; Loi, M. A. Approaching Bulk Mobility in PbSe Colloidal Quantum Dots 3D Superlattices. *Adv. Mater.* **2023**, *35* (8), e2207364. DOI: 10.1002/adma.202207364.
- [108] Geuchies, J. J.; van Overbeek, C.; Evers, W. H.; Goris, B.; de Backer, A.; Gantapara, A. P.; Rabouw, F. T.; Hilhorst, J.; Peters, J. L.; Konovalov, O.; et al. In Situ Study of the Formation Mechanism of Two-Dimensional Superlattices from PbSe Nanocrystals. *Nat. Mater.* **2016**, *15* (12), 1248-1254. DOI: 10.1038/nmat4746.
- [109] Wang, Y.; Peng, X. X.; Abelson, A.; Zhang, B. K.; Qian, C.; Ercius, P.; Wang, L. W.; Law, M.; Zheng, H. M. In Situ TEM Observation of Neck Formation During Oriented Attachment of PbSe Nanocrystals. *Nano Research* **2019**, *12* (10), 2549-2553. DOI: 10.1007/s12274-019-2483-8.
- [110] Capiod, P.; van der Sluijs, M.; de Boer, J.; Delerue, C.; Swart, I.; Vanmaekelbergh, D. Electronic Properties of Atomically Coherent Square PbSe Nanocrystal Superlattice Resolved by Scanning Tunneling Spectroscopy. *Nanotechnology* **2021**, *32* (32). DOI: 10.1088/1361-6528/abfd57.
- [111] Walravens, W.; Solano, E.; Geenen, F.; Dendooven, J.; Gorobtsov, O.; Tadjine, A.; Mahmoud, N.; Ding, P. P.; Ruff, J. P. C.; Singer, A.; et al. Setting Carriers Free: Healing Faulty Interfaces Promotes Delocalization and Transport in Nanocrystal Solids. *ACS Nano* **2019**, *13* (11), 12774-12786. DOI: 10.1021/acsnano.9b04757.
- [112] Schliehe, C.; Juarez, B. H.; Pelletier, M.; Jander, S.; Greshnykh, D.; Nagel, M.; Meyer, A.; Foerster, S.; Kornowski, A.; Klinke, C.; et al. Ultrathin PbS Sheets by Two-Dimensional Oriented Attachment. *Science* **2010**, *329* (5991), 550-553. DOI: 10.1126/science.1188035.
- [113] Kalesaki, E.; Evers, W. H.; Allan, G.; Vanmaekelbergh, D.; Delerue, C. Electronic Structure of Atomically Coherent Square Semiconductor Superlattices with Dimensionality Below Two. *Phys. Rev. B* **2013**, *88* (11), 115431. DOI: 10.1103/PhysRevB.88.115431.
- [114] Kalesaki, E.; Delerue, C.; Morais Smith, C.; Beugeling, W.; Allan, G.; Vanmaekelbergh, D. Dirac Cones, Topological Edge States, and Nontrivial Flat Bands in Two-Dimensional Semiconductors with a Honeycomb Nanogeometry. *Phys. Rev. X* **2014**, *4* (1), 011010. DOI: 10.1103/PhysRevX.4.011010.
- [115] Beugeling, W.; Kalesaki, E.; Delerue, C.; Niquet, Y. M.; Vanmaekelbergh, D.; Morais Smith, C. Topological States in Multi-Orbital HgTe Honeycomb Lattices. *Nat. Commun.* **2015**, *6*, 6316. DOI: 10.1038/ncomms7316.
- [116] Weidman, M. C.; Nguyen, Q.; Smilgies, D. M.; Tisdale, W. A. Impact of Size Dispersity, Ligand Coverage, and Ligand Length on the Structure of PbS Nanocrystal Superlattices. *Chem. Mater.* **2018**, *30* (3), 807-816. DOI: 10.1021/acs.chemmater.7b04322.
- [117] Geuchies, J. J.; Soligno, G.; Geraffy, E.; Hendrikx, C. P.; van Overbeek, C. V.; Montanarella, F.; Slot, M. R.; Konovalov, O. V.; Petukhov, A. V.; Vanmaekelbergh, D. Unravelling Three-Dimensional Adsorption Geometries of PbSe Nanocrystal Monolayers at a Liquid-Air Interface. *Commun. Chem.* **2020**, *3* (1). DOI: 10.1038/s42004-020-0275-4.

CHAPTER 3

Oriented Attachment: From Natural Crystal Growth to a Materials Engineering Tool

Based on:
Bastiaan B.V. Salzmann*, **Maaïke M. van der Sluijs***, Giuseppe Soligno and Daniel Vanmaekelbergh,
Accounts of Chemical Research **2021**, 54 (4), 787-797.

*These authors contributed equally

Intuitively, chemists see crystals grow atom-by-atom or molecule-by-molecule, very much like a mason builds a wall, brick by brick. It is much more difficult to grasp that small crystals can meet each other in a liquid or at an interface, start to align their crystal lattices and then grow together to form one single crystal. In analogy, that looks more like prefab building. Yet, this is what happens on many occasions and can, with reason, be considered as an alternative mechanism of crystal growth. Oriented attachment is the process in which crystalline colloidal particles align their atomic lattices and grow together into a single crystal. Hence, two aligned crystals become one larger crystal by epitaxy of two specific facets, one of each crystal. If we simply consider the system of two crystals, the unifying attachment reduces the surface energy and results in an overall lower (free) energy of the system. Oriented attachment often occurs with massive numbers of crystals dispersed in a liquid phase, a sol or crystal suspension. In that case, oriented attachment lowers the total free energy of the crystal suspension, predominantly by removal of the nanocrystal/liquid interface area. Accordingly, we should start by considering colloidal suspensions with crystals as the dispersed phase, i.e., “sols”, and discuss the reasons for their thermodynamic (meta)stability and how this stability can be lowered such that oriented attachment can occur as a spontaneous thermodynamic process. Oriented attachment is a process observed both for charge-stabilized crystals in polar solvents and for ligand capped nanocrystal suspensions in nonpolar solvents. In this last system different facets can develop a very different reactivity for oriented attachment. Due to this facet selectivity, crystalline structures with very specific geometries can be grown in one, two, or three dimensions; controlled oriented attachment suddenly becomes a tool for material scientists to grow architectures that cannot be reached by any other means. We will review the work performed with PbSe and CdSe nanocrystals. The entire process, i.e., the assembly of nanocrystals, atomic alignment, and unification by attachment, is a very complex and intriguing process. Researchers have succeeded in monitoring these different steps with in situ wave scattering methods and real-space (S)TEM studies. At the same time coarse-grained molecular dynamics simulations have been used to further study the forces involved in self-assembly and attachment at an interface. We will briefly come back to some of these results in the last sections of this review.

3.1 Suspensions with (nano-)crystals as dispersed phase

We discuss systems in which crystalline solid particles are dispersed in a continuous liquid medium, hence the specific case of a “sol”. The colloidal particles have dimensions between 1 and 1000 nm, thus from a few unit cells to several thousands in one direction. Such sols can remain stable as a two-phase system for years: their (meta)stable state corresponds to a (local) minimum in the free energy. To understand the microscopic origin of colloidal stability, we have to distinguish crystal suspensions in water or other polar solvents from suspensions in organic apolar media, such as, e.g., hexane or toluene.

3.1.1 Charge-stabilized suspensions

Suspensions of inorganic crystals in water are stabilized against agglomeration by a double layer of charges: positive or negative ions at the surface of the crystals and an equal amount of counter charge present in the diffuse part of the double layer.¹ The width of this charge double layer is dependent on the concentration of ions in the medium, allowing for a subtle engineering of repulsion and attraction between the particles.² Oriented attachment between inorganic crystals in water is observed in natural biological conditions and is assumed to be important for

biomineral formation. Commonly, crystal growth by oriented attachment is coined nonclassical crystal growth,^{3,4} to distinguish it from the classical atom-by-atom (molecule-by-molecule) growth of crystals. In oriented attachment, attractions between specific facets are dominant and when facets connect, the crystal surface energy is reduced. Oriented attachment thus lowers the enthalpy of the system in a thermodynamic spontaneous process. A further review of attachment in polar solvents can be found in [supporting information S3.1](#).

3.1.2 Sterically stabilized nanocrystals dispersed in an organic phase

In the rise of colloidal nanoscience that started around 1985, a second type of sol became very prominent, namely, that in which crystals with dimensions in the 1–20 nm range (thus nanocrystals, NCs) are dispersed in nonpolar organic solvents.⁵ The nanocrystals are sterically stabilized against aggregation by organic ligand molecules bound with a chemical functionality to the nanocrystal surface and have an alkyl chain immersed in the liquid. The interaction between the ligands of two adjacent nanocrystals is very similar to the interaction between the ligands and the solvent molecules. As a consequence, the ligand–ligand attraction is screened by the “ideal” solvent; the only attractive interaction is then the van der Waals type attraction between the nanocrystal cores on a distance defined by the two ligand layers.^{6,7} For sufficiently small nanocrystals, the attractions constitute an energy in the order of the thermal energy, weak enough to keep such suspensions stable. To initiate colloidal crystallization, the system has to be destabilized. This is possible by making the solvent less “ideal”, for example by adding a polar nonsolvent.^{6,8} To initiate oriented attachment, the attraction between specific facets has to be increased, e.g., by replacing the ligands bound to a specific type of facet with a smaller surface-active species or by desorption of the ligands from a specific facet due to the presence of a second liquid phase with a high affinity for the ligands. The binding strength of the ligands on the facets, and the ligand density depends on the atomic structure of the facet in question.^{9–11} Running ahead on what comes, we provide here the example of truncated cubic PbSe crystals; oleate ligands are only weakly bound to the 6 (100) facets, while the (110) and polar (111) facets are firmly covered with these ligands. In 2005 it was found that oriented attachment by (100) facet-to-facet connection can result in highly anisotropic PbSe rods, with their long axis being $\langle 100 \rangle$.¹² But with other ligands (or amines) the reactivity of the facets can be changed and oriented attachment could be achieved involving exclusively the (110) or (111) facets.^{12,13} The exclusiveness of only one facet type being active in oriented attachment is remarkable, and more pronounced for organic sols, then for aqueous suspensions.

3.2 A brief history of oriented attachment in non-polar organic solvents

In the early 1990s, wet chemical methods using precursors and ligands soluble in organic solvents were developed to prepare nanocrystals of semiconductor compounds.^{14,15} Exemplary for this development is the publication in 1993 by Murray, Norris, and Bawendi on CdSe nanocrystals of 1–10 nm in diameter;⁵ see [Figure 3.1a](#). In this work the nanocrystals were capped with organic ligands which bind to the surface Cd atoms and dispersed in an organic solvent. Due to the favorable interactions between the solvent and the alkyl chains, such dispersions are sterically stabilized. Upon optical excitation, an (e, h) exciton eigenstate was formed that recombined radiatively. Both the absorption and luminescence spectra showed that the exciton was strongly confined in the nanocrystal. Hence, by changing the size of the nanocrystals the emission color could be tuned over a wide energy range. Further research resulted in devel-

opment of nanocrystals of other II-VI, III-V, and IV-VI compounds synthesized with similar methods.¹⁶ Nanocrystals of the IV-VI compounds, especially the PbX family (X = S, Se, Te), were extensively investigated as their band gap spans the near IR and can, again, be tuned by the degree of exciton confinement. Over three decades these interesting properties have led to an explosion of fundamental and applied research, and to innovative opto-electronical applications.¹⁷⁻²¹

3.2.1 Oriented attachment as a new tool in nanomaterials science

The synthesis of semiconductor nanocrystals with hot-injection techniques has had a tremendous effect on fundamental nanocrystal science and its applications. The surface passivation by organic and inorganic ligands resulted in electronic passivation, such that electronic and excitonic eigenstates instead of surface trapped states become fully visible in spectroscopy. This opened the gate to fundamental studies of the electron energy levels and exciton dynamics of semiconductor nanocrystals with a plethora of optical spectroscopic techniques and electron tunnelling spectroscopy.^{22,23} Electrons, holes, and electron-hole pairs have a wave nature, and when they are confined in nanocrystals, they experience a quantum confinement effect that increases their kinetic energy. Hence, the single-electron energy levels and exciton energies in nanocrystals are strongly size dependent. This, and the strongly radiative emission, boosted the scientific interest in semiconductor nanocrystals. It has resulted in largescale applications using well-defined CdSe and InP nanocrystals as spectral converters in displays and TV screens.²¹

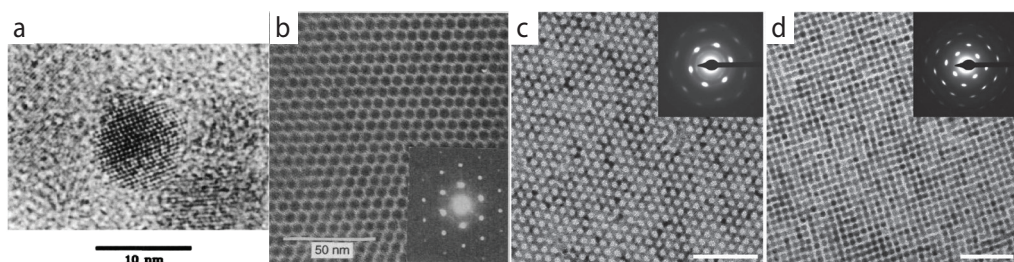


Figure 3.1 From single building blocks to superlattices prepared via oriented attachment. High-resolution TEM image of a single CdSe quantum dot (a) which can be self-assembled into a superlattice in which the nanocrystals are ordered although not connected (b). Panel a reproduced with permission from reference 5. Copyright 1993 American Chemical Society. Panel b reproduced with permission from reference 25. Copyright 1995 AAAS. In the case of PbSe nanocrystals, further modification of the reaction conditions results in the formation of nanocrystals attached via the (100) facets, resulting in either honeycomb (c) or square superlattices (d). Scale bar represents 50 nm and insets show SAED patterns, indicating the high crystallinity of the formed structures. Panels c and d reproduced with permission from reference 40. Copyright 2013 American Chemical Society.

3.2.2 Driving forces and facet specificity in oriented attachment

Nanocrystals prepared by hot-injection methods in organic solvents can have a well-defined crystal structure and shape and are terminated by facets with a specific surface chemistry and energy. As a consequence, the binding energy and density of the ligand molecules on specific facets differs considerably. Hence, oriented attachment of organic-capped crystals is facet-specific in a more pronounced way than for charge-stabilized nanocrystals. At the same time the shape of the nanocrystals is influenced by the capping density of the facets. For instance, a well-capped PbSe nanocrystal has the shape of truncated octahedron, but if the ligand density is lowered by washing, the shape changes toward that of a truncated cube.²⁴ Therefore, PbSe nanocrystals with a simple rock salt structure provide the best example to illustrate the pronounced facet specificity in oriented attachment.

3.2.3 Colloidal crystallization, formation of superlattices

Suspensions of semiconductor nanocrystals in good organic solvents are well-stabilized against aggregation and can thus be prepared in highly concentrated suspensions. In these suspensions the ligand-ligand interactions are screened by the solvent molecules, and the semiconductor core-core attractions are small.^{6,7} Only for larger crystals, rods, and metallic crystals, the attractions between the nanocrystals start to increase to a few times the thermal energy at room temperature. The colloidal crystallization of these nanocrystals from suspensions became a matter of interest around 1995.²⁵ Since nanocrystal suspensions are stable, the suspension can be destabilized in a subtle way; in other words, *colloidal crystal engineering with the formation of well-ordered superlattices is possible*. An example of this can be seen in **Figure 3.1b**. From a nanoscience materials perspective, truly new material platforms emerged, since nanocrystal assembly is the only way to bring nanoscale building blocks in close contact in an ordered structure.^{26,27} The superstructures formed by increased concentration in the suspension can be seen as a hard-sphere framework forming a face-centered cubic structure (fcc). In contrast, by adding a more polar but miscible component, the solvent medium becomes less ideal and colloidal crystallization driven by the nanocrystal attractions (ligands and cores) occurs. At a lower ligand density the interactions become more soft-sphere-like, and the resulting structures are body-centered tetragonal (bct) or even body-centered cubic (bcc).^{28,29} However, the organic ligands still present tend to form a tunnelling barrier for the charge carriers, resulting in weak electronic coupling and carrier mobilities substantially below $1 \text{ cm}^2/(\text{V s})$.³⁰⁻³² Coupling between the nanocrystals could be improved by exchanging the long organic ligands for shorter ones,^{33,34} or by exchanging for ligands that specifically couple the nanocrystals, or exchanging for ligands that change the band alignment between different quantum dots from type-I to type-II.^{35,36} With this advanced engineering, reasonable carrier mobilities of $0.1\text{--}20 \text{ cm}^2/(\text{V s})$ have been reached in NC solids.^{33,37-39}

A considerable increase in carrier mobility could, in principle, be achieved by oriented attachment, which ideally results in a crystalline neck between the nanocrystals in a self-assembled structure. The coupling is then only limited by the width of the neck. Below, we will discuss the formation of 2D superlattices consisting of a monolayer of nanocrystals that are epitaxially connected. In the case of PbSe (and PbS, PbTe) atomically coherent superlattices could be prepared,⁴⁰⁻⁴⁵ that have a square geometry (thus also with a square periodicity of voids) and a honeycomb geometry (hexagonal periodicity of voids); see **Figure 3.1c** and **d**. It was shown that the electronic band structure of square and honeycomb superlattices was different

from the simple 2D sheets or quantum wells prepared by oriented attachment.¹³ Honeycomb semiconductors show a conventional band gap, but the electron conduction bands (hole valence bands) show Dirac-type bands, similar to those of graphene!^{46,47} This brings the exciting opportunity to combine typical semiconductor properties with electron and hole excitations that are “massless” as in graphene. So far, experimental evidence for these compelling predictions has not been found, as the electronic mobilities are relatively low ($1\text{--}10\text{ cm}^2/(\text{V s})$), being limited by imperfect necks and geometrical disorder.^{48–50} However, the big message here is that the electronic band structure of 2D crystals can be engineered by the lateral nanogeometry of the system.⁵¹ Specific geometries can be achieved by NC assembly followed by oriented attachment. The big challenge in this very promising field is to grow 2D structures using identical nanocrystal building blocks, resulting in 2D superstructures without geometrical disorder and with uniform necks.^{52,53}

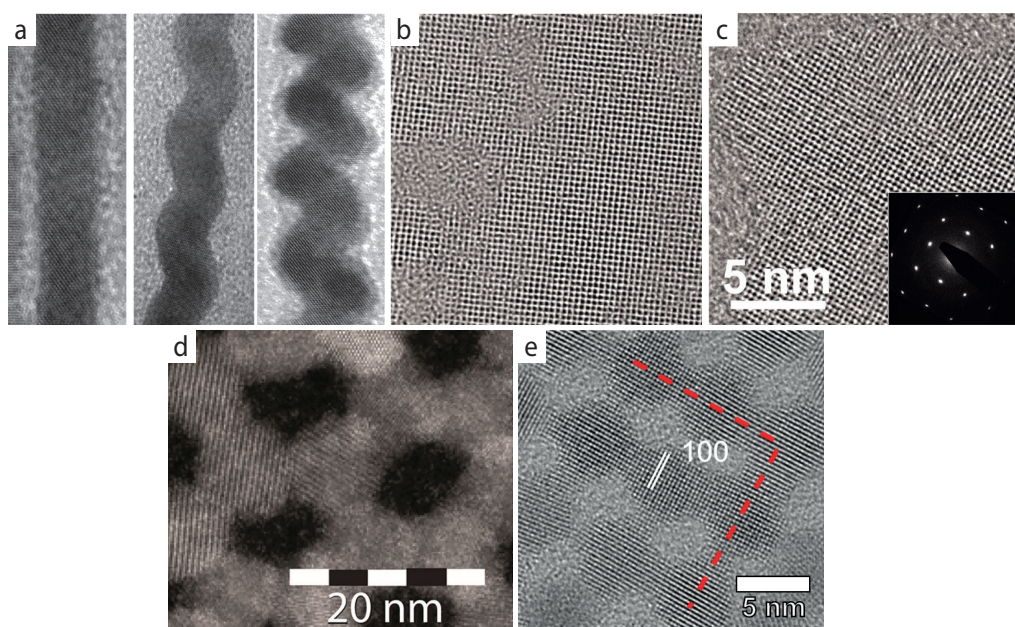


Figure 3.2 Oriented attachment of lead chalcogenide nanocrystals resulting in a variety of nanostructured materials. Depending on the reaction conditions, oriented attachment of PbSe nanocrystals lead to 1D single-crystal wires (a) which are either straight (left) or zigzag (middle and right). Panel a reproduced with permission from reference 12. Copyright 2005 American Chemical Society. Alternatively, 2D sheets can be prepared by selective attachment of (110) facets. In an early stage, small holes are visible in the crystal structure (b), whereas at a later stage single crystalline particles are obtained (c), confirmed with SAED (inset). Panels b and c reproduced with permission from reference 13. Copyright 2010 AAAS. Oriented attachment of pre-synthesized PbS nanocrystals can result in either square or honeycomb superlattices by attaching at (100) facets; corresponding high-resolution HAADF-STEM images are shown in (d) and (e). Panels d and e respectively reproduced with permission from reference 24 and 64. Copyright 2017 and 2016 American Chemical Society.

3.3 Oriented attachment in PbX nanocrystals

3.3.1 Formation of highly anisotropic 1D and 2D crystals in the rock salt family

In a one-pot synthesis of PbSe nanocrystals using limited amounts of oleate ligands, PbSe nanorods and long nanowires (up to 30 μm in length and 4–20 nm in diameter) can be formed along the $\langle 100 \rangle$ direction;^{12,54,55} see also **Figure 3.2a**. It is hypothesized that nanocubes are formed first, which act as intermediates that attach via their (100) facets. Since there are six (100) facets in the three orthogonal directions, one expects the formation of 3D superlattices. Nevertheless, strong anisotropic one-dimensional (1D) structures are observed, built from centrosymmetric rock salt nanocrystals.¹² An explanation on the basis of NC dipoles has been proposed, but independent information on the existence of an electric dipole in PbSe NCs is lacking.⁵⁶ In the case of rock salt PbSe, usually the low-energy (100) facets are active in oriented attachment, as they are most easily liberated from the oleate ligand molecules.^{57,58} However, when amines are applied in the one-pot synthesis, used to exchange the oleate capping on existing nanocrystals or when a cosolvent is added, novel 1D rods, wires, and sheets are observed that can only be understood by exclusive (110)/(110), or even (111)/(111), facet-to-facet attachment.¹² Hence, in some cases specific ligand capping can alter the relative reactivity of the facets for oriented attachment. Later on, a one-step method was developed for the preparation 2D PbS sheets;¹³ see **Figure 3.2b** and **c**. Here, the nucleation and growth of PbS nanocrystals are followed by oriented attachment at (110) facets in two directions due to the addition of a chlorine-containing cosolvent. The resulting well-defined PbS quantum wells have a thickness of about 4 nm and showed photoconductivity.

3.3.2 Formation of 2D atomically coherent superlattices with a square or honeycomb geometry

The formation of atomically coherent superlattices with a square and a honeycomb geometry by NC assembly and oriented attachment came to us as a big surprise. In 2012 we were performing experiments on the self-assembly of PbSe NCs in the framework of understanding the interactions between the nanocrystals. PbSe NC suspensions were dropcasted on ethylene glycol (EG), which we considered at the time as an inert liquid substrate. With additional oleate present, simple monolayers (bilayers) with hexagonal ordering of NCs were formed. However, if the nanocrystals were well-washed, we observed different geometries (**Figure 3.2d** and **e**): we found monolayers in which the NCs were organized in square arrays, also showing a square array of voids due to the truncation of the cubic shape of the NCs. Alternatively, we observed 2D systems, with a hexagonal array of voids, which means that the semiconductor material structure must have the honeycomb geometry. Often domains with square and honeycomb geometry were found together. Most interestingly, we found that, in both cases, the PbSe NCs were attached via the (100) facets, with four connections in the case of the square superlattice, and three connections in the case of the honeycomb lattice. Clearly, the ligand density of the (100) facets reduced due to the washing step, but very probably also due to the EG liquid interface. While the (100)/(100) connection is simple to understand for the square geometry, for the honeycomb geometry we realized that the (100) connections also imply that the nanocrystals are aligned with the (111) axis upward and that the honeycomb is buckled, unlike graphene, but very similar to silicene and germanene.^{41,44}

The formation of PbSe superlattices with a honeycomb geometry is surely the most intriguing process of oriented attachment so far. It is also the most difficult to reproduce in many respects. It was found that very slow evaporation of the suspension solvent (usually toluene) over

15 hours (h) and lowering of the (100) facets reactivity, e.g., by adding 1,4-butanol to the liquid substrate, can result in well-ordered and large domains.⁴⁴ The system can be so well-ordered that point defects and line defects in the structure become visible as in classic crystallography. An example of this is presented in **Figure 3.2d**. The formation of square and honeycomb structures is a complex process, with several consecutive phases. It is clear that the nanocrystals should be able to align in a reversible way, thus before irreversible epitaxial connections are formed. The question of which forces drive the alignment of the nanocrystals, before they attach and form an atomically coherent structure, is an interesting one. The orientation of nanocrystals at the air/toluene interface has been put forward;^{59–63} as well as the chemical attraction between bare (100) facets. The evolution of the entire process has been monitored in situ with synchrotron radiation and ex situ electron microscopy, which will be discussed in **section 3.5**. As this interfacial assembly and oriented attachment opened the gate to truly novel material classes (see above), our initial experiments were extended by beautiful efforts of several other groups.

In an effort by a group in Ghent, the formation of the epitaxial connection was triggered by addition of amines or Na₂S to the liquid substrate. This resulted in the formation of square lattices in a short time, with lattice domain sizes of about 100 nm (15–20 nanocrystal unit cells); see **Figure 3.2e**. These chemical triggers were chosen on the basis of the idea that interdot connections can only form between (100) facets which face each other and have a stoichiometric surface; then S²⁻ adds sulfur to a (100) surface with Pb excess, while amines pull excess lead ions away. After addition of these chemical triggers, it takes only 5 min for the epitaxially connected superlattice to form domains of ~100 nm in size. With the amine trigger the basicity can be tuned, resulting in a gentler ligand displacement with a weaker base, which appears to increase the domain size of the superlattice.⁶⁴

The formation of 2D square and honeycomb superlattices, and straight and zigzag 1D structures as well, is not limited to PbSe NCs; formation of these structures also occurs with PbS and PbTe nanocrystals.⁴⁵ The studies so far are very limited, but it is justified to say that PbTe NCs are the most reactive PbX system. Therefore, the attachment is challenging to control, and it is difficult to obtain ordered structures with a reasonable domain size.

3.4 Oriented attachment in CdX nanocrystals

The family of CdX nanocrystals (X = S, Se, Te), with CdSe here as the dominant example, have a relatively rigid lattice due to covalent bonding. This means that the nanocrystals are not so easily reshaped as those from the PbX family and thus show less propensity for oriented attachment. Still, there is strong evidence that oriented attachment (or a process like this) occurs during the preparation of wires and sheets; there are multiple reports on the attachment of mature NCs or small magic-size clusters, which we will discuss below. Compared to the rock salt PbX family, oriented attachment of CdX nanocrystals is more difficult to study as both wurtzite (hexagonal and polar along the c-axis) and zinc blende (cubic and isotropic) NCs with very different chemistry and polarity of the facets can play a role.

3.4.1 Growth of CdX nanowires: a case of oriented attachment?

Tang et al. revealed that wurtzite CdTe nanowires could be grown via the attachment of smaller zinc blende nanocrystals.⁶⁵ Epitaxial connections were achieved by controlled removal of ligands from the nanocrystals' surface. Aliquots taken at short reaction times showed pearl neck-

lace aggregates which evolve to wires with aspect ratios up to 500. The final CdTe nanowires have the same diameter as the original nanocrystal building blocks which supports oriented attachment as the growth method. Dipole-dipole interactions between the nanocrystals were invoked as the driving force for the attachment process. The observation of nanowire photoluminescence confirmed the single crystalline nature of the wires and a reasonable electronic passivation of the surface.

3.4.2 Nanocrystals formed by “attachment” of magic-size clusters

We have put attachment between quotation marks: magic-size clusters (MSCs) have a well-defined structure, but without genuine periodicity and crystal facets. Hence, if magic-size clusters unify, and a nanocrystal is eventually formed, atomic reconfigurations must have occurred which go beyond the formation of necks. By reacting cadmium oleate and selenourea with amines at relatively low temperature, CdSe nanowires can be prepared out of magic-sized clusters.⁶⁶ In the first stage, these clusters are formed, which attach and yield prewire aggregates (also called “pearl necklaces”). Subsequent annealing converts these structures into single crystalline wurtzite wires. Later work by Liu et al. showed the preparation of zinc blende CdSe wires via attachment of CdSe magic-size clusters (Figure 3.3a).⁶⁷

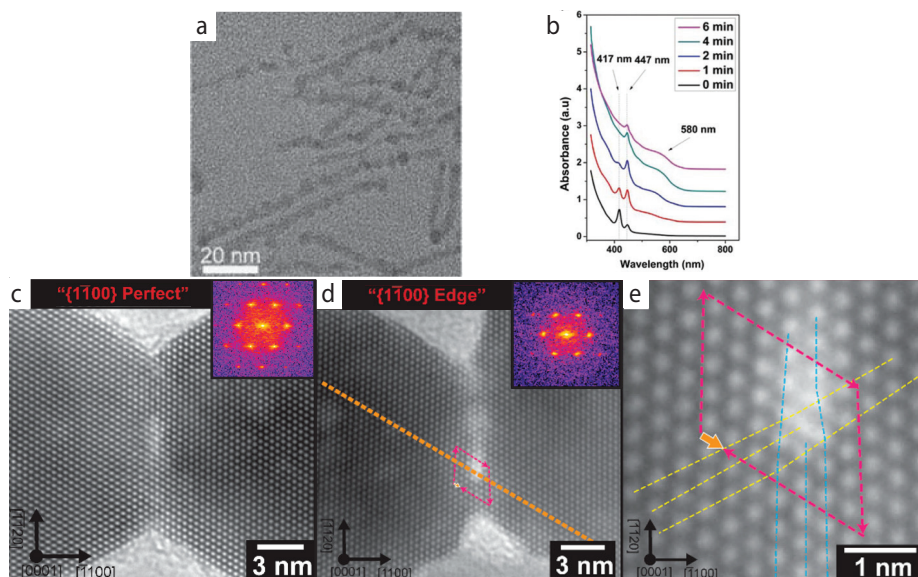


Figure 3.3 Oriented attachment of cadmium chalcogenide nanocrystals. The formation of pearl necklaces, composed of small nanocrystals, is clearly visible due to the different thicknesses in a single wire and is strong proof for oriented attachment of smaller nanocrystals (a). In several cases, magic-sized clusters have been observed as intermediates during the formation of these wires (b). In here, characteristic absorption features at 417 and 447 nm appear and disappear during the preparation. Panels a and b reproduced with permission from reference 67. Copyright 2015 American Scientific Publishers. In situ TEM shows the absence (c) or presence (d) of defects between two CdS nanocrystals. High-resolution imaging (e) enables the study of local defects. Panels c-e reproduced with permission from reference 69. Copyright 2019 American Chemical Society.

Absorption spectroscopy of aliquots showed the formation and disappearance of a magic-sized cluster composed of $(\text{CdSe})_{33}$ and $(\text{CdSe})_{45}$, absorbing at 417 nm, which consequently unifies into larger magic-size clusters absorbing at 447 nm; see **Figure 3.3b**. More importantly, during further evolution of the reaction, the signatures of the magic-size clusters disappear, and absorption of a broad band emerges around 580 nm, signaling the formation of CdSe nanowires. Due to the emergence of an electrical dipole of increasing magnitude along the [111] direction, the attachment of new MSCs is accelerated.

3.4.3 Formation of 2D sheets and quantum wells by oriented attachment

Oriented attachment of CdTe nanocrystals capped with aminothiols resulted in monolayers of attached NC building blocks with lateral extension up to several micrometers.⁶⁸ The experimental results, combined with molecular simulations, indicated that in addition to dipole-dipole interactions, small positive charges, and hydrophobic interactions between the nanocrystals are required driving forces for the self-assembly process.

3.4.4 Investigating the attachment of single nanocrystals

Ondry et al. studied the attachment of two wurtzite CdSe nanocrystals and the removal of defected connections in the presence of an electron beam during in situ transmission electron microscopy.⁶⁹ Upon treating the sample with Na_2Se , the ligands were removed and the nanocrystals attached via their (1100) or (1120) side facets; see **Figure 3.3c**. It was found that the formation of epitaxial connections between the crystals comes with crystal dislocations due to the presence of half-finished planes at a facet; an example of this is shown in **Figure 3.3d** and **e**. In some cases, annealing induced by the electron beam allowed removal of the crystal dislocation; its gradual shift toward the surface and “escape” could be followed in situ.

3.5 In situ monitoring of oriented attachment with scattering methods

Transmission electron microscopy (TEM) has given great insight into the structure and order of superlattices, but it is limited to the in situ study of attachment on a very small scale,^{69,70} or the study of an already formed superlattice on the larger scale. The only way to study the attachment process with TEM is by samples taken during formation that are immediately dried to be studied later.^{44,71} Alternatively, the fast temporal resolution (200 ms) of synchrotron-based specialized X-ray scattering techniques is a strong tool for the study of large-scale superlattice formation. As superlattices are formed on a liquid interface, a grazing incidence (GI) geometry setup is used; see **Figure 3.4a**. Instead of transmission scattering, the collimated X-ray beam is bent down toward the liquid surface to scatter the superlattice. The technique is especially interesting as superlattices are crystalline on both the nanocrystal and the atomic length scales. At wide scattering angles (GIWAXS), the signal consists of the atomic form factor (scattering strength of the atoms) and the structure factor (positions of the atoms in the unit cell). At small scattering angles (GISAXS), the signal consists of the form factor from the nanocrystal size and shape and the structure factor from the position of the nanocrystals. Combining these techniques with a chamber allows these experiments to be performed in an inert atmosphere where the solvent-vapor pressure can be regulated, allowing for in situ study of the formation under different conditions.^{28,72,73}

Interest has shifted to the study of the different steps observed in the attachment of a mono-

layer of nanocrystals. Using synchrotron-based in situ GISAXS, the initial spread of a PbSe NC dispersion (6 nm particles) on the liquid EG substrate was studied. With remote control, 1 μL of a concentrated dispersion was drop-cast ~ 1.5 cm from the beam, allowing the droplet spreading to be captured (taking ~ 30 s). Weak Bragg peaks are observed in the GISAXS immediately after dropcasting, suggesting a “precursor film” spreading quickly ahead of the bulk droplet, a phenomenon known in classical wetting theory as a “molecular” film bridging the interfacial energy discontinuity at the contact line.⁷⁴ Within the first 2–5 s the bulk droplet follows, and as the solvent evaporates the nanocrystal concentration in the film gradually increases. A phase transition to a dense liquid, and then a network of solvated but correlated quantum dots, is observed. When at last (after ~ 26 s) all of the solvent has evaporated, strong scattering rods are observed, resulting in an fcc-like superstructure. However, the simultaneous GIWAXS measurements show only rings, indicating no preferential orientation of the NCs at these time scales.⁷⁵ However, more recent experiments showed that in the presence of additional oleate ligands crystallographic alignment is observed. After 2 h of evaporation, medium and large NCs (5.5–9 nm) showed orientation with the [100] axis perpendicular to the liquid/air interface; see **Figure 3.4b**.⁷⁶

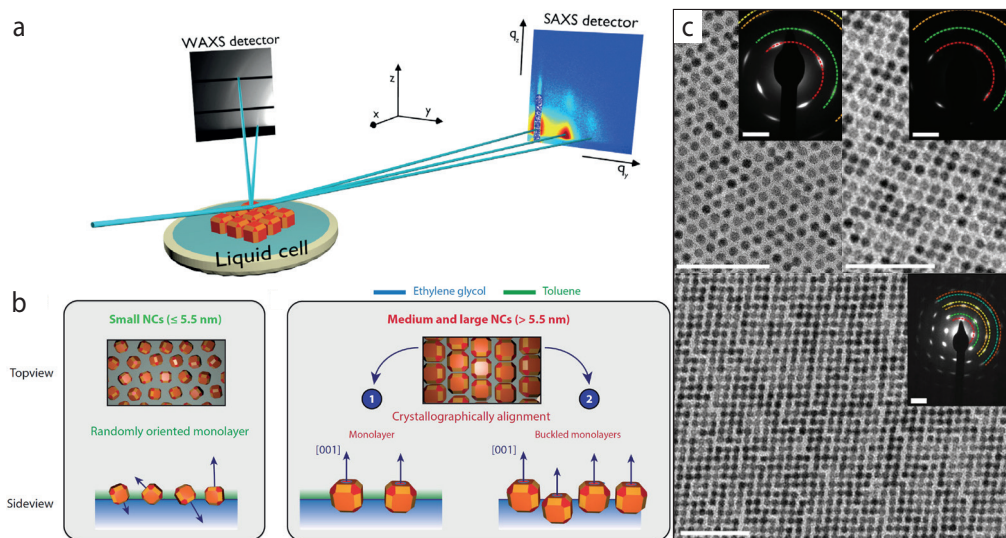


Figure 3.4 Schematic setup used for in situ grazing incidence X-ray scattering experiments (a). The solvent from a NC dispersion evaporated in a liquid cell, placed in a chamber (not depicted). The assembly and attachment are studied by simultaneously monitoring atomic ordering on the wide-angle detector (WAXS) and nanoscale ordering on the small-angle detector (SAXS). Schematic representation of the orientation of nanoparticles at the ethylene glycol–air interface based on in situ scattering experiments (b). Small NCs are randomly oriented, while larger particles (5.5–9 nm) have a more cubic shape, with larger (100) facets of which one aligns favorably perpendicular to the interface. Panel b reproduced with permission from reference 76. (c) TEM images from samples taken during in situ experiments. They show a pseudo-hexagonal phase (top left), an initial square phase (top right) before complete attachment, and the final square phase (bottom); the scale bars correspond to 50 nm. The inset shows ED patterns which transform from arcs to distinct spots. Panels a and c reproduced with permission from reference 43. Copyright 2016 Nature.

In attachment experiments on longer time scales (evaporation of 1 h), the formation mechanism of 2D PbSe superlattices with square geometry was observed. In these experiments GISAXS/GIWAXS was combined with ex situ TEM and electron diffraction to elucidate the phase transfers. After drop-casting 350 μL of a dilute dispersion of ~ 5.7 nm PbSe NCs, Bragg peaks are observed at the EG interface after 16 min, indicating the presence of a hexagonal monolayer. Hard-sphere interaction still dominates the particle interaction at this point. However, in another 15 min, it transforms via a pseudohexagonal phase (bond angles deviating from 60°) to a phase with square ordering (bond angles of 90°); see **Figure 3.4c**. These phase transitions are interpreted as increasing NC attractions, as ligands gradually strip from the lower energy (100) facets and square ordering of the structure is driven to maximize facet overlap. During this transformation, the orientational freedom of the NCs also decreases gradually (bands in the GIWAXS), until the NCs attach via necks (spots in the GIWAXS). The resulting square superlattice has a NC–NC distance of 7.6 nm, which is 34% larger than the original PbSe NC core diameter, and an average atomic coherence length of 13.2 nm, again indicating attachment of the quantum dots to on average a lower limit of two to three NC diameters.⁴³

3.6 Molecular dynamics simulations of nanocrystal assembly and atomic alignment at an interface

Despite efforts to develop a predictive theoretical framework for modelling crystallization by oriented attachment,⁷⁷ the observation of remarkable 2D superstructures with a square or silicene-type honeycomb geometry on the length scale of the nanocrystals (roughly 10 nm) showing epitaxial connections between the nanocrystals raises many intriguing questions. To date, these questions are still not fully resolved. Intuitively, the formation of 2D structures points to nanocrystals that absorb at an interface; the results of in situ synchrotron experiments described above suggests that this could be the liquid/air interface. On the other hand, it could also be that nanocrystals form a thin film within a thin layer of organic solvent at the end of the solvent evaporation process. By intuition again, the formation of large NC systems (sometimes thousands of unit cells) with nanoscale order and alignment suggests that the process of irreversible oriented attachment (crystal necking) is relatively slow and that ordered and aligned phases of many NCs form. The big question that rises is then, what types of forces are responsible for the alignment of the cubic PbSe nanocrystals?

Realistic course-grained molecular dynamic simulations (MD simulations) have been carried out in our group in order to resolve these questions and, more generally, to get an answer to whether large phases of aligned nanocrystals can form spontaneously without epitaxial connections. In coarse-grained models, atomic-scale details are sacrificed, but features such as size, shape, and softness of the NCs- which can be modelled on a larger scale than the atomic one- are retained, allowing simulations in the order of 10000 NCs.⁷⁸ Soligno and Vanmaekelbergh,^{61,62} calculated the free energy change of nanocrystal adsorption at the toluene/air interface. It was found that the free energy change of adsorption is many times the thermal energy, indicating that a 2D layer of nanocrystals can form at an interface. For PbSe nanocrystals with a truncated cubic shape it was observed that the adsorption geometry with a vertical (100) or (111) axis is favored with respect to other orientations. Hence, oriented nanocrystal adsorption may, in principle, result in a partial alignment of the crystals at the interface, although there is a remaining rotational degree of freedom in the plane of the interface. Realistic MD simulations were carried out, accounting for attractive and repulsive interactions between the nanocrystals, entropic effects, and forces due to capillary deformations of the solvent/liquid interface. It

was convincingly shown that both square superlattices and silicene honeycomb lattices could arise from NCs adsorbed at the toluene/air interface. Recently, these simulations have been extended to phases consisting of as much as 10^4 nanocrystals, with a further relaxation of the boundary conditions by allowing no preferential absorption at an interface at time $t = 0$. A still of the MD simulations is shown in **Figure 3.5**. Again, honeycomb lattices and linear structures were observed after a certain simulation time. Moreover, the natures of the disorder in these phases, consisting of small superlattice domains, linear NC structures, linear zigzag structures, and very remarkable vacancies, were all present in the simulations, very similar to how they were observed in a large number of TEM analyses of samples from experiments. Although MD simulations can successfully reproduce the experimentally observed superlattices and the disorder that arises in them, the question of which forces are key for the nanocrystal alignment (interfacial adsorption, entropic ordering of hard cubes, or (100)/(100) facet/facet attractions) is not fully answered yet. The enigma of the beautiful honeycomb silicene superlattices with ordering over hundreds of unit cells, which has been observed on several occasions, is not yet fully resolved.

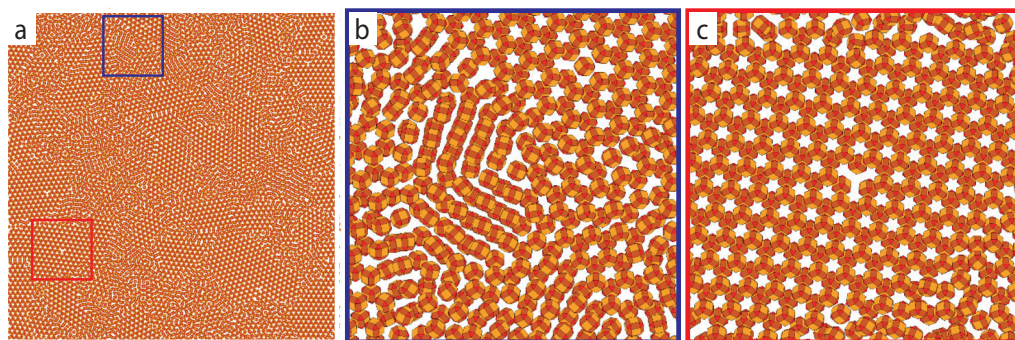


Figure 3.5 Molecular dynamics simulation of the self-assembly and oriented attachment of nanocrystals with a truncated cubic shape, presented by a still taken after $0.15 \mu\text{s}$ of simulation. (a) Overview of a simulation with 10000 nanocrystals, showing crystalline domains of the honeycomb phase together with amorphous (disordered) parts; (b) detailed picture showing zigzag linear structures that were not able to organize into the honeycomb lattice; (c) detail with a crystalline-like vacancy defect in the honeycomb structure.

3.7 Summary and outlook

Oriented attachment, the unification of two separate crystals to form one single crystal, was once not much more than a curiosum, based on a number of observations in biological mineral formation and geology. However, it became known as “non-classical” crystal growth and got a complementary place next to the atom-by-atom, row-by-row, or plane-by-plane crystal growth that has been observed and modelled in classic crystallography. The new age of nanocrystal synthesis in nonpolar organic solvents, starting at the beginning of the 1990s, provided a new and compelling chapter to oriented attachment. These nanocrystals have simpler shapes and well-defined crystal facets, and the chemical bonding strength of ligands is facet-specific. This results in reactive facets of one sort, and compelling atomically coherent “unified” crystals in one and two dimensions. In two dimensions, nanostructured single crystals emerge that have not only atomic order but also a second periodic geometry on the nanoscale; for instance, a 2D

sheet with a square array of nanovoids or a honeycomb structure, with a geometry similar to that in silicene. It is clear that once scientists are able to master the nanocrystals' shapes, ligand chemistry of the different facets, self-assembly into ordered reversible superstructures, and, finally, the atomic motion by which crystalline necks are formed and a single crystal emerges, nanocrystal assembly and oriented attachment will become a strong engineering tool for crystalline materials with concomitant atomic and nano-periodic order, of large interest in catalysis, in optoelectronics and for materials in the quantum age.

References

- [1] Verwey, E. J. W.; Overbeek, J. T. G. *Theory of Stability of Lyophobic Colloids*; Dover Publications, 1999.
- [2] Banfield, J. F.; Welch, S. A.; Zhang, H. Z.; Ebert, T. T.; Penn, R. L. Aggregation-Based Crystal Growth and Microstructure Development in Natural Iron Oxyhydroxide Biomineralization Products. *Science* **2000**, *289* (5480), 751-754. DOI: 10.1126/science.289.5480.751.
- [3] Niederberger, M.; Colfen, H. Oriented Attachment and Mesocrystals: Non-Classical Crystallization Mechanisms Based on Nanoparticle Assembly. *Phys. Chem. Chem. Phys.* **2006**, *8* (28), 3271-3287. DOI: 10.1039/b604589h.
- [4] De Yoreo, J. J.; Gilbert, P. U.; Sommedijk, N. A.; Penn, R. L.; Whitelam, S.; Joester, D.; Zhang, H.; Rimer, J. D.; Navrotsky, A.; Banfield, J. F.; et al. Crystallization by Particle Attachment in Synthetic, Biogenic, and Geologic Environments. *Science* **2015**, *349* (6247), aaa6760. DOI: 10.1126/science.aaa6760.
- [5] Murray, C. B.; Norris, D. J.; Bawendi, M. G. Synthesis and Characterization of Nearly Monodisperse CdE (E = sulfur, selenium, tellurium) Semiconductor Nanocrystallites. *J. Am. Chem. Soc.* **1993**, *115* (19), 8706-8715. DOI: 10.1021/ja00072a025.
- [6] Vanmaekelbergh, D. Self-Assembly of Colloidal Nanocrystals as Route to Novel Classes of Nanostructured Materials. *Nano Today* **2011**, *6* (4), 419-437. DOI: 10.1016/j.nantod.2011.06.005.
- [7] Evers, W. H.; De Nijs, B.; Filion, L.; Castillo, S.; Dijkstra, M.; Vanmaekelbergh, D. Entropy-Driven Formation of Binary Semiconductor-Nanocrystal Superlattices. *Nano Lett.* **2010**, *10* (10), 4235-4241. DOI: 10.1021/nl102705p.
- [8] Bodnarchuk, M. I.; Kovalenko, M. V.; Heiss, W.; Talapin, D. V. Energetic and Entropic Contributions to Self-Assembly of Binary Nanocrystal Superlattices: Temperature as the Structure-Directing Factor. *J. Am. Chem. Soc.* **2010**, *132* (34), 11967-11977. DOI: 10.1021/ja103083q.
- [9] Drijvers, E.; De Roo, J.; Martins, J. C.; Infante, I.; Hens, Z. Ligand Displacement Exposes Binding Site Heterogeneity on CdSe Nanocrystal Surfaces. *Chem. Mater.* **2018**, *30* (3), 1178-1186. DOI: 10.1021/acs.chemmater.7b05362.
- [10] Puzder, A.; Williamson, A. J.; Zaitseva, N.; Galli, G.; Manna, L.; Alivisatos, A. P. The Effect of Organic Ligand Binding on the Growth of CdSe Nanoparticles Probed by Ab Initio Calculations. *Nano Lett.* **2004**, *4* (12), 2361-2365. DOI: 10.1021/nl0485861.
- [11] Yin, Y.; Alivisatos, A. P. Colloidal Nanocrystal Synthesis and the Organic-Inorganic Interface. *Nature* **2005**, *437* (7059), 664-670. Review. DOI: 10.1038/nature04165.
- [12] Cho, K. S.; Talapin, D. V.; Gaschler, W.; Murray, C. B. Designing PbSe Nanowires and Nanorings Through Oriented Attachment of Nanoparticles. *J. Am. Chem. Soc.* **2005**, *127* (19), 7140-7147. DOI: 10.1021/ja050107s.
- [13] Schliehe, C.; Juarez, B. H.; Pelletier, M.; Jander, S.; Greshnykh, D.; Nagel, M.; Meyer, A.; Foerster, S.; Kornowski, A.; Klinke, C.; et al. Ultrathin PbS Sheets by Two-Dimensional Oriented Attachment. *Science* **2010**, *329* (5991), 550-553. DOI: 10.1126/science.1188035.
- [14] Brennan, J. G.; Siegrist, T.; Carroll, P. J.; Stuczynski, S. M.; Brus, L. E.; Steigerwald, M. L. The Preparation of Large Semiconductor Clusters via the Pyrolysis of a Molecular Precursor. *J. Am. Chem. Soc.* **1989**, *111* (11), 4141-4143.
- [15] Steigerwald, M. L.; Brus, L. E. Synthesis, Stabilization, and Electronic Structure of Quantum Semiconductor Nanoclusters. *Annu. Rev. Mater. Sci.* **1989**, *19*, 471-495.
- [16] Talapin, D. V.; Shevchenko, E. V. Introduction: Nanoparticle Chemistry. *Chem. Rev.* **2016**, *116* (18), 10343-10345. DOI: 10.1021/acs.chemrev.6b00566.
- [17] Talapin, D. V.; Steckel, J. Quantum Dot Light-Emitting Devices. *MRS Bull.* **2013**, *38* (9), 685-695. DOI: 10.1557/mrs.2013.204.
- [18] Kovalenko, M. V.; Manna, L.; Cabot, A.; Hens, Z.; Talapin, D. V.; Kagan, C. R.; Klimov, V. I.; Rogach, A. L.; Reiss, P.; Milliron, D. J.; et al. Prospects of Nanoscience with Nanocrystals. *ACS Nano* **2015**, *9* (2), 1012-10157. DOI: 10.1021/nn506223h.
- [19] Lim, J.; Park, Y. S.; Wu, K. F.; Yun, H. J.; Klimov, V. I. Droop-Free Colloidal Quantum Dot Light-Emitting Diodes. *Nano Lett.* **2018**, *18* (10), 6645-6653. DOI: 10.1021/acs.nanolett.8b03457.
- [20] Erickson, C. S.; Bradshaw, L. R.; McDowall, S.; Gilbertson, J. D.; Gamelin, D. R.; Patrick, D. L. Zero-Reabsorption Doped-Nanocrystal Luminescent Solar Concentrators. *ACS Nano* **2014**, *8* (4), 3461-3467. DOI: 10.1021/nn406360w.
- [21] Frecker, T.; Bailey, D.; Arzeta-Ferrer, X.; McBride, J.; Rosenthal, S. J. Review-Quantum Dots and Their Application in Lighting, Displays, and Biology. *ECS J. Solid State Sci. Technol.* **2016**, *5* (1), R3019-R3031. DOI: 10.1149/2.0031601jsss.
- [22] Araujo, J. J.; Brozek, C. K.; Kroupa, D.; Gamelin, D. R. Degenerately n-Doped Colloidal PbSe Quantum Dots: Band Assignments and Electrostatic Effects. *Nano Lett.* **2018**, 3893-3900. DOI: 10.1021/acs.nanolett.8b01235.

- [23] Swart, I.; Liljeroth, P.; Vanmaekelbergh, D. Scanning Probe Microscopy and Spectroscopy of Colloidal Semiconductor Nanocrystals and Assembled Structures. *Chem. Rev.* **2016**, *116* (18), 11181-11219. DOI: 10.1021/acs.chemrev.5b00678.
- [24] Peters, J. L.; van den Bos, K. H. W.; Van Aert, S.; Goris, B.; Bals, S.; Vanmaekelbergh, D. Ligand-Induced Shape Transformation of PbSe Nanocrystals. *Chem. Mater.* **2017**, *29* (9), 4122-4128. DOI: 10.1021/acs.chemmater.7b01103.
- [25] Murray, C. B.; Kagan, C. R.; Bawendi, M. G. Self-Organization of CdSe Nanocrystallites into Three-Dimensional Quantum Dot Superlattices. *Science* **1995**, *270* (5240), 1335-1338. DOI: 10.1126/science.270.5240.1335.
- [26] Rosenberg, R.; Murray, C. B. From Materials to Devices: Scaling and Integration. *Annu. Rev. Mater. Sci.* **2000**, *30* (XII-XV).
- [27] Boles, M. A.; Engel, M.; Talapin, D. V. Self-Assembly of Colloidal Nanocrystals: From Intricate Structures to Functional Materials. *Chem. Rev.* **2016**, *116* (18), 11220-11289. DOI: 10.1021/acs.chemrev.6b00196.
- [28] Bian, K.; Choi, J. J.; Kaushik, A.; Clancy, P.; Smilgies, D. M.; Hanrath, T. Shape-Anisotropy Driven Symmetry Transformations in Nanocrystal Superlattice Polymorphs. *ACS Nano* **2011**, *5* (4), 2815-2823. DOI: 10.1021/nn103303q.
- [29] Choi, J. J.; Bealing, C. R.; Bian, K.; Hughes, K. J.; Zhang, W.; Smilgies, D. M.; Hennig, R. G.; Engstrom, J. R.; Hanrath, T. Controlling Nanocrystal Superlattice Symmetry and Shape-Anisotropic Interactions Through Variable Ligand Surface Coverage. *J. Am. Chem. Soc.* **2011**, *133* (9), 3131-3138. DOI: 10.1021/ja110454b.
- [30] Roest, A. L.; Houtepen, A. J.; Kelly, J. J.; Vanmaekelbergh, D. Electron-Conducting Quantum-Dot Solids with Ionic Charge Compensation. *Faraday Discuss.* **2004**, *125*, 55-62. DOI: 10.1039/b302839a.
- [31] Chandler, R. E.; Houtepen, A. J.; Nelson, J.; Vanmaekelbergh, D. Electron Transport in Quantum Dot Solids: Monte Carlo Simulations of the Effects of Shell Filling, Coulomb Repulsions, and Site Disorder. *Phys. Rev. B* **2007**, *75* (8). DOI: 10.1103/PhysRevB.75.085325.
- [32] Houtepen, A. J.; Kockmann, D.; Vanmaekelbergh, D. Reappraisal of Variable-Range Hopping in Quantum-Dot Solids. *Nano Lett.* **2008**, *8* (10), 3516-3520. DOI: 10.1021/nl8020347.
- [33] Lee, J.-S.; Kovalenko, M. V.; Huang, J.; Chung, D. S.; Talapin, D. V. Band-Like Transport, High Electron Mobility and High Photoconductivity in All-Inorganic Nanocrystal Arrays. *Nature Nanotechnology* **2011**, *6* (6), 348-352. DOI: 10.1038/nnano.2011.46.
- [34] Woo, J. Y.; Ko, J. H.; Song, J. H.; Kim, K.; Choi, H.; Kim, Y. H.; Lee, D. C.; Jeong, S. Ultrastable PbSe Nanocrystal Quantum Dots via In Situ Formation of Atomically Thin Halide Adlayers on PbSe(100). *J. Am. Chem. Soc.* **2014**, *136* (25), 8883-8886. DOI: 10.1021/ja503957r.
- [35] Baumgardner, W. J.; Whitham, K.; Hanrath, T. Confined-but-Connected Quantum Solids via Controlled Ligand Displacement. *Nano Lett.* **2013**, *13* (7), 3225-3231. DOI: 10.1021/nl401298s.
- [36] Grimaldi, G.; van den Brom, M. J.; du Fossé, I.; Crisp, R. W.; Kirkwood, N.; Gudjonsdottir, S.; Geuchies, J. J.; Kinge, S.; Siebbeles, L. D. A.; Houtepen, A. J. Engineering the Band Alignment in QD Heterojunction Films via Ligand Exchange. *J. Phys. Chem. C* **2019**, *29599*-29608. DOI: 10.1021/acs.jpcc.9b09470.
- [37] Yu, D.; Wang, C. J.; Guyot-Sionnest, P. n-Type Conducting CdSe Nanocrystal Solids. *Science* **2003**, *300* (5623), 1277-1280.
- [38] Lan, X. Z.; Chen, M. L.; Hudson, M. H.; Kamysbayev, V.; Wang, Y. Y.; Guyot-Sionnest, P.; Talapin, D. V. Quantum Dot Solids Showing State-Resolved Band-Like Transport. *Nat. Mater.* **2020**, *19* (3), 323-329. DOI: 10.1038/s41563-019-0582-2.
- [39] Oh, S. J.; Wang, Z.; Berry, N. E.; Choi, J.-H.; Zhao, T.; Gaulding, E. A.; Paik, T.; Lai, Y.; Murray, C. B.; Kagan, C. R. Engineering Charge Injection and Charge Transport for High Performance PbSe Nanocrystal Thin Film Devices and Circuits. *Nano Lett.* **2014**, *14* (11), 6210-6216. DOI: 10.1021/nl1502491d.
- [40] Evers, W. H.; Goris, B.; Bals, S.; Casavola, M.; de Graaf, J.; van Roij, R.; Dijkstra, M.; Vanmaekelbergh, D. Low-Dimensional Semiconductor Superlattices Formed by Geometric Control over Nanocrystal Attachment. *Nano Lett.* **2013**, *13* (6), 2317-2323. DOI: 10.1021/nl303322k.
- [41] Boneschanscher, M. P.; Evers, W. H.; Geuchies, J. J.; Altantzis, T.; Goris, B.; Rabouw, F. T.; van Rossum, S. A.; van der Zant, H. S.; Siebbeles, L. D.; Van Tendeloo, G.; et al. Long-Range Orientation and Atomic Attachment of Nanocrystals in 2D Honeycomb Superlattices. *Science* **2014**, *344* (6190), 1377-1380. DOI: 10.1126/science.1252642.
- [42] Sandeep, C. S. S.; Azpiroz, J. M.; Evers, W. H.; Boehme, S.-C.; Moreels, I.; Kinge, S.; Siebbeles, L. D. A.; Infante, I.; Houtepen, A. J. Epitaxially Connected PbSe Quantum-Dot Films: Controlled Neck Formation and Optoelectronic Properties. *ACS Nano* **2014**, *8* (11), 11499-11511. DOI: 10.1021/nn504679k.
- [43] Geuchies, J. J.; van Overbeek, C.; Evers, W. H.; Goris, B.; de Backer, A.; Gantapara, A. P.; Rabouw, F. T.; Hilhorst, J.; Peters, J. L.; Konovalov, O.; et al. In Situ Study of the Formation Mechanism of Two-Dimensional Superlattices from PbSe Nanocrystals. *Nat. Mater.* **2016**, *15* (12), 1248-1254. DOI: 10.1038/nmat4746.

- [44] Peters, J. L.; Altantzis, T.; Lobato, I.; Jazi, M. A.; van Overbeek, C.; Bals, S.; Vanmaekelbergh, D.; Sinai, S. B. Mono- and Multilayer Silicene-Type Honeycomb Lattices by Oriented Attachment of PbSe Nanocrystals: Synthesis, Structural Characterization, and Analysis of the Disorder. *Chem. Mater.* **2018**, *30* (14), 4831-4837. DOI: 10.1021/acs.chemmater.8b02178.
- [45] van Overbeek, C.; Peters, J. L.; van Rossum, S. A. P.; Smits, M.; van Huis, M. A.; Vanmaekelbergh, D. Interfacial Self-Assembly and Oriented Attachment in the Family of PbX (X = S, Se, Te) Nanocrystals. *J. Phys. Chem. C* **2018**, *122* (23), 12464-12473. DOI: 10.1021/acs.jpcc.8b01876.
- [46] Kalesaki, E.; Delerue, C.; Morais Smith, C.; Beugeling, W.; Allan, G.; Vanmaekelbergh, D. Dirac Cones, Topological Edge States, and Nontrivial Flat Bands in Two-Dimensional Semiconductors with a Honeycomb Nanogeometry. *Phys. Rev. X* **2014**, *4* (1), 011010. DOI: 10.1103/PhysRevX.4.011010.
- [47] Beugeling, W.; Kalesaki, E.; Delerue, C.; Niquet, Y. M.; Vanmaekelbergh, D.; Morais Smith, C. Topological States in Multi-Orbital HgTe Honeycomb Lattices. *Nat. Commun.* **2015**, *6*, 6316. DOI: 10.1038/ncomms7316.
- [48] Evers, W. H.; Schins, J. M.; Aerts, M.; Kulkarni, A.; Capiod, P.; Berthe, M.; Grandidier, B.; Delerue, C.; van der Zant, H. S.; van Overbeek, C.; et al. High Charge Mobility in Two-Dimensional Percolative Networks of PbSe Quantum Dots Connected by Atomic Bonds. *Nat. Commun.* **2015**, *6*, 8195. DOI: 10.1038/ncomms9195.
- [49] Alimoradi Jazi, M.; Janssen, V.; Evers, W. H.; Tadjine, A.; Delerue, C.; Siebbeles, L. D. A.; van der Zant, H. S. J.; Houtepen, A. J.; Vanmaekelbergh, D. Transport Properties of a Two-Dimensional PbSe Square Superstructure in an Electrolyte-Gated Transistor. *Nano Lett.* **2017**, *17* (9), 5238-5243. DOI: 10.1021/acs.nanolett.7b01348.
- [50] Jazi, M. A.; Kulkarni, A.; Sinai, S. B.; Peters, J. L.; Geschiere, E.; Failla, M.; Delerue, C.; Houtepen, A. J.; Siebbeles, L. D. A.; Vanmaekelbergh, D. Room-Temperature Electron Transport in Self-Assembled Sheets of PbSe Nanocrystals with a Honeycomb Nanogeometry. *J. Phys. Chem. C* **2019**, *123* (22), 14058-14066. DOI: 10.1021/acs.jpcc.9b03549.
- [51] Tadjine, A.; Allan, G.; Delerue, C. From Lattice Hamiltonians to Tunable Band Structures by Lithographic Design. *Phys. Rev. B* **2016**, *94* (7). DOI: 10.1103/PhysRevB.94.075441.
- [52] Walravens, W.; Solano, E.; Geenen, F.; Dendooven, J.; Gorobtsov, O.; Tadjine, A.; Mahmoud, N.; Ding, P. P.; Ruff, J. P. C.; Singer, A.; et al. Setting Carriers Free: Healing Faulty Interfaces Promotes Delocalization and Transport in Nanocrystal Solids. *ACS Nano* **2019**, *13* (11), 12774-12786. DOI: 10.1021/acsnano.9b04757.
- [53] Delerue, C. Nanocrystal Solids: Order and Progress. *Nat. Mater.* **2016**, *15* (5), 498-499. DOI: 10.1038/nmat4597.
- [54] Koh, W. K.; Bartnik, A. C.; Wise, F. W.; Murray, C. B. Synthesis of Monodisperse PbSe Nanorods: a Case for Oriented Attachment. *J. Am. Chem. Soc.* **2010**, *132* (11), 3909-3913. DOI: 10.1021/ja9105682.
- [55] Moayed, M. M. R.; Li, F.; Beck, B.; Schober, J. C.; Klinke, C. Anisotropic Circular Photogalvanic Effect in Colloidal Tin Sulfide Nanosheets. *Nanoscale* **2020**, *12* (11), 6256-6262. DOI: 10.1039/d0nr01189d.
- [56] Klokkenburg, M.; Houtepen, A. J.; Koole, R.; de Folter, J. W. J.; Erne, B. H.; van Faassen, E.; Vanmaekelbergh, D. Dipolar Structures in Colloidal Dispersions of PbSe and CdSe Quantum Dots. *Nano Lett.* **2007**, *7* (9), 2931-2936. DOI: 10.1021/nl10714684.
- [57] Schapotschnikow, P.; van Huis, M. A.; Zandbergen, H. W.; Vanmaekelbergh, D.; Vlugt, T. J. Morphological Transformations and Fusion of PbSe Nanocrystals Studied Using Atomistic Simulations. *Nano Lett.* **2010**, *10* (10), 3966-3971. DOI: 10.1021/nl101793b.
- [58] Fang, C.; van Huis, M. A.; Vanmaekelbergh, D.; Zandbergen, H. W. Energetics of Polar and Nonpolar Facets of PbSe Nanocrystals from Theory and Experiment. *ACS Nano* **2010**, *4* (1), 211-218. DOI: 10.1021/nn9013406.
- [59] Soligno, G.; Dijkstra, M.; van Roij, R. Self-Assembly of Cubes into 2D Hexagonal and Honeycomb Lattices by Hexapolar Capillary Interactions. *Phys. Rev. Lett.* **2016**, *116* (25), 258001. DOI: 10.1103/PhysRevLett.116.258001.
- [60] Soligno, G.; Dijkstra, M.; van Roij, R. Self-Assembly of Cubic Colloidal Particles at Fluid-Fluid Interfaces by Hexapolar Capillary Interactions. *Soft Matter* **2018**, *14* (1), 42-60. DOI: 10.1039/c7sm01946g.
- [61] Soligno, G.; Vanmaekelbergh, D. Understanding the Formation of PbSe Honeycomb Superstructures by Dynamics Simulations. *Phys. Rev. X* **2019**, *9* (2), 021015. DOI: 10.1103/PhysRevX.9.021015.
- [62] Soligno, G.; Vanmaekelbergh, D. Phase Diagrams of Honeycomb and Square Nanocrystal Superlattices from the Nanocrystal's Surface Chemistry at the Dispersion-Air Interface. *J. Chem. Phys.* **2019**, *151* (23), 234702. DOI: 10.1063/1.5128122.
- [63] Gupta, U.; Escobedo, F. A. Implicit Solvent Model for the Interfacial Configuration of Colloidal Nanoparticles and Application to the Self-Assembly of Truncated Cubes. *J. Chem. Theory Comput.* **2020**, *16* (9), 5866-5875. DOI: 10.1021/acs.jctc.0c00283.
- [64] Walravens, W.; De Roo, J.; Drijvers, E.; Ten Brinck, S.; Solano, E.; Dendooven, J.; Detavernier, C.; Infante, I.; Hens, Z. Chemically Triggered Formation of Two-Dimensional Epitaxial Quantum Dot Superlattices. *ACS Nano* **2016**, *10* (7), 6861-6870. DOI: 10.1021/acsnano.6b02562.
- [65] Tang, Z.; Kotov, N. A.; Giersig, M. Spontaneous Organization of Single CdTe Nanoparticles into Luminescent Nanowires. *Science* **2002**, *297* (5579), 237-240. DOI: 10.1126/science.1072086.

- [66] Pradhan, N.; Xu, H.; Peng, X. Colloidal CdSe Quantum Wires by Oriented Attachment. *Nano Lett.* **2006**, *6* (4), 720-724. DOI: 10.1021/nl052497m.
- [67] Liu, X.; Wan, J.; Xiong, Y.; Liang, S.; Gao, Y.; Tang, Z. Synthesis of Uniform CdSe Quantum Wires via Oriented Attachment. *Journal of Nanoscience and Nanotechnology* **2015**, *15* (8), 5798-5806. DOI: 10.1166/jnn.2015.9768.
- [68] Tang, Z.; Zhang, Z.; Wang, Y.; Glotzer, S. C.; Kotov, N. A. Self-Assembly of CdTe Nanocrystals into Free-Floating Sheets. *Science* **2006**, *314* (5797), 274-278. DOI: 10.1126/science.1128045.
- [69] Ondry, J. C.; Philbin, J. P.; Lostica, M.; Rabani, E.; Alivisatos, A. P. Resilient Pathways to Atomic Attachment of Quantum Dot Dimers and Artificial Solids from Faceted CdSe Quantum Dot Building Blocks. *ACS Nano* **2019**, *13* (10), 12322-12344. DOI: 10.1021/acs.nano.9b03052.
- [70] Wang, Y.; Peng, X. X.; Abelson, A.; Zhang, B. K.; Qian, C.; Ercius, P.; Wang, L. W.; Law, M.; Zheng, H. M. In Situ TEM Observation of Neck Formation During Oriented Attachment of PbSe Nanocrystals. *Nano Research* **2019**, *12* (10), 2549-2553. DOI: 10.1007/s12274-019-2483-8.
- [71] daSilva, J. C.; Smeaton, M. A.; Dunbar, T. A.; Xu, Y.; Balazs, D. M.; Kourkoutis, L. F.; Hanrath, T. Mechanistic Insights into Superlattice Transformation at a Single Nanocrystal Level Using Nanobeam Electron Diffraction. *Nano Lett.* **2020**, *20* (7), 5267-5274. DOI: 10.1021/acs.nanolett.0c01579.
- [72] Choi, J. J.; Bian, K.; Baumgardner, W. J.; Smilgies, D. M.; Hanrath, T. Interface-Induced Nucleation, Orientational Alignment and Symmetry Transformations in Nanocube Superlattices. *Nano Lett.* **2012**, *12* (9), 4791-4798. DOI: 10.1021/nl3026289.
- [73] Weidman, M. C.; Smilgies, D. M.; Tisdale, W. A. Kinetics of the Self-Assembly of Nanocrystal Superlattices Measured by Real-Time In Situ X-Ray Scattering. *Nat. Mater.* **2016**, *15* (7), 775-781. DOI: 10.1038/nmat4600.
- [74] Afsar-Siddiqui, A. B.; Luckham, P. F.; Matar, O. K. The Spreading of Surfactant Solutions on Thin Liquid Films. *Adv. Colloid Interface Sci.* **2003**, *106* (1-3), 183-236. DOI: 10.1016/s0001-8686(03)00111-8.
- [75] Balazs, D. M.; Dunbar, T. A.; Smilgies, D. M.; Hanrath, T. The Coupled Dynamics of Colloidal Nanoparticle Spreading and Self-Assembly at a Fluid-Fluid Interface. *Langmuir* **2020**, *36* (22), 6106-6115. DOI: 10.1021/acs.langmuir.0c00524.
- [76] Geuchies, J. J.; Soligno, G.; Geraffy, E.; Hendriks, C. P.; van Overbeek, C. V.; Montanarella, F.; Slot, M. R.; Kononov, O. V.; Petukhov, A. V.; Vanmaekelbergh, D. Unravelling Three-Dimensional Adsorption Geometries of PbSe Nanocrystal Monolayers at a Liquid-Air Interface. *Commun. Chem.* **2020**, *3* (1). DOI: ARTN 2810.1038/s42004-020-0275-4.
- [77] Sushko, M. L. Understanding the Driving Forces for Crystal Growth by Oriented Attachment Through Theory and Simulations. *J. Mater. Res.* **2019**, *34* (17), 2914-2927. DOI: 10.1557/jmr.2019.151.
- [78] van der Sluijs, M. M.; Sanders, D.; Jansen, K. J.; Soligno, G.; Vanmaekelbergh, D.; Peters, J. L. On the Formation of Honeycomb Superlattices from PbSe Quantum Dots: The Role of Solvent-Mediated Repulsion and Facet-to-Facet Attraction in NC Self-Assembly and Alignment. *J. Phys. Chem. C* **2022**. DOI: 10.1021/acs.jpcc.1c07430.

S3 Supporting Information

Key references

Boneschanscher, M. P.; Evers, W. H.; Geuchies, J. J.; Altantzis, T.; Goris, B.; Rabouw, F. T.; van Rossum, S. A.; van der Zant, H. S.; Siebbeles, L. D.; Van Tendeloo, G.; Swart, I.; Hilhorst, J.; Petukhov, A. V.; Bals, S.; Vanmaekelbergh, D., Long-Range Orientation and Atomic Attachment of Nanocrystals in 2D Honeycomb Superlattices. *Science* 2014, 344, 1377-1380.¹

Two-dimensional honeycomb superlattices are prepared by oriented attachment of PbSe nanocrystals. Direct imaging and wave scattering methods reveal that the superlattices are atomically coherent and have a buckled octahedral symmetry.

Geuchies, J. J.; van Overbeek, C.; Evers, W. H.; Goris, B.; de Backer, A.; Gantapara, A. P.; Rabouw, F. T.; Hilhorst, J.; Peters, J. L.; Konovalov, O.; Petukhov, A. V.; Dijkstra, M.; Siebbeles, L. D. A.; van Aert, S.; Bals, S.; Vanmaekelbergh, D., In Situ Study of the Formation Mechanism of Two-Dimensional Superlattices from PbSe Nanocrystals. *Nature Materials* 2016, 15, 1248-1254.²

The formation mechanism of PbSe square superlattices was revealed by combining wave scattering techniques with electron microscopy and Monte Carlo simulations. We observe different intermediate stages and final attachment of the nanocrystals at the (100) planes.

Peters, J. L.; Altantzis, T.; Lobato, I.; Jazi, M. A.; van Overbeek, C.; Bals, S.; Vanmaekelbergh, D.; Sinai, S. B., Mono- and Multilayer Silicene-Type Honeycomb Lattices by Oriented Attachment of PbSe Nanocrystals: Synthesis, Structural Characterization, and Analysis of the Disorder. *Chemistry of Materials* 2018, 30, 4831-4837.³

Large-scale uniform mono- and multilayer silicene-type honeycomb PbSe superlattices are prepared by oriented attachment. Different classes of disorder in the lattices are explained in terms of position and atomic alignment of the nanocrystals.

S3.1 Oriented attachment as an alternative crystal growth process in aqueous solvents

Oriented attachment of charge-stabilized crystals in aqueous solvents is of interest in the research on biominerals, geology, materials science, and of course for crystallography itself. A selection of reports from this millennium are presented in supporting information **Table S3.1** and **Table S3.2**. Commonly, crystal growth by oriented attachment is coined non classical crystal growth,¹ to distinguish it from the classical atom-by-atom (molecule-by molecule) growth of crystals. Oriented attachment between crystals is observed in natural biological conditions and is assumed to be important for biomineral formation.⁴⁻⁷ Oriented attachment of hydroxyapatite ($\text{Ca}_5(\text{PO}_4)_3(\text{OH})$) and calcium carbonate (CaCO_3) crystals has been studied to understand bone formation and bio-skeletons. Analytical studies of oriented attachment are partially impeded by the existence of a plethora of crystal polymorphs for these compounds. For relatively stable crystals consisting of for example TiO_2 , SnO_2 , magnetite, hematite, and ZnO, the crystal formation by oriented attachment is enhanced by so called “hydrothermal coarsening”, which means high temperatures and pressures applied in an autoclave.⁸⁻¹² Crystals of Fe-oxide compounds (magnetite, hematite) are of interest from a geological perspective and magnetism as well.

The common scientific questions are related to the driving force for oriented attachment, the type of crystallographic facets involved, the precise mechanism on an atomic scale, the origin of defects in crystals such as twinning planes, edge- and screw dislocations.⁴ In a minority of cases the crystals formed by oriented attachment under hydrothermal aging are considered as building blocks of technological interest, for instance in opto-electronics (solar cells).^{13,14}

S3.1.1 Driving forces and facet specificity

Sols in water are stable due to the electrical double layer around the crystals; with one type of charges on the crystal surface counteracted by a diffuse layer of counter charge. Regarding the facet specificity, one can imagine that the density of two charges on the crystals can depend on the chemical surface termination of specific facets. For a number of crystals, the surface energy or crystal/liquid interfacial energy per unit area is understood to a certain extent; in reports one finds the notions of higher – and lower –energy surfaces.^{13,15-17} The energy lowered by crystal attachment will be strongest if two high-energy facets are eliminated by connection. Often, strong adsorption of H₂O to specific facets can be a factor that decides which facets are involved in the epitaxial connection between crystals during hydrothermal coarsening. Frequently oriented attachment between charge-stabilized crystals has been observed when the temperature is raised above room temperature, described in the literature as hydrothermal treatment;^{5,12,15,16,18-20} this means that Brownian motion of the dispersed crystals becomes so vivid that the protecting charge double layer breaks up in a collision, and facets face each other on a short distance. The increase of oriented attachment by raising the temperature is thus mostly a kinetic effect.

One of the best studied cases is oriented attachment of anatase TiO₂ nanocrystals. Penn et al.¹² reported oriented attachment via the high energy (001) and (112) facets. Adachi et al.¹⁰ showed that these facets can be blocked by certain ligands, and that oriented attachment then occurs via lower energy facets. During hydrothermal coarsening it is often found that nanocrystals attach to form rods, mostly with the polar facets involved. In a second stage these rods adhere along their long direction and finally attach to form sheets or 3D materials, either fully closed or with pores present. The hierarchical construction of porous materials for opto-electronic applications and energy storage is an interesting engineering pathway, provided that the building blocks as well as the facet selectivity in the attachment can be precisely controlled.

S3.1.2 The study of crystal defects and annealing of crystal defects

Crystal defects originating from imperfect oriented attachment have been studied by ex situ high resolution transmission electron microscopy (HR-TEM). An early study of TiO₂ showed that twinning planes in a crystal, and edge and screw dislocations can be caused by imperfect oriented attachment.^{15,21} The presence crystal defects constituted the first strong indication that oriented attachment is a prominent mechanism of crystal growth, abundant in natural and laboratory conditions. Twinning can occur when identical crystallographic facets face each other and attach, sharing the same crystal lattice points between them. An edge dislocation results from an atomic plane that ends halfway between the two planes that connect; a screw dislocation is more intricate to understand. Later on, the annealing of defects has been monitored in time under two types of conditions: (i) in the vacuum and beam conditions of an electron microscope,²² (ii) with special samples containing ultra-thin films of nanocrystals and the liquid medium.²³⁻²⁵

Table S3.1 Overview of reports on oriented attachment of charge-stabilized crystals in water or polar solvents.

Compound	Reference	Building blocks - crystal structure - shape - size - active facet	Solvent, ligands (?), and experimental conditions	Type of crystals formed by oriented attachment	Scientific interest	Application
TiO ₂	21	Anatase nanocrystals, - multi-faceted - 5 nm - active facets: high energy facets (112), (001)	Water, hydrothermal coarsening	Larger crystals formed from two or more nanocrystals	Understanding the formation of edge- and screw dislocations formed by imperfect oriented attachment	Fundamental knowledge
TiO ₂	15	Preformed nanocrystals - anatase, brookite - multi-faceted - 5 nm - active (112) and (001) facets	Water, hydrothermal coarsening	Larger crystals with epitaxial connections and twinned interfaces	Understanding twinning and polytypism in crystal growth	Fundamental knowledge
TiO ₂	13	- preformed anatase nanocrystals - few nm in size - high energy (001) facet covered with surfactants, (101) active	Polar solvent	Anatase nanowires along the <101> direction by (101) facet attachment, different from Penn et al.	Understanding the type of facets used in oriented attachment	Assemblies of attached TiO ₂ rods as high-surface area material for dye-sensitized solar cells
TiO ₂	10	Ti(IV)Oxides → fibers → branched rutile mesocrystals via oriented attachment	Acidic water	- rutile fibers with c-axis as long axis - more complex and larger crystals with attachment via the lateral (110) facets	Hierarchical assembly and oriented attachment on different stages of the hydrothermal coarsening	--
TiO ₂	26	TiO ₂ nanocrystals, anatase, charge-stabilized in water Atomistic simulations of attachment	Water and salts	Larger crystals with attachment via (112) facets, and (001) and (100) facets: single crystals and twinned crystals	Understanding facet-selectivity in OA of anatase NCs, charge-stabilized: attractive interactions between double layers, water molecules on facets can prevent OA	--
TiO ₂	27	Synthesis in autoclave starting from Ti-isopropoxide, trimethyl ammonium hydroxide resulting in TiO ₂ nanocrystals, anatase, (001) high energy facets	Autoclave, water, 230 °C	- anatase nanorods along <001>, attachment via high-energy (001) facets - further ripening to ellipsoids	--	Anode material for quantum dot-sensitized cells
TiO ₂	28	TiCl ₄ and H ₂ O	Atomic layer deposition on a graphene crystal, 300 °C	Anatase rods and V-shaped structures in alignment with underlying graphene crystal	Understanding non-typical ALD growth: formation of small flat NCs that move along the surface, coalescence, restructuring and rod crystallization	--
TiO ₂	29	Ti(IV) complex and water	Water, hydrothermal. Coarsening	- primary 6 nm elongated NCs with <001> as long direction - spindle-like large structures (500 nm) with pores formed by oriented attachment of primary NCs along (001) direction and sides ways	Understanding hierarchical growth	Anode material for Na-ion battery

Table S3.1 Overview of reports on oriented attachment of charge-stabilized crystals in water or polar solvents (continued).

Compound	Reference	Building blocks - crystal structure - shape - size - active facet	Solvent, ligands (?), and experimental conditions	Type of crystals formed by oriented attachment	Scientific interest	Application
SnO ₂	16	Preformed SnO ₂ nanocrystals: - nearly spherical, 1-2 nm, multi-faceted - charge stabilized - (100) facets lowest in energy	Water, coagulation at isoelectric point,	Disordered rods of a few attached nanocrystals	Understanding the effect of Brownian motion vs. nanocrystal alignment by facet/facet interactions	--
SnO ₂	30	SnCl ₂ in water/ethanol mixture Endured aging at 120 °C.	Water/ethanol	Disordered sheets, rutile, non-stoichiometric	Understanding sheet formation in one pot-synthesis, small NCs as intermediates	Li battery
SnO ₂	31	Sn(citrate) ₂ and manganese(citrate) ₂ heating up to 500 °C results in NCs, truncated octahedrons	Nanocrystals formed in polar solvent; oriented attachment performed under dry conditions at 700 °C.	2D/3D disordered agglomerates, Mn ²⁺ ions at facets impede or slow down oriented attachment	HR TEM study of facet/facet connections in NC clusters with strong misalignment	--
SnO ₂	32	- NCs in water - 5 nm	Basic water, coarsening for several days	- Nanocrystals attach to wires <112> direction - Wires attach via their sizes to sheets and 3D crystals	- Understanding of hierarchical steps in crystal formation via oriented attachment on several stages	--
SnO ₂	17	- SnCl ₂ in water at very high pressure → elongated monodisperse dodecahedrons 200 nm, - active (100), (110) facets in OA, (111) facets protected by NMe ₃	Water, autoclave, 220 °C, very high pressure	3D very well-ordered structures, with attachment mostly via (100) facets	- Understanding crystal growth under high pressure - Understanding assembly of large monodisperse crystals into ordered superstructures under high pressure	--
CaCO ₃	33	CaCl ₂ , NH ₄ Cl, CO ₂ in water	--	Ca ²⁺ ions → amorphous CaCO ₃ → vaterite (100) terminated sheets (>100nm) stabilized with NH ₄ ⁺ → stacks → 3-D calcite by OA	Biominerization via intermediate steps in which OA is important	--
CaCO ₃	6	Ca(OH) ₂ + CO ₂ → 30-50 nm truncated nanocubes, with (104) facets	Water, room temperature	Linear structures and multi-branched 2D and 3D aggregates by OA of the nanocubes	Understanding interaction between charged facets (Ca ²⁺ , CO ₃ ²⁻ terminated) in biomineralization	--
CaCO ₃	34	Rod-like structures formed from NCs (see above)	Water	Lateral attachment of rods forming bundles	Attachment directed by surface charge	--
Ca ₅ (PO ₄) ₃ (OH), hydroxyapatite	5	Amorphous particles and nanocrystals	Water, hydrothermal aging	- Wurtzite nanorods along polar c-axis, 5 nm in diameter, 20-100 nm in length - Assemblies of oriented nanorods	Understanding bone formation with biomimetic experiments	--

Table S3.1 Overview of reports on oriented attachment of charge-stabilized crystals in water or polar solvents (continued).

Compound	Reference	Building blocks - crystal structure - shape - size - active facet	Solvent, ligands (?), and experimental conditions	Type of crystals formed by oriented attachment	Scientific interest	Application
Fe ₃ O ₄ (magnetite)	35	Preformed 5 nm Fe ₃ O ₄ nanocrystals	Polar solvent	Large porous spheres 100 nm in diameter formed by OA of 5 nm crystals	Understanding oriented attachment	--
Fe ₂ O ₃ (hematite)	36	100 nm hematite nanocrystals, with facets	Water, hydrothermal	<ul style="list-style-type: none"> - 1D chains and extended hexagonal monolayers and films by OA of 100 nm hematite NCs - OA via (110) planes, while (001) facets have lowest surface energy 	<ul style="list-style-type: none"> - Understanding oriented attachment of large crystals in water - Interplay of facet-specific interactions and magnetic dipoles 	Formation of magnetic materials
Fe ₂ O ₃ (e- and a-phase)	37	Fe(NO ₃) ₃ in water/(NH ₄) ₂ HPO ₄	Hydrothermal reaction at 200 °C in autoclave	<ul style="list-style-type: none"> - Primary nanocrystals: e-Fe₂O₃, 10-15 nm in size - Formation of nanoflakes and ellipsoid-shaped structures, 200-500 nm in size with a-crystal structure, formed by OA 	<ul style="list-style-type: none"> - Formation of e-Fe₂O₃ nanocrystals with beneficial magnetic properties - Slow decay of this phase to large aggregates of Fe₂O₃ with smaller coercivity 	--
FeO(OH) goethite	38	Fe(OH) ₃ in water + O ₂	Water	<ul style="list-style-type: none"> - Nanorods by isotropic crystal growth - OA of rods via lateral (110) facets to larger crystalline rods (30 nm in width, 200 nm in length) 	<ul style="list-style-type: none"> - Understanding the formation of Goethite rods via a hierarchical process 	--
ZnO	39	Ligand-free NCs, 5 nm in size	Polar solvent aging of the NCs in MeOH/chloroform	Monodisperse nano-porous ellipsoids, about 200 nm in length, 100 nm in width, 8 nm pores	Proof that mesoscopic 3D systems can be formed by OA in polar solvents	Photocatalysis, photodegradation of organic waste
ZnO	40	One-pot synthesis, based on Zn(acetate) ₂ in ethanol, NCs are intermediates in rod formation	Water/Ethanol Enduring hydrothermal coarsening in autoclave	ZnO nanocrystals 1-3 nm diameter, ZnO nanorods with <0001> wurtzite long axis, 15 nm in diameter, 100 nm in length	Oriented attachment on diverse hierarchical moments in the coarsening, during formation of 7 nm crystals, which then form (15,100 nm) wurtzite rods Axial oriented attachment of small nanocrystals vs. lateral attachment	--
ZnO	12	One pot synthesis based on hydrolysis of Zn(OH) ₂ under hydrothermal conditions, ZnO NCs as intermediate phase	Water, sodium dodecyl sulfonate as ligand, presumable adsorbed at the lateral facets of the wires	ZnO nanowires along <0001> wurtzite axis, 20-80 μm, 50-200 nm diameter	Role of sodium dodecyl sulfonate ligands adsorbing at the lateral (100) facets, promoting stronger anisotropy	Opto-electronic devices, sensitive UV photodetector
ZnO	41	Measurement of (0001) facet-to-facet forces by AFM	Water	--	Understanding facet-to-facet forces as a function of distance (intervening water layers) and relative in-plane angle	--

Table S3.1 Overview of reports on oriented attachment of charge-stabilized crystals in water or polar solvents (continued).

Compound	Reference	Building blocks - crystal structure - shape - size - active facet	Solvent, ligands (?), and experimental conditions	Type of crystals formed by oriented attachment	Scientific interest	Application
BaTiO ₃	42	- Multi-faceted BaTiO ₃ NCs in water - Cubic NCs in organic solvent, oleic acid capped	- Water, hydrothermal - Organic solvents	Systems with a few nanocrystals attached, with alignment of the nanocrystals	Model study based on results of two other reports, competition between van der Waals facet/facet interactions, and assembly directed by the NC dipole moment around the c-axis	--
MnS	43	Manganocene (Mn-C) and elemental sulfur	Dry mixture, autoclave, 500-800 °C	Porous mesoscopic carbon/MnS architectures by oriented attachment of MnS 200-400 nm crystals in the carbon support	--	Anode material for Li batteries
MnO ₂	44	Structures with interconnected MnO ₂ octahedra forming linear pores	Monitoring oriented attachment of the building blocks in a liquid cell	- primary building blocks attach - finally, a nanowire with several pore-channels is formed	Peculiar crystal structures with molecular-like binding mechanisms	--
Mn ₂ O ₃ , MnO ₂	45	Interconnected MnO ₂ octahedra form hexagonal nanoflakes along a <100> direction	Water	Nanoflakes attach in imperfect way to form multi-domain nanoflower structures	Understanding edge-to-edge oriented attachment of nanoflakes promoted by hydrogen bonds	--
CoO	46	CoCO ₃ forms CoO nanorods in solvothermal conditions	Water	- Rods attach side-by-side to plates - Plates attach to form book-like structures	Understanding hierarchical OA using several facet types	Energy storage in supercapacitors
Au	47	Au NCs dispersed	Water, laser-light in the near IR	Hierarchical oriented attachment: - NCs attach to form rods, - rods attach in length and laterally, - longer rods attach to form micron sized wires	Understanding hierarchical OA, driven by heating and plasmon resonances	--
Au	48	Citrate-stabilized Au nanocrystals, 2 nm in size, multi-faceted	Water, liquid cell	NC dimers attached via (111) facets	In-situ study of rotational motion of nanocrystals, and finally epitaxial connection	--
PbSe	49	Pb(CH ₃ COO) ₂ and Na ₂ SeO ₃ Chemical bath deposition of a GaAs wafer	Water at pH = 13	Small cubic PbSe nanocrystals formed in solution, attach via (100)/(100) interactions to columns	Preparing electronic grade and quantized thin PbSe films	--
PbTiO ₃ perovskite fibers	20	Pb(NO ₃) ₂ and Ti(OH) ₄	Water, hydrothermal conditions	PbTiO ₃ nanorods that evolve into ribbons with diameters of 250 nm via lateral OA, using (110) planes	Formation of high-quality crystalline ribbons, photoluminescence in visible region	--

Table S3.2 Overview of reports on oriented attachment in organic non-polar solvents.

Compound	Reference	Building blocks - crystal structure - shape - size - active facet	Suspension, ligand, method	Crystal formed by oriented attachment	Scientific interest	Application
PbSe	50	Nanocrystals - rock salt - truncated cube - octahedron - few nm - (100) or (110) or (111) depending on ligands	Organic, ligand-stabilized nanocrystals	- Direct synthesis of straight nanowires along <100>, 4-20 nm diameter, micrometer length - Nanorods by oriented attachment of nanocrystals with use of: (100) facets (oleates), (110) facets (amines) (111) facets (hexadecylamine)	Study of active facet selectivity depending on the ligand stabilization, strong anisotropy with centrosymmetric crystal structure	Opto-electronic materials
PbSe	51	- One-pot synthesis with Pb- and Se-precursors - 5 nm PbSe nanocube intermediates	Organic	- PbSe nanowires formed by O'A attachment of 5 nm nanocrystal intermediates aligned along a <100> direction - Liquid crystals of aligned nanorods	- study of anisotropic crystal growth with centrosymmetric rock salt crystal structure	Opto-electronics
PbS	52	- One-pot synthesis, PbS nanocrystals as intermediates, dense packing of oleates on (100) planes	Organic, Cl-containing co-solvent	- Extended (μm) 2D sheets, 5 nm in thickness, OA attachment of nanocrystals, presumably along the (110) direction	- formation of 2D opto-electronic materials by wet chemistry	Opto-electronics
Mn ₂ O ₄	53	- Autoclave synthesis in water of 20-30 nm truncated cuboids - 6 (100) facets - oleic acid capped	Hexane and toluene, solvent evaporation, NC assembly at liquid/air interface, heating	- Linear rods <100> direction, with epitaxial connection via the (100) facets - Square monolayers with attachment at 4 (100) facets	- Understanding assembly of capped nanocubes at organic liquid/air interface, OA upon removal of oleic acid	--
ZnS	54	Nanocrystals - zinc blende - multi-faceted - 5 nm	Organic solvents, oleic acid, hexadecylamine	- Direct synthesis of nanorods of 5nm diameter, 20 nm length - Oriented attachment of nanocrystals to rods	Facet-selective oriented attachment	Opto-electronic materials
CdSe	55	Direct one-pot synthesis, nanocrystals as intermediates	Organic, alkylamine ligands of different lengths	- Direct synthesis of CdSe nanorods 1.5 – 6nm in diameter, via intermediate phases of pearl-necklace or string-of-pearls agglomerates	Understanding nanowire growth, via intermediate agglomeration, and OA	Opto-electronic materials
Au	56	Chloroauric acid and oleylamine (reductor) in a toluene medium	Organic solvents	- Ionic precursors → Au nanocrystals 2 nm in size → Au nanowires with of 2 nm in diameter up to μm , growth along the <111> axis - Arrays of nanowires	- Understanding anisotropic growth by OA of cubic fcc nanocrystals - Formation of twin defects, and atomic reconstructions, smoothing the nanowires	--

References

- [1] Boneschanscher, M. P.; Evers, W. H.; Geuchies, J. J.; Altantzis, T.; Goris, B.; Rabouw, F. T.; van Rossum, S. A.; van der Zant, H. S.; Siebbeles, L. D.; Van Tendeloo, G.; et al. Long-Range Orientation and Atomic Attachment of Nanocrystals in 2D Honeycomb Superlattices. *Science* **2014**, *344* (6190), 1377-1380. DOI: 10.1126/science.1252642.
- [2] Geuchies, J. J.; van Overbeek, C.; Evers, W. H.; Goris, B.; de Backer, A.; Gantapara, A. P.; Rabouw, F. T.; Hilhorst, J.; Peters, J. L.; Kononov, O.; et al. In Situ Study of the Formation Mechanism of Two-Dimensional Superlattices from PbSe Nanocrystals. *Nat. Mater.* **2016**, *15* (12), 1248-1254. DOI: 10.1038/nmat4746.
- [3] Peters, J. L.; Altantzis, T.; Lobato, I.; Jazi, M. A.; van Overbeek, C.; Bals, S.; Vanmaekelbergh, D.; Sinai, S. B. Mono- and Multilayer Silicene-Type Honeycomb Lattices by Oriented Attachment of PbSe Nanocrystals: Synthesis, Structural Characterization, and Analysis of the Disorder. *Chem. Mater.* **2018**, *30* (14), 4831-4837. DOI: 10.1021/acs.chemmater.8b02178.
- [4] Niederberger, M.; Colfen, H. Oriented Attachment and Mesocrystals: Non-Classical Crystallization Mechanisms Based on Nanoparticle Assembly. *Phys. Chem. Chem. Phys.* **2006**, *8* (28), 3271-3287. DOI: 10.1039/b604589h.
- [5] Chen, J. D.; Wang, Y. J.; Wei, K.; Zhang, S. H.; Shi, X. T. Self-Organization of Hydroxyapatite Nanorods Through Oriented Attachment. *Biomaterials* **2007**, *28* (14), 2275-2280. DOI: 10.1016/j.biomaterials.2007.01.033.
- [6] Takasaki, M.; Kimura, Y.; Yamazaki, T.; Oaki, Y.; Imai, H. 1D Oriented Attachment of Calcite Nanocrystals: Formation of Single-Crystalline Rods Through Collision. *RSC Advances* **2016**, *6* (66), 61346-61350. DOI: 10.1039/c6ra09452j.
- [7] Alivisatos, A. P. Biomineralization. Naturally Aligned Nanocrystals. *Science* **2000**, *289* (5480), 736-737. DOI: 10.1126/science.289.5480.736.
- [8] Liu, J.; Wei, A.-X.; Zhang, C.-X. Synthesis of Density-Controllable TiO₂ Nanowire Bundle Arrays and Their Application in Quantum Dot Sensitized Solar Cell. *J. Inorg. Mater.* **2013**, *28* (6), 639-643. DOI: 10.3724/sp.j.1077.2013.12468.
- [9] Gao, H.; Sui, X.; Dai, D.; Si, C.; Liu, G. Hierarchical Honeycomb Anatase TiO₂ with (100) Facet: Facile Hydrothermal Preparation and Enhanced Photocatalytic Performance. *Journal of Nanoscience and Nanotechnology* **2015**, *15* (7), 5193-5197. DOI: 10.1166/jnn.2015.9843.
- [10] Jordan, V.; Javornik, U.; Plavec, J.; Podgornik, A.; Recnik, A. Self-Assembly of Multilevel Branched Rutile-Type TiO₂ Structures via Oriented Lateral and Twin Attachment. *Scientific Reports* **2016**, *6*, 24216. DOI: 10.1038/srep24216.
- [11] Sun, Y.; Ndifor-Angwafor, N. G.; Riley, D. J.; Ashfold, M. N. R. Synthesis and Photoluminescence of Ultra-Thin ZnO Nanowire/Nanotube Arrays Formed by Hydrothermal Growth. *Chem. Phys. Lett.* **2006**, *431* (4-6), 352-357. Article. DOI: 10.1016/j.cplett.2006.09.100.
- [12] Wang, J.; Li, X.; Teng, C. J.; Xia, Y.; Xu, J. L.; Xie, D.; Xiang, L.; Komarneni, S. Ligand-Directed Rapid Formation of Ultralong ZnO Nanowires by Oriented Attachment for UV Photodetectors. *J. Mater. Chem. C* **2016**, *4* (24), 5755-5765. DOI: 10.1039/c6tc01054g.
- [13] Adachi, M.; Murata, Y.; Takao, J.; Jiu, J.; Sakamoto, M.; Wang, F. Highly Efficient Dye-Sensitized Solar Cells with a Titania Thin-Film Electrode Composed of a Network Structure of Single-Crystal-Like TiO₂ Nanowires Made by the "Oriented Attachment" Mechanism. *J. Am. Chem. Soc.* **2004**, *126* (45), 14943-14949. DOI: 10.1021/ja048068s.
- [14] Zhu, L. Z.; Richardson, B. J.; Yu, Q. M. Anisotropic Growth of Iron Pyrite FeS₂ Nanocrystals via Oriented Attachment. *Chem. Mater.* **2015**, *27* (9), 3516-3525. DOI: 10.1021/acs.chemmater.5b00945.
- [15] Penn, R. L.; Banfield, J. F. Oriented Attachment and Growth, Twinning, Polytypism, and Formation of Metastable Phases; Insights from Nanocrystalline TiO₂. *Am. Mineral.* **1998**, *83* (9-10), 1077-1082. DOI: 10.2138/am-1998-9-1016.
- [16] Lee, E. J. H.; Ribeiro, C.; Longo, E.; Leite, E. R. Oriented Attachment: An Effective Mechanism in the Formation of Anisotropic Nanocrystals. *J. Phys. Chem. B* **2005**, *109* (44), 20842-20846. DOI: 10.1021/jp0532115.
- [17] Wang, J.; Lian, G.; Si, H. B.; Wang, Q. L.; Cui, D. L.; Wong, C. P. Pressure-Induced Oriented Attachment Growth of Large-Size Crystals for Constructing 3D Ordered Superstructures. *ACS Nano* **2016**, *10* (1), 405-412. DOI: 10.1021/acsnano.5b05108.
- [18] Dalod, A. R. M.; Grendal, O. G.; Skjaervo, S. L.; Inzani, K.; Selbach, S. M.; Henriksen, L.; van Beek, W.; Grande, T.; Einarsrud, M. A. Controlling Oriented Attachment and in Situ Functionalization of TiO₂ Nanoparticles During Hydrothermal Synthesis with APTES. *J. Phys. Chem. C* **2017**, *121* (21), 11897-11906. DOI: 10.1021/acs.jpcc.7b02604.

- [19] Lavric, V.; Isopescu, R.; Maurino, V.; Pellegrino, F.; Pellutic, L.; Ortel, E.; Hodoroaba, V. D. A New Model for Nano-TiO₂ Crystal Birth and Growth in Hydrothermal Treatment Using an Oriented Attachment Approach. *Cryst. Growth Des.* **2017**, *17* (11), 5640-5651. DOI: 10.1021/acs.cgd.7b00302.
- [20] Zhao, R. Y.; Li, M.; Ren, Z. H.; Zhu, Y. H.; Han, G. R. Three-Dimensional Oriented Attachment Growth of Single-Crystal Pre-Perovskite PbTiO₃ Hollowed Fibers. *CrystEngComm* **2018**, *20* (4), 448-453. DOI: 10.1039/c7ce01780d.
- [21] Penn, R. L.; Banfield, J. F. Imperfect Oriented Attachment: Dislocation Generation in Defect-Free Nanocrystals. *Science* **1998**, *281* (5379), 969-971. DOI: 10.1126/science.281.5379.969.
- [22] van Huis, M. A.; Kunneman, L. T.; Overgaag, K.; Xu, Q.; Pandraud, G.; Zandbergen, H. W.; Vanmaekelbergh, D. Low-Temperature Nanocrystal Unification Through Rotations and Relaxations Probed by In Situ Transmission Electron Microscopy. *Nano Lett.* **2008**, *8* (11), 3959-3963. DOI: 10.1021/nl8024467.
- [23] Yuk, J. M.; Park, J.; Ercius, P.; Kim, K.; Hellebusch, D. J.; Crommie, M. F.; Lee, J. Y.; Zettl, A.; Alivisatos, A. P. High-Resolution EM of Colloidal Nanocrystal Growth using Graphene Liquid Cells. *Science* **2012**, *336* (6077), 61-64. DOI: 10.1126/science.1217654.
- [24] Hauwiller, M. R.; Frechette, L. B.; Jones, M. R.; Ondry, J. C.; Rotskoff, G. M.; Geissler, P.; Alivisatos, A. P. Unraveling Kinetically-Driven Mechanisms of Gold Nanocrystal Shape Transformations Using Graphene Liquid Cell Electron Microscopy. *Nano Lett.* **2018**, *18* (9), 5731-5737. DOI: 10.1021/acs.nanolett.8b02337.
- [25] Ondry, J. C.; Hauwiller, M. R.; Alivisatos, A. P. Dynamics and Removal Pathway of Edge Dislocations in Imperfectly Attached PbTe Nanocrystal Pairs: Toward Design Rules for Oriented Attachment. *ACS Nano* **2018**, *12* (4), 3178-3189. DOI: 10.1021/acsnano.8b00638.
- [26] Sushko, M. L.; Rosso, K. M. The Origin of Facet Selectivity and Alignment in Anatase TiO₂ Nanoparticles in Electrolyte Solutions: Implications for Oriented Attachment in Metal Oxides. *Nanoscale* **2016**, *8* (47), 19714-19725. DOI: 10.1039/c6nr06953c.
- [27] Zhang, K.; Zhou, W.; Zhang, X.; Qu, Y.; Wang, L.; Hu, W.; Pan, K.; Li, M.; Xie, Y.; Jiang, B.; et al. Large-Scale Synthesis of Stable Mesoporous Black TiO₂ Nanosheets for Efficient Solar-Driven Photocatalytic Hydrogen Evolution via an Earth-Abundant Low-Cost Biotemplate. *RSC Advances* **2016**, *6* (56), 50506-50512. DOI: 10.1039/c6ra06751d.
- [28] Grillo, F.; La Zara, D.; Mulder, P.; Kreutzer, M. T.; Ruud van Ommen, J. Oriented Attachment and Nanorod Formation in Atomic Layer Deposition of TiO₂ on Graphene Nanoplatelets. *J. Phys. Chem. C* **2018**, *122* (34), 19981-19991. DOI: 10.1021/acs.jpcc.8b05572.
- [29] Ling, L.; Bai, Y.; Wang, H.; Ni, Q.; Zhang, J.; Wu, F.; Wu, C. Mesoporous TiO₂ Microparticles Formed By the Oriented Attachment of Nanocrystals: A Super-Durable Anode Material for Sodium-Ion Batteries. *Nano Research* **2018**, *11* (3), 1563-1574. DOI: 10.1007/s12274-017-1772-3.
- [30] Wang, D.; Li, X.; Wang, J.; Yang, J.; Geng, D.; Li, R.; Cai, M.; Sham, T.-K.; Sun, X. Defect-Rich Crystalline SnO₂ Immobilized on Graphene Nanosheets with Enhanced Cycle Performance for Li Ion Batteries. *J. Phys. Chem. C* **2012**, *116* (42), 22149-22156. DOI: 10.1021/jp306041y.
- [31] Chang, C.-H.; Gong, M.; Dey, S.; Liu, F.; Castro, R. H. R. Thermodynamic Stability of SnO₂ Nanoparticles: The Role of Interface Energies and Dopants. *J. Phys. Chem. C* **2015**, *119* (11), 6389-6397. DOI: 10.1021/jp512969k.
- [32] Zhuang, Z.; Xue, X.; Lin, Z. Self-Assembly of SnO₂ Quantum Dots into Hierarchically Ordered Structures Assisted by Oriented Attachment. *Phys. Chem. Chem. Phys.* **2015**, *17* (7), 4845-4848. DOI: 10.1039/c4cp05057f.
- [33] Gehrke, N.; Cölfen, H.; Pinna, N.; Antonietti, M.; Nassif, N. Superstructures of Calcium Carbonate Crystals by Oriented Attachment. *Cryst Growth Des.* **2005**, *5* (4), 1317-1319. DOI: 10.1021/cg050051d.
- [34] Takasaki, M.; Kezuka, Y.; Tajika, M.; Oaki, Y.; Imai, H. Evolution of Calcite Nanocrystals Through Oriented Attachment and Fragmentation: Multistep Pathway Involving Bottom-Up and Break-Down Stages. *ACS Omega* **2017**, *2* (12), 8997-9001. DOI: 10.1021/acsomega.7b01487.
- [35] Zhu, Y.; Zhao, W.; Chen, H.; Shi, J. A Simple One-Pot Self-Assembly Route to Nanoporous and Monodispersed Fe₃O₄ Particles with Oriented Attachment Structure and Magnetic Property. *J. Phys. Chem. C* **2007**, *111* (14), 5281-5285. DOI: 10.1021/jp0676843.
- [36] Chen, J. S.; Zhu, T.; Li, C. M.; Lou, X. W. Building Hematite Nanostructures by Oriented Attachment. *Angew. Chem. Int. Ed.* **2011**, *50* (3), 650-653. DOI: 10.1002/anie.201005365.
- [37] Ma, J.; Chen, K. Silica-Free Hydrothermal Synthesis of ε-Fe₂O₃ Nanoparticles and Their Oriented Attachment to Nanoflakes with Unique Magnetism Evolution. *Ceram. Int.* **2018**, *44* (16), 19338-19344. DOI: 10.1016/j.ceramint.2018.07.162.
- [38] Gildenpfennig, A.; Distaso, M.; Klupp Taylor, R. N.; Peukert, W. Modelling the Two-Dimensional Growth and Oriented Attachment of Goethite Nanorods Synthesized via Oxidation of Aqueous Ferrous Hydroxide Slurries. *Chem. Eng. J.* **2018**, *347*, 798-807. DOI: 10.1016/j.cej.2018.04.150.

- [39] Liu, Y.; Wang, D.; Peng, Q.; Chu, D.; Liu, X.; Li, Y. Directly Assembling Ligand-Free ZnO Nanocrystals into Three-Dimensional Mesoporous Structures by Oriented Attachment. *Inorg. Chem.* **2011**, *50* (12), 5841-5847. DOI: 10.1021/ic2009013.
- [40] Zhang, X. L.; Zhang, J. D.; Phuyal, D.; Du, J.; Tian, L.; Oberg, V. A.; Johansson, M. B.; Cappel, U. B.; Karis, O.; Liu, J. H.; et al. Inorganic CsPbI₃ Perovskite Coating on PbS Quantum Dot for Highly Efficient and Stable Infrared Light Converting Solar Cells. *Adv Energy Mater* **2018**, *8* (6). DOI: ARTN 1702049 10.1002/aenm.201702049.
- [41] Zhang, X.; Shen, Z.; Liu, J.; Kerisit, S. N.; Bowden, M. E.; Sushko, M. L.; De Yoreo, J. J.; Rosso, K. M. Direction-Specific Interaction Forces Underlying Zinc Oxide Crystal Growth by Oriented Attachment. *Nat. Commun.* **2017**, *8* (1), 835. DOI: 10.1038/s41467-017-00844-6.
- [42] Yasui, K.; Kato, K. Oriented Attachment of Cubic or Spherical BaTiO₃ Nanocrystals by Van der Waals Torque. *J. Phys. Chem. C* **2015**, *119* (43), 24597-24605. DOI: 10.1021/acs.jpcc.5b06798.
- [43] Ning, J.; Zhang, D.; Song, H.; Chen, X.; Zhou, J. Branched Carbon-Encapsulated MnS Core/Shell Nanochains Prepared via Oriented Attachment for Lithium-Ion Storage. *J. Mater. Chem. A* **2016**, *4* (31), 12098-12105. DOI: 10.1039/c6ta04441g.
- [44] Yuan, Y.; Wood, S. M.; He, K.; Yao, W.; Tompsett, D.; Lu, J.; Nie, A.; Islam, M. S.; Shahbazian-Yassar, R. Atomistic Insights into the Oriented Attachment of Tunnel-Based Oxide Nanostructures. *ACS Nano* **2016**, *10* (1), 539-548. DOI: 10.1021/acsnano.5b05535.
- [45] Liang, X.; Zhao, Z.; Zhu, M.; Liu, F.; Wang, L.; Yin, H.; Qiu, G.; Cao, F.; Liu, X.; Feng, X. Self-Assembly of Birnessite Nanoflowers by Staged Three-Dimensional Oriented Attachment. *Environ. Sci.: Nano* **2017**, *4* (8), 1656-1669. DOI: 10.1039/c6en00619a.
- [46] Xiao, Y.; Zhao, X.; Jin, Q.; Su, D.; Wang, X.; Wu, S.; Zhou, L.; Fang, S. 3D Hierarchical Porous Cobalt Monoxide Nanoplates With a Book-Like Structure Derived from Co(CO)_{0.5}(OH)·0.11H₂O: Two-Steps Oriented Attachment and High-Performance Asymmetric Supercapacitors. *Mater. Res. Express* **2017**, *4* (10). DOI: 10.1088/2053-1591/aa9210.
- [47] Zhou, J.; Zhu, M.; Meng, R.; Qin, H.; Peng, X. Ideal CdSe/CdS Core/Shell Nanocrystals Enabled by Entropic Ligands and Their Core Size-, Shell Thickness-, and Ligand-Dependent Photoluminescence Properties. *J. Am. Chem. Soc.* **2017**, *139* (46), 16556-16567. DOI: 10.1021/jacs.7b07434.
- [48] Zhu, C.; Liang, S.; Song, E.; Zhou, Y.; Wang, W.; Shan, F.; Shi, Y.; Hao, C.; Yin, K.; Zhang, T.; et al. In-Situ Liquid Cell Transmission Electron Microscopy Investigation on Oriented Attachment of Gold Nanoparticles. *Nat. Commun.* **2018**, *9* (1), 421. DOI: 10.1038/s41467-018-02925-6.
- [49] Templeman, T.; Sengupta, S.; Maman, N.; Bar-Or, E.; Shandalov, M.; Ezersky, V.; Yahel, E.; Sarusi, G.; Visoly-Fisher, I.; Golan, Y. Oriented Attachment: A Path to Columnar Morphology in Chemical Bath Deposited PbSe Thin Films. *Cryst. Growth Des.* **2018**, *18* (2), 1227-1235. DOI: 10.1021/acs.cgd.7b01771.
- [50] Cho, K. S.; Talapin, D. V.; Gaschler, W.; Murray, C. B. Designing PbSe Nanowires and Nanorings Through Oriented Attachment of Nanoparticles. *J. Am. Chem. Soc.* **2005**, *127* (19), 7140-7147. DOI: 10.1021/ja050107s.
- [51] Koh, W. K.; Bartnik, A. C.; Wise, F. W.; Murray, C. B. Synthesis of Monodisperse PbSe Nanorods: A Case for Oriented Attachment. *J. Am. Chem. Soc.* **2010**, *132* (11), 3909-3913. DOI: 10.1021/ja9105682.
- [52] Schliehe, C.; Juarez, B. H.; Pelletier, M.; Jander, S.; Greshnykh, D.; Nagel, M.; Meyer, A.; Foerster, S.; Kornowski, A.; Klinke, C.; et al. Ultrathin PbS Sheets by Two-Dimensional Oriented Attachment. *Science* **2010**, *329* (5991), 550-553. DOI: 10.1126/science.1188035.
- [53] Nakagawa, Y.; Kageyama, H.; Oaki, Y.; Imai, H. Formation of Monocrystalline 1D and 2D Architectures via Epitaxial Attachment: Bottom-Up Routes Through Surfactant-Mediated Arrays of Oriented Nanocrystals. *Langmuir* **2015**, *31* (22), 6197-6201. DOI: 10.1021/acs.langmuir.5b00502.
- [54] Yu, J. H.; Joo, J.; Park, H. M.; Baik, S. I.; Kim, Y. W.; Kim, S. C.; Hyeon, T. Synthesis of Quantum-Sized Cubic ZnS Nanorods By the Oriented Attachment Mechanism. *J. Am. Chem. Soc.* **2005**, *127* (15), 5662-5670. DOI: 10.1021/ja044593f.
- [55] Pradhan, N.; Xu, H.; Peng, X. Colloidal CdSe Quantum Wires by Oriented Attachment. *Nano Lett.* **2006**, *6* (4), 720-724. DOI: 10.1021/nl052497m.
- [56] Halder, A.; Ravishankar, N. Ultrafine Single-Crystalline Gold Nanowire Arrays by Oriented Attachment. *Adv. Mater.* **2007**, *19* (14), 1854-1858. DOI: 10.1002/adma.200602325.

CHAPTER 4

From PbSe Nanocrystals to Honeycomb Superlattices

Semiconductor superstructures made from assembled and epitaxially connected colloidal nanocrystals (NCs) hold promise for crystalline solids with atomic and nanoscale periodicity, whereby the band structure can be tuned by the geometry. The formation of especially the honeycomb superstructure on a liquid substrate is far from understood and suffers from weak replicability. Here, we introduce 1,4-butanediol as an unreactive substrate component, which is mixed with reactive ethylene glycol to tune for optimal reactivity. It shows us that the honeycomb superlattice has a NC precursor state before oriented attachment occurs, in the form of a self-assembled hexagonal bilayer. We propose that the difference between the formation of the square or honeycomb superstructure occurs during the self-assembly phase. To form a honeycomb superstructure, it is crucial to stabilize the hexagonal bilayer in the presence of solvent-mediated repulsion. In contrast, a square superstructure benefits from the contraction of a hexagonal monolayer due to the absence of a solvent. A second experiment shows the very last stage of the process, where the increasing alignment of NCs is quantified using selected-area electron diffraction (SAED). The combination of transmission electron microscopy (TEM), SAED, and tomography used in these experiments shows that the (100)/(100) facet-to-facet attraction is the main driving force for NC alignment and attachment. These findings are validated by coarse-grained molecular dynamic simulations, where we show that an optimal NC repulsion is crucial to create the honeycomb superstructure.

Based on:

Maaïke M. van der Sluijs, Dinja Sanders, Kevin J. Jansen, Giuseppe Soligno, Daniel Vanmaekelbergh and Joep L. Peters, *Journal of Physical Chemistry C* 2022, 126 (2), 986-996.

4.1 Introduction

For the fabrication of inorganic crystals that feature atomic and nanoscale periodicity, top-down lithographic approaches have been used.¹ However, due to high costs and wavelength limitations, this method reaches its limits at a period of roughly 20 nm.² A cheaper method, while achieving even smaller features (down to 6.5 nm), would be the well-controlled oriented attachment of monodisperse nanocrystals.³ In the classical crystal growth model, monomers are attached one-by-one to the growing crystal. By utilizing differences in chemical composition and reactivity of facets, it is often possible to manipulate the direction of this growth. In oriented attachment, this principle of distinctive facet reactivity also holds but now for the facet-specific attachment of nanocrystals to form a periodic solid. Such superstructures have been obtained with a variety of nanocrystals and under different conditions. Advanced structures and control of the process have only been obtained in apolar solvents by attachment via stoichiometric facets.⁴⁻⁸

Lead chalcogenide nanocrystals (NCs) covered by deprotonated fatty acids lead this research field.^{3,5,6} These NCs have six chemically identical stoichiometric {100} crystal facets and eight nonstoichiometric {111} facets. It has been shown that the {100} facets can epitaxially attach to a (100) facet of a neighboring NC, if ligands are removed. Attachment does not happen for the inactive {111} facets, where ligands are bound much stronger and therefore not easily removed.⁹ The epitaxial connection ensures strong electronic coupling between NCs,^{10,11} and may even result in a specific electronic band structure depending on the geometry of the superstructure.⁹⁻¹¹ Of special interest is the two-dimensional (2D) silicene-type honeycomb superstructure, which could combine typical semiconductor properties, with Dirac cones in the valence and conduction band.^{10,11} Unfortunately, a full understanding and control of the honeycomb superstructure formation from PbSe NCs has not yet been achieved. A growing number of studies demonstrate the importance of the NC organization preceding oriented attachment.¹²⁻¹⁵ A study by Geuchies et al. (using grazing incidence small- and wide-angle X-ray scattering, GISAXS/GIWAXS) showed that a hexagonal assembly of PbSe NCs contracted in-plane and transformed gradually to a square assembly, prior to NC attachment with (100)/(100) interactions as the driving force.¹⁶ This structural contraction from the hexagonal NC assembly to a square assembly is necessary to reach the correct bonding geometry and to bring the opposing (100)/(100) facets close enough. This transition is presumably due to the soft character of the ligand shell and the removal of residual solvent.¹⁷⁻²⁰ After that, the ligands strip from the surface, NCs align, and stoichiometric {100} facets become free, which makes a reduction of the surface energy possible by an epitaxial connection (attachment) between opposing {100} facets.²¹⁻²³ To form structures with other nanogeometries, i.e., honeycomb structures, the continued presence of the residual solvent in the ligand shell or additional unbound ligands was found to be essential.^{23,27,28}

In this work, we use transmission electron microscopy (TEM), selected-area electron diffraction (SAED) and molecular dynamic simulations to study the honeycomb superstructure formation by casting a PbSe NC dispersion on ethylene glycol and controlling solvent evaporation. Samples, taken during the process, were immediately placed under vacuum to preserve the sampled superstructure, enabling an *ex situ*, real-time study of self-assembly and attachment. The first experiment utilizes 1,4-butanediol, mixed in varying ratios with the ethylene glycol liquid substrate, to slow down the ligand stripping and therefore the attachment of NCs. It provides a powerful method to balance and study the attraction between the {100} facets. NCs

which are too reactive attach quickly and form uncontrolled structures. In contrast, without ligand stripping, NCs do not align and stay in the precursor state of hexagonal mono- or bilayers. The second experiment studies the last stage; NCs are then organized in a hexagonal bilayer and are initially only slightly oriented with a preferred orientation of the $\langle 111 \rangle$ axis upwards. Over time, NC-NC alignment becomes more and more pronounced, until attachment occurs. To complement the experiments, we use coarse-grained molecular dynamic simulations. With these modelling results, we substantiate the hypothesis that solvent inclusion in the NC ligand shell allows the formation of the hexagonal bilayer precursor phase and provides the stability and NC density necessary to form honeycomb superstructures. Without these space-filling molecules, the NC precursor phase is not stable enough, resulting in disordered or square structures.

4.2 Results

4.2.1 In situ sampling of nanocrystal structures, avoiding perturbative drying effects

The typical synthesis for two-dimensional PbSe honeycomb superstructures is as follows: a PbSe quantum dot dispersion is dropcasted on an ethylene glycol (EG) liquid substrate, after which the toluene solvent evaporates under atmospheric nitrogen pressure,³ or under nearly solvent-saturated conditions.²⁴ After toluene evaporation, NCs were shown to float on top of the EG.²⁵ The EG plays a crucial role in the experiment, as it gradually removes ligands from the NC surface and makes $\{100\}$ NC facets available for attachment.^{3,6,26} The mechanism behind oleate removal by EG is not yet fully understood; however, in literature, two mechanisms have been suggested. When oleate ligands are considered to be X-type,²⁷⁻²⁹ a proton transfer could induce displacement and exchange of the oleate ligand.³⁰ Previously, short-chain alcohols were suggested to enable this proton transfer to ligands.²⁸ More recent work has shown that amines injected in the EG liquid can induce epitaxial fusion in assembled PbSe NCs.^{22,31} The amines (or other L-type ligands) induce ligand displacement as a metal carboxylate complex (Z-type displacement of lead oleate) from the NC surface, allowing attachment between bare $\{100\}$ facets.³² Although these publications have given tentative hints at a mechanism for ligand removal during superstructure formation, a complete understanding has not yet been achieved (**supporting information S4.2**).³⁸ As soon as enough ligands have been stripped or exchanged, the facets become reactive and attachment can occur. Often, this results in a superstructure which is a mixture of different geometries instead of an ordered superstructure. We hypothesized that slowing the removal of ligands with an effectively less reactive liquid substrate would give us a method to improve control over the superstructure formation, even when using highly reactive NCs with a low ligand density. We narrowed the search by concentrating on a compound with similar properties as EG; it should be a liquid with two hydroxide groups to keep it barely mixable with apolar NCs solvents.

In **Figure 4.1**, TEM images show the results of casting the dispersion on 100% 1,4-butanediol (BD), which has two hydroxide groups and the proper melting point. As can be observed in the upper left of **Figure 4.1a** and the upper left of **Figure 4.1b**, monolayers are (pseudo-) hexagonally ordered, and NCs show no attachment, indicating that $\{100\}$ facets have a significantly lower reactivity. We concluded that BD is not able to remove ligands from PbSe NCs on similar time scales as EG, making it a good candidate to vary the liquid substrate reactivity. Nevertheless, as shown in **Figure S4.1**, at higher temperatures, BD can induce removal of sufficient ligands to induce attachment.

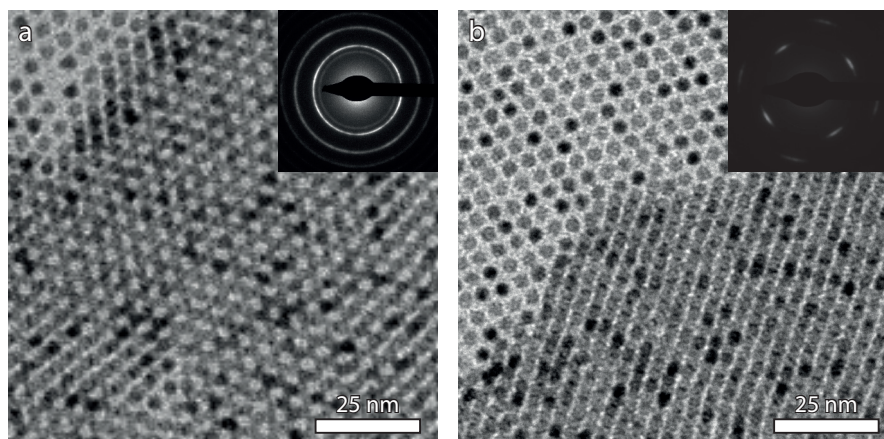


Figure 4.1 Two examples of self-assembled mono- and bilayer PbSe NCs formed over a 15 h experiment on 100% BD, in which we waited (a) 5 seconds and (b) 10 minutes between sampling and applying vacuum to “freeze” the sample. The small amount of toluene remaining on the sample does not result in strong turbulence during evaporation. However, when waiting before vacuum application, the organization of NCs changed from a hexagonal mono- or bilayer with random orientation (a) to a denser quasi-hexagonal mono- or bilayer with a preferred orientation of NCs with a (100) facet upwards (b).

It is important to note distinct differences in the double layers of these samples. In **Figure 4.1a**, the hexagonal bilayer is preserved with random orientation of NCs, as seen in the SAED inset, which shows full diffraction rings. The double layer in **Figure 4.1b** shows a structural change with a preferred orientation of NCs. This difference is attributed to the TEM sample treatment immediately after sampling of the superstructure. Prompt placement of the TEM sample under vacuum, in the small antechamber of the glovebox, “freezes” the structure and retains randomly rotated NCs (**Figure 4.1a**). Thus, the NC system that is absorbed at the interface or NCs which are present in a thin layer of toluene can be collected and preserved. Waiting too long before applying the vacuum allows evaporation of the residual solvent present in the ligand shell. Then, the NC shape becomes a more prominent factor, which induces structural changes in the superstructure and the preferred orientation of NCs. In three-dimensional structures (3D), a similar effect is observed in several NC systems, where it is described as the Bain deformation.^{20,33-41} In all experiments presented below, the TEM samples were placed under vacuum immediately after sampling, “freezing” the superstructures as they have formed on the liquid substrate. The next step is to synthesize PbSe superstructures on the mixtures of BD and EG, to tune the superstructure attachment.

4.2.2 Tuning the NC reactivity, utilizing the liquid substrate

The conditions for these experiments are similar to previously described; slow solvent evaporation occurs under a nearly saturated toluene gas phase above the glycol/NC dispersion system (**Figure S4.5**).²⁴ For this experiment, we used 7 nm PbSe NCs with a relatively low ligand density of 2.2 oleate/nm², as determined by FTIR and NMR (**supporting information S4.3**). In **Figure 4.2**, we increased the ratio of BD to EG going from a 0:1 (a) to a 3.33:1 ratio (f).

Without the addition of BD, attachment of NCs is observed, resulting in disordered nonperiodic structures (Figure 4.2a). With an increasing ratio of BD:EG, the degree of nanoscale periodicity increases, forming larger periodic superstructures with a honeycomb geometry (Figure 4.2b–d). The optimal liquid substrate mixture has a BD:EG ratio of 1:1.17, yielding long-range honeycomb superstructures with areas up to $10\ \mu\text{m}^2$ (Figure 4.2d). This long-range order is also illustrated by Fourier transforms (Figure S4.6). At the same time, the SAED image inset shows six sharp peaks on the 220 ring, indicative of NCs oriented with their $\langle 111 \rangle$ axis perpendicular to the substrate and no rotational freedom within the plane. With this orientation, three of the $\{100\}$ facets face the $\{100\}$ facets of neighboring NCs, forming a honeycomb structure.⁶ A further increase of the BD:EG ratio results in unattached NCs ordered in mixed phases of hexagonal mono- and bilayers (Figure 4.2e and 2f). It is important to note that while these hexagonal bilayers look exactly like attached honeycomb superstructures in TEM images (see supporting information S4.4, Figure S4.7 for a detailed comparison), the SAED image inset still shows rings, i.e., random orientation, confirming that NCs are not attached.

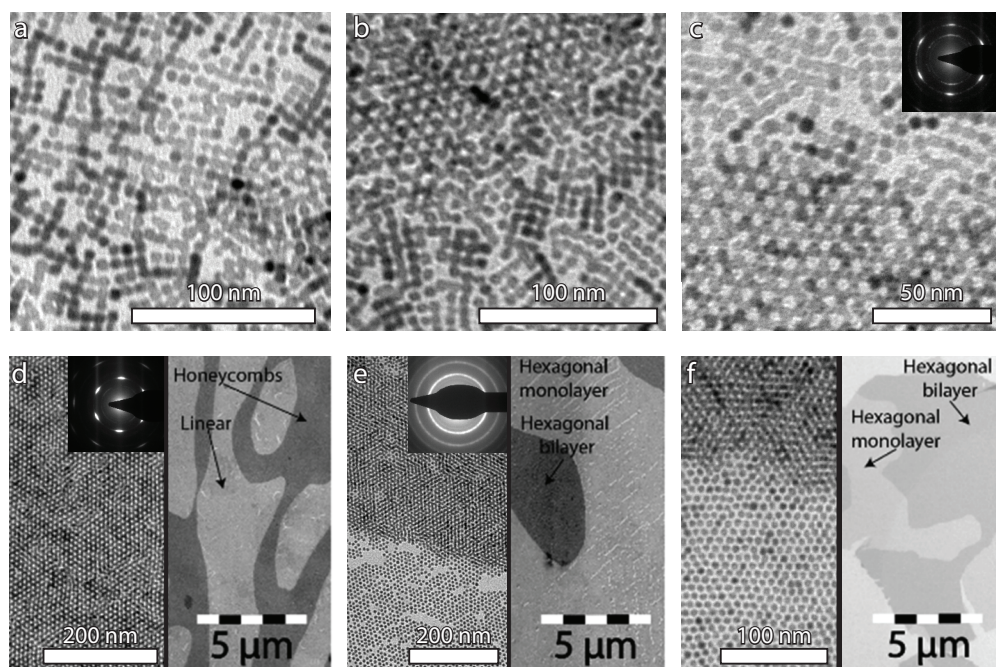


Figure 4.2 Honeycomb formation with an increasing concentration of 1,4-butanediol. The amount of 1,4-butanediol to ethylene glycol is, respectively, in (a) 0:6.5, (b) 1:5.5, (c) 2:4.5, (d) 3:3.5, (e) 4:2.5, and (f) 5:1.5 mL. The quantity and quality of the honeycomb structure improve with an increasing amount of BD, until no attachment is observed in (e) and (f). The insets in (d) and (e) are the SAED patterns of the bilayer area, showing strongly aligned and attached NCs in (d) and NCs with random orientations in (e). The right part of (d–f) shows a lower magnification TEM image, where the large domains of a linearly attached (see Figure S4.10a), honeycomb and self-assembled structures are visible.

These results demonstrate the tremendous improvement in quantity and quality of the honeycomb structure with an increase in the relative amount of BD in the liquid substrate. The addition of the less reactive BD to EG provides a direct method to tune the formation of superstructures for NCs with different ligand densities. The results presented in **Figure 4.2** confirm that ligand removal from the NC surface by EG is crucial to induce attachment of {100} facets, which is driven by surface energy reduction. They also suggest that the hexagonal bilayer is a precursor phase to the honeycomb superstructure, something additionally inferred from the similarities of the nanoscale and microscale organization of NCs between **Figure 4.2d**, **2e** and **2f**.

4.2.1 Final stage of alignment and attachment, facet-to-facet interactions

Below, we show a second experiment that monitors the formation of PbSe NC honeycomb superlattices in real time, confirming the key role of (100)/(100) facet-to-facet interactions in aligning NCs. Ideally, this study involves GISAXS/GIWAXS, as utilized in previous studies.^{16,31,35,42} However, the formation of honeycomb structures requires ultraslow evaporation of the toluene solvent over 15 hours (h) in a nearly closed system under an inert atmosphere. In principle, in situ X-ray measurements over such a long period are possible. Nevertheless, they demand long occupation of the synchrotron measurement station, while self-assembling structures might be prone to beam damage and residual oxidation, making in situ GISAXS/GIWAXS very demanding. We have chosen for an ex situ, real-time study of superlattice formation by monitoring the sample at gradually longer times of toluene evaporation using TEM, tomography, and SAED. To avoid ex situ drying effects and preserve the in situ state of the structure (see above), the samples were immediately placed under vacuum. **Figure 4.3** shows the representative TEM images of samples obtained after 3, 9, and 15 h of slow toluene evaporation at 20 °C for 6.1 nm PbSe NCs with a medium ligand density of 3.7 oleate/nm², as determined by FTIR and NMR (**supporting information S4.3**, additional results are presented in **Figure S4.8** and **S4.9**). We dropcasted the equivalent of approximately 1.5 monolayers of PbSe NCs on the liquid substrate surface. After 1–3 h (**Figure 4.3a** left, **S4.8**), only some of the NCs are present at the interface, while the rest is still suspended. The SAED diffractogram inset shows two rings corresponding to 200 and 220 diffraction rings with uniform intensity, an indication that NCs near an interface still have a random orientation.

The samples acquired at 6–12 h (**Figure 4.3a** middle and **S4.8**) show an increased density of NCs resulting in mono- and bilayers with a hexagonal geometry. The number of NCs on the TEM grid suggests that all NCs originally present in the dispersion are now at, or close to the interface. The SAED diffractogram inset top right shows that NCs in the monolayer are not aligned and thus still have random orientations. This is in line with GISAXS/GIWAXS patterns obtained previously for experiments with more rapid toluene evaporation.¹⁶ However, bilayers show SAED patterns (top left), with a lower intensity on the 200 ring, a relatively strong intensity on the 220 ring, and the occurrence of six broad spots. These spots originate from an interference pattern of diffraction on the three sets of {110} crystal planes, showing that the <111> axis of NCs is oriented vertically to the interface, while NCs have limited rotational freedom. Thus, these bilayers should not be considered as consisting of “hard” spheres with a random orientation; the gradual alignment is due to NC rotations that try to maximize the attractions between the {100} facets of NC neighbors in the hexagonal bilayer.

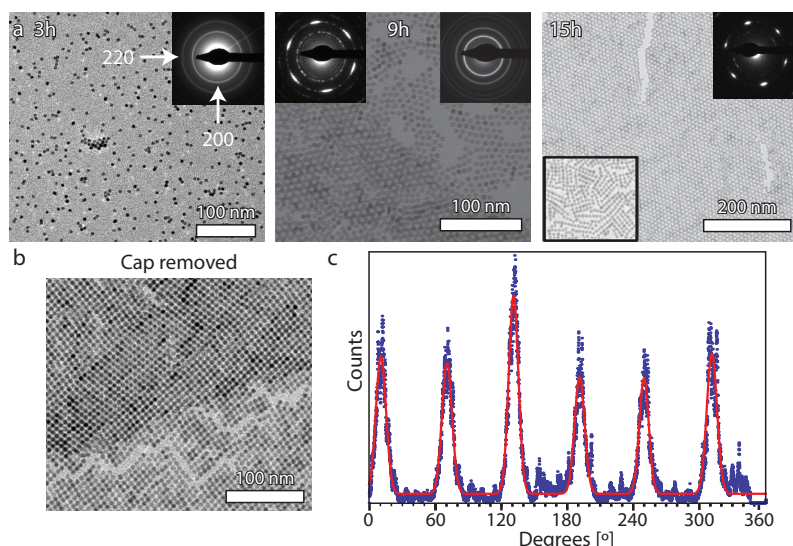


Figure 4.3 Real-time, ex situ study of the formation of a honeycomb superlattice. (a) TEM images of samples obtained by horizontal contact of TEM grids with the toluene–air interface, after 3, 9, and 15 h of experiment time. The sample at 9 h shows PbSe NC hexagonal mono- and bilayers. The upper-left inset shows the SAED of a bilayer: the spots indicate limited random orientation. The upper-right inset is a diffractogram of the hexagonal monolayer, indicating random NC orientations. After 15 h, all NCs in the bilayer are oriented with the $\langle 111 \rangle$ axis perpendicular to the plane of the superlattice. The lower-left TEM inset of the hexagonal monolayer at 15 h shows that linear structures have been formed as well. (b) TEM image of the superstructure formed after 3 h of experiment time and an additional 1 h after the removal of the cap (resulting in a low solvent vapor pressure). (c) Width of the six spots on the 220 ring after 9 h and the background scattering intensity on the azimuthal trace are analyzed using Gaussian fits (red). The values are presented in Table 4.1 and discussed in the text.

The samples acquired after 15, and even 24 h (Figure 4.3a right, S4.8, and S4.9), show large bilayer domains. The SAED inset now shows almost no intensity on the 200 ring, while the 220 ring has six intense and small-angled spots, indicative of improved $\langle 111 \rangle$ orientation and alignment in the bilayer superstructure. This means that $\{100\}$ facets must have a 45° orientation with respect to the plane, and it is very hard to discern from these TEM pictures whether attachment has already taken place (see below).

Besides large bilayer domains, monolayer domains are observed as well. In the monolayer (Figure 4.3a right, left corner inset), NCs are clearly attached in a linear geometry and oriented with $\{100\}$ facets upwards (Figure S4.10a). These linear structures imply a symmetry breaking, as bonding sites are available in two orthogonal directions; the origin of this symmetry breaking is not well understood. The SAED and a Fourier transform of linear structures in Figure S4.10 show that although NCs are linearly attached, they are still organized in a disordered hexagonal symmetry. This indicates that unattached NCs in the hexagonal monolayer attach via opposing (100) facets that are vertically oriented in these linear structures while retaining some of their original position. Attachment of NCs in this area is an indication that NCs in the bilayer are attached as well.

4.3.4 Formation of square versus honeycomb superstructures

As was previously shown in **Figure 4.1**, the presence of residual solvent in the ligand corona already plays a huge role in the geometry observed in the sample. A similar phenomenon was observed during the formation of the superstructures in **Figure 4.3**. When the cap of the setup is removed at different times during the experiment, the solvent vapor pressure drops and if superstructure formation is allowed to continue for another hour, different structures than those under near solvent saturation are formed. If the cap is removed during the first 3 h, only some of the NCs are present at the interface while the rest is still suspended (**Figure 4.3a** left). As shown in **Figure 4.3b**, an experiment continued at low solvent pressure for 1 h forms a superstructure with a square geometry, for which the detailed formation mechanism has been described before.¹⁶ However, if the cap was removed in a much later stage of the process, after 6–12 h, the self-assembled hexagonal double layer evolved into an attached honeycomb structure. *It suggests that the difference in the formation of square or honeycomb structures occurs during self-assembly, prior to NC alignment and attachment.* The solvent makes up approximately 40% of the space in a self-assembled hexagonal layer, compared to ~20 and ~40% for the NC core and ligands, respectively, as shown by a simple calculation in **supporting information S4.5**. It is therefore no surprise that the NC organization in a self-assembled superlattice can change by solvent removal. This effect was previously described in literature for several NC systems.^{19,33,35,43–45}

For the honeycomb formation, it is beneficial to have an ordered, unattached, “hard” sphere like hexagonal bilayer as a precursor phase, before (100)/(100) interactions between NCs pull them together. Losing solvent molecules from the ligand shell before this precursor phase causes too much contraction, resulting in square-like superstructures.^{19,33,35,43–45} We therefore hypothesize that the removal of the solvent early in the hexagonal (bi)layer precursor phase, changes the NC self-assembly from barely interactive NCs at long NC–NC distances to an assembly with attractive interactions resulting in a denser structure with shorter NC–NC distances. This indicates that the number of solvent molecules incorporated in the structure is critical for the stage at which (100)/(100) interactions come into play; if this occurs in an early stage, square-type monolayers are favored, while assembly under a nearly solvent-saturated atmosphere favors large bilayer domains that eventually evolve in buckled honeycomb structures.

4.3.5 SAED analysis of NC alignment during honeycomb formation

A way to study the NC alignment in this experiment is to analyze the 200 and 220 diffraction rings in SAED patterns. The total intensity of the rings, as compared to a powder diffraction pattern of bulk PbSe gives information on the percentage of NCs with a random orientation that are still present in the selected area. **Table 4.1** lists the percentage of NCs in a random orientation observed in the experiments of **Figure 4.3**, which gradually decreases from 32 to 3% (**supporting information S4.6**). At the same time, an interference pattern of six peaks begins to emerge on the 220 ring. In **Figure 4.3c**, this 220 ring is represented as an azimuthal trace (blue), and the six peaks are fitted with Gaussians (red). This provides quantitative values for the FWHM of the peaks during the entire 24 h after the dispersion was dropcasted on the liquid substrate. Additionally, the decreasing background intensity of the ring shows the increasing percentage of NCs aligned to neighboring NCs. To validate this analysis, the measured superlattice values are compared to the instrumental broadening and background values, measured with a molybdenum single crystal.

Time [h]	NCs with random orientation [%]	NCs aligned to neighboring NCs [%]	Average 220 peak width [°]
6	32	64	6.1
9	13	86	5.0
12	12	86	4.5
15	4	96	2.7
24	3	92	2.7

Table 4.1 Overview of the average peak width and the percentage of background scattering. The data is extracted from SAED patterns at different stages after NC deposition, for further discussion see supporting information S4.6.

Over the 6–15 h period, the 220 peak widths gradually decrease from 6.1 to 2.7°, while the overall percentage of oriented and aligned NCs increases from 64 to 96%, due to the increasing order in bilayers, i.e., a smaller and smaller number of PbSe NCs have a random rotation. However, for all of the SAED values, after 15 h, no further improvement of the alignment is observed, suggesting that irreversible necking between the (100)/(100) facets has occurred. The decreasing trend of randomly oriented NCs (Table 4.1, column 2) corresponds to the increasing percentage of NCs aligned to neighboring NCs (Table 4.1, column 3) and the decrease in average peak width (Table 4.1, column 4). This suggests that the alignment in the last stages of the process is caused by NC reorientations, which maximize the (100)/(100) attractions between NC neighbors. Other sources of NC alignment, for example, caused by NC–interface interactions are therefore less likely.

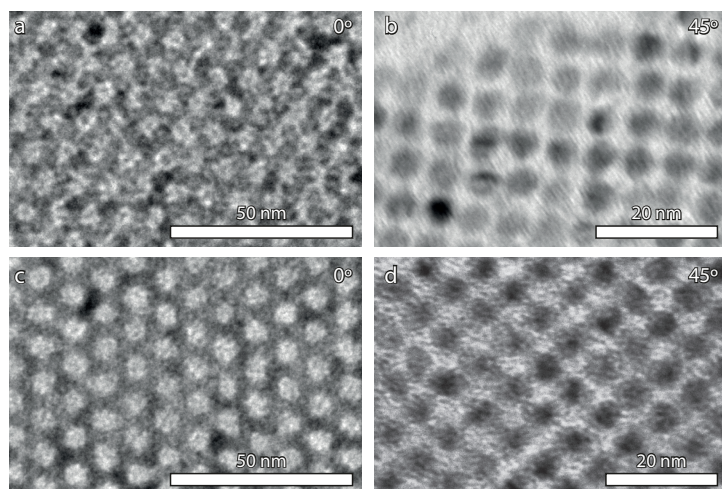


Figure 4.4 Electron tomography of a PbSe NC bilayer (a, b) and honeycomb superstructure (c, d) obtained after 9 and 15 h, respectively. (a) TEM image after 9 h viewed in the $\langle 111 \rangle$ direction, while panel (b) shows a TEM image of the same sample with a 45° tilted TEM grid. Similar for (c, d), except that the sample is taken after 15 h. Note that the top view of the nontilted samples (a, c) looks similar. When tilted, the images show the simple cubic structure in which NCs are not attached in (b), while crystalline necks have formed in (d).

After 15 h, linear attachment observed in the hexagonal monolayer region suggests that NCs in the bilayer are also attached, but the conclusive proof is still missing. This is complicated by the fact that attachment occurs in $\langle 100 \rangle$ directions,⁶ which have a 45° angle compared to the substrate plane. Therefore, shading from PbSe NCs prevents direct observation of bonds in this structure. By rotating the TEM samples over a 45° angle, the connections become visible and NC attachment can be confirmed. In **Figure 4.4**, the TEM samples taken at 9 and 15 h are shown at a 0° and 45° tilt. At a 45° rotation, the simple cubic bonding pattern,^{24,46} of the silicene-type honeycomb structure becomes clearly visible.

The sample taken at 9 h shows that all of the PbSe NCs are aligned and face each other via $\{100\}$ facets, but except for a few positions, crystalline necks between nanocrystals are not present. This suggests that the NC alignment is driven by attractive interactions between these facets, resulting in an average peak width of 5.0° at the 220 ring. In contrast, the sample acquired after 15 h shows that nearly each NC in the structure has necks to its nearest neighbors (with a maximum of three in a silicene-type honeycomb structure). Therefore, this sample represents an attached honeycomb superlattice, with the smallest peak width of 2.7° .

The combination of all experiments shown above points to three distinct steps in the formation of honeycomb superlattices: (1) the formation of a well-ordered hexagonal bilayer, from unconnected “hard sphere like” NCs with the solvent incorporated in the ligand shell, as a “precursor” phase, (2) increasing alignment of NCs driven by $(100)/(100)$ interactions, and (3) NC attachment by the formation of necks between nanocrystals, resulting in the final superstructure. To achieve long-range order, separation of these steps is crucial; this means that the precursor phase should result in large well-ordered domains, which should be retained until NC alignment due to $(100)/(100)$ attraction occurs.

4.3.6 Modelling superstructure formation for NCs with different repulsion potentials

As indicated by earlier theoretical predictions,⁴⁷ NCs fully covered by ligands are thought to have rotational freedom at the solvent–air interface, while NCs having ligands chemisorbed only on their $\{110\}$ and $\{111\}$ facets, but not on their $\{100\}$ facets, are expected to have a preferred orientation (with a (111) facet up) at the solvent–air interface. Therefore, it was previously thought that the interface-induced orientation of NCs could play a role in the formation of the buckled honeycomb structure.^{47–49} In previous models, the self-assembly pathway was based on an early NC orientation at the solvent–air interface to move to the correct position to form square or honeycomb superlattices. However, the *ex situ*, real-time study of superlattice formation presented above shows the importance of a well-ordered hexagonal bilayer before the introduction of the $(100)/(100)$ interaction for the alignment of NCs (**Figure 4.2e**, **4.2f**, and **4.3a**).

To further investigate the self-assembly pathway, we present results from coarse-grained molecular dynamics simulations of up to 10^4 NCs. In these simulations, each NC is modelled as a polybead structure with a rhombicuboctahedron shape of roughly 6 nm (**supporting information S4.7**, **Figure S4.11**), where each bead in the structure represents a few atoms. Such a simplified coarse-grained model requires a lower computational cost for the simulations than a fully atomistic model, allowing the study of larger-scale systems. The dynamics of NCs are simulated using the position-Verlet algorithm,⁵⁰ while the distance between beads belonging to the same NC is kept fixed by constrained forces.⁵¹ Bead–bead pair potentials are used to reproduce

the NC-NC short-range facet-specific interactions, while the solvent is treated implicitly by modelling the NC Brownian motion. Further details on this model are reported in [supporting information S4.7](#) and a recent publication.⁴⁸ In the simulations presented here, up to 10^4 NCs are initially randomly dispersed in a cubic box of side L aligned with a Cartesian coordinate system x, y, z and with periodic boundary conditions. The external force $-dU_{2D}(z_c)/(dz_c)$ is applied to each NC center of mass, with z_c the z coordinate of the NC center of mass, to model the effect of the evaporating solvent, which compresses the NCs in a 2D plane. The external potential U_{2D} is defined

$$U_{2D}(z_c) = \begin{cases} u_z(z_c)^2, & \text{if } z_c < 0 \\ u_z(z_c - 4)^2, & \text{if } z_c > 4 \text{ nm} \end{cases} \quad (4.1)$$

Basically, NCs only feel an external force if their center of mass is not within a planar film of 4 nm thickness, then their center of mass is pushed toward this film forcing NCs to form a self-assembled mono- or bilayer. The parameter u_z is 10^{-19} J, in line with predicted solvent-air adsorption potentials of NCs.⁴⁸ During the first 0.1 μs of simulation, the beads of different NCs interact with each other only by a soft repulsive pair potential, mimicking the effect of ligand molecules chemisorbed on the NC surface

$$U_R(r) = \begin{cases} \epsilon_R[(\sigma_R/r)^6] - 1, & \text{if } r \leq \sigma_r \\ 0, & \text{otherwise} \end{cases} \quad (4.2)$$

where r is the bead-bead center-of-mass distance, ϵ_R is the magnitude of the repulsive potential, and σ_r is the ligand length. After 0.1 μs , the attractive pair potentials between beads belonging to NCs' $\{100\}$ facets are (gradually) turned on, mimicking ligands detaching from $\{100\}$ facets (thus allowing the facet-facet interaction). This second simulation phase, in which NCs attract each other by $\{100\}$ facets, is continued for at least 0.05 μs . A complete overview of the parameters used in the simulations is reported in [supporting information S4.7](#).

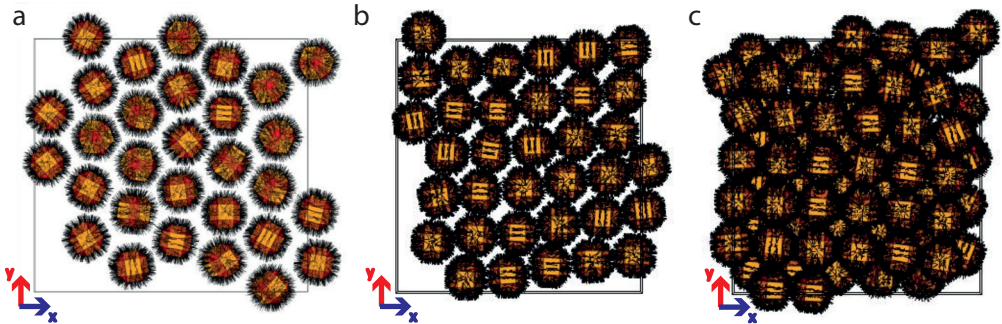


Figure 4.5 Top view of the quasi-2D structure formed in a molecular dynamics simulation with different parameters. In panels (a–c), NCs are randomly dispersed in a 3D box with dimensions $L = 70$ nm at the beginning and $L = 32$ nm at the end of the simulation, but before $\{100\}$ facet attraction is turned on. In panel (a) with a $\epsilon_R = 8 \times 10^{-21}$ J repulsion, a free rotational hexagonal structure is formed. In panels (b, c) with a $\epsilon_R = 0.2 \times 10^{-21}$ J repulsion, a square structure with predominantly $\{100\}$ facets up is formed both in the monolayer (with 35 NCs) and double layer (with 70 NCs) simulation.

Initially we performed small scale simulations, with 35 and 70 NCs, for only the first phase – i.e. before turning on the attractions between the $\{100\}$ facets. The NCs are placed in a box shrinking linearly from $L = 70$ nm (at the beginning) to $L = 32$ nm (at the end of the simulation), to simulate the evaporating solvent. This reduction is slow enough to allow equilibration of the NCs. The resulting top view (the z direction is orthogonal to the paper plane) of these simulations is shown in **Figure 4.5**.

When the NCs are allowed to self-assemble with a strong repulsive potential (of $\epsilon_r = 8 \times 10^{-21}$ J, **Figure 4.5a**), emulating NCs with a full ligand shell and solvent inclusion, a hexagonal monolayer is formed by randomly oriented NCs. However, in simulations with a lower repulsive potential (of $\epsilon_r = 0.2 \times 10^{-21}$ J, the particle shape becomes more dominant during the self-assembly. Then, square geometries are formed with the particles predominantly oriented with their $\{100\}$ facets up, both in the monolayer and the bilayer (**Figure 4.5b** and **Figure 4.5c**). It is an indication that with high repulsive potential, both in simulation and under experimental conditions with high solvent vapor pressure (**Figure 4.1a**, **Figure 4.2e** and **2f**), the particles can self-assemble like barely interactive (hard) spheres and form hexagonal geometries with free orientation.

In larger simulations with 280 NCs, the entire attachment process was studied in two phases. During the first simulation phase (**Figure 4.6a**), the soft repulsive pair potential again emulates a full ligand corona with solvent inclusion, allowing NCs to self-assemble as barely interacting spheres. Then, during the second phase, the facet–facet interaction is gradually turned on (**Figure 4.6b**). Both the top view and side view are displayed at the end of each simulation phase. As NCs only interact via a soft repulsive pair potential during the first phase, they self-assemble into a hexagonal double layer, with some particle orientation of (100) and (111) facet up.

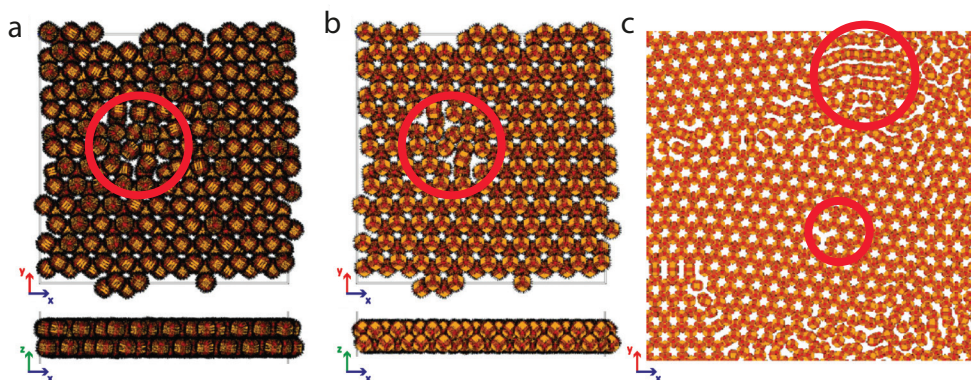


Figure 4.6 Top view of the quasi-2D structure formed in large-scale molecular dynamic simulations. In panels (a, b), the top and side views of a simulation with 280 NCs are shown with only repulsive potential (a) and with $\{100\}$ facet–facet attraction turned on (b). In panel (a), a hexagonal double layer is formed with areas of (100) facet up (yellow facet) and (111) facet up (red). This hexagonal double layer then evolves to a silicene-type honeycomb superstructure (b). In panel (c), a zoomed-in portion of Figure S4.12 is shown, a simulation with 10^4 randomly dispersed NCs in a 3D box of sides $L = 620$ nm compressed in a thin planar film. NC–NC attraction by $\{100\}$ facets (yellow) is switched on after $0.1 \mu\text{s}$ forming domains of silicene-type honeycomb superstructures. The red circles indicate defect areas in all simulations, which are shown in detail in Figure S4.13.

During the second simulation phase, the overall thickness of the double layer decreases, as the facet-facet interaction allows a closer approach of NCs. At the same time, the previously formed hexagonal bilayer clearly evolves into a silicene-type honeycomb structure. The honeycomb structure is formed both in the areas initially showing PbSe NCs with $\langle 111 \rangle$ orientation and $\langle 100 \rangle$ orientation. An indication that the formation of the ordered precursor phase, a double hexagonal layer without aligned NCs, is more important than the individual NC orientation in the initial stages of the self-assembly. The increasing alignment of nanocrystals agrees with our experimental observations (Table 4.1). In addition, the defects observed in the self-assembly phase and after attachment are very similar (red circles in Figure 4.6) to what we already observed. These defects are discussed further in Figure S4.13.

In simulations performed at an even larger scale with 10^4 NCs, the final structure is obtained with $L = 620$ nm and the complete simulation is shown in Figure S4.12 (Figure 4.6c shows a part of Figure S4.12). The formation of silicene-type honeycomb superstructures, by turning on attractions between NC $\{100\}$ facets, is observed only in areas where a hexagonal bilayer precursor phase was preformed.

The results obtained in simulations suggest that a coarse-grained model can reproduce the NC self-assembly and the defects in the structure. The results corroborate the hypothesis that for honeycomb formation, a large steric repulsion is needed during the self-assembly of NCs to form hexagonal double layers. In experiments, this was achieved using nearly solvent-saturated conditions, which swell the ligand corona.^{33,34,43,45,52} Previous works on the self-assembly of NCs show that this causes a larger NC-NC separation and more repulsion.^{33,34,43,52-54} The results of time-monitoring reported here, supported by large-scale simulations with compressive and slow solvent evaporation, show that honeycomb formation is driven by the formation of hexagonal bilayers in a confined quasi-2D space. NCs not (yet) aligned with the $\langle 111 \rangle$ axis upwards, in the hexagonal bilayer, are able to reorient, allowing for maximal attraction between opposing $\{100\}$ facets and eventually neck formation.

4.4 Conclusion

We show that the formation of PbSe honeycomb superstructures proceeds via the following sequence: NC self-assembly, alignment, and oriented attachment. Both the experimental and model results show that to achieve high-quality long-range superstructures, it is important that these steps are separated. Therefore, it is crucial that $\{100\}/\{100\}$ attractive interactions do not dominate during the self-assembly phase. If facet attractions occur in a too early stage, small domains with square and linear attachments break long-range order in an irreversible way. Experimentally, long-range self-assembly was achieved by the addition of less reactive 1,4-butanediol to the reactive ethylene glycol liquid substrate, which helps to control the facet reactivity. In addition to the quality, the type of two-dimensional superstructure will be determined by the self-assembly process. At a high solvent vapor pressure, the relatively open hexagonal double layer will be stabilized during the self-assembly, as solvent molecules included in the NC ligand shell allow NCs to act more like “hard spheres.” When ligands are removed during this organization, NCs will align under the influence of attractive $\{100\}/\{100\}$ attractions and finally attach irreversibly to form a honeycomb superstructure.

References

- [1] Franchina Vergel, N. A.; Post, L. C.; Sciacca, D.; Berthe, M.; Vaurette, F.; Lambert, Y.; Yarekha, D.; Troadec, D.; Coinon, C.; Fleury, G.; et al. Engineering a Robust Flat Band in III–V Semiconductor Heterostructures. *Nano Lett.* **2021**, *21* (1), 680–685. DOI: 10.1021/acs.nanolett.0c04268.
- [2] Post, L. C.; Xu, T.; Franchina Vergel, N. A.; Tadjine, A.; Lambert, Y.; Vaurette, F.; Yarekha, D.; Desplanque, L.; Stievenard, D.; Wallart, X.; et al. Triangular Nanoperforation and Band Engineering of InGaAs Quantum Wells: a Lithographic Route Toward Dirac Cones in III–V Semiconductors. *Nanotechnology* **2019**, *30* (15), 155301. DOI: 10.1088/1361-6528/aafd3f.
- [3] Evers, W. H.; Goris, B.; Bals, S.; Casavola, M.; de Graaf, J.; van Roij, R.; Dijkstra, M.; Vanmaekelbergh, D. Low-Dimensional Semiconductor Superlattices Formed by Geometric Control over Nanocrystal Attachment. *Nano Lett.* **2013**, *13* (6), 2317–2323. DOI: 10.1021/nl303322k.
- [4] Yao, K. X.; Yin, X. M.; Wang, T. H.; Zeng, H. C. Synthesis, Self-Assembly, Disassembly, and Reassembly of Two Types of Cu₂O Nanocrystals Unifaceted With {001} or {110} Planes. *J. Am. Chem. Soc.* **2010**, *132* (17), 6131–6144. DOI: 10.1021/ja100151f.
- [5] Baumgardner, W. J.; Whitham, K.; Hanrath, T. Confined-but-Connected Quantum Solids via Controlled Ligand Displacement. *Nano Lett.* **2013**, *13* (7), 3225–3231. DOI: 10.1021/nl401298s.
- [6] Boneschanscher, M. P.; Evers, W. H.; Geuchies, J. J.; Altantzis, T.; Goris, B.; Rabouw, F. T.; van Rossum, S. A.; van der Zant, H. S.; Siebbeles, L. D.; Van Tendeloo, G.; et al. Long-Range Orientation and Atomic Attachment of Nanocrystals in 2D Honeycomb Superlattices. *Science* **2014**, *344* (6190), 1377–1380. DOI: 10.1126/science.1252642.
- [7] Nakagawa, Y.; Kageyama, H.; Oaki, Y.; Imai, H. Formation of Monocrystalline 1D and 2D Architectures via Epitaxial Attachment: Bottom-Up Routes Through Surfactant-Mediated Arrays of Oriented Nanocrystals. *Langmuir* **2015**, *31* (22), 6197–6201. DOI: 10.1021/acs.langmuir.5b00502.
- [8] Salzmann, B. B. V.; van der Sluijs, M. M.; Soligno, G.; Vanmaekelbergh, D. Oriented Attachment: From Natural Crystal Growth to a Materials Engineering Tool. *Acc. Chem. Res.* **2021**, *54* (4), 787–797. DOI: 10.1021/acs.accounts.0c00739.
- [9] Kalesaki, E.; Evers, W. H.; Allan, G.; Vanmaekelbergh, D.; Delerue, C. Electronic Structure of Atomically Coherent Square Semiconductor Superlattices with Dimensionality Below Two. *Phys. Rev. B* **2013**, *88* (11), 115431. DOI: 10.1103/PhysRevB.88.115431.
- [10] Kalesaki, E.; Delerue, C.; Morais Smith, C.; Beugeling, W.; Allan, G.; Vanmaekelbergh, D. Dirac Cones, Topological Edge States, and Nontrivial Flat Bands in Two-Dimensional Semiconductors with a Honeycomb Nanogeometry. *Phys. Rev. X* **2014**, *4* (1), 011010. DOI: 10.1103/PhysRevX.4.011010.
- [11] Delerue, C.; Vanmaekelbergh, D. Electronic Band Structure of Zinc Blende CdSe and Rock Salt PbSe Semiconductors with Silicene-Type Honeycomb Geometry. *2D Mater.* **2015**, *2* (3), 1583/2/3/034008. DOI: 10.1088/2053-1583/2/3/034008.
- [12] Yang, H. G.; Zeng, H. C. Self-Construction of Hollow SnO₂ Octahedra Based on Two-Dimensional Aggregation of Nanocrystallites. *Angew. Chem. Int. Ed.* **2004**, *43* (44), 5930–5933. DOI: 10.1002/anie.200461129.
- [13] Liu, B.; Zeng, H. C. Mesoscale Organization of CuO Nanoribbons: Formation of "Dandelions". *J. Am. Chem. Soc.* **2004**, *126* (26), 8124–8125. DOI: 10.1021/ja048195o.
- [14] Colfen, H.; Antonietti, M. Mesocrystals: Inorganic Superstructures Made by Highly Parallel Crystallization and Controlled Alignment. *Angew. Chem. Int. Ed.* **2005**, *44* (35), 5576–5591. DOI: 10.1002/anie.200500496.
- [15] Imai, H. Mesostructured Crystals: Growth Processes and Features. *Prog. Cryst. Growth Charact. Mater.* **2016**, *62* (2), 212–226. DOI: 10.1016/j.pcrysgrow.2016.04.011.
- [16] Geuchies, J. J.; van Overbeek, C.; Evers, W. H.; Goris, B.; de Backer, A.; Gantapara, A. P.; Rabouw, F. T.; Hilhorst, J.; Peters, J. L.; Kononov, O.; et al. In Situ Study of the Formation Mechanism of Two-Dimensional Superlattices from PbSe Nanocrystals. *Nat. Mater.* **2016**, *15* (12), 1248–1254. DOI: 10.1038/nmat4746.
- [17] Radha, B.; Senesi, A. J.; O'Brien, M. N.; Wang, M. X.; Auyeung, E.; Lee, B.; Mirkin, C. A. Reconstitutable Nanoparticle Superlattices. *Nano Lett.* **2014**, *14* (4), 2162–2167. DOI: 10.1021/nl500473t.
- [18] Wei, J.; Schaeffer, N.; Pileni, M.-P. Solvent-Mediated Crystallization of Nanocrystal 3D Assemblies of Silver Nanocrystals: Unexpected Superlattice Ripening. *Chem. Mater.* **2015**, *28* (1), 293–302. DOI: 10.1021/acs.chemmater.5b04120.
- [19] Fan, Z.; Grunwald, M. Orientational Order in Self-Assembled Nanocrystal Superlattices. *J. Am. Chem. Soc.* **2019**, *141* (5), 1980–1988. DOI: 10.1021/jacs.8b10752.
- [20] Winslow, S. W.; Swan, J. W.; Tisdale, W. A. The Importance of Unbound Ligand in Nanocrystal Superlattice Formation. *J. Am. Chem. Soc.* **2020**, *142* (21), 9675–9685. DOI: 10.1021/jacs.0c01809.
- [21] Li, D.; Nielsen, M. H.; Lee, J. R.; Frandsen, C.; Banfield, J. F.; De Yoreo, J. J. Direction-Specific Interactions Control Crystal Growth by Oriented Attachment. *Science* **2012**, *336* (6084), 1014–1018. DOI: 10.1126/science.1219643.

- [22] Walravens, W.; De Roo, J.; Drijvers, E.; Ten Brinck, S.; Solano, E.; Dendooven, J.; Detavernier, C.; Infante, I.; Hens, Z. Chemically Triggered Formation of Two-Dimensional Epitaxial Quantum Dot Superlattices. *ACS Nano* **2016**, *10* (7), 6861-6870. DOI: 10.1021/acsnano.6b02562.
- [23] van Overbeek, C.; Peters, J. L.; van Rossum, S. A. P.; Smits, M.; van Huis, M. A.; Vanmaekelbergh, D. Interfacial Self-Assembly and Oriented Attachment in the Family of PbX (X = S, Se, Te) Nanocrystals. *J. Phys. Chem. C* **2018**, *122* (23), 12464-12473. DOI: 10.1021/acs.jpcc.8b01876.
- [24] Peters, J. L.; Altantzis, T.; Lobato, I.; Jazi, M. A.; van Overbeek, C.; Bals, S.; Vanmaekelbergh, D.; Sinai, S. B. Mono- and Multilayer Silicene-Type Honeycomb Lattices by Oriented Attachment of PbSe Nanocrystals: Synthesis, Structural Characterization, and Analysis of the Disorder. *Chem. Mater.* **2018**, *30* (14), 4831-4837. DOI: 10.1021/acs.chemmater.8b02178.
- [25] Geuchies, J. J.; Soligno, G.; Geraffy, E.; Hendriks, C. P.; van Overbeek, C. V.; Montanarella, F.; Slot, M. R.; Konovalov, O. V.; Petukhov, A. V.; Vanmaekelbergh, D. Unravelling Three-Dimensional Adsorption Geometries of PbSe Nanocrystal Monolayers at a Liquid-Air Interface. *Commun. Chem.* **2020**, *3* (1). DOI: 10.1038/s42004-020-0275-4.
- [26] Peters, J. L.; van den Bos, K. H. W.; Van Aert, S.; Goris, B.; Bals, S.; Vanmaekelbergh, D. Ligand-Induced Shape Transformation of PbSe Nanocrystals. *Chem. Mater.* **2017**, *29* (9), 4122-4128. DOI: 10.1021/acs.chemmater.7b01103.
- [27] Moreels, I.; Lambert, K.; De Muynck, D.; Vanhaecke, F.; Poelman, D.; Martins, J. C.; Allan, G.; Hens, Z. Composition and Size-Dependent Extinction Coefficient of Colloidal PbSe Quantum Dots. *Chem. Mater.* **2007**, *19* (25), 6101-6106. DOI: 10.1021/cm071410q.
- [28] Hassinen, A.; Moreels, I.; De Nolf, K.; Smet, P. F.; Martins, J. C.; Hens, Z. Short-Chain Alcohols Strip X-Type Ligands and Quench the Luminescence of PbSe and CdSe Quantum Dots, Acetonitrile Does Not. *J. Am. Chem. Soc.* **2012**, *134* (51), 20705-20712. DOI: 10.1021/ja308861d.
- [29] Owen, J. S. The Coordination Chemistry of Nanocrystal Surfaces. *Science* **2015**, *347* (6222), 615-616. DOI: 10.1126/science.1259924.
- [30] Fritzing, B.; Capek, R. K.; Lambert, K.; Martins, J. C.; Hens, Z. Utilizing Self-Exchange to Address the Binding of Carboxylic Acid Ligands to CdSe Quantum Dots. *J. Am. Chem. Soc.* **2010**, *132* (29), 10195-10201. DOI: 10.1021/ja104351q.
- [31] Abelson, A.; Qian, C.; Salk, T.; Luan, Z.; Fu, K.; Zheng, J. G.; Wardini, J. L.; Law, M. Collective Topo-Epitaxy in the Self-Assembly of a 3D Quantum Dot Superlattice. *Nat. Mater.* **2020**, *19* (1), 49-55. DOI: 10.1038/s41563-019-0485-2.
- [32] Anderson, N. C.; Hendricks, M. P.; Choi, J. J.; Owen, J. S. Ligand Exchange and the Stoichiometry of Metal Chalcogenide Nanocrystals: Spectroscopic Observation of Facile Metal-Carboxylate Displacement and Binding. *J. Am. Chem. Soc.* **2013**, *135* (49), 18536-18548. DOI: 10.1021/ja4086758.
- [33] Bian, K.; Choi, J. J.; Kaushik, A.; Clancy, P.; Smilgies, D. M.; Hanrath, T. Shape-Anisotropy Driven Symmetry Transformations in Nanocrystal Superlattice Polymorphs. *ACS Nano* **2011**, *5* (4), 2815-2823. DOI: 10.1021/nn103303q.
- [34] Missoni, L. L.; Tagliazucchi, M. The Phase Behavior of Nanoparticle Superlattices in the Presence of a Solvent. *ACS Nano* **2020**, *14* (5), 5649-5658. DOI: 10.1021/acsnano.0c00076.
- [35] Weidman, M. C.; Smilgies, D. M.; Tisdale, W. A. Kinetics of the Self-Assembly of Nanocrystal Superlattices Measured by Real-Time In Situ X-Ray Scattering. *Nat. Mater.* **2016**, *15* (7), 775-781. DOI: 10.1038/nmat4600.
- [36] Bain, E. C.; Dunkirk, N. The Nature of Martensite. *Trans. AIME* **1924**, *70* (1), 25-47.
- [37] Lee, B.; Littrell, K.; Sha, Y.; Shevchenko, E. V. Revealing the Effects of the Non-solvent on the Ligand Shell of Nanoparticles and Their Crystallization. *J. Am. Chem. Soc.* **2019**, *141* (42), 16651-16662. DOI: 10.1021/jacs.9b06010.
- [38] Maiti, S.; Andre, A.; Maiti, S.; Hodas, M.; Jankowski, M.; Scheele, M.; Schreiber, F. Revealing Structure and Crystallographic Orientation of Soft Epitaxial Assembly of Nanocrystals by Grazing Incidence X-ray Scattering. *J. Phys. Chem. Lett.* **2019**, 6324-6330. DOI: 10.1021/acs.jpcllett.9b02373.
- [39] Quan, Z.; Wu, D.; Zhu, J.; Evers, W. H.; Boncella, J. M.; Siebbeles, L. D.; Wang, Z.; Navrotsky, A.; Xu, H. Energy Landscape of Self-Assembled Superlattices of PbSe Nanocrystals. *Proc. Natl. Acad. Sci. U. S. A.* **2014**, *111* (25), 9054-9057. DOI: 10.1073/pnas.1408835111.
- [40] Wang, Z.; Schliehe, C.; Bian, K.; Dale, D.; Bassett, W. A.; Hanrath, T.; Klinke, C.; Weller, H. Correlating Superlattice Polymorphs to Internanoparticle Distance, Packing Density, and Surface Lattice in Assemblies of PbS Nanoparticles. *Nano Lett.* **2013**, *13* (3), 1303-1311. DOI: 10.1021/nl400084k.
- [41] Zaluzhnyy, I. A.; Kurta, R. P.; Andre, A.; Gorobtsov, O. Y.; Rose, M.; Skopintsev, P.; Besedin, I.; Zozulya, A. V.; Sprung, M.; Schreiber, F.; et al. Quantifying Angular Correlations between the Atomic Lattice and the Superlattice of Nanocrystals Assembled with Directional Linking. *Nano Lett.* **2017**, *17* (6), 3511-3517. DOI: 10.1021/acs.nanolett.7b00584.

- [42] Choi, J. J.; Bealing, C. R.; Bian, K.; Hughes, K. J.; Zhang, W.; Smilgies, D. M.; Hennig, R. G.; Engstrom, J. R.; Hanrath, T. Controlling Nanocrystal Superlattice Symmetry and Shape-Anisotropic Interactions Through Variable Ligand Surface Coverage. *J. Am. Chem. Soc.* **2011**, *133* (9), 3131-3138. DOI: 10.1021/ja110454b.
- [43] Wan, Y.; Goubet, N.; Albouy, P. A.; Schaeffer, N.; Pileni, M. P. Hierarchy in Au Nanocrystal Ordering in a Supracrystal: II. Control of Interparticle Distances. *Langmuir* **2013**, *29* (44), 13576-13581. DOI: 10.1021/la403583q.
- [44] Quan, Z.; Xu, H.; Wang, C.; Wen, X.; Wang, Y.; Zhu, J.; Li, R.; Sheehan, C. J.; Wang, Z.; Smilgies, D. M.; et al. Solvent-Mediated Self-Assembly of Nanocube Superlattices. *J. Am. Chem. Soc.* **2014**, *136* (4), 1352-1359. DOI: 10.1021/ja408250q.
- [45] Kaushik, A. P.; Clancy, P. Solvent-Driven Symmetry of Self-Assembled Nanocrystal Superlattices - A Computational Study. *J. Comput. Chem.* **2013**, *34* (7), 523-532. DOI: 10.1002/jcc.23152.
- [46] Tadjine, A.; Delerue, C. Colloidal Nanocrystals as LEGO(R) Bricks for Building Electronic Band Structure Models. *Phys. Chem. Chem. Phys.* **2018**, *20* (12), 8177-8184. DOI: 10.1039/c7cp08400e.
- [47] Soligno, G.; Vanmaekelbergh, D. Phase Diagrams of Honeycomb and Square Nanocrystal Superlattices from the Nanocrystal's Surface Chemistry at the Dispersion-Air Interface. *J. Chem. Phys.* **2019**, *151* (23), 234702. DOI: 10.1063/1.5128122.
- [48] Soligno, G.; Vanmaekelbergh, D. Understanding the Formation of PbSe Honeycomb Superstructures by Dynamics Simulations. *Phys. Rev. X* **2019**, *9* (2), 021015. DOI: 10.1103/PhysRevX.9.021015.
- [49] Gupta, U.; Escobedo, F. A. Implicit Solvent Model for the Interfacial Configuration of Colloidal Nanoparticles and Application to the Self-Assembly of Truncated Cubes. *J. Chem. Theory Comput.* **2020**, *16* (9), 5866-5875. DOI: 10.1021/acs.jctc.0c00283.
- [50] Frenkel, D.; Smit, B. *Understanding Molecular Simulation: From Algorithms to Applications*; Elsevier, 2002. DOI: 10.1016/b978-0-12-267351-1.X5000-7.
- [51] Ciccotti, G.; Ryckaert, J. P. Molecular-Dynamics Simulation of Rigid Molecules. *Comput. Phys. Rep.* **1986**, *4* (6), 345-392. DOI: 10.1016/0167-7977(86)90022-5.
- [52] Zhang, J.; Luo, Z.; Martens, B.; Quan, Z.; Kumbhar, A.; Porter, N.; Wang, Y.; Smilgies, D. M.; Fang, J. Reversible Kirkwood-Alder Transition Observed in Pt₃Cu₂ Nanooctahedron Assemblies under Controlled Solvent Annealing/Drying Conditions. *J. Am. Chem. Soc.* **2012**, *134* (34), 14043-14049. DOI: 10.1021/ja304108n.
- [53] Pool, R.; Schapotschnikow, P.; Vlugt, T. J. H. Solvent Effects in the Adsorption of Alkyl Thiols on Gold Structures: A Molecular Simulation Study. *J. Phys. Chem. C* **2007**, *111* (28), 10201-10212. DOI: 10.1021/jp071491d.
- [54] Goubet, N.; Richardi, J.; Albouy, P.-A.; Pileni, M.-P. Which Forces Control Supracrystal Nucleation in Organic Media? *Adv. Funct. Mater.* **2011**, *21* (14), 2693-2704. DOI: 10.1002/adfm.201100382.

S4 Supporting Information

S4.1 Experimental methods and characterization

Chemicals

Benzene (99.8%, anhydrous), n-butanol (99.8%, anhydrous), 1-chloropentane (99%), cyclohexyl isocyanide (98%), diphenylphosphine (98%), hexane (mixture of isomers, $\geq 99\%$, anhydrous), isopropanol (99.5%, anhydrous), lead acetate trihydrate ($\geq 99.99\%$), methanol (99.8%, anhydrous), 1-octadecene (90%), octane ($\geq 99\%$, anhydrous), oleic acid (90%), pyrrolidine ($\geq 99\%$), selenium powder (99.99%, -100 mesh), tetrachloroethylene ($\geq 99\%$, anhydrous), toluene (99.8%, anhydrous), triethylamine ($\geq 99\%$), trifluoroacetic acid (99%), trifluoroacetic anhydride ($\geq 99\%$), trimethylbenzene (98%) and trioctylphosphine (90%) were purchased from Sigma-Aldrich and used without further purification. Lead (II) oxide (99.999+%) was purchased from Strem Chemicals. 1,4-Butanediol (BD, 99%, ReagentPlus®), diethylene glycol (DEG, 99%), diphenyl ether ($\geq 99\%$), ethylene glycol (EG, 99.8%, anhydrous) and hexadecane ($\geq 99\%$) were purchased from Sigma-Aldrich and degassed under vacuum for ~14 hours at 60 °C prior use. For superlattice formation, distillation of the EG did not result in a significant difference in the quality of the formed superlattice (Figure S4.1).

PbSe synthesis

The PbSe NCs were synthesized with two different procedures. The first method was developed by J. Steckel et al.¹ In brief, 4.77 g $\text{Pb}(\text{C}_2\text{H}_3\text{O}_2)_2 \cdot 3\text{H}_2\text{O}$, 10.35 g oleic acid (Pb:oleic acid ratio of 1:2.91), and 39.75 g 1-octadecene were mixed and degassed at 120 °C under vacuum for 5 hours to remove water and acetate. The selenium precursor was prepared by dissolving 3.52 g selenium powder in 0.41 g diphenylphosphine and 46.59 g trioctylphosphine. The selenium precursor was injected into a heated solution of the lead precursor (180 °C) under vigorous stirring. After 70 seconds, the reaction was quenched via injection of 30 mL of a methanol/butanol mixture (1:2). The mixture was centrifuged, and the black residue was dispersed in toluene (10 mL). Methanol was added (8 mL) to precipitate the suspension, which was subsequently centrifuged. The black residue was dispersed in toluene and the cycle was repeated for two more times. The second method was developed by Campos et al.,² with a lead oleate precursor prepared via the method of Hendricks et al.³ In short, lead(II) oxide (10.00 g, 44.8 mmol) and acetonitrile (~20 mL) are added to a 100 mL round bottom flask. The suspension was stirred while being cooled in an ice bath, after which trifluoroacetic acid (0.7 mL, 8.96 mmol, 0.2 equivalent) and trifluoroacetic anhydride (6.2 mL, 44.8 mmol, 1 equivalent) were added. After ten minutes, the yellow lead oxide dissolved, resulting in a clear and colorless solution that was allowed to warm to room temperature. Oleic acid (25.44 g, 90.05 mmol, 2.01 equivalent), isopropanol (~180 mL), and triethylamine (10.25 g, 101.25 mmol, 2.26 equivalent) were added in to 500 mL Erlenmeyer flask. The lead trifluoroacetate solution was slowly added to the oleic acid solution while stirring, resulting in the formation of a white precipitate. The mixture was heated to reflux, to dissolve the precipitate after which a clear and colorless solution was obtained. The heat was turned off and the flask was allowed to slowly cool to room temperature, followed by further cooling in a -20 °C freezer for >2 hours. The resulting white powder was isolated by suction filtration using a glass fritted funnel and the filtrate was thoroughly washed with methanol (3 x 300 mL). Large pieces were crushed to get a white powder, which was subsequently dried under vacuum for >6 hours to get a fluffy white powder.

Selenium precursor

The selenium precursor (N-cyclohexylpyrrolidine-1-carboselenoamide) was prepared by mixing selenium (0.71 g, 9.0 mmol), pyrrolidine (0.64 g, 9.0 mmol), cyclohexyl isocyanide (0.983 g, 9.0 mmol) and 10 mL toluene. This mixture was heated to ~ 100 °C until the solution turned clear. Additional pyrrolidine and/or cyclohexyl isocyanide was added if not all selenium reacted. The mixture was allowed to cool to room temperature where the selenourea precipitated. The liquid was decanted, and the obtained white solid was placed under vacuum for 24 hours. Subsequently, the solid was redissolved in 10 mL toluene at 100 °C and allowed to cool down. The precipitate was filtered and the solid placed under vacuum for another 24 hours. The synthesis of the NCs was performed in a Schlenk line where 1.6 g (2.08 mmol, 1.2 equivalent) $\text{Pb}(\text{oleate})_2$ was dissolved in 140 mL hexadecane in a 250 mL three neck flask. 0.45 g (1.7 mmol, 1 equivalent) N-cyclohexylpyrrolidine-1-carboselenoamide was dissolved in 8 mL diphenyl ether. Both precursors were heated to 100 °C to yield a clear colorless solution. The selenourea was quickly injected into the $\text{Pb}(\text{oleate})_2$ solution which turned brown in approximately 8 seconds. After 110 minutes, the reaction was cooled down with an ice bath and brought inside the glovebox. 90 mL of n-butanol and 60 mL of methanol was added to precipitate the NCs. The mixture was centrifuged, and the black residue was dispersed in 10 mL toluene. This solution was washed three more times with methanol. The ligand density was determined via a previously published method.⁴ We used NMR spectroscopy to determine if no free ligands were present and FTIR with a $\text{Pb}(\text{oleate})_2$ calibration curve to determine the number of ligands per NC (**supporting information S4.2**).

Superstructure formation

All experiments were performed based on the experimental procedure as previously reported.⁵ A small Petri dish (\varnothing 27 mm) was filled with 6.5 mL ethylene glycol (or a mixture of EG and BD), creating a flat surface. This Petri dish was placed in another bigger Petri dish containing 2 mL toluene. Subsequently, 350 μL of a diluted NCs solution (7.7×10^{-8} M) in toluene was drop-casted on top of the 6.5 mL EG (or a mixture), resulting in a height of ~ 0.061 cm and both Petri dishes were covered with a bigger beaker (400 mL). The honeycomb structure was formed on top of the liquid substrate during 15 hours of slow toluene evaporation, and could then be transferred to any substrate. The whole experiment is performed in a glove box containing <0.1 ppm O_2 , free of amines and other volatile gasses. The superstructure formation was successful for NCs with sizes between 5 and 7 nm. To minimize distortion every sample in the time series (**Figure 4.3**), was prepared independently.

FTIR measurements were performed with a Bruker Vertex 70. A special airtight liquid cell was used, purchased from International Crystal Laboratories, with a path length of 0.5 mm and two KBr crystals at the back and front side to make it transparent for IR light. Spectra were recorded from 400 cm^{-1} - 7500 cm^{-1} , with a KBr beam splitter, a DLATGS D301 detector, and a mid IR source. For all the measurements, tetrachloroethylene (TCE) was used as solvent. A calibration curve with $\text{Pb}(\text{oleate})_2$ was used to determine the concentration ligands on the NCs. The NC concentration was determined by integration of the exciton peak.⁶

Proton nuclear magnetic resonance (^1H -NMR) measurements were performed using an Agilent MRF400 equipped with a OneNMR probe and Optima Tune system. Spectra were recorded according to the following parameters: 400 MHz, CDCl_3 , 25 °C. PbSe NCs were

measured to determine if there were free ligands or other pollution present. Measurements of PbSe were performed using a longer relaxation delay (30 seconds) to allow complete relaxation. For NC-Pb(oleate)₂ Δ = 5.54 (m, 4H, HC=CH), 2.37 (t, 4H, 3JHH = 7.3 Hz, CH₂), 2.15 (m, 8H, CH₂), 1.77 (p, 4H, 3JHH = 7.8 Hz, CH₂), 1.5-1.2 (m, 42H, CH₂), 0.93 (t, 6H, 3JHH = 6.7 Hz, CH₃).

TEM and SAED measurements were performed at a Philips Tecnai operating at 200 kV. In bright-field TEM the contrast in the images scales relatively to the highest contrast in the image, therefore without additional measures quantitative comparison between different samples is not possible. To ensure the reproducibility of the measurement of the SAED peak width, the sample needs to be perpendicular to the electron beam while it is made sure that the diffraction peaks do not oversaturate the detector (see example in the main text and [supporting information S4.5](#)).

S4.2 Liquid Substrates and their chemical properties

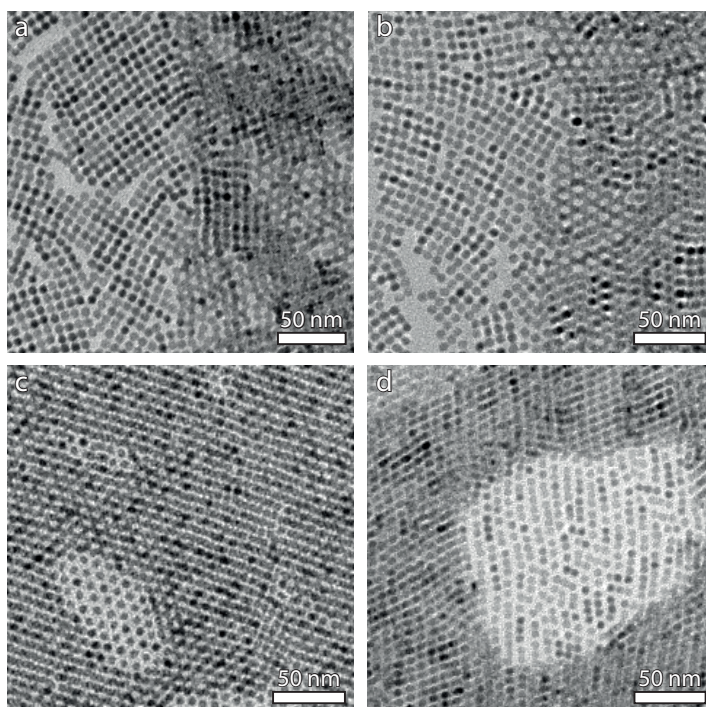


Figure S4.1 Two TEM images of superlattices formed on 100% EG with 6.1 nm PbSe NCs (3.7 oleate/nm²) are shown in (a) and (b), both showing oriented attachment. No distinct differences were observed between the superlattices formed on degassed (a) and on degassed and distilled EG (b), excluding the influence of impurities on superlattice formation. Two TEM images of self-assemblies formed on 100% BD with 5.5 nm PbSe NCs (2.99 oleate/nm²) are shown in (c) and (d). After toluene evaporation under atmospheric nitrogen pressure for 45 minutes at 27 °C, hexagonally ordered self-assemblies were formed (c). Epitaxial (linear) attachment is only observed at higher temperatures (20 minutes at 35 °C followed by 20 minutes at 85 °C). Showing that at higher temperatures BD can become reactive.

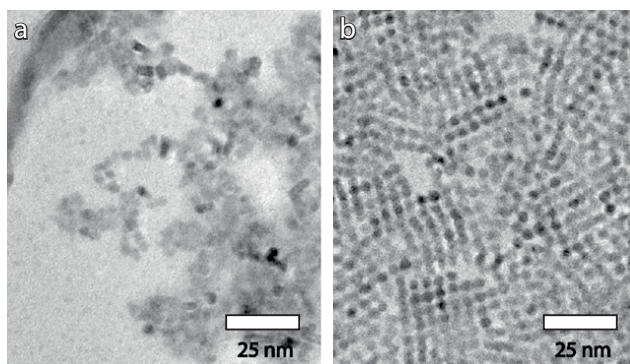
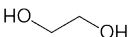
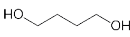
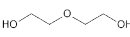


Figure S4.2 TEM images depicting superlattices formed with 5.2 nm PbSe NCs ($3.3 \text{ oleate}/\text{nm}^2$) on a mixture of liquid substrates, containing EG and diethylene glycol (DEG) in an amount of (a): 5.5 mL EG and 1 mL DEG and (b) 6.4 mL EG and 0.1 mL DEG. The agglomerates formed in (a) and disordered superlattice formed in (b) show that DEG is more reactive than EG. Even addition of only 0.1 mL to the liquid substrate induces attachment on a faster timescale, resulting in the disordered structures.

Table S4.1 Chemical properties of ethylene glycol, 1,4-butanediol and diethylene glycol.

	Molecular formula	pK_a expected vs EG	pK_a experimental	pK_a calculated highest acidic	Viscosity (mPa·s) (water = 1)	Polarizability calculated (10^{-24} cm^3)	Length (nm)
ethylene glycol (EG)	$\text{C}_2\text{H}_6\text{O}_2$ 	EG	14.22* 14.52 ¹⁴ 14.77** 15.1* ¹⁵	14.83***	16.1 at 25°C	5.7 ± 0.5 ****	~0.43
1,4-butanediol (BD)	$\text{C}_4\text{H}_{10}\text{O}_2$ 	> EG	14.5* ¹³ 15.0 ¹⁴ 15.1*** ¹⁵	14.73 ± 0.1 ** 15.67***	84.9 at 20°C	9.4 ± 0.5 ****	~0.74
diethylene glycol (DEG)	$\text{C}_4\text{H}_{10}\text{O}_3$ 	< EG	-	14.03 ± 0.1 ** 15.42***	35.7 at 20°C	10.1 ± 0.5 **** *	~0.87

*Chemical book

* PubChem

** Internet Bond-energy Databank - iBond

*** ChemAxon

****Chempidder: ACD/Labs

Table S4.1 lists the chemical properties of the three liquid substrates used in experiments in this manuscript. From self-assembly and attachment experiments we have concluded that in terms of ligand removal from NC surfaces, 1,4-butanediol (BD) is less reactive than ethylene glycol (EG), while diethylene glycol (DEG) is much more reactive than EG. The aliphatic diols used as liquid substrates for superlattice formation, all contain two hydroxide groups, which we suspect to play a role in the ligand removal from the {100} facets of PbSe NCs. However, the chemical mechanism behind this process is not yet fully understood, here we would like to tentatively discuss some possibilities.

Previous research has shown that the oleate ligands capping the PbSe NCs are X-type carboxylates,¹⁻³ which require protonation to induce ligand desorption.⁴ When NC dispersions S4 were mixed with short-chain alcohols such as methanol (weak acids with a pK_a of 15-18), protonation was possible resulting in the release of oleic acid (as observed with NMR). After protonating the carboxylates with their hydroxide group these alcohols then bind as alkoxides to the NC surface, effectively completing a ligand exchange. Efficacy of the ligand exchange was shown to depend on the acidity constants: a stronger acid (lower pK_a) displaces the ligands more effectively than a weaker acid (higher pK_a).⁷

More recent work has shown that amines injected in the EG liquid can induce epitaxial fusion in assembled PbSe NCs.^{8,9} It was shown that for PbSe NCs self-assembled on EG, the injection of a 1,2-ethylene diamine solution in the liquid substrate can induce ligand displacement. The amines (as L-type ligands) can induce metal carboxylate complex displacement from the NC surface (Z-type displacement of lead oleate as observed with NMR and FTIR), allowing attachment between bare {100} facets.^{10,11} A paper by Anderson et al. suggests that the polar EG wicks into the film as the oleates are replaced by ethylene glycoxide.⁸ The experiments presented in this manuscript make no use of amines, but earlier work showed that primary alcohols (such as methanol) are able to induce the same Z-type ligand displacement, albeit less efficiently than amines.¹⁰ The efficiency of this displacement was shown to depend significantly on the polarizability and steric profile of the incoming ligand, being more efficient with a polarizable and smaller ligand which can cooperatively bind to the NC surface.

The aliphatic diols used as liquid substrates for superlattice formation (EG, BD and DEG), all contain two hydroxide groups. We therefore suspect that these diols induce ligand desorption via a similar mechanism as primary alcohols i.e. by L-type promoted Z-type displacement or by protonation of the X-type oleates. Experimentally the presence of alkoxides in a film formed on EG was shown,⁸ indicating that the polar liquid substrate can interpenetrate the superstructure, but as this occurred in the presence of an amine, the presence of the ethylene S5 glycoxide does not allow differentiation between these mechanisms. Further experimental studies are needed to understand which of these chemical mechanisms causes the liquid substrate to displace ligands. To attempt and elucidate the different reactivity in superlattice formation for these liquid substrates, we have listed the chemical properties which were indicated as playing a role in these two mechanisms.

The acid ionization constants are expected to indicate reactivity based on the protonation of the X-type oleates. Column 2 shows the pK_a value in relation to EG we would expect based upon our superlattice experiments. However, the experimentally determined pK_a values reported in literature shown in column 3, show substantial variation, presumably because the determination of pK_a for weak organic acids is challenging.¹² The expected decrease in acidity from EG to BD (a trend shown for the short-chain alcohols) is not clearly observed. In experi-

ments performed by Woolley et al., the high acidity of BD was explained by a possible favorable bond angle for intramolecular hydrogen bonding in the singly ionized acid anion of BD.¹³ These effective intra-molecular hydrogen bonds could also contribute to the high viscosity of BD (column 6). When pK_a values are calculated, especially using the same software, the acidity trend becomes more clear (column 5). Then, BD indeed shows a weaker acidity than EG, indicating a lower reactivity. Please notice that the DEG value is not lower than the calculated EG value. In addition, these calculated values deviate considerably from the experimental values. For L-type promoted Z-type displacement, the polarizability and the steric profile of the incoming ligand was shown to have a significant impact on the reactivity. However, the polarizability of each molecule (column 7), as well as the length of the molecule does not follow the reactivity trend (column 8).

Despite the potential mechanisms discussed above, the relation between the chemical properties of the liquid substrate and effective ligand displacement (experimentally observed as oriented attachment) is not clear. A single chemical property cannot explain our experimental observations. Likely there is a combination of factors in play which is not yet understood. A detailed chemical analytic study on the chemical mechanism of ligand stripping of pure EG, pure BD and mixtures of EG and BD is therefore highly desired.

S4.3 Ligand density as determined by $^1\text{H-NMR}$ and FTIR

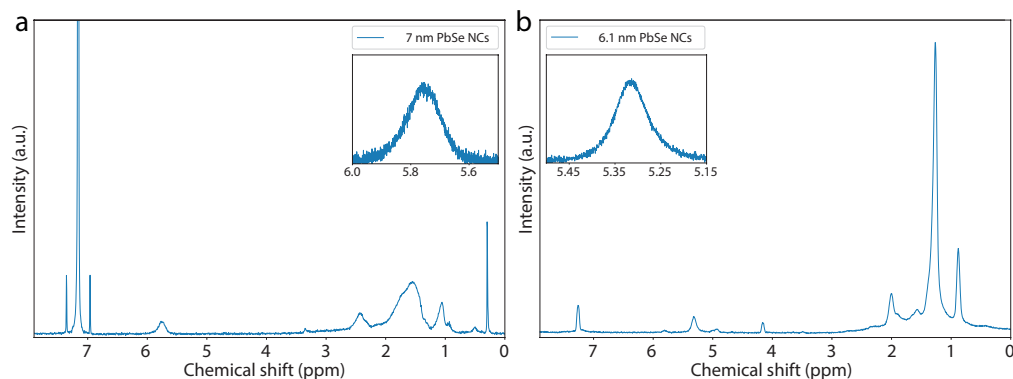


Figure S4.3 $^1\text{H-NMR}$ spectra of PbSe NCs of 7 nm dispersed in d-chloroform (a) and 6.1 nm dispersed in d-benzene (b). The peak positions and characterization are listed in the Table S4.2 below. The vinyl peak of the ligands, shown in the insets at 5.75 and 5.3 ppm respectively, is broadened, indicating that only ligands bound to the surface of the NCs are present while no additional hydrocarbons are observed.

Table S4.2 Table listing the resonances observed in Figure S4.3 and attributed to the protons present in the reaction mixture. Note that thiocyanate does not contain any protons and therefore cannot be characterized with $^1\text{H-NMR}$.

Chemical shift (ppm)	Corresponds to	Group
0.9 (b) / 1.0 (a)	OA	$-\text{CH}_3$
1.3 (b)/ 1.55 (a)	OA	$-\text{CH}_2-$
2.0 (b)	OA	$-\text{CH}_2, \text{O}=\text{COH}-\text{CH}_2$
2.4 (a)	OA	$\text{O}=\text{COH}-\text{CH}_2$
4.1 (b)	Ferrocene	-
5.3 (b) / 5.75 (a)	OA	$-\text{HC}=\text{CH}-$
7.16 (a) / 7.3 (b)	$\text{C}_6\text{D}_6 / \text{CDCl}_3$	solvent

Table S4.3 Table providing an overview of the ligand densities calculated based on the FTIR spectra shown in Figure S4.4.

NC size (nm)	NC concentration (μM)	Oleate concentration (mM)	Oleate/NC ratio	Surface area sphere (nm^2)	Oleate molecules per nm^2
7.07	23.3	8.01	343.6	158.26	2.17
6.12	4.42	1.91	432	118.38	3.65

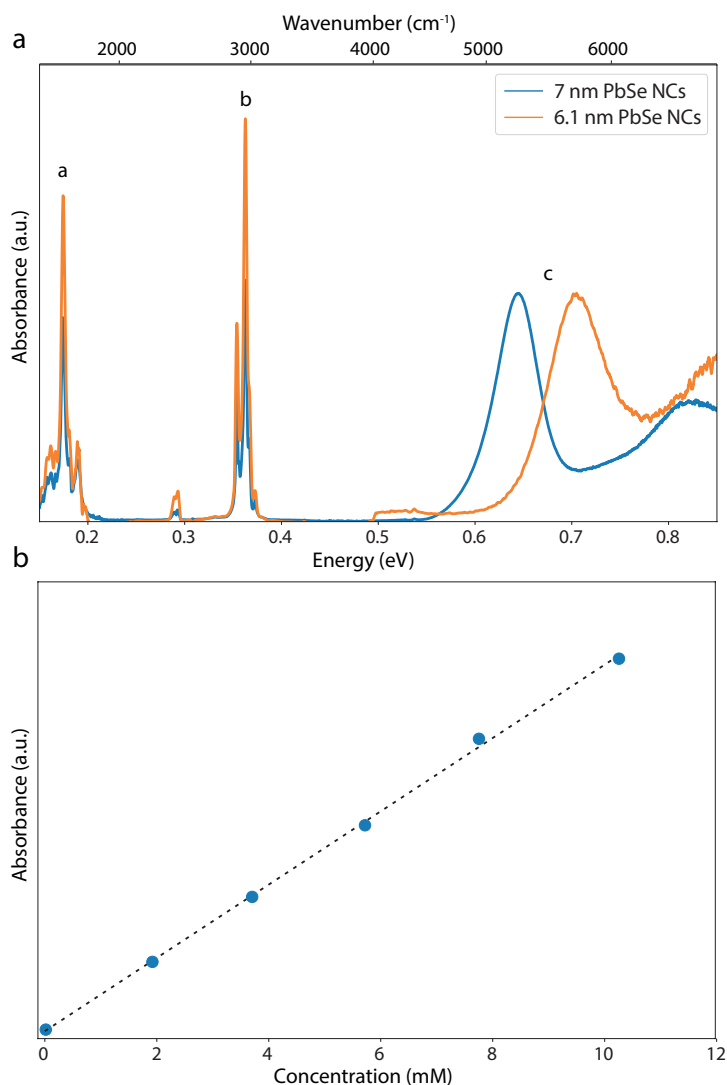


Figure S4.4 FTIR spectrum of well-washed oleate-capped PbSe NCs dispersed in tetrachloroethylene. (a) FTIR spectrum of PbSe NCs (7 nm and 6.1 nm in size) dispersed in tetrachloroethylene showing three regions of interest: a) region of C-O vibrations b) a peak due to the CH₂ asymmetric stretching vibrations of oleate molecules (bound to the surface or free in solution), and c) the absorption peak due to the band-edge exciton in the PbSe NCs which is directly dependent on the size of the NCs. From the integration of region c, the concentration of NCs in the solution can be determined while the integration of peak b shows the total concentration of oleate in the dispersion when compared to the calibration curve shown in panel (b). The calibration is the integrated absorbance peak b versus the Pb(oleate)₂ concentration in a solution containing only Pb(oleate)₂ ($R^2 = 0.999$).

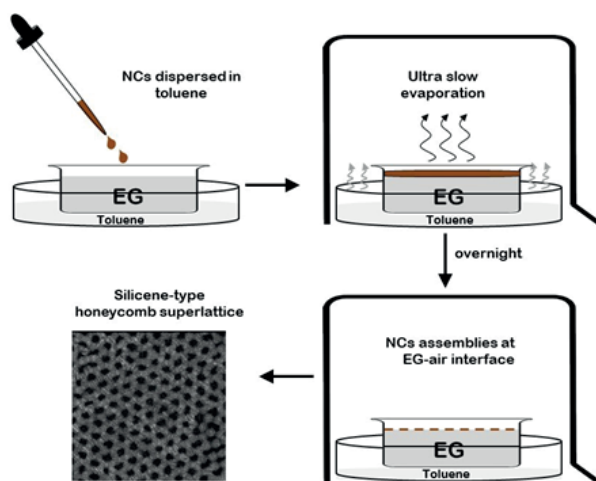


Figure S4.5 A schematic illustration of the experimental setup to make PbSe superstructures under a nearly saturated solvent pressure. It starts with a Petri dish filled with the immiscible liquid substrate, EG or BD in this case. This Petri dish is placed inside a larger Petri dish containing 2 mL of toluene. A NCs dispersion is drop-casted onto the liquid substrate and a cap is placed on top to slow the evaporation. Meanwhile, the NCs will self-assemble and ligands are removed from the NC surface. At the end of the process, the NC facets will align (100)/(100) and attach.

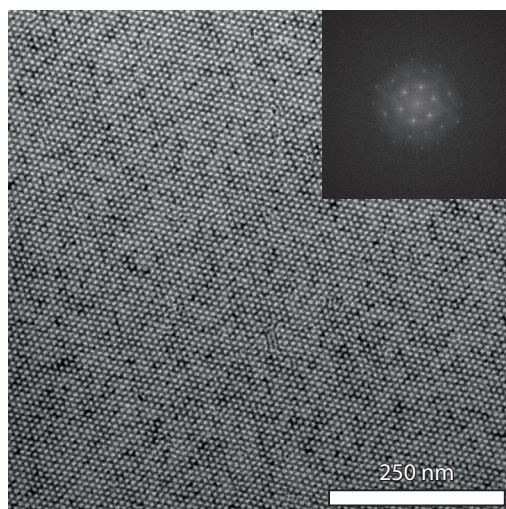


Figure S4.6 A TEM image of a long-range honeycomb structure prepared following the same procedure as Figure 4.2d (a BD:EG ratio of 1:1.17). The Fourier transform in the upper right corner, confirms that the periodicity holds for the entire picture.

S4.4 Comparison of hexagonal bilayers and silicene honeycomb structure: the diffusion of nanocrystals compared to the liquid/air interface recession during drying

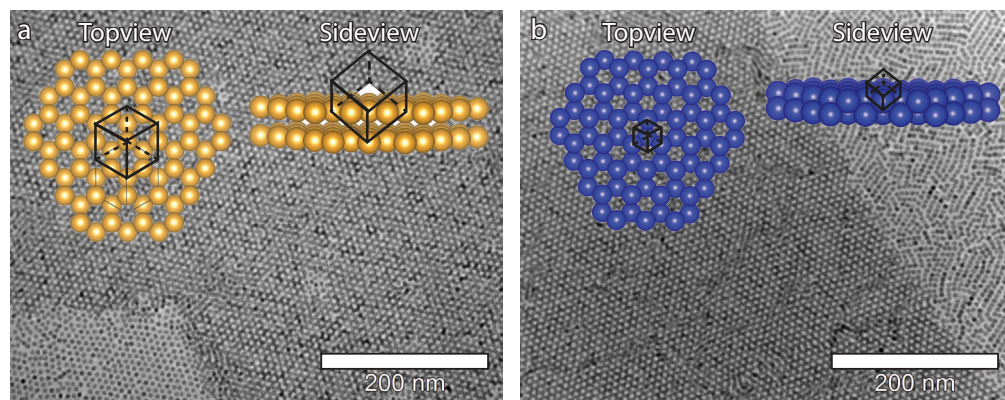


Figure S4.7 Similarity of hexagonal bilayer (a) and silicene honeycomb structure (b), if viewed along the perpendicular direction. The insets show an illustration of the position of the NCs in both cases. This scheme shows that the structures are indistinguishable viewed perpendicular to the plane, but can be distinguished clearly by a side view. Also note that the crystal structure, when you consider the NCs are atomic entities, is face centered cubic or hexagonal close packed in (a) and simple cubic in (b).

At lower magnification in TEM there is a huge similarity between the geometry of domains of the attached honeycomb structures and the geometry of the unattached hexagonal mono- and bilayer domains (5 μm scale in **Figure 4.2d-f**),⁵ these smooth edged patterns are due to the slow evaporation of the solvent under an almost saturated toluene atmosphere.^{16,17} Under these circumstances the gas-liquid interface retreats much slower than the diffusion rate of the NCs (see below), giving the hydrophobic NCs time to gather in places with residual solvent and to self-assemble in hexagonal mono- and bilayers.¹⁵⁻¹⁶ The smooth edges are due to minimization of their energy,¹⁷ with no irregularities like the formation of coffee rings,¹⁸ or a NC “skin” on top of the toluene.¹⁹ Hence, the slow evaporation is beneficial for long range self-assembly of the NCs, while also beneficial for long range structural integrity of the superstructure, as it S13 separates two phases; 1), the self-assembly into hexagonal layers and 2), attachment of the NCs. At higher magnification, these hexagonal bilayers still look very similar to attached honeycomb superstructures as is shown in **Figure S4.7**. However, the absence of attachment in these hexagonal structures (**Figure S4.7a**) is clearly recognizable in three ways. First, as a quick check, if the hexagonal monolayer shows unattached dots it is an indication that the bilayer is also unattached. The silicene honeycomb structure always shows attachment in the monolayer as well, in either a linear or square structure (**Figure 4.1d-f**, **Figure S4.7b**). Second, the SAED in the upper right inset of **Figure 4.2e** shows rings, similar to a hexagonal bilayer of “hard” spheres as observed in **Figure 4.1a**. Therefore, the rotational freedom of the unattached NCs has been preserved. Third, by tilting the TEM sample by 45 degrees, as done in **Figure 4.4**, any necks present between the particles will be observed.

The diffusion coefficient can be calculated with the Stokes-Einstein equation $D = \frac{kT}{6\pi\eta r}$ with k , the Boltzmann constant, T absolute temperature, η the dynamic viscosity and r the hydrodynamic radius of the particles. Since the ligand shell is covalently bound to a NC, we took a value of 5 nm for r , the value of the viscosity is 5.6×10^{-4} Pa·s. The diffusion coefficient becomes 7.7×10^{-11} m²·s⁻¹ and the diffusion time can be approximated by $t \approx \frac{x^2}{2D}$.

The height of the 350 μ L NC dispersion drop-casted on an EG filled glass petri-dish (θ 27 mm) is ~ 0.061 cm. The NCs need on average ~ 40 minutes to diffuse that distance. In these experiments it takes at least 3 hours to evaporate the solvent, which means that the NC can diffuse to the interface before they are captured by the downwards moving evaporation front.

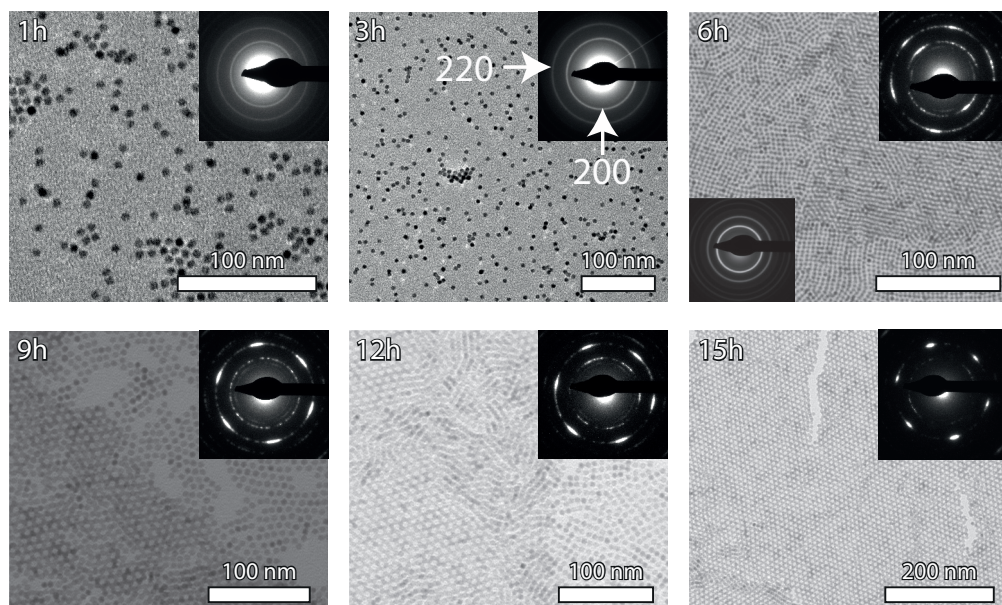


Figure S4.8 Representative TEM images and SAED patterns of self-assembled PbSe NCs at different stages of the NC assembly process. The samples were obtained by horizontal contact of the TEM grid with the toluene/ethylene glycol surface, at different times after drop-casting of the dispersion on the EG liquid substrate and start of the solvent evaporation process. The TEM images taken after 6-12 hours show the border between NC monolayers and bilayers. The analysis of the SAED patterns is discussed in the main text.

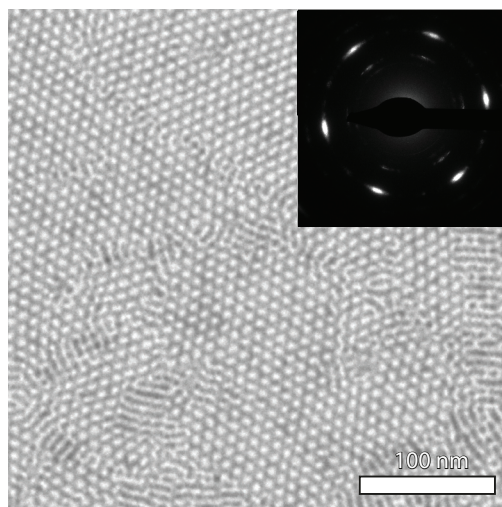


Figure S4.9 A TEM image of the silicene-type honeycomb lattice and the corresponding SAED pattern 24 hours after deposition of the NC dispersion.

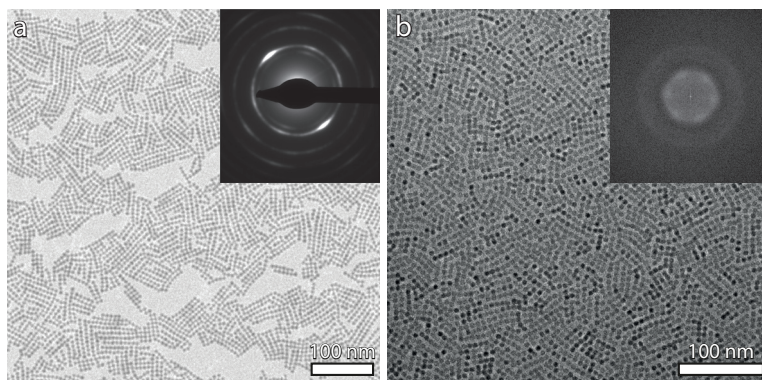


Figure S4.10 (a) A TEM image and the corresponding SAED pattern of the monolayer region, 15 hours after deposition of the NCs. The NCs show linear attachment and the SAED shows a preferred orientation of 100 facets upwards (the 200 ring has areas of higher intensity compared to randomly oriented NCs see for example Figure S4.7). The broad spots on the 200 ring show that more (100) facets are preferentially pointing in 6 directions. Meaning that most linear structures are oriented in the same direction. (b) A TEM image and the corresponding Fourier transform of the monolayer region, 24 hours after deposition. The Fourier transform of the image contains six vague spots, which tells us that the NCs are imperfectly organized in a hexagonal packing. These two observations suggest that the linear structures are rapidly formed from a self-assembled hexagonal monolayer, as the original hexagonal positioning of the monolayer is somewhat maintained in this attached structure.

S4.5 Calculation of volume of nanocrystal core, ligand and solvent within a face centered cubic lattice

We calculated the volume fraction of all molecules in FCC crystal (or hexagonal bilayer), with 6 nm NCs (assuming a spherical shape), a ligand density of 2.5 oleates/nm² (377 oleates/NC) and a NC separation of 2 times the ligand length (1.6 nm). The unit cell of an FCC lattice contains 4 NCs and has a packing density of ~74% when using hard spheres.

The total volume of the unit cell would be $2\sqrt{2}(3 + 1.6)^3 = 2202.5 \text{ nm}^3$. The volume occupied by the inorganic cores, ligands, solvent within the ligand corona and other solvent molecules is respectively 21%, 36%, 17% and 26%. Hence, solvent fills most of the space in an FCC lattice of NCs.

Table S4.4 Calculation of volume of NC core, ligand and solvent in an FCC lattice.

Part	Volume (nm ³)	Volume within FCC lattice (nm ³)	Percentage (%)
NC core	113	452	21
Ligands (377 oleate/NC)	197	788	36
Solvent within ligand shell	98	391	17
Solvent in between spheres	-	793	26

S4.6 SAED analysis on nanocrystal alignment during honeycomb formation

Table S4.5 Overview of the average peak width and the percentage of background scattering. The data is extracted from the SAED patterns at different stages after NC deposition.

Time [h]	220 ring intensity vs 200 ring intensity	NCs with random orientation [%]	Background scattering 220 ring [%]	NCs aligned to neighboring NCs [%]	Average 220 peak width [°]
Powder	1 : 2.80	100	-	0	-
6	1 : 0.9	32	48	64	6.1
9	1 : 0.35	13	26	86	5.0
12	1 : 0.32	12	26	86	4.5
15	1 : 0.11	4	18	96	2.7
24	1 : 0.08	3	20	92	2.7
Mo	-	-	12	-	0.39

In **Table S4.5** the results of the SAED analysis for each diffractogram are shown. With Crystbox ringGUI software the diffractograms were integrated to determine the intensity on both the 200 and 220 diffraction ring.¹⁸ The software automatically scales the ring with the highest intensity to 1, which in every SAED pattern here was the 220 ring. The 200 ring intensity shows a decrease over time from 0.9 to 0.08, ten times as low as the 220 ring intensity, an indication that more NCs are oriented with the $\langle 111 \rangle$ axis up. Comparing the 200 intensities to a bulk PbSe powder XRD pattern which shows random orientation, the percentage of NCs with random orientation can be calculated (column 3).

In **Figure 4.3c** (main text), the 220 ring was represented as an azimuthal trace, and the 6 peaks are fitted with Gaussians, providing quantitative values for the background intensity of the ring in between these peaks (column 4), and the FWHM of the peaks (column 6). Initially the background scattering is high, indicating $\langle 111 \rangle$ oriented NCs in the z-direction, but which still have a random rotation in the x-y plane. As more NCs align facet-to-facet, the background scattering in between the peaks decreases to 20%, or 8% when taking instrumental broadening as determined by a molybdenum single crystal (Mo) into account. To calculate the percentage of NCs aligned to neighboring NCs, we determine the corrected background scattering by removing the Mo determined instrumental background from the determined backgrounds 220 scattering. This value is then subtracted from 100% alignment to give an indication of the percentage of NCs aligned to neighboring NCs (column 5). It shows that an increasing percentage of NCs, up to 96%, is aligned to neighboring NCs. At the same time the average peak width decreases to 2.7°.

S4.7 Parameters used in the coarse-grained molecular dynamics simulations

The simulations are carried out using the coarse-grained molecular dynamics model introduced in a recent publication by Soligno et al.¹⁹ Each NC is modelled as a polybead structure with rhombicuboctahedron shape of roughly 6 nm size, see [Figure S4.11](#). Each bead of the polybead structures represents a few atoms. Such a coarse-grained model requires a lower computational cost for the simulations than a fully-atomistic model, allowing the study of larger-scale systems. Here we report an overview of the model parameters used for the simulations presented in this work and additional simulation results.

Note that, in this work, the NCs do not experience the external potentials U_z , U_φ and U_ψ used previously,²¹ to impose NC adsorption to the solvent-air interface.²¹ Instead, the NCs experience the external potential U_{2D} which represents the effect of the evaporating solvent compressing the NCs in a planar film (without preferred orientation of the NCs), see text in the main paper.

NC-NC Interactions

During the first phase of the simulation (i.e. from 0 until 0.1 μ s), each bead of a NC interacts with each bead of the other NCs by the bead-bead pair potential

$$U_R(r) = \begin{cases} \varepsilon_R [(\sigma_R/r)^6] - 1, & \text{if } r \leq \sigma_r \\ 0, & \text{otherwise} \end{cases} \quad (\text{S4.1})$$

where r is the bead-bead center-of-mass distance, $\varepsilon_R = 8 \times 10^{-21}$ J and $\sigma_R = 4$ nm. During the subsequent phase of the simulation (i.e. after 0.1 μ s), to mimic ligands detaching from the NCs {100} facets (thus allowing NCs to attract each other by these facets), the pair potential U_R is deactivated for bead-bead pairs between blue, light-blue, and/or black beads, see [Figure S4.11](#), while for bead-bead pairs between orange and/or red beads is active using $\varepsilon_R = 4 \times 10^{-21}$ J and $\sigma_R = 4$ nm. For the other bead-bead pairs, i.e. involving only one orange or red bead, U_R is active using $\varepsilon_R = 4 \times 10^{-21}$ J and $\sigma_R = 1.95$ nm. Note that the parameters ε_R and σ_R of U_R , for each bead-bead pair, are not changed abruptly after 0.1 μ s of simulation, but they are linearly tuned, for a transition phase of 0.1 μ s. This smooth transition of the bead-bead pair potentials allows for a more realistic representation of the ligand detachment from the NC {100} facets (which, in the experiments, reasonably does not occur *all at once*). In the results of [Figure S4.12](#), the parameter is defined as $a \equiv (\sigma_R - \sigma)/2$

The Lennard-Jones pair potential

$$U_{LJ}(r) = \begin{cases} 4\varepsilon[(\sigma/r)^{12}] - (\sigma/r)^6, & \text{if } r \leq \sigma \\ 0, & \text{otherwise} \end{cases} \quad (\text{S4.2})$$

is activated between all bead-bead pairs, using $\sigma = 1.6$ nm for all bead-bead pairs, and $\varepsilon = 4 \times 10^{-21}$ J for bead-bead pairs between light-blue beads, $\varepsilon = 10^{-21}$ J for bead-bead pairs not involving light-blue beads, and $\varepsilon = 2.5 \times 10^{-21}$ J otherwise.

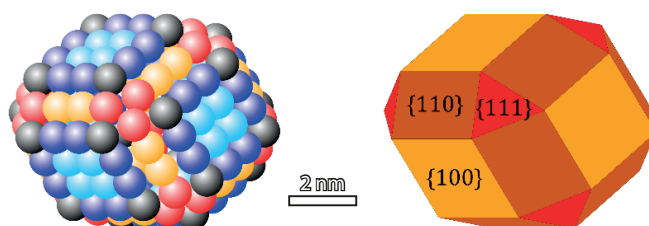


Figure S4.11 Beads, here plotted as spheres with diameter 1 nm, reproducing the surface of a NC in our coarse-grained molecular dynamics model (see reference 19 for details). On the right, we show the corresponding representation of the faceted NC.

Nanocrystal Brownian Motion

The Brownian motion of the NCs is modelled as described in a recent publication by Soligno et al.¹⁹ The two parameters λ and r_B regulating the translational and rotational diffusion of the NCs are $\lambda = 3 \times 10^{-11}$ kg/s and $r_B = 3.3$ nm for the first phase of the simulation (i.e. from 0 till 0.1 μ s). They represent the expected NC diffusion in solvent (toluene). For the subsequent phase of simulation (i.e. after 0.1 μ s) they are $\lambda = 1.5 \times 10^{-9}$ kg/s and $r_B = 3.6$ nm. They then mimic the fully evaporated solvent where the NCs are expected to be in a more viscous environment (with viscosity similar to that of oleic acid).

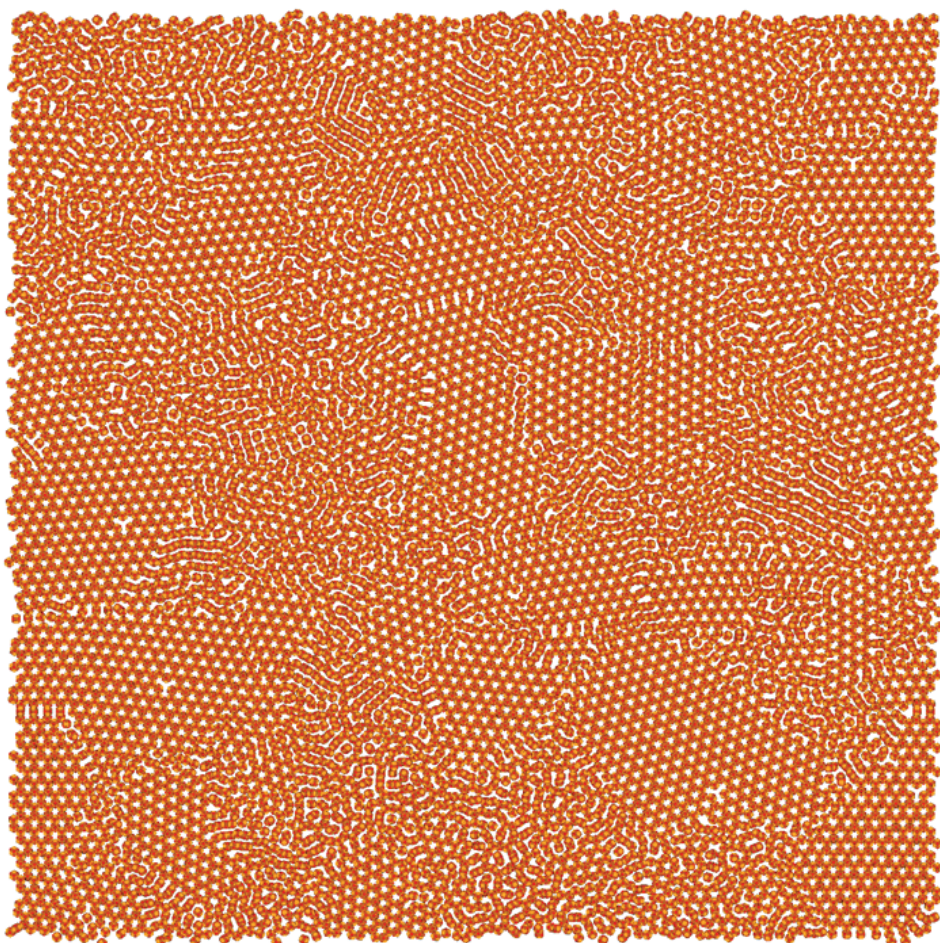


Figure S4.12 Top view of the quasi-2D structure formed in a molecular dynamics simulation of 10^4 NCs, initially randomly dispersed in a 3D box of side $L = 620$ nm, upon compression in a thin planar film. NC-NC attraction by $\{100\}$ facets (yellow) is switched on after $0.1 \mu\text{s}$. Figure 4.6c shows only a zoomed portion of this simulation. See the text in the main paper and supporting information S4.4 for details on the simulation model.

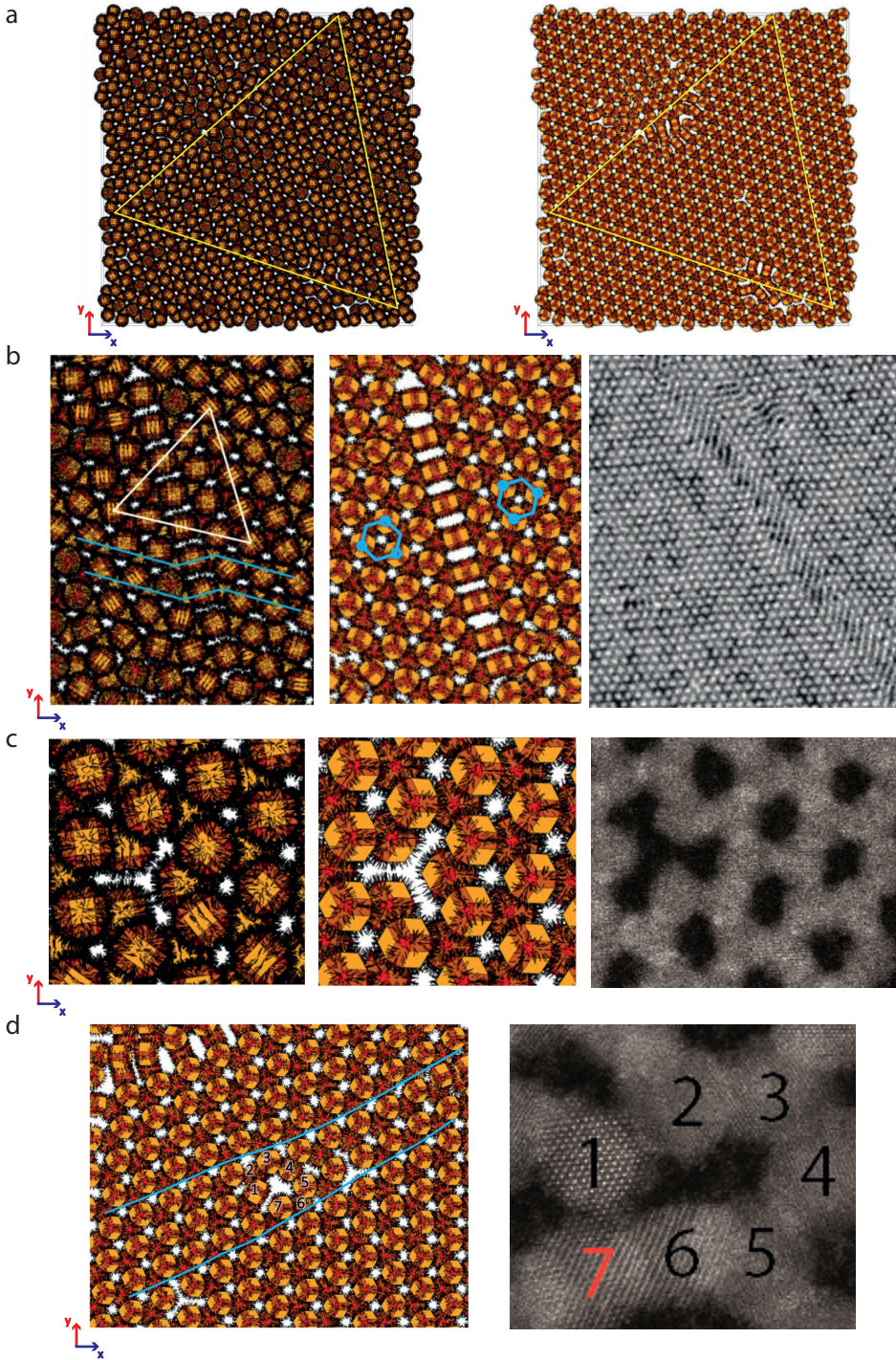


Figure S4.13 Overview of different defects in the silicene honeycomb structure observed both in simulations and experimentally formed samples. Note that linear areas (as observed in Figure 4.2, Figure 4.3 and Figure S4.10a) are not observed in simulations, as drying-effects presumably causing density differences (mono- and bilayer areas) were not taken into account. (a) Top view of the 2D structure formed after the first phase of simulation (left) and second phase of simulation (right). The triangle indicates the preservation of long range order in the silicene honeycomb superstructures, despite containing patches with both the $\{111\}$ and $\{100\}$ facets up. (b) As indicated by a triangle in the left image, the organization of the NCs is as a hexagonally packed bilayer, while the bottom is shifted half a unit cell as indicated with blue lines. As shown in the middle image this results in an inversion of the silicene honeycomb superstructure during phase two of the simulations, connected by a $\{110\}$ up zigzag pattern. The hexagons show how the structure is essentially inverted, or rotated 180° . This result is similar to the experimentally observed periodicity shift in the right image.⁵ (c) One NC is missing in the packing, which results in a vacancy in the silicene honeycomb superstructure, as observed in experimental results as well.⁵ (d) This simulation shows an extra row of NCs, causing a strained 7-ring. This ring is fully surrounded by one silicene honeycomb domain, which is another example of the flexibility of silicene honeycomb superstructures, since it smoothly fits in the extra row, as previously observed in experimental results as well.⁵

References

- [1] Steckel, J. S.; Coe-Sullivan, S.; Bulović, V.; Bawendi, M. G. 1.3 μ m to 1.55 μ m Tunable Electroluminescence from PbSe Quantum Dots Embedded within an Organic Device. *Adv. Mater.* **2003**, *15* (21), 1862-1866. DOI: 10.1002/adma.200305449.
- [2] Campos, M. P.; Hendricks, M. P.; Beecher, A. N.; Walravens, W.; Swain, R. A.; Cleveland, G. T.; Hens, Z.; Sfeir, M. Y.; Owen, J. S. A Library of Selenourea Precursors to PbSe Nanocrystals with Size Distributions near the Homogeneous Limit. *J. Am. Chem. Soc.* **2017**, *139* (6), 2296-2305. DOI: 10.1021/jacs.6b11021.
- [3] Hendricks, M. P.; Campos, M. P.; Cleveland, G. T.; Jen-La Plante, I.; Owen, J. S. A Tunable Library of Substituted Thiourea Precursors to Metal Sulfide Nanocrystals. *Science* **2015**, *348* (6240), 1226-1230. DOI: 10.1126/science.aaa2951.
- [4] Peters, J. L.; van den Bos, K. H. W.; Van Aert, S.; Goris, B.; Bals, S.; Vanmaekelbergh, D. Ligand-Induced Shape Transformation of PbSe Nanocrystals. *Chem. Mater.* **2017**, *29* (9), 4122-4128. DOI: 10.1021/acs.chemmater.7b01103.
- [5] Peters, J. L.; Altantzis, T.; Lobato, I.; Jazi, M. A.; van Overbeek, C.; Bals, S.; Vanmaekelbergh, D.; Sinai, S. B. Mono- and Multilayer Silicene-Type Honeycomb Lattices by Oriented Attachment of PbSe Nanocrystals: Synthesis, Structural Characterization, and Analysis of the Disorder. *Chem. Mater.* **2018**, *30* (14), 4831-4837. DOI: 10.1021/acs.chemmater.8b02178.
- [6] Moreels, I.; Lambert, K.; De Muynck, D.; Vanhaecke, F.; Poelman, D.; Martins, J. C.; Allan, G.; Hens, Z. Composition and Size-Dependent Extinction Coefficient of Colloidal PbSe Quantum Dots. *Chem. Mater.* **2007**, *19* (25), 6101-6106. DOI: 10.1021/cm071410q.
- [7] Hassinen, A.; Moreels, I.; De Nolf, K.; Smet, P. F.; Martins, J. C.; Hens, Z. Short-Chain Alcohols Strip X-Type Ligands and Quench the Luminescence of PbSe and CdSe Quantum Dots, Acetonitrile Does Not. *J. Am. Chem. Soc.* **2012**, *134* (51), 20705-20712. DOI: 10.1021/ja308861d.
- [8] Abelson, A.; Qian, C.; Salk, T.; Luan, Z.; Fu, K.; Zheng, J. G.; Wardini, J. L.; Law, M. Collective Topo-Epitaxy in the Self-Assembly of a 3D Quantum Dot Superlattice. *Nat. Mater.* **2020**, *19* (1), 49-55. DOI: 10.1038/s41563-019-0485-2.
- [9] Walravens, W.; De Roo, J.; Drijvers, E.; Ten Brinck, S.; Solano, E.; Dendooven, J.; Detavernier, C.; Infante, I.; Hens, Z. Chemically Triggered Formation of Two-Dimensional Epitaxial Quantum Dot Superlattices. *ACS Nano* **2016**, *10* (7), 6861-6870. DOI: 10.1021/acsnano.6b02562.
- [10] Anderson, N. C.; Hendricks, M. P.; Choi, J. J.; Owen, J. S. Ligand Exchange and the Stoichiometry of Metal Chalcogenide Nanocrystals: Spectroscopic Observation of Facile Metal-Carboxylate Displacement and Binding. *J. Am. Chem. Soc.* **2013**, *135* (49), 18536-18548. DOI: 10.1021/ja4086758.
- [11] Whitham, K.; Yang, J.; Savitzky, B. H.; Kourkoutis, L. F.; Wise, F.; Hanrath, T. Charge Transport and Localization in Atomically Coherent Quantum Dot Solids. *Nat. Mater.* **2016**, *15* (5), 557-563. DOI: 10.1038/nmat4576.
- [12] Slater, A. M. The IUPAC Aqueous and Non-Aqueous Experimental pK_a Data Repositories of Organic Acids and Bases. *J. Comput. Aided Mol. Des.* **2014**, *28* (10), 1031-1034. DOI: 10.1007/s10822-014-9764-9.
- [13] Woolley, E. M.; George, R. E. Ionization Constants for Water and for Very Weak Organic Acids in Aqueous Organic Mixtures. *J. Solution Chem.* **1974**, *3* (2), 119-126. DOI: 10.1007/Bf00646881.
- [14] Woolley. Ionization Constants for Very Weak Organic Acids in Aqueous Solution and Apparent Ionization Constants for Water in Aqueous Organic Mixtures. *J. Solution Chem.* **1972**, *1* (4), 341-351.
- [15] Serjeant, E. P.; Dempsey, B. *Ionisation Constants of Organic Acids in Aqueous Solution*; Pergamon Press, 1979.
- [16] Rabani, E.; Reichman, D. R.; Geissler, P. L.; Brus, L. E. Drying-Mediated Self-Assembly of Nanoparticles. *Nature* **2003**, *426* (6964), 271-274. DOI: 10.1038/nature02087.
- [17] Lee, W. C.; Kim, B. H.; Choi, S.; Takeuchi, S.; Park, J. Liquid Cell Electron Microscopy of Nanoparticle Self-Assembly Driven by Solvent Drying. *J. Phys. Chem. Lett.* **2017**, *8* (3), 647-654. DOI: 10.1021/acs.jpcllett.6b02859.
- [18] Klinger, M.; Jager, A. Crystallographic Tool Box (CrysTBox): Automated Tools for Transmission Electron Microscopists and Crystallographers. *J. Appl. Crystallogr.* **2015**, *48* (Pt 6), 2012-2018. DOI: 10.1107/S1600576715017252.
- [19] Soligno, G.; Vanmaekelbergh, D. Understanding the Formation of PbSe Honeycomb Superstructures by Dynamics Simulations. *Phys. Rev. X* **2019**, *9* (2), 021015. DOI: 10.1103/PhysRevX.9.021015.

CHAPTER 5

The Increasing Crystallinity in the Self-Templated Growth of Ultrathin PbS Nanosheets

Colloidal 2D semiconductor nanocrystals, the analogue of solid-state quantum wells, have attracted strong interest in material science and physics. Molar quantities of suspended quantum objects with spectrally pure absorption and emission can be synthesized. For the visible region, CdSe nanoplatelets with atomically precise thickness and tailorable emission have been (almost) perfected. For the near-infrared region, PbS nanosheets (NSs) hold strong promise, but the photoluminescence quantum yield is low and many questions on the crystallinity, atomic structure, intriguing rectangular shape, and formation mechanism remain to be answered. Here, we report on a detailed investigation of the PbS NSs prepared with a lead thiocyanate single source precursor. Atomically resolved HAADF-STEM imaging reveals the presence of defects and small cubic domains in the deformed orthorhombic PbS crystal lattice. Moreover, variations in thickness are observed in the NSs, but only in steps of 2 PbS monolayers. To study the reaction mechanism, a synthesis at a lower temperature allowed for the study of reaction intermediates. Specifically, we studied the evolution of pseudo-crystalline templates toward mature, crystalline PbS NSs. We propose a self-induced templating mechanism based on an oleylamine-lead-thiocyanate (OLAM-Pb-SCN) complex with two Pb-SCN units as a building block; the interactions between the long-chain ligands regulate the crystal structure and possibly the lateral dimensions.

Based on:

Maaïke M. van der Sluijs, Bastiaan B. V. Salzmänn, Daniel Arenas Esteban, Chen Li, Daen Jannis, Laura C. Brafine, Tim D. Laning, Joost W. C. Reinders, Natalie S. A. Hijmans, Jesper R. Moes, Johan Verbeeck, Sara Bals and Daniel Vanmaekelbergh, *Chemistry of Materials* **2023**, 35 (7), 2988-2998.

5.1 Introduction

Two-dimensional (2D) semiconducting nanocrystals (NCs) have opto-electronic properties differing from their zero- and one-dimensional counterparts. The two long lateral dimensions result in a dispersion relation between the kinetic electron energy and momentum while quantum confinement dominates in the thin vertical direction. Hence, these systems share characteristics with epitaxial quantum wells. Moreover, in some systems, such as CdX (X = Se, S or Te) nanoplatelets, the thickness is atomically defined and these show well-defined spectral features without inhomogeneous broadening.^{1,2} Colloidal synthesis can thus result in molar quantities of solution-processable quantum objects with spectrally pure and tunable optical transitions, which is of large interest in material science and physics.³⁻⁵

Synthesis procedures have been developed for a broad range of 2D NCs, varying from CdSe^{1,6} and ZnSe⁷ to In₂S₃,⁸ and PbSe,⁹⁻¹¹ mainly with optical transitions in the visible spectral region. Expansion of this field toward 2D systems with efficient near-infrared emission would be beneficial for technological applications such as tissue imaging and telecommunication devices.^{12,13} Recently, progress has been made in the preparation of 2D lead sulfide nanosheets (PbS NSs).¹⁴⁻²⁰ Intriguingly the PbS nanocrystals, naturally occurring with an isotropic cubic structure, emerge as rectangular sheets with a thickness of a few PbS units and lateral sizes in the 100 nm range. In contrast to CdSe nanoplatelets, control over the overall crystallinity, atomic structure, and electronic passivation of the top and bottom surface has not yet been achieved.²¹⁻²³ In contrast to truncated PbS cubes, which crystallize as cubic rock salt ($a = b = c$),²⁴⁻²⁶ these PbS sheets show a deformed orthorhombic crystal structure ($a \neq b \neq c$),^{17,19} a quasi-tetragonal unit cell with bonding angles slightly different from 90°. ²⁷ Here, this specific crystal structure will be indicated as “deformed orthorhombic”. The common cubic crystal structure of lead chalcogenides can show a similar transition to conventional orthorhombic at elevated pressures.^{28,29} The specific origin of the deviation from the cubic crystal structure to deformed orthorhombic is unknown, but it has been proposed that the strain exerted on the crystal structure by ligands at the surface induces a phase transformation.^{17,19,30} Recent density functional theory (DFT) calculations of the bulk band structure for these crystal structures show an indirect bandgap for the conventional orthorhombic crystal structure at 0.5 eV, whereas direct bandgaps are observed for cubic and deformed orthorhombic PbS (0.74 eV).²⁷ Thus, a small deformation in the crystal structure has a strong influence on the optical properties, such as the absorption and emission spectrum. Therefore, a thorough understanding of the PbS NSs crystal structure is required to understand the optical properties (or lack thereof).

Over the past few years, several synthesis methods have been reported for the preparation of PbS NSs. Early works have shown that oriented attachment and templated formation yield PbS NSs in which the 2D nanostructures are formed by the connection of small NCs.^{14,31} More recent synthesis routes have utilized single-source precursors, including lead xanthate and lead thiocyanate (Pb(SCN)₂).^{17,19} These precursors are advantageous for upscaling,³² as a metal salt decomposes in an organic solvent at elevated temperatures (>150 °C), providing both the lead and sulfur atoms for the synthesis while ligands stabilize the generated NCs in situ.

In this work, we apply atomically resolved high-angle annular dark-field scanning transmission electron microscopy (HAADF-STEM) and characterize the crystal structure and defects of the sheets in detail. The intriguingly rectangular sheets have low polydispersity both in shape and lateral dimensions, despite their extended size in the 100 nm range. High-resolution imaging reveals the presence of point defects as well as cubic and conventional orthorhombic domains

within the principal deformed orthorhombic crystal lattice. Moreover, we show that the sheets grow with a thickness that varies by 2 PbS units. By lowering the temperature of the synthesis, the slower reaction enables us to study the formation and evolution in the crystallinity of the intermediary reaction products by *ex situ* characterization. Initially, we observe rectangular pseudo-crystalline PbS templates, with a close to amorphous framework that gradually evolves into the deformed orthorhombic structure. We propose a mechanism for the formation of the PbS NSs in which an oleylamine-lead-thiocyanate (OLAM-Pb-SCN) complex, with edges that encompass 2 PbS units, is a key building block for NS formation. The surface stress exerted by the organized oleylamine capping layer is taken as responsible for the remarkable crystal structure (deformed orthorhombic) of the PbS sheets. Further analysis of the sheets grown at longer reaction times was performed with 4D STEM, a technique that scans the sample with a STEM probe in a rasterized manner and records the diffraction pattern (2D in reciprocal space) at each position on the sample (2D in real space). The dataset results in a map showing the major changes in the diffraction patterns throughout the image. Here, this analysis clearly shows a reduction in crystalline misorientations and thus an evolution toward greater crystalline homogeneity of the deformed orthorhombic PbS sheets.

5.2 Results

5.2.1 Atomically resolved HAADF-STEM imaging

PbS nanosheets (NSs) were synthesized by the decomposition of lead thiocyanate ($\text{Pb}(\text{SCN})_2$) with oleylamine (OLAM) and oleic acid (OA), in octadecene (ODE). A procedure previously published by Akkerman *et al.*,¹⁹ which results in PbS NSs with well-defined geometrical features (Figure S5.1a and Figure 5.1a), observed both in bright-field transmission electron microscopy (BF-TEM) and high-angle annular dark-field scanning transmission electron microscopy (HAADF-STEM). The sheets have a rectangular shape, straight edges, and sharp 90° corners with lateral dimensions of 142 ± 34 by 25 ± 3 nm (Figure S5.1b). Moreover, differences in contrast at lower magnification are observed within and between the NSs (Figure 5.1a, b and Figure S5.1c) most likely as a result of the remaining diffraction contrast or thickness differences (i.e., the number of Pb atoms in projection). With atomic resolution, the crystal structure can be studied directly (Figure 5.1c, Figure S5.2), also showing contrast differences within a single sheet.

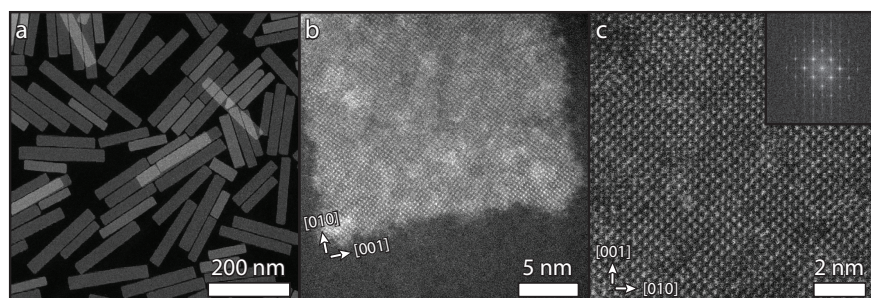


Figure 5.1 Electron microscopy images of PbS NSs prepared at 165 °C. Low-resolution HAADF-STEM images show the rectangular NSs with sharp 90° corners (a). High-resolution HAADF-STEM images show the serrated edges of the NSs (b) and a deformed orthorhombic PbS structure with dumbbell atom columns in the [100] direction (c). The inset shows the corresponding Fourier transform.

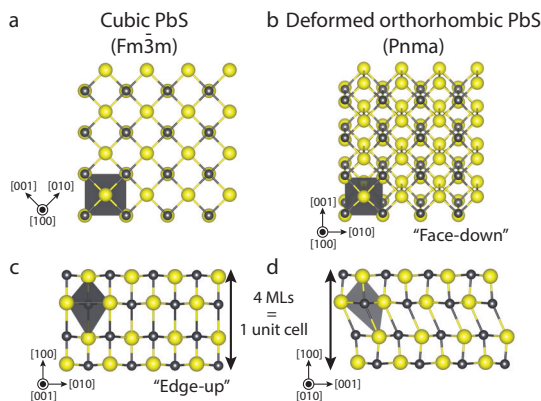


Figure 5.2 Schematic depictions of the cubic ($a = b = c$) and deformed orthorhombic PbS crystal lattices ($a \neq b \neq c$). The lead and sulfur atoms are represented respectively by the gray and yellow spheres. In panels (a) and (b), the face-down orientation ([100] in zone axis) of both crystal structures is shown. In panels (c) and (d), the edge-up orientation on the long ([001] in panel (c)) and short edge ([010] in panel (d)) of the deformed orthorhombic NSs is shown for 4 MLs, one deformed orthorhombic unit cell. The gray octahedra clearly show that deformation occurs only in the [010] direction (d). See Figure S5.3 for a comparison with the cubic unit cell that consists of only 2 MLs as well as a table comparing the unit cells of the various crystal structures.

For bulk PbS and PbS nanomaterials, the isotropic cubic PbS crystal structure is common (Figure 5.2a).²⁷ However, both bulk and nanomaterials have been shown to deform from cubic to anisotropic conventional orthorhombic PbS under external high pressure conditions.^{28,29,33,34} Previously, the crystal structure of the PbS NSs was assigned by fitting the powder X-ray diffraction (XRD) patterns. It was determined to be a “layered (SnS like) orthorhombic phase” with a quasi-tetragonal unit cell ($a = 11.90 \text{ \AA}$, $b = 4.22 \text{ \AA}$, $c = 4.20 \text{ \AA}$),¹⁹ which shows dumbbell-shaped atom columns in the [100] direction (Figure 5.2b). This is a less pronounced deformation than the conventional orthorhombic PbS structure ($a = 11.28 \text{ \AA}$, $b = 4.02 \text{ \AA}$, $c = 4.29 \text{ \AA}$),²⁷ but with bond angles deviating from 90° . Here, we refer to the crystal structure of the NSs as “deformed orthorhombic”, as even the slight shift between the monolayers (MLs) of the unit cell induces the characteristic atomic configuration. In the face-down orientation of the NSs (Figure 5.1c and 2b), the [100] direction is in zone axis, clearly displaying the dumbbell atom columns. Meanwhile, the long edge of the NSs is along the [010] axis of the deformed orthorhombic structure, whereas the [001] axis forms the short edge (Figure 5.2c, d and 5.3a).

To image the atomic structure of the sheets along the planar direction and study their thickness, an antisolvent (MeOH/ BuOH in a 1:2 ratio) was added to the dispersion before further sample preparation, inducing face-to-face stacking of the NSs.³⁵ With the HAADF-STEM viewing direction parallel to the sheet surface, the [001] direction is in the zone axis (Figure 5.2c) and the atomic columns in the edge-up orientation can be clearly observed (Figure 5.3a). Previously, the PbS NSs were reported to be $1.2 \pm 0.3 \text{ nm}$ thick, corresponding to 1 deformed orthorhombic unit cell of 4 MLs.¹⁹ Here, we observe NSs with a thickness of 4 MLs ($1.2 \pm 0.1 \text{ nm}$) but also a second equally significant population of 6 ML NSs (Figure 5.3b). These have a thickness of $1.8 \pm 0.1 \text{ nm}$, similar to the conventional orthorhombic NSs previously reported by Khan et al.¹⁷ Direct observation of these two populations suggests that the contrast differences

between the NSs along the face-down orientation (**Figure 5.1a**), can be attributed to the 2 MLs (0.6 nm) difference in thickness. Addition of the antisolvent decreases the NS-to-NS distance (0.8 ± 0.3 nm instead of 3.6 ± 0.3 nm,¹⁹ or 4.4 nm,³⁶). At some points, the NSs even merge or grow together, indicating a lack of surface passivation (see the blue arrow in **Figure 5.3a** and **supporting information S5.2** for an NMR and FTIR analysis of the surface passivation of the sheets).

The stepwise increase in thickness of the sheets is reminiscent of the atomic control in the thickness of zinc blende CdSe nanoplatelets. There, the top and bottom facets are terminated by Cd ligands, resulting in effective passivation and non-stoichiometry in the platelets.^{37,38} The opto-electronic properties are determined by the thickness of the NCs as the lateral dimensions are significantly larger than the exciton Bohr radius of 5.6 nm.^{1,39} This resulted in a stepwise atomic control of both the absorption and emission transitions.^{6,38} As the PbS NSs show a stepwise increase with half a unit cell (2 MLs), termination of the top and bottom facets is conventional, without an additional layer of lead. However, with an exciton Bohr radius of 23.5 nm for PbS,⁴⁰ we expect a strong 2D confinement and qualitatively a similar relation between the thickness and the optical properties of PbS NSs (albeit with steps of 2 MLs) as observed for CdSe nanoplatelets.

The absorption spectrum of a PbS NSs dispersion with 4 and 6 MLs sheets in a 1:1 ratio lacks clear features due to scattering (**Figure S5.7**). Only the previously reported onset (usually ~ 1.6 eV) is observed.¹⁹ By second-derivative analysis,⁴¹ the spectrum resolves to a single transition at 1.77 eV. Very similar to what the previously published absorption spectrum resolves to which is a single transition at 1.81 eV.¹⁹ Thus, we attribute the 1.77 eV transition to the 4 MLs sheets. As the reaction time increases (see below), the transition shifts to 1.64 eV (**Figure S5.7**), which we attribute to the contribution of the NSs with 6 MLs to the absorption spectrum.

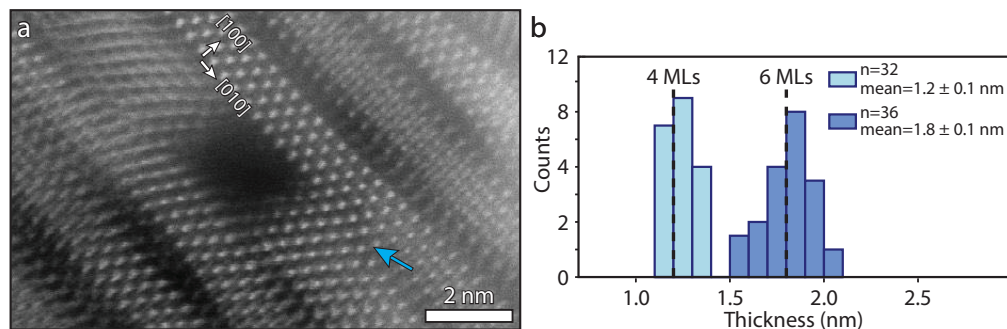


Figure 5.3 In the edge-up orientation ($[001]$ in zone axis), the thickness of the PbS NSs can be studied with atomic precision, taking into account that some of the sheets are tilted. (a) A high-resolution HAADF-STEM image shows there are both sheets with a thickness of 4 and 6 MLs of PbS. No sheets with an intermediate thickness (3, 5, or 7 MLs) were observed. Some of the NSs merge together (blue arrow), indicating a lack of surface passivation (further discussed in supporting information S5.2). (b) The corresponding histogram indicates the 1:1 ratio of NSs with an average thickness of 1.2 (4 MLs) and 1.8 nm (6 MLs).

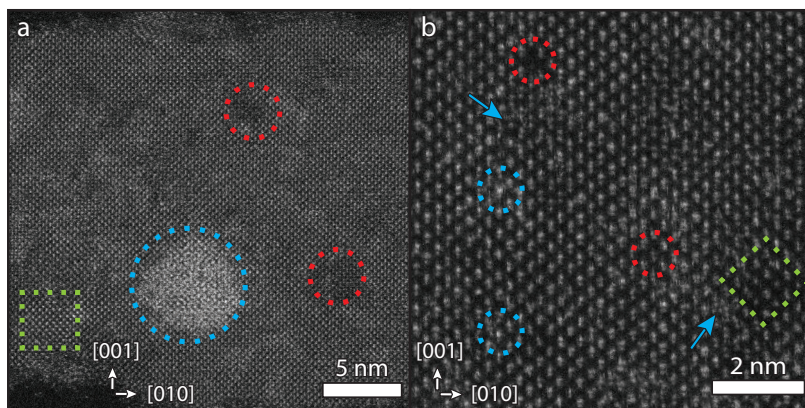


Figure 5.4 Atomically resolved HAADF-STEM images of PbS NSs, with the various irregularities in the sheets indicated by the red, blue, and green dashed outlines. (a) PbS sheet with an additional lead-rich region (blue dashed circle) and areas with a lower contrast, potentially due to a lead deficiency (red dashed circles). (b) At higher magnification, point defects (red and blue circles) and some irregularities within the structure (blue arrows) are observed. In both panels (a) and (b), a coherently incorporated small domain with a lower contrast is observed (green dashed square).

Having confirmed the presence of two thickness populations in the ensemble of PbS NSs, we studied the [100] direction of the NSs with atomic resolution. Within the deformed orthorhombic NSs, the high-contrast area (blue circle) in **Figure 5.4a** can be assigned to a lead-rich cluster (~ 5 nm) attached to the top or bottom facet of the NS. Occasionally, these clusters were observed free standing in the sample as well (**Figure S5.8**). The low contrast regions (red circle) could be attributed to a collection of lead deficiencies in the crystal structure, possibly due to incomplete growth of the NS or a defect in the crystal structure, which could either be a different crystal structure or an amorphous area. Within the atom columns, similar low and high contrast is observed as well, as indicated in **Figure 5.4b**. The blue arrows indicate the presence of some point-like irregularities in the structure.

In addition to the defects, the NSs also show several domains that are coherently incorporated in the deformed orthorhombic lattice but have a different crystal structure (indicated by the dashed green squares in **Figure 5.4**). The characterization of these small domains (1 to 4 unit cells) is not trivial. **Figure 5.5** clearly shows two small domains with a different structure than the deformed orthorhombic structure. In real space, a common feature among these domains is their lower contrast with respect to the dominant crystal structure, mainly due to the absence of the characteristic dumbbell atom columns (**Figure 5.5a**). The corresponding Fourier transform patterns can be indexed according to the conventional orthorhombic (90° angles with 4.0 Å lattice spacing along the [010] zone axis) or the cubic crystal structure (with 3.0 Å lattice spacing along the [100] zone axis, **Figure 5.5b**). We hypothesize that these defects in the NSs contribute to the reported lack of photoluminescent properties.^{19,27}

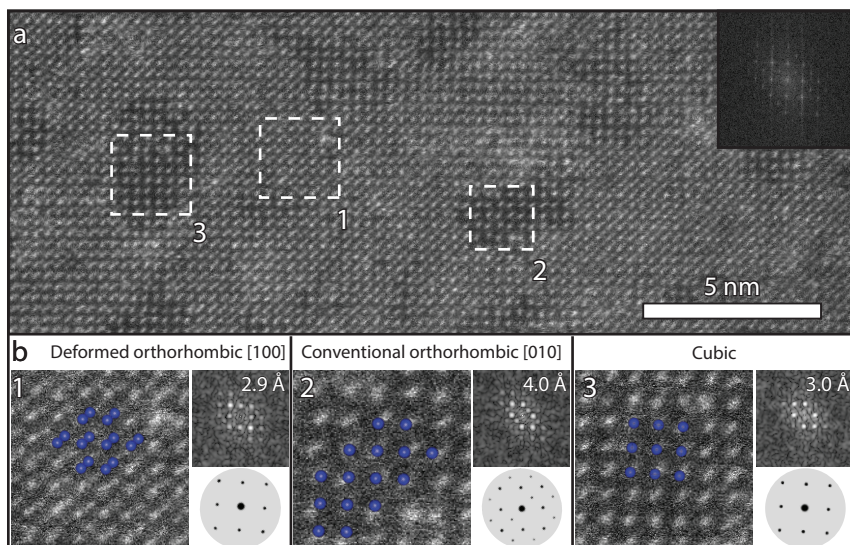


Figure 5.5 Three areas within the deformed orthorhombic PbS NS are indicated by the white dashed boxes (a), which are characterized in panel (b). The corresponding Fourier transform of domain 1 has a lattice spacing of 2.9 Å and is indexed according to the deformed orthorhombic crystal structure. Domains 2 and 3 are coherently incorporated in the principal structure, but their low-diffraction contrast and corresponding Fourier transform are different. Domain 2 is indexed as a conventional orthorhombic crystal structure with a lattice spacing of 4.0 Å along the [010] zone axis. Domain 3 is indexed as a cubic crystal structure with a spacing of 3.0 Å along the [100] axis.

5.2.2 Evolution of the Crystallinity of Nanosheets in Time

The deformed orthorhombic crystal structure of the PbS NSs has various crystal defects seamlessly incorporated, while sheets of both 4 and 6 MLs thick were observed in a 1:1 ratio. To understand both the origin of the deformed orthorhombic structure and the stepwise thickness increase by 2 MLs of the NSs, we studied the reaction in more detail. For colloidal 2D nanocrystals, the often suggested reaction mechanism is soft templated growth; the long organic ligands that are present are supposed to form close-packed lamellar mesophases, which could guide 2D growth.^{5,31,42-46}

Relatively few studies have unambiguously shown the in situ presence of such soft templates during the growth of 2D nanostructures.^{31,47} An exception is PbS NSs synthesized with lead acetate, octylamine, and oleic acid, where the existence of a lamellar mesophase before nanocrystal formation was shown with low-angle XRD measurements in combination with TEM images.³¹ Another exception is the synthesis of Cu_{2-x}S NSs, where templates observed in TEM images were tentatively described as Cu-thiolate frameworks, that maintain their 2D structural integrity at high temperatures when stabilized by halides.⁴⁷ During the reaction, these templates gradually disappear due to Cu-catalyzed thermolysis of the carbon/sulfur bond, resulting in the formation of the NSs. For the PbS NSs studied here, it was previously proposed that a lead-oleate-thiocyanate complex forms at 110 °C, which decomposes quickly at higher temperatures yielding the PbS NSs. Even with no direct proof for the presence of templates, a similarity was drawn to the templated formation of Cu_{2-x}S NSs.^{19,47} Here, the standard PbS

NS synthesis is very fast, effectively occurring while the mixture heats up to 165 °C. However, with a lower temperature (145 °C), the reaction occurs slower. This allowed us to take aliquots and isolate intermediary reaction products to study them ex situ and gain insight into the mechanism.

Upon reaching 145 °C, the reaction mixture is still transparent but after 1 minute (min) and 30 seconds (s), the color changes to light brown and the first aliquot was taken. Despite the color change, no NCs were isolated (Figure S5.9a), but all subsequent aliquots showed rectangular NSs with 90° corners (Figure S5.9). Initially, these NSs have an average size of 161 by 18 nm (Figure 5.6a, Figure S5.9b and S5.10a), slightly longer and thinner than the standard synthesis at 165 °C (142 by 25 nm). In time (6.5 min), the NSs grow to 293 by 38 nm with some serrated edges (Figure 5.6c, Figure S5.9d and S5.10b).

At higher magnification (Figure 5.6b), the earliest isolated PbS NSs are markedly different than the standard synthesis products at 165 °C. Instead of a crystalline structure, the sheets have an amorphous and disordered framework interspersed with crystalline areas. These domains exhibit a wide range of sizes but average $25 \pm 17 \text{ nm}^2$ (Figure S5.11), and whereas some have the deformed orthorhombic structure with the characteristic dumbbells, they primarily have one of the previously discussed defect structures.

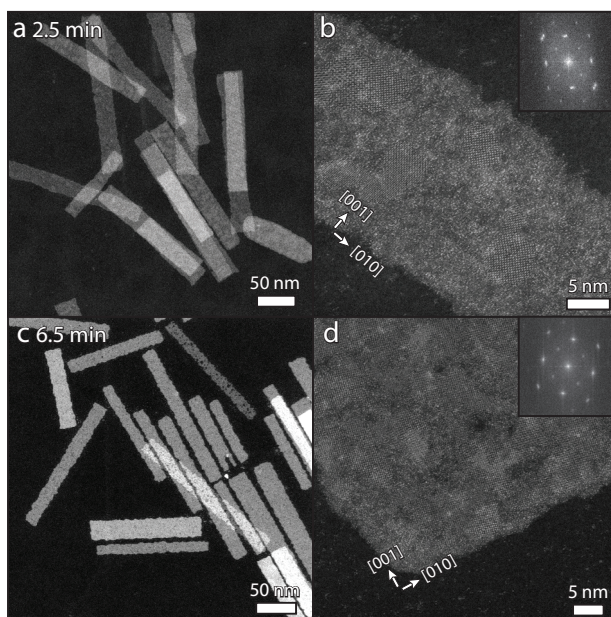


Figure 5.6 HAADF-STEM images of aliquots taken 2.5 and 6.5 min after the reaction mixture reaches 145 °C, see Figure S5.9 for the other aliquots. (a) Rectangular NSs with a lateral size of 160 ± 27 by 18 ± 3 nm are already present. The image with atomic resolution in panel (b) shows that the sheets are pseudo-crystalline, roughly 23% of the sheet is crystalline (on average the domain size is $25 \pm 17 \text{ nm}^2$, Figure S5.11). The Fourier transform of the sheet shows clear diffraction maxima but has some broadening in the long lateral direction. (c) After an additional 4 min, the NSs grow to an average size of 293 ± 79 by 38 ± 8 nm, while the crystallinity was estimated to be approximately 67% of the area with limited residual amorphous strips, as determined through direct visualization of the image (d).

Surprisingly, the Fourier transform of the sheet shows diffraction maxima, with only some broadening in the long lateral direction (inset **Figure 5.6b**). Thus, despite the amorphous framework between them, the domains have a common orientation within the sheet. The individual deformed orthorhombic areas are oriented with the [010] axis in the long lateral direction of the NS (equivalent to the [01 $\bar{1}$] direction for cubic PbS), just like the NSs from the standard synthesis. Even when the NSs are broken, i.e., not well defined and less rectangular, the domains are oriented (see Fourier transform inset in **Figure S5.12**). When stacked, both 4 and 6 MLs are observed in a 2:1 ratio, although these sheets are more crystalline than expected from **Figure 5.6b** (see **Figures S5.13–S5.15** for a further discussion). When the NSs are kept at 145 °C for an additional 4 min, their overall crystallinity increases, and only thin amorphous strips remain (**Figure 5.6d**). In absorption measurements, the optical transition gradually shifts from 1.77 eV early in the reaction (2.5 min) to 1.64 eV (**Figure S5.16a**), indicating that also the fraction of 6 ML NSs increases over time.

5.2.3 Proposed mechanism for the growth of the PbS nanosheets

The surprisingly rectangular NSs early in the reaction, with little crystallinity but a uniform orientation of the crystalline domains with [010] in the long lateral dimension, are an indication for a (soft) templating mechanism. Intensity profiles along the short lateral direction of this “pseudo-crystalline” NS show no significant intensity difference between the amorphous and crystalline areas (**Figure S5.17**), suggesting a uniform thickness throughout the sheet, albeit with ordered and disordered parts. The alignment of the isolated crystalline areas and the overall increase in crystallinity of the NSs as the reaction progresses means that the initial disordered amorphous areas are arranged along the main crystallographic axes, without atomic order in the unit cells. As such, a templating mechanism as previously proposed, where the template only guides the synthesis before it disappears, does not fit with our observations.⁴⁷ While the long chain primary amine and oleate ligands are the usual suspects for templates, the single source precursor Pb(SCN)₂ contains the thiocyanate ion (SCN⁻), an ambidentate ligand. Hence, the pseudo-crystalline template, which crystallizes and forms the sheet, can only form with the involvement of the single source precursor.⁵² Here, we propose a self-induced template that imposes a 2D constraint during the reaction but is also part of the eventually formed NSs.

As it is ambidentate, the thiocyanate ion can form coordinating bonds with a metal ion (M) via sulfur (S) or nitrogen (N) via their unshared electrons. N-bonding is favored when a borderline or hard acid is present whereas a soft acid will induce S-bonding, resulting in M-NCS or M-SCN complexes, respectively. In the case of a borderline acid (such as Cd²⁺ and Pb²⁺), both complexes can be formed and the electronic and steric factors of other ligands bound to the metal center become very influential.^{48–50} Here, OA and OLAM are present during the decomposition of Pb(SCN)₂ and as both ligands can coordinate with lead, the electron density on the lead atom can vary. In a complex with OA (an X-type electron donating/accepting ligand),^{51,52} the electron density on the lead ion is lower, resulting in an OA-Pb-NCS complex. However, in a complex with OLAM (an L-type electron donating ligand),⁵³ the lead ion will have an increased electron density, and an OLAM-Pb-SCN complex can form.⁵⁰

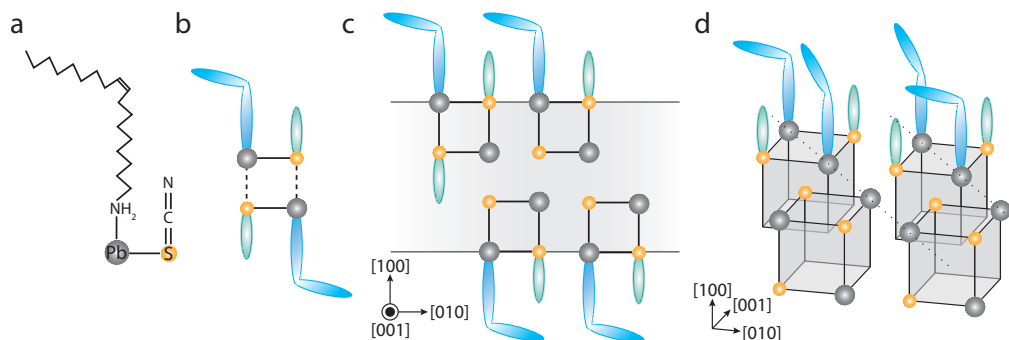


Figure 5.7 Schematic formation of PbS NS via a self-induced templating mechanism. Starting with an OLAM-Pb-SCN complex with a 90° angle between the Pb/S and C/S bonds (a). By cross-coordination, two OLAM-Pb-SCN complexes can form a square, the central building block of the self-templating mechanism (b). Two-dimensional formation of the pseudo-crystalline structure as observed in the edge-up orientation of the PbS NS (c). Growth of the NSs along the lateral directions via cubes (four cross-coordinated OLAM-Pb-SCN complexes) with diagonal alignment of the favorable ligand–ligand interaction resulting in the $[01\bar{1}]$ orientation of the lead atoms (d).

Previously, the presence of excess ligands during the reaction was shown to result in polydisperse NSs or cubic nanocubes.¹⁹ However, with an equivalent amount of only OA, no discernible nanocrystals are formed (**Figure S5.18a**), while with only OLAM 2D structures and some cubes form (**Figure S5.18b**). This indicates the importance of an amine in this reaction. Additional experiments with a shorter acid and amine ligand (nonanoic acid and octylamine, **Figure S5.19**) showed that the variation in the width of the NSs increases significantly with octylamine. Instead of the usual 25–35 nm width (also achieved with nonanoic acid **Figure S5.19c**), the resulting NSs had an average of 130 nm with standard deviation of 60 nm (**Figure S5.19d**). Thus, a shorter amine ligand allows more freedom in the formation of the sheets, whereas shorter acidic ligands still result in NSs with a similar constraint in width.

Hence, we propose that an OLAM-Pb-SCN complex is the precursor to the central building block for a self-induced template resulting in PbS NSs. An amine group bound to the lead ion will induce S site bonding of the thiocyanate, already placing the lead and sulfur in proximity (**Figure 5.7a**). In this complex, the angle between the lead/sulfur (Pb/S) bond and the carbon/sulfur (C/S) double bond is expected to be around 90° , previously shown to be the case for both cadmium-SCN and zinc-SCN complexes.⁵⁰ The angled complex allows ample space for coordination with another complex, resulting in a building block with 2 Pb–S units (**Figure 5.7b**), in line with the 2 ML stepwise increase in the NSs thickness (**Figure 5.3**). As no NSs consisting of 2 MLs were observed in the experiments, we consider these building blocks too unstable to form NSs with an ionic lattice. However, as they interact with other building blocks, a system with 4 Pb–S units begins to form. Depending on the bond strength of the ligands, and the C/S double bond, cross-correlation begins, eventually forming the basis for the ionic lattice of the NSs (**Figure 5.7c**). The pseudo-crystalline NSs in **Figure 5.6b** can be described by this part of the mechanism. Favorable ligand–ligand interaction occurs as the building blocks are roughly organized with an $[01\bar{1}]$ orientation of the lead atoms, corresponding to an $[010]$ orientation of the deformed orthorhombic structure. However, the building blocks are not yet fully crystal-

lized, i.e., the C/S double bond has not yet broken and the PbS lattice not yet formed in the entire template. In this mixed system, containing both pseudo-crystalline and crystalline parts, the strain induced by the strong ligand–ligand interaction can still be distributed throughout the entire system. It does not yet affect the smaller predominantly cubic crystalline areas. Upon continued thermal annealing, the bonds in the building blocks break and the ionic lattice forms (Figure 5.7d). The favorable diagonal long-range organization of the ligands increases, resulting in an increased surface tension that can no longer be accommodated in the ultrathin PbS sheets, thus inducing the cubic to deformed orthorhombic transition of the crystalline domains.

The mechanism described above is a self-induced templating mechanism in which the basic building blocks already favorably interact with each other, helped along by their templating long-chain organic ligands. Upon further annealing, the bonds in the building block break resulting in the formation of the ionic PbS lattice.

5.2.4 Improving the crystallinity of the nanosheets

With the crystalline structure of the NSs and its defects characterized, the thickness of the NSs studied and our understanding of the mechanism increased, we set out to improve the NSs. As previously discussed, the sheets have not yet shown any photoluminescence, not even after chloride surface treatments,¹⁹ presumably due to the intrinsic defects in the sheets synthesized by the standard synthesis, a fast decomposition reaction that is quenched when reaching 165 °C. By prolonging the reaction at 165 °C for 5, or even 10 min, we effectively annealed the NSs to improve their crystallinity.

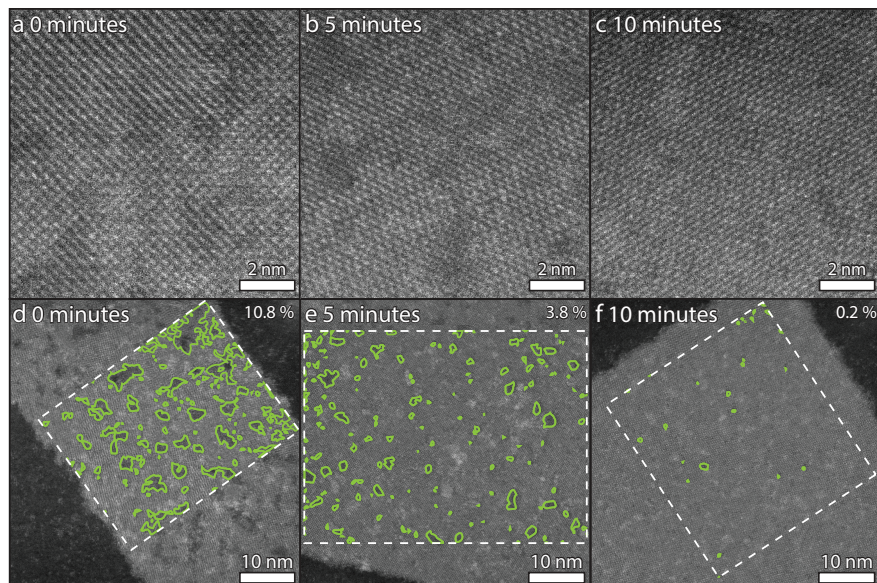


Figure 5.8 When annealing the NSs at 165 °C for an additional 5 or 10 min, the uniformity of the deformed orthorhombic crystal structure increases (a–c). With intensity threshold analysis applied to the low-contrast defect areas in the NSs (indicated by a green outline), a quantitative estimation on the improvement can be made. The defect areas decrease from 10.8% to 3.8% and then 0.2% (c–e).

Figure 5.8b shows an HAADF-STEM image of a PbS NS annealed for 5 min at 165 °C, still clearly with the dumbbells of the [100] direction of the deformed orthorhombic crystal structure and some low-contrast areas. Based upon their Fourier transform, these areas are characterized as different crystal structures such as cubic and conventional orthorhombic (**Figure S5.20**). Although the crystal structure becomes more uniform after an additional 5 min (**Figure 5.8c**), there are still some defects present (**Figure S5.20b**). At the same time, the previously observed 1:1 ratio of 4 and 6 MLs thick NSs (**Figure 5.3b**) shifts firmly to 6 MLs (**Figure S5.21**). In adsorption spectra of the dispersion, the scattering increases while the transition becomes more pronounced. The second-derivative analysis shows a transition at 1.64 eV, indicating that the NSs predominantly have a thickness of 6 MLs (**Figure S5.22a**). When the absorbance of a PbS NSs film was measured (**Figure S5.22b**), the absorbance increased from ~10% to ~40%, indicating an increase in the overall concentration of fully crystalline NSs.

Considering that the dumbbell atom columns of the deformed orthorhombic structure give the NSs higher intensity at low magnification with respect to the defect areas, we can apply intensity threshold image analysis. This allows for the tentative estimation of the defect percentage in the sheets. Synthesized by the standard procedure, they show up to 10.8% defect areas in a 25 by 35 nm area, as indicated by the green outlines in **Figure 5.8d**. As the NSs are annealed at 165 °C for 5 or 10 min, the defect percentage decreases to 3.8 and 0.2%, respectively (**Figure 5.8e** and **f**).

While an indication that the areas with a lower diffraction contrast are quite common, a technique such as 4D STEM can be of tremendous help in visualizing homogeneity of the crystal orientations in the sheets. With a STEM electron probe, the sample is scanned in a rasterized manner and at each position a diffraction pattern is acquired. The result has been interpreted as an HAADF-STEM image (2D in real space) where the pixel size is determined by the probe size and where the diffraction pattern of each pixel is known (2D in reciprocal space, **Figure S5.23**). 4D STEM was utilized to map changes in the reciprocal space of the sheets, effectively displaying the enhancement in crystal orientation as synthesis time increases.

When characterizing each pixel in the HAADF-STEM image based upon the intensity of the {011} family planes in the diffraction pattern (at a lattice spacing of 0.29 nm), the changes in orientation of the crystal structure can be tracked. **Figure 5.9** displays the color maps generated by assigning red or green to the intensities of diffraction maxima on perpendicular distances. When the structure is imaged along the zone axis (**Figure 5.9a**, middle image) the map appears dark yellow, as the red and green spots contribute equally to the overall intensity. If the structure is tilted along a certain direction, one of the intensities will decrease, resulting in a red or green color (**Figure 5.9a**, left and right). The corresponding maps in **Figure 5.9b–d** show the folded areas in the NSs. The NSs immediately quenched upon reaching 165 °C (**Figure 5.9b**) show some voids in the maps, some of which are also observed in the HAADF-STEM image. Otherwise, they correspond either to a possible dealignment with the main crystal structure or the presence of the small domains discussed above with different crystal structures. Initially, the thinner NSs have large folds where the structure is tilted in one direction, right next to areas tilted in the other direction, i.e., green right next to red areas (**Figure 5.9b**). However, as the NSs are effectively annealed for longer times, the folds become less prominent; hence, as the NSs become thicker (6 MLs), they also become more rigid (**Figure 5.9c** and **d**) and their crystal structure improves.

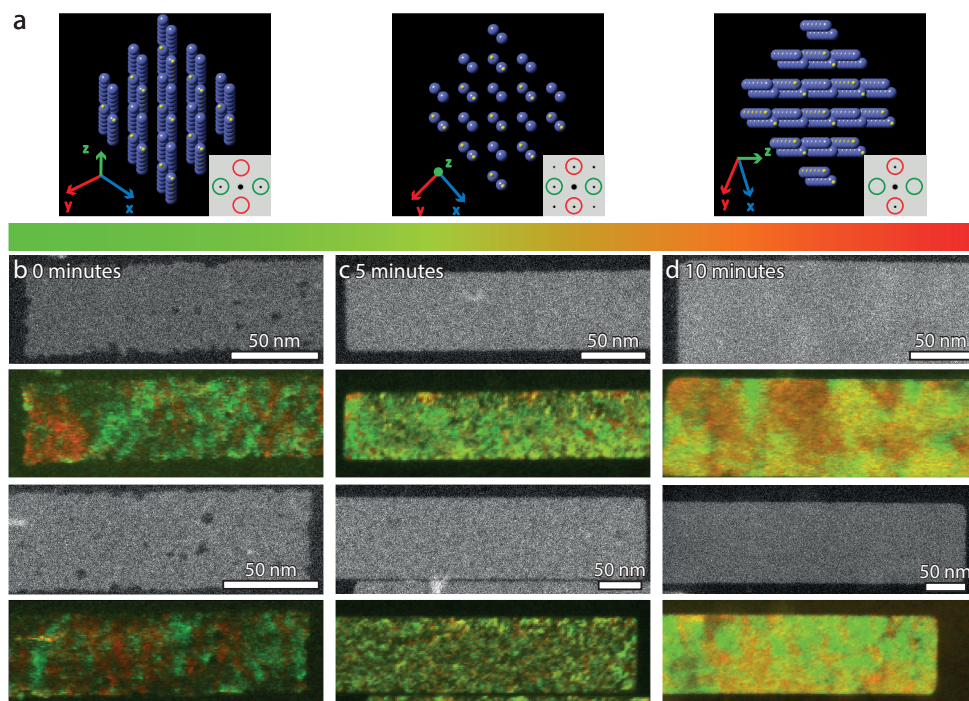


Figure 5.9 With 4D STEM the changes in orientation of crystal structure can be tracked in the PbS NSs. (a) The deformed orthorhombic crystal structure is schematically depicted as it tilts in the short (left) and long (right) lateral direction of the sheet. With the [100] direction in zone axis, the diffraction pattern shows 4 spots with a lattice spacing of 0.29 nm contributing equally (middle image inset, yellow color). As the structure tilts, the contribution of the diffraction maxima changes and each pixel in the 4D STEM image was characterized based on the contribution of the diffraction maxima, green for a tilt in the short lateral direction and red for the long lateral direction. The HAADF-STEM image, and its reconstructed 4D STEM map are shown for 0 min (b), 5 min (c), and 10 min (d) at 165 °C. In panel (b) NSs immediately quenched upon reaching 165 °C have some voids in the HAADF-STEM image, while the maps also show large regions with different parallel orientations in the NSs. A significant improvement in the tilt toward zone axis can be observed in panel (b) and even more in panel (c) where large homogeneous areas of dark yellow can be observed.

5.3 Conclusions

In summary, atomically resolved HAADF-STEM imaging was used to characterize the deformed orthorhombic PbS NSs, both during their formation and as final products. The 2D ultrathin sheets allowed for observation of contrast differences within and between the sheets. When stacked, two populations of 4 and 6 MLs were observed in a 1:1 ratio (1.2 and 1.8 nm). In absorption spectra, strong light scattering obscures the optical transitions, but analysis with the second-derivative elucidates an optical transition at 1.77 eV for 4 MLs and 1.64 eV for 6 MLs thick NSs. This is far above the gap of PbS bulk and quantum dots with a cubic crystal structure. With atomic resolution, the subtly incorporated low-contrast crystal defects stand out; by Fourier analysis, these specific areas could be characterized as cubic or conventional orthorhombic areas.

By studying the intermediary products of the reaction at a lower temperature (145 °C), we gained insight into the reaction mechanism. Initially, a pseudo-crystalline rectangular template is formed, consisting of amorphous and crystalline areas, which are uniformly oriented with the [010] axis in the long lateral dimension. We propose that these PbS NSs form via a self-induced templating mechanism, in which the single source precursor $\text{Pb}(\text{SCN})_2$ plays a key part. We suspect that an OLAM-Pb-SCN complex initiates the 2D formation of the self-induced template. Favorable ligand–ligand interaction of the complexes induces the [010] orientation, even before the formation of an ionic lattice in these pseudo-crystalline templates. The surface strain induced by the long OLAM ligands on the ionic lattice induces the deformed orthorhombic crystal structure when the crystallinity in the sheet increases. Only some additional thermal annealing is needed to form a deformed orthorhombic PbS lattice from the pseudo-crystalline template.

A further reduction of the number of intrinsic crystal defects, edge imperfections, and lead-rich clusters will be required to eliminate the non-radiative recombination channels in the NSs. To improve the crystallinity of the sheets, continued reaction at high temperature (5 or 10 min at 165 °C) proved to be quite effective. The number of crystal defects in the sheets decreases significantly, resulting in almost perfect deformed orthorhombic PbS NSs predominantly with a 6 MLs thickness. The 4D STEM technique effectively demonstrates a reduction in both occurrence and severity of crystal misorientations in the sheets over the course of annealing and therefore an increased crystallinity over synthesis time. Obtaining PbS sheets with a respectable opto-electronic performance will be a challenge since the radiative life-times in the near-infrared are relatively large compared to the visible region. However, it will be worth the effort as the deformed orthorhombic crystal structure, the related uncommon electronic band structure, and the two-dimensionality offer a pathway to novel 2D semiconductors with a bandgap in the interesting energy region just below the visible.

References

- [1] Ithurria, S.; Tessier, M. D.; Mahler, B.; Lobo, R. P.; Dubertret, B.; Efron, A. L. Colloidal Nanoplatelets with Two-Dimensional Electronic Structure. *Nat. Mater.* **2011**, *10* (12), 936-941. DOI: 10.1038/nmat3145.
- [2] Joo, J.; Son, J. S.; Kwon, S. G.; Yu, J. H.; Hyeon, T. Low-Temperature Solution-Phase Synthesis of Quantum Well Structured CdSe Nanoribbons. *J. Am. Chem. Soc.* **2006**, *128* (17), 5632-5633. DOI: 10.1021/ja0601686.
- [3] Kagan, C. R.; Bassett, L. C.; Murray, C. B.; Thompson, S. M. Colloidal Quantum Dots as Platforms for Quantum Information Science. *Chem. Rev.* **2021**, *121* (5), 3186-3233. DOI: 10.1021/acs.chemrev.0c00831.
- [4] Bai, B.; Zhang, C.; Dou, Y.; Kong, L.; Wang, L.; Wang, S.; Li, J.; Zhou, Y.; Liu, B.; et al. Atomically Flat Semiconductor Nanoplatelets for Light-Emitting Applications. *Chem. Soc. Rev.* **2023**, *52* (1), 318-360. DOI: 10.1039/d2cs00130f.
- [5] Diroll, B. T.; Guzelturk, B.; Po, H.; Dabard, C.; Fu, N.; Makke, L.; Lhuillier, E.; Ithurria, S. 2D II-VI Semiconductor Nanoplatelets: From Material Synthesis to Optoelectronic Integration. *Chem. Rev.* **2023**, *123* (7), 3543-3624. DOI: 10.1021/acs.chemrev.2c00436.
- [6] Ithurria, S.; Dubertret, B. Quasi 2D Colloidal CdSe Platelets with Thicknesses Controlled at the Atomic Level. *J. Am. Chem. Soc.* **2008**, *130* (49), 16504-16505. DOI: 10.1021/ja807724e.
- [7] Cunningham, P. D.; Coropceanu, I.; Mulloy, K.; Cho, W.; Talpin, D. V. Quantized Reaction Pathways for Solution Synthesis of Colloidal ZnSe Nanostructures: A Connection Between Clusters, Nanowires, and Two-Dimensional Nanoplatelets. *ACS Nano* **2020**, *14* (4), 3847-3857. DOI: 10.1021/acsnano.9b09051.
- [8] Park, K. H.; Jang, K.; Son, S. U. Synthesis, Optical Properties, and Self-Assembly of Ultrathin Hexagonal In₂S₃ Nanoplates. *Angew. Chem.* **2006**, *118* (28), 4724-4728. DOI: 10.1002/ange.200601031.
- [9] Koh, W. K.; Dandu, N. K.; Fidler, A. F.; Klimov, V. I.; Pietryga, J. M.; Kilina, S. V. Thickness-Controlled Quasi-Two-Dimensional Colloidal PbSe Nanoplatelets. *J. Am. Chem. Soc.* **2017**, *139* (6), 2152-2155. DOI: 10.1021/jacs.6b11945.
- [10] Galle, T.; Khoshkhoo, M. S.; Martin-Garcia, B.; Meerbach, C.; Sayevich, V.; Koitzsch, A.; Lesnyak, V.; Eychmuller, A. Colloidal PbSe Nanoplatelets of Varied Thickness with Tunable Optical Properties. *Chem. Mater.* **2019**, *31* (10), 3803-3811. DOI: 10.1021/acs.chemmater.9b01330.
- [11] Galle, T.; Spittel, D.; Weiss, N.; Shamraienko, V.; Decker, H.; Georgi, M.; Hubner, R.; Metzkwon, N.; Steinbach, C.; Schwarz, D.; et al. Simultaneous Ligand and Cation Exchange of Colloidal CdSe Nanoplatelets Toward PbSe Nanoplatelets for Application in Photodetectors. *J. Phys. Chem. Lett.* **2021**, 5214-5220. DOI: 10.1021/acs.jpcclett.1c01362.
- [12] Xiang, H.; Cheng, J.; Ma, X.; Zhou, X.; Chruma, J. J. Near-Infrared Phosphorescence: Materials and Applications. *Chem. Soc. Rev.* **2013**, *42* (14), 6128-6185. DOI: 10.1039/c3cs60029g.
- [13] Hemmer, E.; Benayas, A.; Legare, F.; Vetrone, F. Exploiting the Biological Windows: Current Perspectives on Fluorescent Bioprobes Emitting Above 1000 nm. *Nanoscale Horiz.* **2016**, *1* (3), 168-184. DOI: 10.1039/c5nh00073d.
- [14] Schliehe, C.; Juarez, B. H.; Pelletier, M.; Jander, S.; Greshnykh, D.; Nagel, M.; Meyer, A.; Foerster, S.; Kornowski, A.; Klinke, C.; et al. Ultrathin PbS Sheets by Two-Dimensional Oriented Attachment. *Science* **2010**, *329* (5991), 550-553. DOI: 10.1126/science.1188035.
- [15] Zhang, Y.; Lu, J.; Shen, S.; Xu, H.; Wang, Q. Ultralarge Single Crystal SnS Rectangular Nanosheets. *Chem. Commun.* **2011**, *47* (18), 5226-5228. DOI: 10.1039/c0cc05528j.
- [16] Khan, A. H.; Pal, S.; Dalui, A.; Pradhan, J.; Sarma, D. D.; Acharya, S. Solution-Processed Free-Standing Ultrathin Two-Dimensional PbS Nanocrystals with Efficient and Highly Stable Dielectric Properties. *Chem. Mater.* **2017**, *29* (3), 1175-1182. DOI: 10.1021/acs.chemmater.6b04508.
- [17] Khan, A. H.; Brescia, R.; Polovitsyn, A.; Angeloni, I.; Martín-García, B.; Moreels, I. Near-Infrared Emitting Colloidal PbS Nanoplatelets: Lateral Size Control and Optical Spectroscopy. *Chem. Mater.* **2017**, *29* (7), 2883-2889. DOI: 10.1021/acs.chemmater.6b05111.
- [18] Kull, S.; Heymann, L.; Hungria, A. B.; Klinke, C. Synthesis of Single-Crystalline Lead Sulfide Nanoframes and Nanorings. *Chem. Mater.* **2019**, *31* (15), 5646-5654. DOI: 10.1021/acs.chemmater.9b01508.
- [19] Akkerman, Q. A.; Martín-García, B.; Buha, J.; Almeida, G.; Toso, S.; Marras, S.; Bonaccorso, F.; Petralanda, U.; Infante, I.; Manna, L. Ultrathin Orthorhombic PbS Nanosheets. *Chem. Mater.* **2019**, *31* (19), 8145-8153. DOI: 10.1021/acs.chemmater.9b02914.
- [20] Manteiga Vazquez, F.; Yu, Q.; Klepzig, L. F.; Siebbeles, L. D. A.; Crisp, R. W.; Lauth, J. Probing Excitons in Ultrathin PbS Nanoplatelets with Enhanced Near-Infrared Emission. *J. Phys. Chem. Lett.* **2021**, 680-685. DOI: 10.1021/acs.jpcclett.0c03461.
- [21] Dogan, S.; Bielewicz, T.; Cai, Y.; Klinke, C. Field-Effect Transistors Made of Individual Colloidal PbS Nanosheets. *Appl. Phys. Lett.* **2012**, *101* (7), 073102. DOI: 10.1063/1.4745786.
- [22] Aerts, M.; Bielewicz, T.; Klinke, C.; Grozema, F. C.; Houtepen, A. J.; Schins, J. M.; Siebbeles, L. D. Highly Efficient Carrier Multiplication in PbS Nanosheets. *Nat. Commun.* **2014**, *5*, 3789. DOI: 10.1038/ncomms4789.

- [23] Li, H.; Zhitomirsky, D.; Grossman, J. C. Tunable and Energetically Robust PbS Nanoplatelets for Optoelectronic Applications. *Chem. Mater.* **2016**, *28* (6), 1888-1896. DOI: 10.1021/acs.chemmater.6b00167.
- [24] Hines, M. A.; Scholes, G. D. Colloidal PbS Nanocrystals with Size-Tunable Near-Infrared Emission: Observation of Post-Synthesis Self-Narrowing of the Particle Size Distribution. *Adv. Mater.* **2003**, *15* (21), 1844-1849. DOI: 10.1002/adma.200305395.
- [25] Cademartiri, L.; Bertolotti, J.; Sapienza, R.; Wiersma, D. S.; von Freymann, G.; Ozin, G. A. Multigram Scale, Solventless, and Diffusion-Controlled Route to Highly Monodisperse PbS Nanocrystals. *J. Phys. Chem. B* **2006**, *110* (2), 671-673. DOI: 10.1021/jp0563585.
- [26] Hendricks, M. P.; Campos, M. P.; Cleveland, G. T.; Jen-La Plante, I.; Owen, J. S. A Tunable Library of Substituted Thiourea Precursors to Metal Sulfide Nanocrystals. *Science* **2015**, *348* (6240), 1226-1230. DOI: 10.1126/science.aaa2951.
- [27] Macias-Pinilla, D. F.; Echeverría-Arroondo, C.; Gualdrón Reyes, A. F.; Agouram, S.; Muñoz-Sanjósé, V.; Planelles, J.; Mora-Seró, I.; Climente, J. I. Morphology and Band Structure of Orthorhombic PbS Nanoplatelets: An Indirect Band Gap Material. *Chem. Mater.* **2021**, *33* (1), 420-429. DOI: 10.1021/acs.chemmater.0c04281.
- [28] Knorr, K.; Ehm, L.; Hytha, M.; Winkler, B.; Depmeier, W. The High-Pressure a/b Phase Transition in Lead Sulphide (PbS). *Eur. Phys. J. B* **2003**, *31* (3), 297-303. DOI: 10.1140/epjb/e2003-00034-6.
- [29] Wang, S.; Zhang, J.; Zhang, Y.; Alvarado, A.; Attapattu, J.; He, D.; Wang, L.; Chen, C.; Zhao, Y. Phase-Transition Induced Elastic Softening and Band Gap Transition in Semiconducting PbS at High Pressure. *Inorg. Chem.* **2013**, *52* (15), 8638-8643. DOI: 10.1021/ic400801s.
- [30] Bertolotti, F.; Dirin, D. N.; Ibanez, M.; Krumeich, F.; Cervellino, A.; Frison, R.; Voznyy, O.; Sargent, E. H.; Kovalenko, M. V.; Guagliardi, A.; et al. Crystal Symmetry Breaking and Vacancies in Colloidal Lead Chalcogenide Quantum Dots. *Nat. Mater.* **2016**, *15* (9), 987-994. DOI: 10.1038/nmat4661.
- [31] Morrison, P. J.; Loomis, R. A.; Buhro, W. E. Synthesis and Growth Mechanism of Lead Sulfide Quantum Platelets in Lamellar Mesophase Templates. *Chem. Mater.* **2014**, *26* (17), 5012-5019. DOI: 10.1021/cm5020702.
- [32] Saldanha, P. L.; Lesnyak, V.; Manna, L. Large Scale Syntheses of Colloidal Nanomaterials. *Nano Today* **2017**, *12*, 46-63. DOI: 10.1016/j.nantod.2016.12.001.
- [33] Grzechnik, A.; Friese, K. Pressure-Induced Orthorhombic Structure of PbS. *J. Phys.: Condens. Matter* **2010**, *22* (9), 095402. DOI: 10.1088/0953-8984/22/9/095402.
- [34] Bai, F.; Bian, K.; Huang, X.; Wang, Z.; Fan, H. Pressure Induced Nanoparticle Phase Behavior, Property, and Applications. *Chem. Rev.* **2019**, *119* (12), 7673-7717. DOI: 10.1021/acs.chemrev.9b00023.
- [35] Abecassis, B.; Tessier, M. D.; Davidson, P.; Dubertret, B. Self-assembly of CdSe Nanoplatelets into Giant Micrometer-Scale Needles Emitting Polarized Light. *Nano Lett.* **2014**, *14* (2), 710-715. DOI: 10.1021/nl4039746.
- [36] Toso, S.; Baranov, D.; Altamura, D.; Scattarella, F.; Dahl, J.; Wang, X.; Marras, S.; Alivisatos, A. P.; Singer, A.; Giannini, C.; et al. Multilayer Diffraction Reveals That Colloidal Superlattices Approach the Structural Perfection of Single Crystals. *ACS Nano* **2021**, 6243-6256. DOI: 10.1021/acsnano.0c08929.
- [37] Li, Z.; Peng, X. Size/Shape-Controlled Synthesis of Colloidal CdSe Quantum Disks: Ligand and Temperature Effects. *J. Am. Chem. Soc.* **2011**, *133* (17), 6578-6586. DOI: 10.1021/ja108145c.
- [38] Hutter, E. M.; Bladt, E.; Goris, B.; Pietra, F.; van der Bok, J. C.; Boneschanscher, M. P.; de Mello Donega, C.; Bals, S.; Vanmaekelbergh, D. Conformal and Atomic Characterization of Ultrathin CdSe Platelets with a Helical Shape. *Nano Lett.* **2014**, *14* (11), 6257-6262. DOI: 10.1021/nl5025744.
- [39] Ekimov, A. I.; Kudryavtsev, I. A.; Efros, A. L.; Yazeva, T. V.; Hache, F.; Schanne-Klein, M. C.; Rodina, A. V.; Ricard, D.; Flytzanis, C. Absorption and Intensity-Dependent Photoluminescence Measurements on CdSe Quantum Dots: Assignment of the First Electronic Transitions. *J. Opt. Soc. Am. B* **1993**, *10* (1), 100-107. DOI: 10.1364/josab.10.000100.
- [40] Murphy, J. E.; Beard, M. C.; Norman, A. G.; Ahrenkiel, S. P.; Johnson, J. C.; Yu, P.; Micic, O. I.; Ellingson, R. J.; Nozik, A. J. PbTe Colloidal Nanocrystals: Synthesis, Characterization, and Multiple Exciton Generation. *J. Am. Chem. Soc.* **2006**, *128* (10), 3241-3247. DOI: 10.1021/ja0574973.
- [41] Koole, R.; Allan, G.; Delerue, C.; Meijerink, A.; Vanmaekelbergh, D.; Houtepen, A. J. Optical Investigation of Quantum Confinement in PbSe Nanocrystals at Different Points in the Brillouin Zone. *Small* **2008**, *4* (1), 127-133. DOI: 10.1002/smll.200700632.
- [42] Son, J. S.; Wen, X. D.; Joo, J.; Chae, J.; Baek, S. I.; Park, K.; Kim, J. H.; An, K.; Yu, J. H.; Kwon, S. G.; et al. Large-Scale Soft Colloidal Template Synthesis of 1.4 nm Thick CdSe Nanosheets. *Angew. Chem. Int. Ed.* **2009**, *48* (37), 6861-6864. DOI: 10.1002/anie.200902791.
- [43] Liu, Y. H.; Wang, F.; Wang, Y.; Gibbons, P. C.; Buhro, W. E. Lamellar Assembly of Cadmium Selenide Nanoclusters into Quantum Belts. *J. Am. Chem. Soc.* **2011**, *133* (42), 17005-17013. DOI: 10.1021/ja206776g.
- [44] Wang, Y.; Liu, Y. H.; Zhang, Y.; Kowalski, P. J.; Rohrs, H. W.; Buhro, W. E. Preparation of Primary Amine Derivatives of the Magic-Size Nanocluster (CdSe)₁₃. *Inorg. Chem.* **2013**, *52* (6), 2933-2938. DOI: 10.1021/ic302327p.

- [45] Wang, F.; Wang, Y.; Liu, Y. H.; Morrison, P. J.; Loomis, R. A.; Buhro, W. E. Two-Dimensional Semiconductor Nanocrystals: Properties, Templated Formation, and Magic-Size Nanocluster Intermediates. *Acc. Chem. Res.* **2015**, *48* (1), 13-21. DOI: 10.1021/ar500286j.
- [46] Nasilowski, M.; Mahler, B.; Lhuillier, E.; Ithurria, S.; Dubertret, B. Two-Dimensional Colloidal Nanocrystals. *Chem. Rev.* **2016**, *116* (18), 10934-10982. DOI: 10.1021/acs.chemrev.6b00164.
- [47] van der Stam, W.; Akkerman, Q. A.; Ke, X.; van Huis, M. A.; Bals, S.; de Mello Donega, C. Solution-Processable Ultrathin Size- and Shape-Controlled Colloidal Cu_{2-x}S Nanosheets. *Chem. Mater.* **2014**, *27* (1), 283-291. DOI: 10.1021/cm503929q.
- [48] Hancock, R. D.; Martell, A. E. Hard and Soft Acid-Base Behavior in Aqueous Solution: Steric Effects Make Some Metal Ions Hard: A Quantitative Scale of Hardness-Softness for Acids and Bases. *J. Chem. Educ.* **1996**, *73* (7). DOI: 10.1021/ed073p654.
- [49] Atkins, P. W.; Overton, T. L.; Rourke, J. P.; Weller, M. T.; Armstrong, F. A. *Shriver and Atkins' Inorganic Chemistry*; Oxford University Press, 2010.
- [50] Hazari, A.; Das, L. K.; Bauza, A.; Frontera, A.; Ghosh, A. The Influence of H-bonding on the 'Ambidentate' Coordination Behaviour of the Thiocyanate Ion to Cd(II): a Combined Experimental and Theoretical study. *Dalton Trans.* **2014**, *43* (21), 8007-8015. DOI: 10.1039/c3dt53318b.
- [51] Anderson, N. C.; Hendricks, M. P.; Choi, J. J.; Owen, J. S. Ligand Exchange and the Stoichiometry of Metal Chalcogenide Nanocrystals: Spectroscopic Observation of Facile Metal-Carboxylate Displacement and Binding. *J. Am. Chem. Soc.* **2013**, *135* (49), 18536-18548. DOI: 10.1021/ja4086758.
- [52] Boles, M. A.; Engel, M.; Talapin, D. V. Self-Assembly of Colloidal Nanocrystals: From Intricate Structures to Functional Materials. *Chem. Rev.* **2016**, *116* (18), 11220-11289. DOI: 10.1021/acs.chemrev.6b00196.
- [53] Owen, J. S. The Coordination Chemistry of Nanocrystal Surfaces. *Science* **2015**, *347* (6222), 615-616. DOI: 10.1126/science.1259924.

S5 Supporting Information

S5.1 Experimental methods and characterization

Chemicals

Acetonitrile (ACN, anhydrous, 99.8%), 1-butanol (BuOH, anhydrous, 99.8%), lead(II) thiocyanate ($\text{Pb}(\text{SCN})_2$, 99.5%), methanol (MeOH, anhydrous, 99.8%), nonanoic acid ($\geq 97\%$), 1-octadecene (ODE, technical grade 90%), octylamine (99%), oleic acid (OA, technical grade 90%) and oleylamine (OLAM, technical grade 70%) were bought from Sigma-Aldrich. Toluene (anhydrous, 99.8%) was purchased from Alfa Aesar, while ethanol (EtOH, anhydrous, $\geq 99.8\%$) was purchased from VWR international.

Synthesis of PbS nanosheets

The PbS nanosheets were prepared following a reported synthesis procedure by Akkerman et al.¹ In a typical synthesis, 32.3 mg (0.1 mmol) $\text{Pb}(\text{SCN})_2$ was added to a 25 mL three-neck flask with 223.8 mg (0.250 mL) OA, 101.6 mg (0.125 mL) OLAM and 7.9 g (10 mL) ODE. The flask was capped with a Vigreux, but the reaction was allowed to proceed in air (oxygen is required for the decomposition of $\text{Pb}(\text{SCN})_2$). To dissolve the $\text{Pb}(\text{SCN})_2$ the reaction flask was heated to 110 °C for 30 minutes, after which the temperature was quickly raised to 165 °C (at a rate of ~ 15 °C per minute). Between 155 °C and 165 °C the reaction mixture turns from transparent to light and then dark brown, as the temperature reaches 165 °C reaction mixture in the flask was quickly cooled with a water bath (~ 2 °C per second). The reaction product was washed by centrifugation at 2750 revolutions per minute (RPM, 840 RCF), redispersed in 5 mL toluene and stored in a nitrogen-filled glovebox. A possible additional washing step was performed with acetonitrile (5 mL) or MeOH/BuOH (3 mL, 1.5 mL) as an antisolvent, again centrifuging at 2750 RPM and redispersing in 5 mL toluene. To slow the PbS NSs formation down and study the reaction mechanism the synthesis was also performed at 145 °C for up to 10 minutes after the color change to light brown. Via aliquots, the intermediary products were studied ex situ with HAADF-STEM and ultraviolet-visible spectroscopy (UV/Vis).

Characterization

Transmission electron microscopy (TEM) samples were prepared by dropcasting a dilute dispersion of NCs on carbon-coated copper TEM grids. To image the atomic structure of the sheets along the planar directions and study their thickness, an antisolvent (MeOH/BuOH in a 1:2 ratio) was added to the dispersion before further sample preparation, inducing face-to-face stacking of the NSs. To diminish hydrocarbon contamination during imaging, the prepared TEM grid was treated with EtOH and activated carbon for 5 minutes, following a recently published procedure.² Bright-field TEM (BF-TEM) images were acquired with a Thermo Fisher T20, a Thermo Fisher Talos L120C, or with a Fei Talos F200X operating at respectively 200, 120 and 200 keV. Low-resolution HAADF-STEM images were acquired with a Fei Talos F200X operating at 200 keV. Atomically-resolved high-resolution HAADF-STEM imaging as well as 4D STEM data collection, was performed on an aberration-corrected Thermo Fisher Titan G2 60-300 microscope, operating at 200 and 300 keV. The 4D STEM measurements were performed at 300 keV in microprobe mode with a convergence semi-angle of 1 mrad, resulting in a diffraction limited probe size of 0.9 nm. With this probe the sample is scanned in a rasterized manner and a diffraction pattern is acquired at each position. The peak finding routine and virtual detector algorithms from the open-source software Pixstem are used for the

analysis of these 4D STEM datasets.³ The datasets consist of the probe position (2D position in real space) where the pixel size is determined by the probe size, and the diffraction pattern of each pixel has been acquired (2D in reciprocal space). The final result is a map showing the major changes in the diffraction patterns i.e. the folds in the sheets.

UV/Vis absorption spectra were measured on a PerkinElmer 950 UV/Vis/NIR spectrophotometer with quartz cuvettes. Fourier transform infrared (FTIR) spectra were measured with a Bruker Vertex 70 and an air-tight liquid cell purchased from International Crystal Laboratories, with two KBr windows and a path length of 0.5 mm. Spectra were recorded from 400 cm^{-1} to 7000 cm^{-1} with a KBr beam splitter, a DTLaTGS D301 detector and a mid-infrared source. FTIR spectra of PbS NS films were measured with the same apparatus and a quartz slide in an air-tight sample holder. Spectra were recorded from 3300 cm^{-1} to 15500 cm^{-1} with a quartz beam splitter, an Si-Diode detector and a near-infrared source.

Proton nuclear magnetic resonance ($^1\text{H-NMR}$) measurements were performed using an Agilent MRF400 equipped with a OneNMR probe and Optima Tune system. Spectra were recorded according to the following parameters: 400 MHz, CDCl_3 , 25 $^\circ\text{C}$. In short, 0.6 or 0.9 mL of the synthesized PbS NSs was dried and redispersed in 0.6 mL CDCl_3 , to which 10 μL (0.05 M) of a ferrocene stock solution was added as an internal standard. The samples were then measured with a longer relaxation delay (25 s) to allow complete relaxation.^{4,5}

Atomic force microscopy samples (AFM) were prepared by dropcasting the dispersion on a cleaved mica substrate. The measurements were performed with a JPK Nanowizard 2, operating in intermittent-contact mode in ambient atmosphere using a Bruker OTESPA-R3 tip.

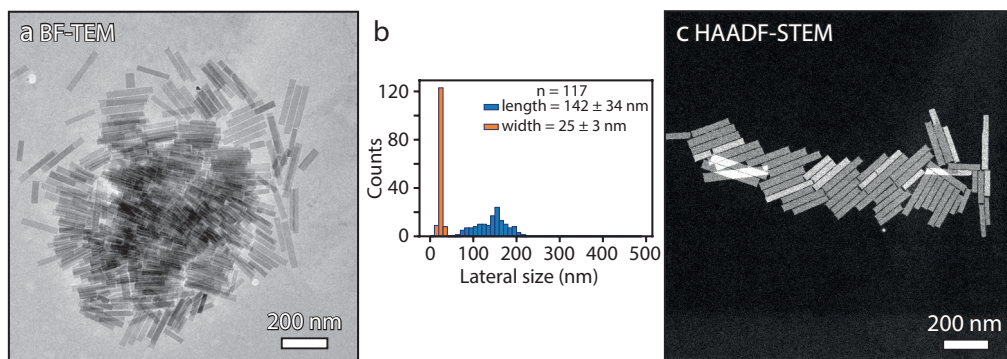


Figure S5.1 Overview images of a standard synthesis of PbS NSs prepared at 165 $^\circ\text{C}$ imaged with BF-TEM (a) and HAADF-STEM (c). The NSs in the TEM images were measured with ImageJ and the histogram shows the lateral dimensions (with average 142 ± 34 by 25 ± 3 nm). The low-resolution HAADF-STEM image of a standard synthesis of PbS NSs (c), shows contrast differences between the NSs.

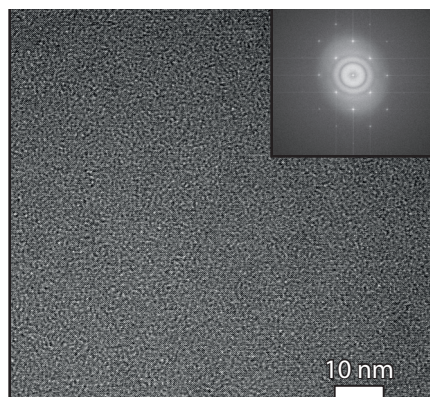


Figure S5.2 High-resolution BF-TEM image showing the atomic columns along the [100] direction in a face-down oriented PbS NS with the corresponding Fourier transform. While the atom columns are visible, additional contrast from the formvar/carbon background makes in-depth characterization of the crystal structure difficult. Therefore, atomically resolved HAADF-STEM is preferred over BF-TEM, see also Figure 5.1c.

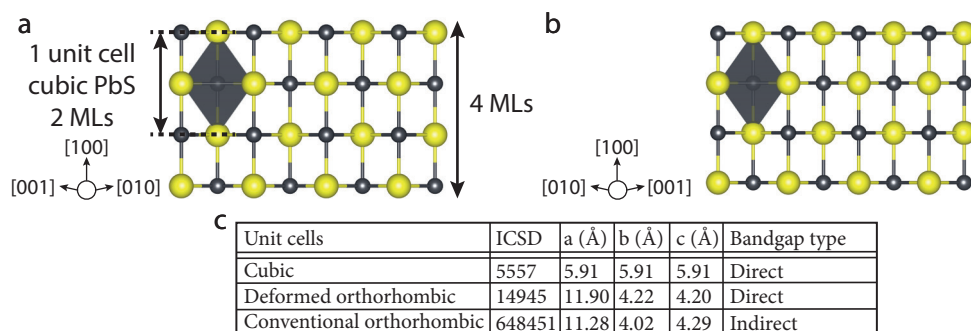


Figure S5.3 Schematic depiction of cubic PbS, as it would show on the side of the NSs if they had a cubic structure (a and b). The grey and yellow symbols represent the Pb and S atoms respectively. As the cubic crystal structure is isotropic, no differences are observed between the long edge (a) and the short edge (b) of the NSs. In panel (c) the unit cell dimensions of the various crystal structures discussed here are shown. Including the bulk bandgap type as calculate by DFT using the unit cells in the table. Showing that the small increase in lattice anisotropy from deformed orthorhombic to conventional orthorhombic is enough to switch the calculated bulk band gap from direct to indirect.⁶

S5.2 NMR and FTIR study of additional purification steps

After addition of an antisolvent to induce stacking of the NSs, the NS-to-NS distance decreases (which is 0.8 ± 0.3 instead of 3.6 ± 0.3 nm,¹ or 4.4 nm,⁷). At some points the NSs even merge or grow together, indicating a lack of surface passivation (see the blue arrow in **Figure 5.3a**). To gain some understanding of the residual precursors in the dispersion of the sheets and to study the surface passivation, we used ¹H-NMR measurements. NSs purified by centrifugation and redispersion in fresh toluene (the purification steps previously reported),¹ show the presence of the organic ligands and ODE (**Figure S5.4**). The characteristic broadening of the 5.3 ppm peak for surface bound OA and/or OLAM is not observed.^{4,8,9} Additional purification by the addition of a protic or aprotic antisolvent removes most of the residual organic ligands and ODE (**Figure S5.5**). After these purification procedures, the thiocyanate is still observed at ~ 2040 cm⁻¹ with FTIR (see inset **Figure S5.6**). We therefore suspect that the residual organic ligands are removed in the stacked NSs, resulting in the decrease of NS-to-NS distance (**Figure 5.3a**). In **Table S5.1**, a complete overview of every resonance and their characterization is given.

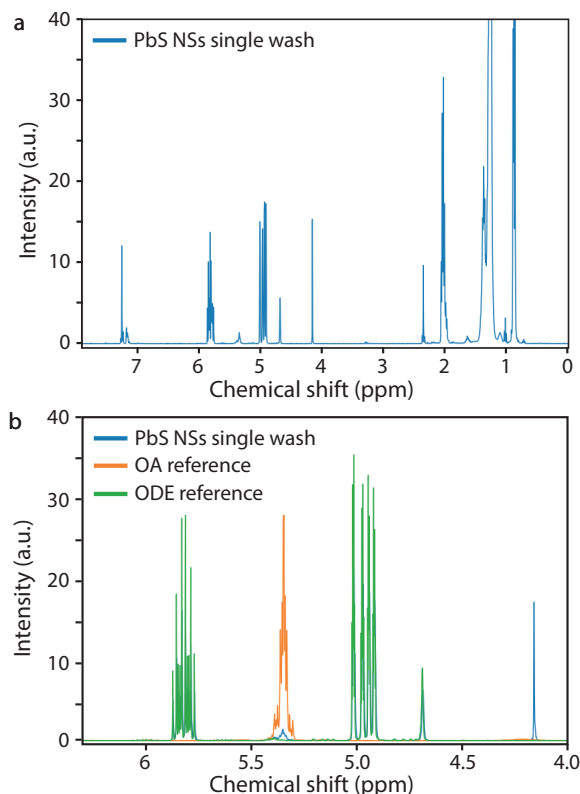


Figure S5.4 NMR spectra of PbS NSs and references. (a) NMR spectrum of PbS NSs, see Table S5.1 for a full reference of each peak. (b) Selection of the NMR spectrum in (a) with reference spectra of OA and ODE. The sharp resonances at 5.8 ppm and 4.9 ppm are attributed to ODE, the 5.3 ppm resonance is attributed to the presence of OA/OLAM, although the characteristic broadening surface bound ligands, previously observed both in 3D and 2D materials is not observed here.^{4,8,9}

Table S5.1 Table listing the resonances observed in Figure S5.4a and attributed to the protons present in the reaction mixture. Note that thiocyanate does not contain any protons and therefore cannot be characterized with $^1\text{H-NMR}$.

Chemical shift (ppm)	Corresponds to	Group
0.9	OA, ODE, OLAM	- CH_3
1.3	OA, ODE, OLAM	- CH_2
2.0	OA, ODE, OLAM	- CH_2 , - NH_2
2.3	OA	$\text{O}=\text{C}-\text{CH}_3$
2.7	OLAM	- CH_2-NH_2
4.1	Ferrocene	-
4.9	ODE	= CH_2
5.3	OA, OLAM	- $\text{HC}=\text{CH}-$
5.8	ODE	- $\text{CH}=\text{CH}_2$
7.3	CDCl_3	-

The concentration ODE and OA/OLAM were determined by the addition of a known concentration of ferrocene (10 μL , 0.05 M).^{4,5} The concentrations ODE and OA/OLAM were determined using the internal standard with the following equations:

$$[\text{ODE}] = \left(\frac{I_{4.9}}{I_{\text{fer}}} \right) \times \left(\frac{10}{2} \right) \times [\text{ferrocene}] \quad (\text{S5.1})$$

$$[\text{OA/OLAM}] = \left(\frac{I_{5.3}}{I_{\text{fer}}} \right) \times \left(\frac{10}{2} \right) \times [\text{ferrocene}] \quad (\text{S5.2})$$

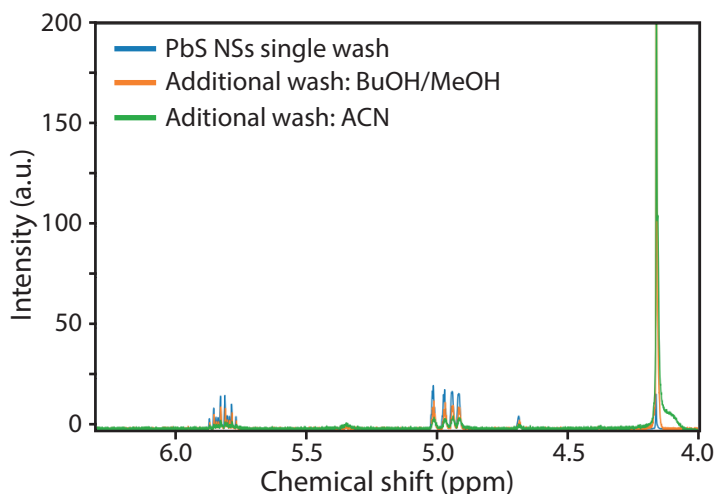


Figure S5.5 NMR spectra of PbS NSs centrifuged and redispersed (blue) and washed with two different antisolvents (orange, green). Ferrocene was added as an internal standard and used to calculate the concentration of ODE and OA/OLAM in the sample.

Table S5.2 A table listing the integrals of the NMR spectra shown in Figure S5.5. Values used to calculate the concentration of the corresponding molecules present in each sample. After additional washing steps with an antisolvent, the concentration has significantly decreased.

Sample	Integral 4.1 ppm (ferrocene)	Integral 4.9 ppm (ODE)	Integral 5.3 ppm (OA/OLAM)	Concentration ODE [μM]	Concentration OA/OLAM [μM]
PbS single washed	1	11.81	0.58	45*	2.2*
PbS Me/Bu	1	0.23	0.01	0.58	0.025
PbS ACN	1	0.13	0.03	0.33	0.075

*Scaled by a factor of 1.5 for comparison with other samples, as only 0.6 mL sample was measured instead of 0.9 mL.

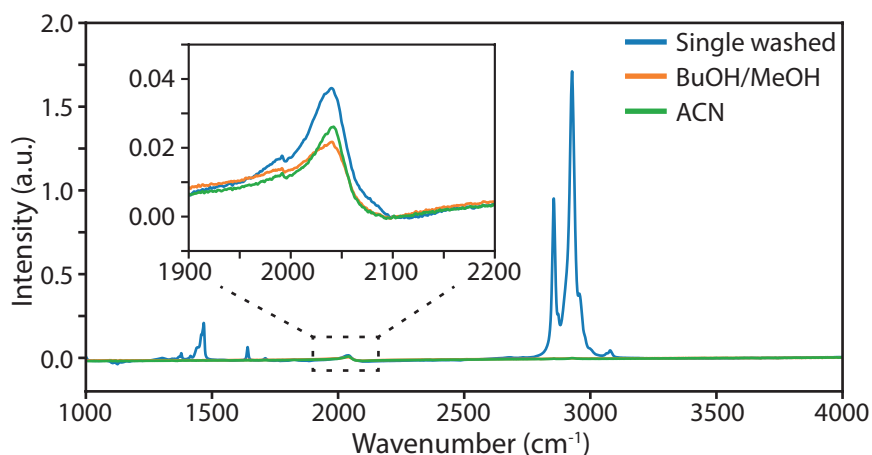


Figure S5.6 FTIR spectra of PbS NSs centrifuged and redispersed (blue) and washed with two different antisolvents (orange, green). Showing the presence of thiocyanate group even after further purification.

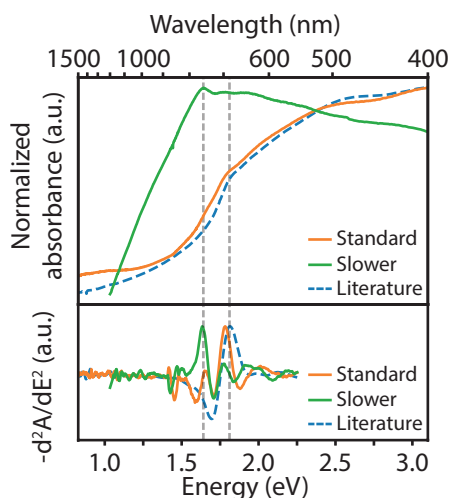


Figure S5.7 Absorption spectra and corresponding second-derivative analysis of a standard synthesis (standard 165 °C, orange), a synthesis with a heating rate of 9 °C per minute (slower 165 °C, green) and previous results of Akkerman et al. (suspension in Figure 5.4a digitized,² dashed blue). The standard sample contains a 1:1 ratio of both 4 and 6 MLs thick PbS NSs, the second-derivative analysis shows a single maximum at 1.77 eV. A maximum of 1.81 eV is observed for the literature absorption spectrum with only a 4 MLs population. Despite the presence of two populations, the absorption features are dominated by the optical transition of the 4 MLs NSs. In the slower synthesis the second-derivative shows a single maximum at 1.64 eV, presumably due to a majority of 6 MLs NSs. The grey dashed lines are a guide to the eye at 1.64 eV and 1.77 eV.

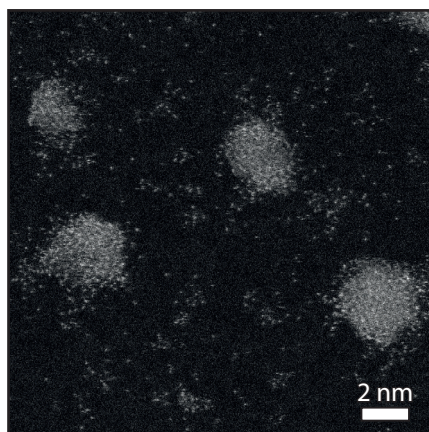


Figure S5.8 High-resolution HAADF-STEM image of free standing clusters roughly 2 nm in size. Their lack of a well-defined crystal structure is similar to previous literature on CdSe nanocrystals, where nanocrystals with a decreased size (below 2 nm) were shown to lack crystallinity.⁸

S5.3 PbS NSs synthesized at 145 °C

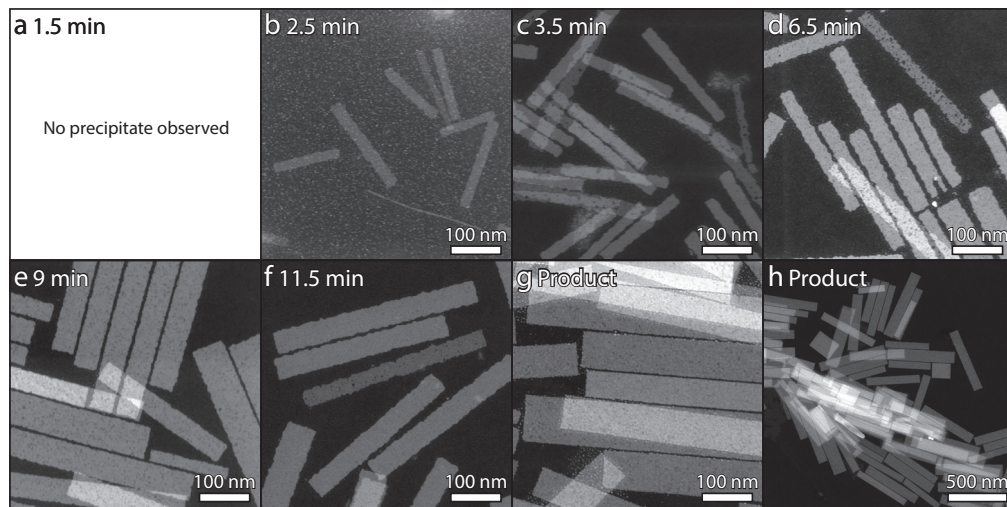


Figure S5.9 HAADF-STEM images of the aliquots taken at 145 °C. Time zero is defined as the moment that the reaction mixture reached 145 °C, the first aliquot was taken the moment that the characteristic color changes from transparent to light brown and did not yield any precipitate (a). All other intermediary products were isolated and studied with HAADF-STEM continually showing the presence of PbS NSs at increasing sizes (b-h).

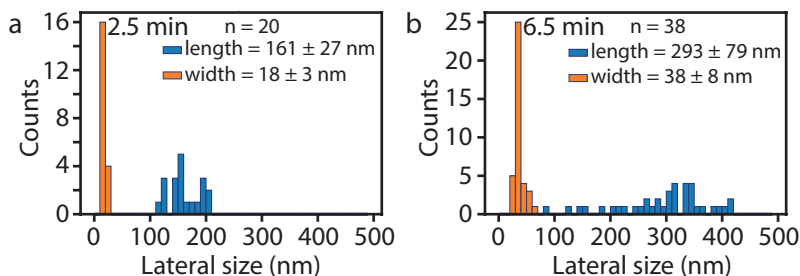


Figure S5.10 Lateral dimensions of PbS NSs prepared at 145 °C after 2.5 minutes (a) and 6.5 minutes (b) of reaction. Show an overall increase from 161 ± 27 by 18 ± 3 nm to 293 ± 79 by 38 ± 8 nm. With a large increase of the standard deviation, although it should be noted that the number of measured NSs is quite low, 20 and 38.

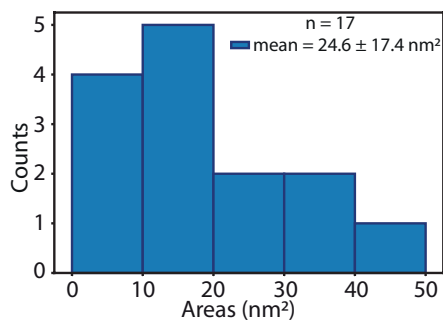


Figure S5.11 The crystalline domains in the pseudo-crystalline sheets synthesized at 145 °C for 2.5 minutes were measured with ImageJ. The histogram clearly indicates a large range in size, resulting in an average of 24.6 nm² but with a standard deviation of 17.4 nm².

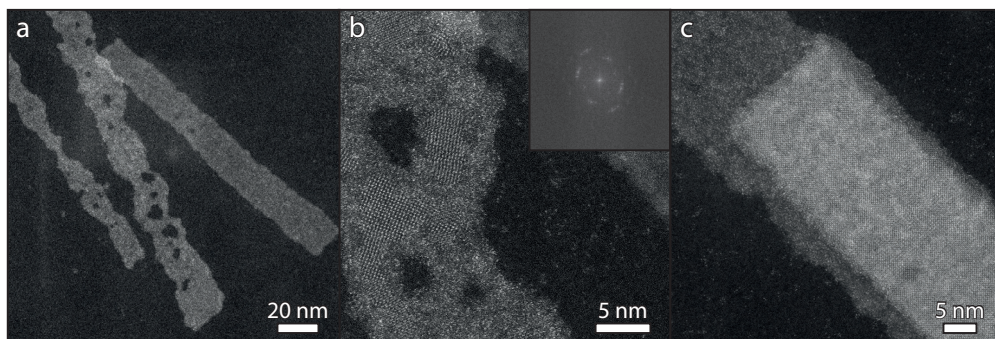


Figure S5.12 PbS nanosheets prepared at 145 °C for 2.5 minutes of reaction time. (a) Several NSs are partially “broken”, having holes in the structure and misaligned edges. (b) The crystalline areas observed in “broken” NSs are still aligned with the [010] direction in the long lateral dimension of the NSs. (c) Two or more amorphous-like NSs located on top of each other show more crystallinity.

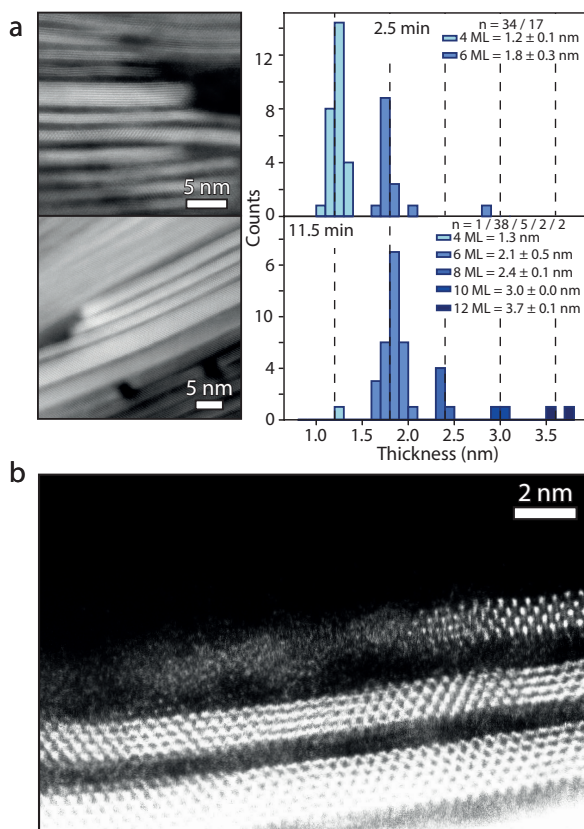


Figure S5.13 Determination of the thickness of PbS NSs prepared at 145 °C after 2.5 and 11.5 minutes (final product) after the sheets were stacked by the addition of an anti-solvent. (a) HAADF-STEM images and histograms of the measured NSs. In the earliest aliquot, 4 and 6 MLs NSs are observed in a 2:1 ratio. In the final product most of the sheets are 6 MLs thick, but a small number of thicker NSs (8, 10 and even 12 MLs) are observed in small numbers. (b) Shows the influence the addition of anti-solvent can have on a less stable sheet, potentially a pseudo-crystalline NS such as in Figure 5.6b. This provides an indication that all the sheets measured in panel (a) are the ones stable enough to stack after anti-solvent addition. Thus, it is possible that the results in panel (a) show the more stable sheets in the dispersion i.e. sheets that are more crystalline and thus mechanically more stable.

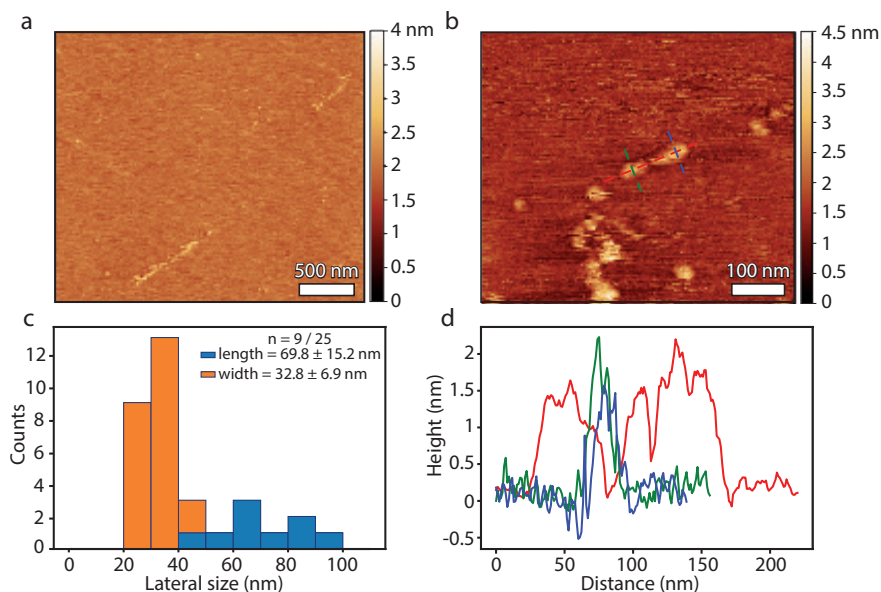


Figure S5.14 In an attempt to determine the thickness of the NSs in the first aliquot of the 145 °C reaction without the addition of an anti-solvent we used atomic force microscopy (AFM). The dispersion was drop-casted on a cleaved mica and AFM was used to image the sheets. Due to clustering and some contamination the sheets are imaged as elongated with round edges (a and b). (c) Histogram of the length and width AFM measurements is shown. The width of the sheets corresponds well to TEM measurements, but due to clustering of the NSs the length is challenging to measure and the resulting value is quite low. (d) Some representative height measurements are shown, both 1.8 nm (green, 6 MLs) and 1.2 nm (red, 4 MLs) are observed, although here we observe even some thinner 0.8 nm (blue). This third population is however slightly thicker than expected, if these are indeed sheets of 2 MLs we would expect 0.6 nm. See Figure S5.15a for the histogram of the measurements.

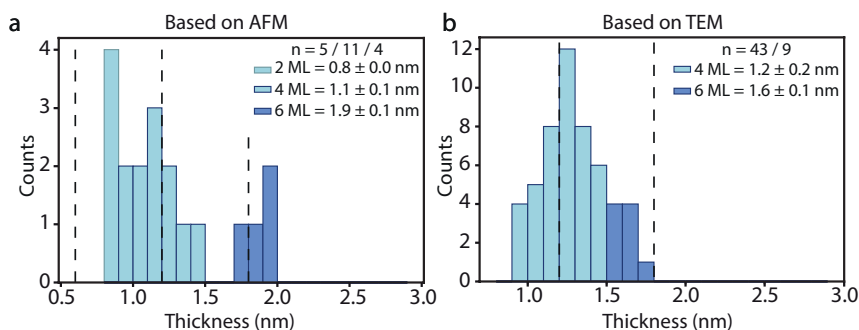


Figure S5.15 Histograms of the thickness of the first sample grown at 145°C. The AFM measurements show on average thinner sheets than TEM measurements of both the NSs stacked by antisolvent addition (Figure S5.13) and stacks naturally occurring in the sample (b). However, the number of sheets measured by AFM is too low to draw any definitive conclusions.

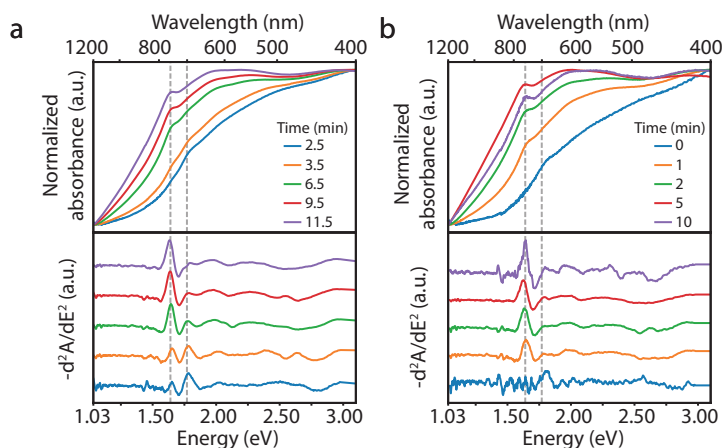


Figure S5.16 Absorption spectra of aliquots from PbS NSs dispersions prepared at 145°C (a) and 160°C (b, top); together with corresponding second-derivative analysis (below). The dashed vertical lines are located at respectively 1.64 and 1.78 eV. In both experiments a shift from 1.78 eV to 1.64 eV is observed over time, indicating an increase in thickness from 4 MLs to 6 MLs.

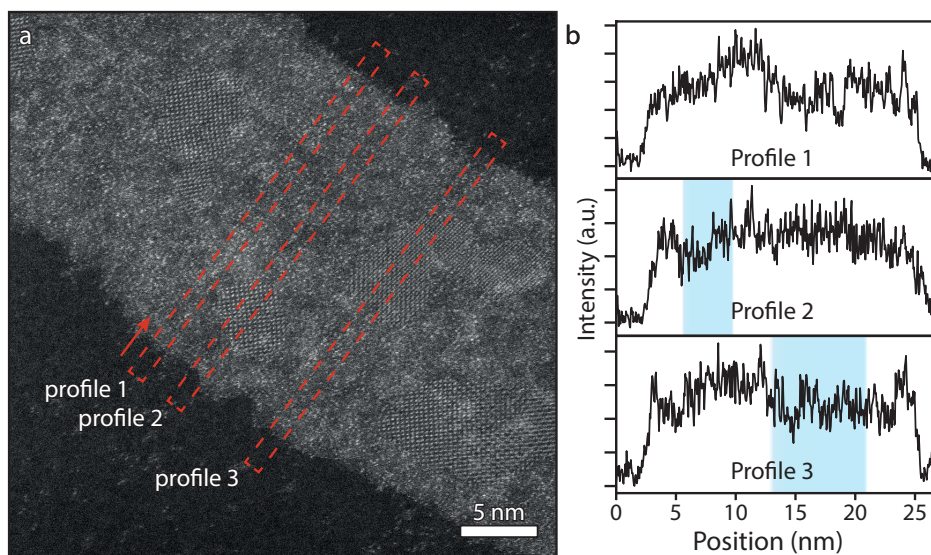


Figure S5.17 To investigate possible thickness differences between the crystalline (rock salt and orthorhombic) and pseudo-crystalline areas of a PbS NSs prepared at 145 °C for 2.5 minutes of reaction, intensity profiles were taken across the NS. (a) High-resolution HAADF-STEM image showing crystalline domains in the pseudo-crystalline structure. (b) Intensity profiles along the corresponding dashed red regions in panel (a). The blue shaded areas correspond to crystalline domains along the profile. No clear relation is observed between the intensity of a crystalline area versus that of a pseudo-crystalline area, indicating a homogeneous thickness in the NSs.

S5.4 Formation mechanism of the PbS NSs

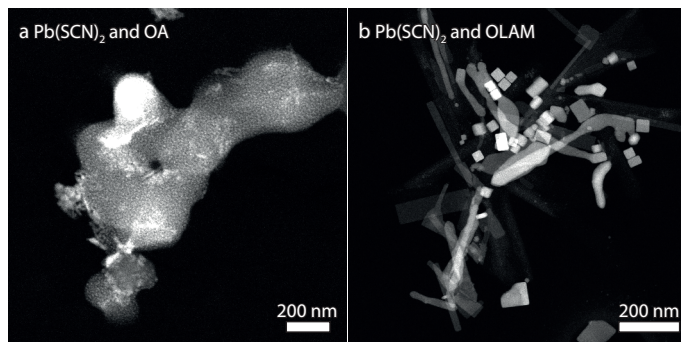


Figure S5.18 To investigate the role of oleic acid (OA) and oleylamine (OLAM) in the $\text{Pb}(\text{SCN})_2$ decomposition reaction, OLAM and OA were replaced with an equal amount of respectively OA (a) and OLAM (b). (a) Replacement of OLAM with OA yields amorphous structures. (b) Replacement of OA with OLAM results in PbS cubes and two-dimensional structures, showing that OLAM is essential for the growth of PbS NSs. Similar influence of OLAM has been shown in dithiocarbamate single source precursor reactions.¹⁰

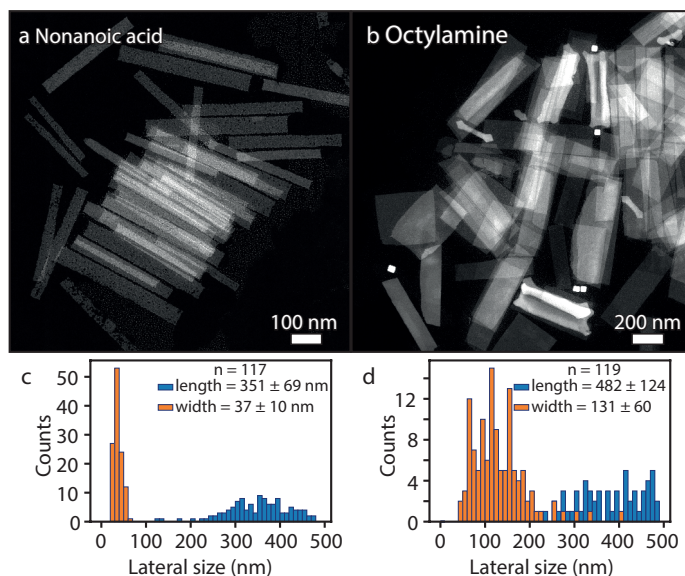


Figure S5.19 (a) Replacing OA with an equivalent amount of nonanoic acid results in PbS NSs with lateral dimensions of 351 ± 69 by 37 ± 10 nm (b) Replacing OLAM for an equivalent of octylamine results in PbS NSs with lateral dimensions of 482 ± 124 by 130 ± 60 nm.

S5.5 Thickness and optical properties of annealed NSs

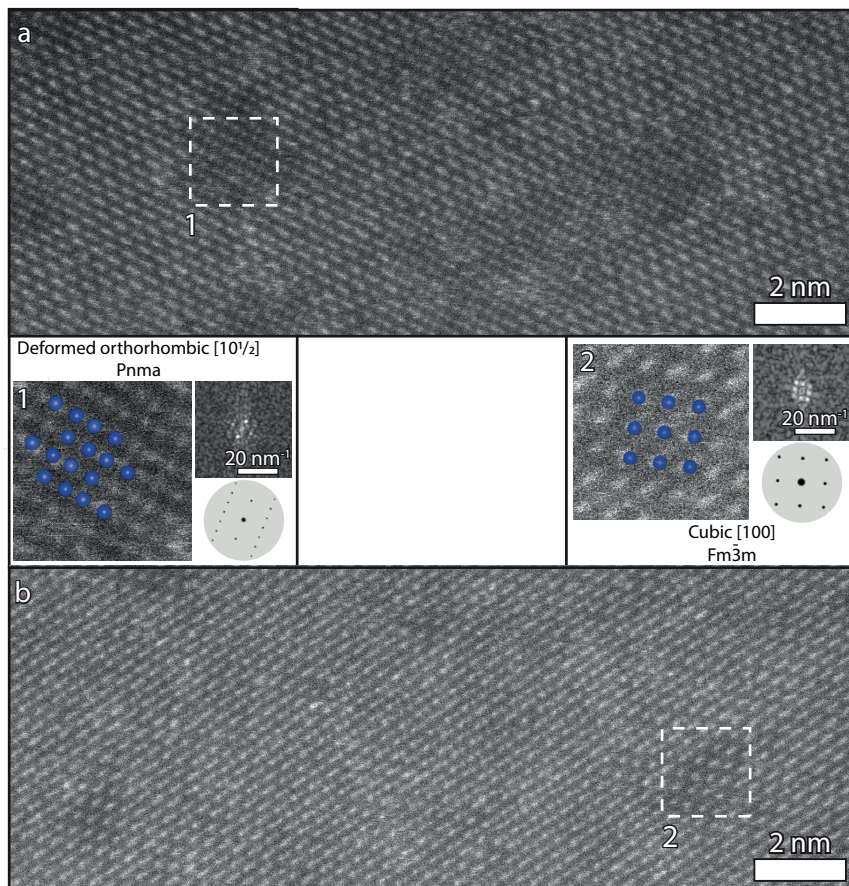


Figure S5.20 High-resolution HAADF-STEM images and Fourier transform of specific domains (also see Figure 5.4). The corresponding Fourier transforms from the various defects in the 5 minute (a) and 10 minute (b) grown sample were studied. In addition to the deformed orthorhombic crystal structure and previously discussed defects in the 5 minute sample, we observed deformed orthorhombic domains with different orientation (area 1). In the 10 minute sample, most of the defects have the cubic crystal structure.

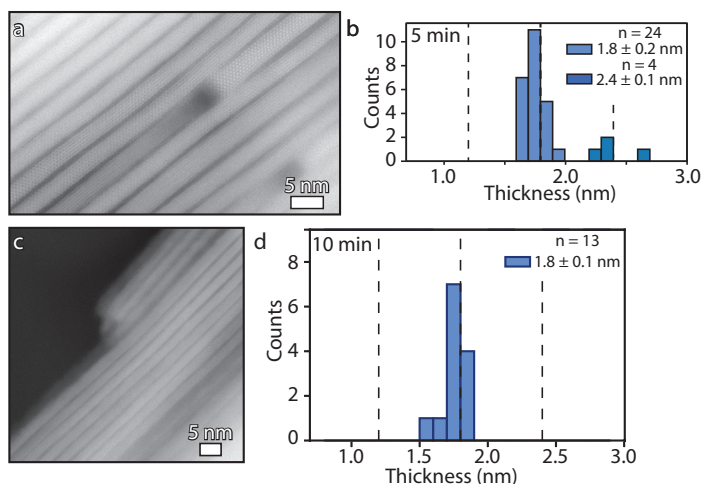


Figure S5.21 Determination of the thickness of PbS NSs with an edge-up orientation, prepared at 165 °C for 5 and 10 minutes. (a) High-resolution HAADF-STEM image showing NSs with thicknesses of 6 MLs and 8 MLs of PbS. (b) Corresponding histogram, indicating the absence of 1.2 nm sheets, but the presence of NSs with a thickness of 1.8 and 2.4 nm. (c) High-resolution HAADF-STEM image showing NSs with thicknesses of 6 MLs of PbS. (d) Corresponding histogram, indicating the absence of 1.2 nm sheets, but the presence of NSs with a thickness of 1.8 nm. It should be noted that the number of measured NSs for this characterization is quite low.

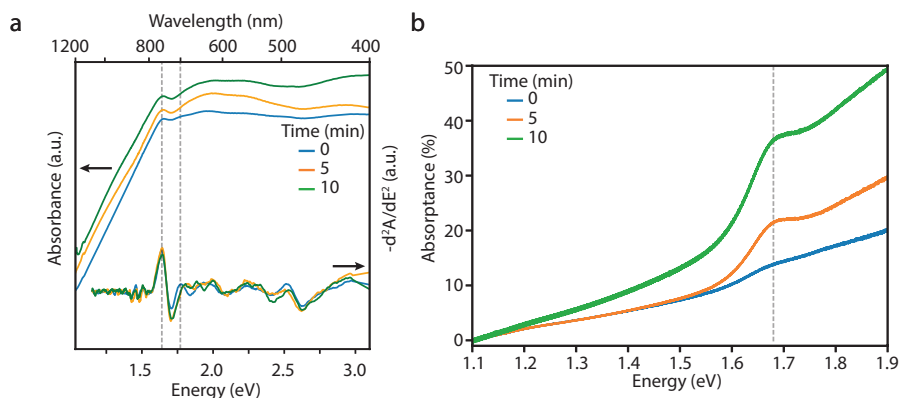


Figure S5.22 (a) The absorption spectra of PbS NSs prepared at 165 °C for 0, 5 and 10 minutes show an increase in background scattering while the absorption transition becomes more pronounced (1.64 and 1.77 eV dashed vertical lines). Analysis with the second-derivative shows a transition at 1.64 eV, indicating that the NSs predominantly attained a thickness of 6 MLs. Hence, prolonged reaction at 165 °C induces a thickness increase from 4 to 6 MLs, resulting in a more uniform population of NSs with a more homogeneous deformed orthorhombic crystal structure. (b) As per recent publications in PbS NSs films an absorbance of 4.6% ($2\pi\alpha$) per independent layer of PbS NSs is expected.^{11,12} The films were prepared by dropcasting 50 μL of the PbS NSs onto a quartz slide. At longer reaction times the absorbance increases from ~ 10 to 40%, which is attributed to an increase in NS concentration. The dashed vertical line is located at 1.68 eV.

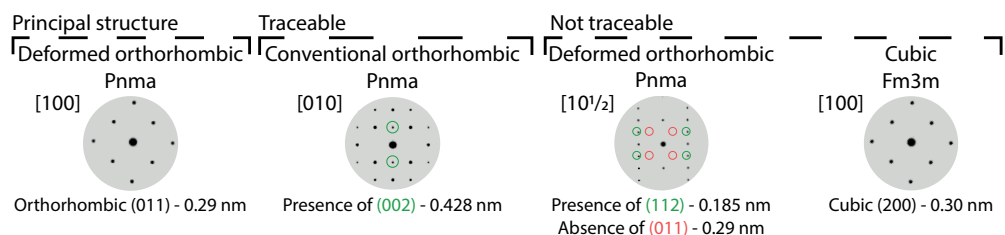


Figure S5.23 Schematic representation of the diffraction patterns of the principal deformed orthorhombic crystal structure and all the defects characterized in the NSs. Considering that the dumbbell atom columns of the deformed orthorhombic structure give the NSs higher intensity in the HAADF-STEM images with respect to the defect areas, we can apply intensity threshold image analysis (Figure 5.8). The diversity of the structures identified as defects, as well as their similarity in the diffraction diagrams (see schematic on the right) makes the analysis of these domains non-trivial. However, 4D STEM allows us to make a general interpretation of the diffraction patterns to gain knowledge in the homogeneity of the crystal orientation in the sheets.

References

- [1] Akkerman, Q. A.; Martín-García, B.; Buha, J.; Almeida, G.; Toso, S.; Marras, S.; Bonaccorso, F.; Petralanda, U.; Infante, I.; Manna, L. Ultrathin Orthorhombic PbS Nanosheets. *Chem. Mater.* **2019**, *31* (19), 8145-8153. DOI: 10.1021/acs.chemmater.9b02914.
- [2] Li, C.; Tardajos, A. P.; Wang, D.; Choukroun, D.; Van Daele, K.; Breugelmans, T.; Bals, S. A Simple Method to Clean Ligand Contamination on TEM Grids. *Ultramicroscopy* **2021**, *221*, 113195. DOI: 10.1016/j.ultramic.2020.113195.
- [3] Nord, M.; Webster, R. W. H.; Paton, K. A.; McVitie, S.; McGrouther, D.; MacLaren, I.; Paterson, G. W. Fast Pixelated Detectors in Scanning Transmission Electron Microscopy. Part I: Data Acquisition, Live Processing, and Storage. *Microsc. Microanal.* **2020**, *26* (4), 653-666. DOI: 10.1017/S1431927620001713.
- [4] Moreels, I.; Fritzing, B.; Martins, J. C.; Hens, Z. Surface Chemistry of Colloidal PbSe Nanocrystals. *J. Am. Chem. Soc.* **2008**, *130* (45), 15081-15086. DOI: 10.1021/ja803994m.
- [5] Anderson, N. C.; Hendricks, M. P.; Choi, J. J.; Owen, J. S. Ligand Exchange and the Stoichiometry of Metal Chalcogenide Nanocrystals: Spectroscopic Observation of Facile Metal-Carboxylate Displacement and Binding. *J. Am. Chem. Soc.* **2013**, *135* (49), 18536-18548. DOI: 10.1021/ja4086758.
- [6] Macias-Pinilla, D. F.; Echeverría-Arrondo, C.; Gualdrón Reyes, A. F.; Agouram, S.; Muñoz-Sanjosed, V.; Planelles, J.; Mora-Seró, I.; Climente, J. I. Morphology and Band Structure of Orthorhombic PbS Nanoplatelets: An Indirect Band Gap Material. *Chem. Mater.* **2021**, *33* (1), 420-429. DOI: 10.1021/acs.chemmater.0c04281.
- [7] Toso, S.; Baranov, D.; Altamura, D.; Scattarella, F.; Dahl, J.; Wang, X.; Marras, S.; Alivisatos, A. P.; Singer, A.; Giannini, C.; et al. Multilayer Diffraction Reveals That Colloidal Superlattices Approach the Structural Perfection of Single Crystals. *ACS Nano* **2021**, 6243-6256. DOI: 10.1021/acsnano.0c08929.
- [8] De Roo, J.; Yazdani, N.; Drijvers, E.; Lauria, A.; Maes, J.; Owen, J. S.; Van Driessche, I.; Niederberger, M.; Wood, V.; Martins, J. C.; et al. Probing Solvent-Ligand Interactions in Colloidal Nanocrystals by the NMR Line Broadening. *Chem. Mater.* **2018**, *30* (15), 5485-5492. DOI: 10.1021/acs.chemmater.8b02523.
- [9] Singh, S.; Leemans, J.; Zaccaria, F.; Infante, I.; Hens, Z. Ligand Adsorption Energy and the Postpurification Surface Chemistry of Colloidal Metal Chalcogenide Nanocrystals. *Chem. Mater.* **2021**, *33* (8), 2796-2803. DOI: 10.1021/acs.chemmater.0c04761.
- [10] Zhang, Y.; Lu, J.; Shen, S.; Xu, H.; Wang, Q. Ultralarge Single Crystal SnS Rectangular Nanosheets. *Chem. Commun.* **2011**, *47* (18), 5226-5228. DOI: 10.1039/c0cc05528j.
- [11] Prins, P. T.; Alimoradi Jazi, M.; Killilea, N. A.; Evers, W. H.; Geiregat, P.; Heiss, W.; Houtepen, A. J.; Delerue, C.; Hens, Z.; Vanmaekelbergh, D. The Fine-Structure Constant as a Ruler for the Band-Edge Light Absorption Strength of Bulk and Quantum-Confined Semiconductors. *Nano Lett.* **2021**, *21* (22), 9426-9432. DOI: 10.1021/acs.nanolett.1c02682.
- [12] Lannoo, M.; Prins, P. T.; Hens, Z.; Vanmaekelbergh, D.; Delerue, C. Universality of Optical Absorbance Quantization in Two-Dimensional Group-IV, III-V, II-VI, and IV-VI Semiconductors. *Phys. Rev. B* **2022**, *105* (3), 035421. DOI: 10.1103/PhysRevB.105.035421.

CHAPTER 6

Cation Exchange and Spontaneous Crystal Repair Resulting in Ultrathin, Planar CdS Nanosheets

Cation exchange has become a major post-synthetic tool to obtain nanocrystals with a combination of stoichiometry, size, and shape that is challenging to achieve by direct wet-chemical synthesis. Here, we report on the transformation of highly anisotropic, ultrathin, and planar PbS nanosheets into CdS nanosheets of the same dimensions. We monitor the evolution of the Cd-for-Pb exchange by ex situ TEM, HAADF-STEM, and EDX. We observe that in the early stages of the exchange the sheets show large in-sheet voids that repair spontaneously upon further exchange and annealing, resulting in ultrathin, planar, and crystalline CdS nanosheets. After cation exchange, the nanosheets show broad sub-band gap luminescence, as often observed in CdS nanocrystals. The photoluminescence excitation spectrum reveals the heavy- and light-hole exciton features, with very strong quantum confinement and large electron-hole Coulomb energy, typical for 2D ultrathin Cd-chalcogenide nanosheets.

Based on:

Maike M. van der Sluijs, Jara F. Vliem, Jur W. de Wit, Jeppe J. Rietveld, Johannes D. Meeldijk, and Daniel A. M. Vanmaekelbergh, *Chemistry of Materials* **2023**, 35 (19), 8301-8308.

6.1 Introduction

Extensive research over the last two decades has developed cation exchange into a powerful post-synthetic tool to obtain colloidal quantum materials that are unattainable, or challenging to achieve by direct synthesis pathways. Colloidal nanocrystals (NCs) enable ion-exchange protocols with reasonable temperature and time scales (minutes to hours). The NCs feature abundant facet/solvent interfaces, and only nanometer-scale diffusion paths need to be overcome to accomplish ion replacement. Specifically, cation exchange has been used to convert NCs with an AX stoichiometry (A being the cation, X being the anion) into BX NCs. It is a process that can be used to completely exchange NCs,¹⁻³ or to form heterostructures (AX/BX) with atomically sharp interfaces and band gap offsets.⁴⁻⁶ From a crystallographic viewpoint, there are two modes of exchange. In the first mode, the new cations spread homogeneously through the crystal replacing the original cation; a type of exchange which has for instance been used for impurity doping with magnetic cations.⁷⁻⁹ In the second mode, a BX phase replaces the AX phase and heterointerfaces form when the cation exchange is arrested before completion,^{1,10,11} when the facet reactivity toward exchange varies over the structure,^{12,13} or when the AX and BX phases have immiscible crystal structures.¹⁴⁻¹⁷ To study the exchange in detail, NCs with a strong anisotropic shape are beneficial as they offer opportunities for transmission electron microscopy (TEM) monitoring of the process in a specific orientation, e.g. crystallographic domains that proceed in specific directions and atomic reconfigurations during or after the exchange process.^{10,18,19} For instance, in 2D CdSe nanoplatelets, the Pb-for-Cd exchange proceeds via PbSe crystal growth, starting from the edges of the nanoplatelets. The interface extends further into the interior upon prolonged exchange, retaining the 2D nature of the nanoplatelets while the corners and lateral dimensions lose definition.^{3,10}

Recently, there have been significant advances in the synthesis and study of ultrathin, highly anisotropic PbS nanosheets (NSs) with a deformed orthorhombic crystal structure. Despite having a thickness of only a few nanometers and lateral dimensions in the range of 100–200 nm, the PbS NSs exhibit a rectangular and planar shape, appearing completely flat in TEM without visible distortion, or curling.^{20,21} This makes them compelling candidates to study the crystallographic aspects of cation exchange. Moreover, strain within CdS NSs was previously shown to strongly perturb the band structure and induce band gap variations up to 20 meV,²² in addition to influencing the self-assembly of the NSs.^{23,24} Thus, distortion in NSs can hamper potential applications and device design. The cation exchange process might offer pathways to ultrathin CdS NSs with extended lateral dimensions and no curling, unlike NSs prepared by direct synthesis.²⁵⁻²⁸

Here, we report on a study of Cd²⁺-for-Pb²⁺ cation exchange in highly anisotropic ultrathin PbS nanosheets (NSs). We followed the incorporation of Cd²⁺ ions into the PbS NSs with ex situ TEM and energy dispersive X-ray (EDX) mapping, which shows the homogeneous distribution of the Cd²⁺ over the NSs from the early stages of exchange. It is an indication that the Cd²⁺-for-Pb²⁺ exchange occurs randomly via the top and bottom facets of the NSs with multiple nucleation points of the CdS. In the early stages of the ion exchange, the sheets show significant voids. Remarkably, this damage becomes less prominent in the ensemble upon extended annealing and exchange. Both intact and damaged CdS NSs are observed in a 1:1.5 ratio and we discuss the potential self-repair mechanism in detail. The exchanged planar CdS NSs have lateral dimensions similar to those of the parent PbS NSs, albeit with a slight increase in thickness (0.5–1 nm).

While the original narrow band gap PbS NSs show no luminescence,^{20,21} the exchanged NSs begin to show a broad luminescence peak centered around 700 nm when roughly 80% of the cations are exchanged. This large redshift with respect to the wide bulk band gap energy (2.42 eV)²⁹ indicates that trap-emission is the dominant recombination mechanism. Probing the broad emission band with excitation spectroscopy, the heavy-hole and light-hole transitions are observed at 3.1 and 3.35 eV, while the onset of free carrier absorption is at 3.8 eV. Comparing these results to the experimental results for CdS nanoplatelets,²⁵ the strong confinement energy and large electron-hole Coulomb interaction (heavy-hole at 3.1 eV versus free carrier absorption at 3.8 eV = 0.7 eV) agree with the ultrathin dimensions of 2.2 ± 0.4 nm of the CdS sheets and the low dielectric constant of the crystal and the environment.³⁰

6.2.1 Original PbS nanosheets and CdS nanosheets after cation exchange

To study the Cd^{2+} -for- Pb^{2+} cation exchange in 2D materials, we selected PbS NSs as synthesized by Akkerman et al.^{20,21} as the parent NSs (Figure 6.1a). We then followed a procedure by Casavola et al., developed for cation exchange in anisotropic PbSe/CdSe core/shell nanomaterials.¹ To PbS NSs dispersed in ODE, a cadmium oleate solution ($\text{Cd}(\text{OA})_2$) is added before heating the vial to temperatures in the range of 100–150 °C with reaction times up to 4 hours (see supporting information S6.1). After 120 minutes (min) at 100 °C, the PbS NSs with a deformed orthorhombic crystal structure have undergone a complete cation exchange to CdS

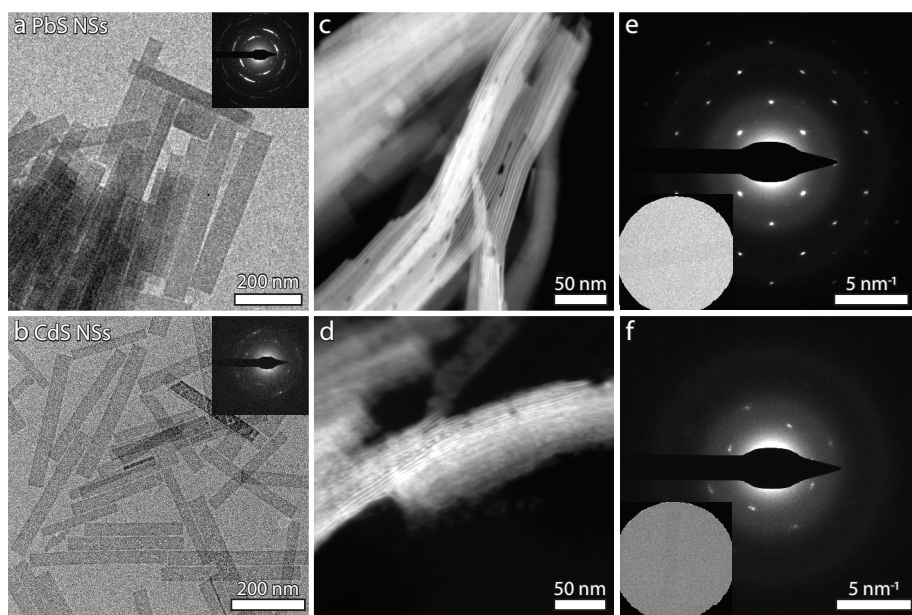


Figure 6.1 Overview TEM images of the original PbS NSs (a) and CdS NSs after 120 min of cation exchange (b); the insets show the corresponding SAED patterns. The sharp corners and lateral dimensions of the parent PbS NSs are preserved in the exchange. In panel (c) and (d), the stacked NSs show a slight increase in thickness to 2.2 ± 0.4 nm (Figure S6.2). The SAED of the overview (a and b) and the single NSs (e and f) indicate a change in crystal structure from deformed orthorhombic PbS to a CdS crystal structure with broadened diffraction maxima (see supporting information S6.2 for further discussion).

NSs. The large lateral dimensions and sharp 90° corners of the PbS NSs (**Figure 6.1a** and **b**) are generally preserved in this reaction. There is a slight reduction of the average length from 231 to 205 nm, accompanied by a small decrease in width from 37 to 30 nm (**Figure S6.1**). Moreover, despite the pronounced structural anisotropy, no visible curling or folding of the thin sheets is observed (different from directly synthesized CdS and CdSe nanoplatelets).^{25,26} By examining vertical stacks of the NSs in HAADF-STEM mode, we determined the thickness of the respective PbS and CdS sheets (**Figure 6.1c** and **d**). The parent PbS sheets were previously shown to be either 1.2 or 1.8 nm thick;²¹ while the CdS sheets are slightly thicker at 2.2 ± 0.4 nm (**Figure S6.2a**). As indicated by the selected area electron diffraction (SAED) of a single nanosheet (inset) in **Figure 6.1e** and **f**, the sharp diffraction maxima of the deformed orthorhombic crystal structure have broadened and shifted, possibly due to misalignments in the crystal structure. However, characterization of the crystal structure in the CdS NSs has been challenging due to the limited number of reflections, thin material, and similarity in potential crystal structures (see **supporting information S6.2** for further discussion).

6.2.2 Evolution of the Cd²⁺-for-Pb²⁺ ion exchange process

To monitor the cation exchange over time, experiments were performed at 100 °C for up to 120 min, sometimes with a prolonged reaction using additional Cd(OA)₂ and a higher temperature (up to 150 °C, see **supporting information S6.1**: sample 240 min high T). All intermediate reaction products were studied ex situ by HAADF-STEM and energy dispersive X-ray spectroscopy (EDX) to follow the cation exchange progression. With ensemble EDX measurements, the Cd fraction of the total cation percentage was determined. On a linear time scale, this fraction initially increases quickly, before saturating around 60 min (**Figure 6.2a**, **Table S6.5** and **Figure S6.9**). The dark green line is a fit of the Cd fractions with the first Langmuir isotherm and will be discussed below. Within one min of placing the reaction vial with Cd(OA)₂ and the parent PbS NSs (46% Pb and 54% S) in a preheated aluminum block (100 °C) the NSs contain Cd (a fraction of 0.18, green). Concurrently, the fraction of Pb decreases (with 0.16, red), indicating that the exchange begins well before the dispersion reaches the reaction temperature of 100 °C (~3 min to reach 90 °C, **Figure S6.4**). In **supporting information Table S6.6** we discuss some additional experiments that show the reaction will even start at room temperature, although higher temperatures are necessary for it to proceed. After 10 min, more than half of the cations in the sheets are Cd (a fraction of 0.65). Then, the exchange rate decreases, and complete replacement is achieved after 120 min (a fraction of 1, 46% Cd) while some residual Pb remains (fraction of 0.1, ~5 ± 2%). During the entire exchange, the S content stays between 55 and 50% (**Figure S6.9**).

With STEM-EDX mapping, we studied the distribution of the elements in the NSs (**Figure 6.2b–d**, with additional maps and quantification in **Figure S6.10**). Already after one min both Pb and Cd (red and green) are homogeneously distributed (**Figure 6.2b**). This distribution is then maintained throughout the reaction (15 min in **Figure 6.2c**), and upon complete exchange a small fraction of Pb remains. However, the residual Pb is not concentrated around the NSs and instead randomly distributed in the maps (both after 120 min at 100 °C, **Figure S6.10f**, and with a prolonged reaction at higher temperature, **Figure 6.2d**). When quantifying a single sheet (indicated by the white box in **Figure S6.10**), these maps show the same trend as the ensemble EDX measurements previously discussed (**Figure 6.2a**, **Table S6.5**).

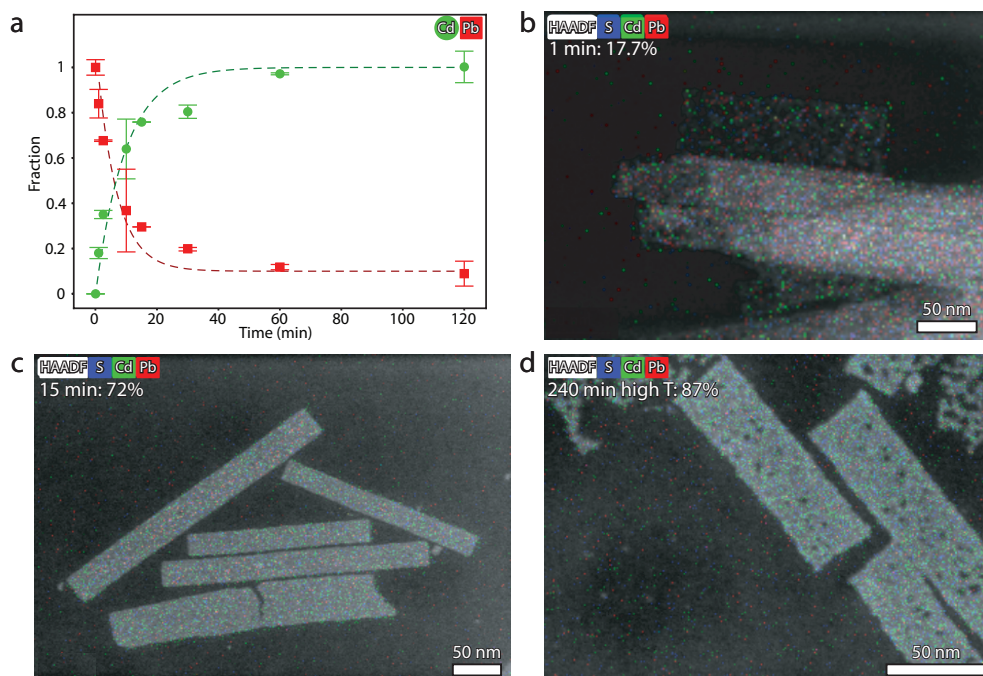


Figure 6.2 Cation exchange in the NSs was studied ex situ with ensemble EDX and STEM-EDX measurements. (a) Plot of the respective Pb and Cd fractions (normalized with respect to the percentage of Pb in the original PbS NSs) as a function of the reaction time. Initially the parent PbS NSs contain 54% S and 46% Pb. After 120 min at 100 °C, a complete Cd^{2+} -for- Pb^{2+} is achieved with 46% Cd (green) and 4% residual Pb (red). The dark green line is a fit to the cadmium fraction with the first Langmuir isotherm (\ominus). In all EDX maps (b–d), the Cd is homogeneously distributed in the NSs. In Figure S6.10 additional maps and quantification are shown.

The persistent homogeneous distribution of both cations in the sheets indicates that the Cd^{2+} -for- Pb^{2+} cation exchange does not proceed from the edges, as previously observed for 2D zinc blende CdSe nanoplatelets. There, a PbSe deposit forms at the edge of the nanoplatelet due to the strong passivation of the top and bottom facets with carboxylic acid.^{27,31} Over time these initial deposits extend into the host and the resulting nanoplatelets have a distorted lateral shape with an increased polydispersity in thickness.^{3,10,32} In the cation exchange of PbS NSs studied here, the homogeneous distribution of the elements occurs in the zone axis. Pb-for-Cd replacements can take place in two different ways: by a genuine CdS/PbS crystal interface proceeding across the NSs or alternatively by starting at individual and randomly dispersed atomic crystal positions. STEM analysis of vertically stacked sheets could be very helpful, as this would enable the study of an alternate zone axis. However, the resolution of the elemental maps of NSs in this orientation was too low due to instability in the NSs during exchange, hydrocarbon contamination (despite applied cleaning techniques)³³ and image drift (**Figure S6.11**).

Fortunately, the plot of the ensemble EDX measurements provides some insight. The increase of the cadmium fraction (θ) follows the first Langmuir function (dark green line in [Figure 6.2a](#) which is discussed in [supporting information S6.3](#)). This points to random exchanges on an atomic level, as a linear increase of the Cd fraction would be expected in case of a progressing CdS/PbS reaction front. Thus, this suggests that the rate-limiting step in the exchange is the random adsorption of the cations to appropriate surface sites, not the ion diffusion into the structure. This is reasonable, especially considering the fact that the parent PbS NSs are only 4 or 6 monolayers thick (1.2 to 1.8 nm) and thus more than 50% (4 MLs) or 33% (6 MLs) of the cations are at the surface and accessible.

6.2.3 Self-repair of CdS nanosheets

A detailed study of the intermediary products with HAADF-STEM shows that although the CdS NSs retain the rectangular shape of the parent NSs, the process of cation exchange causes many voids in the structure. Such “damaged” sheets are particularly abundant in the early stages of the reaction ([Figure 6.3a](#)). The voids in the sheets are surrounded by both amorphous and crystalline areas ([Figure 6.3b](#)), but a corresponding Fourier transform (inset) shows the uniform orientation of the crystalline domains with only a slight broadening of the diffraction maxima. This retention of orientation is reminiscent of the formation of the parent PbS NSs, where early in the synthesis crystallographic domains form with remarkable alignment of orientation in rectangular but amorphous or pseudocrystalline self-induced templates.²¹ In the early stages of the cation exchange the number of damaged sheets is high (>80%, $n = 18$ sheets after 1 and 2.5 min of reaction, see [Figure 6.3a](#), [Figure S6.14](#)). At 10 min more than >95% of the sheets are damaged ($n = 48$). However, as the exchange reaction continues, the quality of the sheets improves; the number and size of the voids in the sheets decrease, while the crystalline area increases ([Figure 6.3c](#) and [3e](#)). At the end of the exchange, 40% of the sheets are intact. Still, 60% of the NSs are damaged, although the degree of damage per NS varies greatly ([Figure S6.13](#)).

The decrease of the voids and increase in crystallinity with time reflect a remarkable self-repair of the NSs. Evidently, the ultrathin sheets experience harsh conditions in the exchange reaction. While we observe a comparative exchange of cations, a local imbalance in stabilizing ligands or cations can cause the fast deterioration of the thin sheets. The subsequent improvement in the quality of the CdS NSs indicates that a repair takes place. The CdS units necessary for the repair may originate from the same sheet (a genuine self-repair), resulting in sheets with smaller lateral dimensions. Alternatively, the required CdS units may originate from strongly damaged NSs that are sacrificed for the repair of others. This is a reasonable assumption since the percentage of damaged sheets is high. With this “parasitic repair by Ostwald ripening”, the thermodynamically more stable NSs are repaired at the expense of those that are less stable and damaged. Of course, these two mechanisms could occur concomitantly, and additional research will be necessary to understand the exact process occurring here.

6.2.4 Optical properties of the CdS nanosheets

In absorption spectra, two-dimensional CdS nanoplatelets obtained by direct wet-chemical synthesis have shown heavy-hole (HH) and light-hole (LH) excitonic transitions. The energy of these transitions depends strongly on the thickness of the platelets (bulk CdS has a band gap of 2.42 eV). In zinc blende CdS nanoplatelets, the absorption features are observed around 3.8

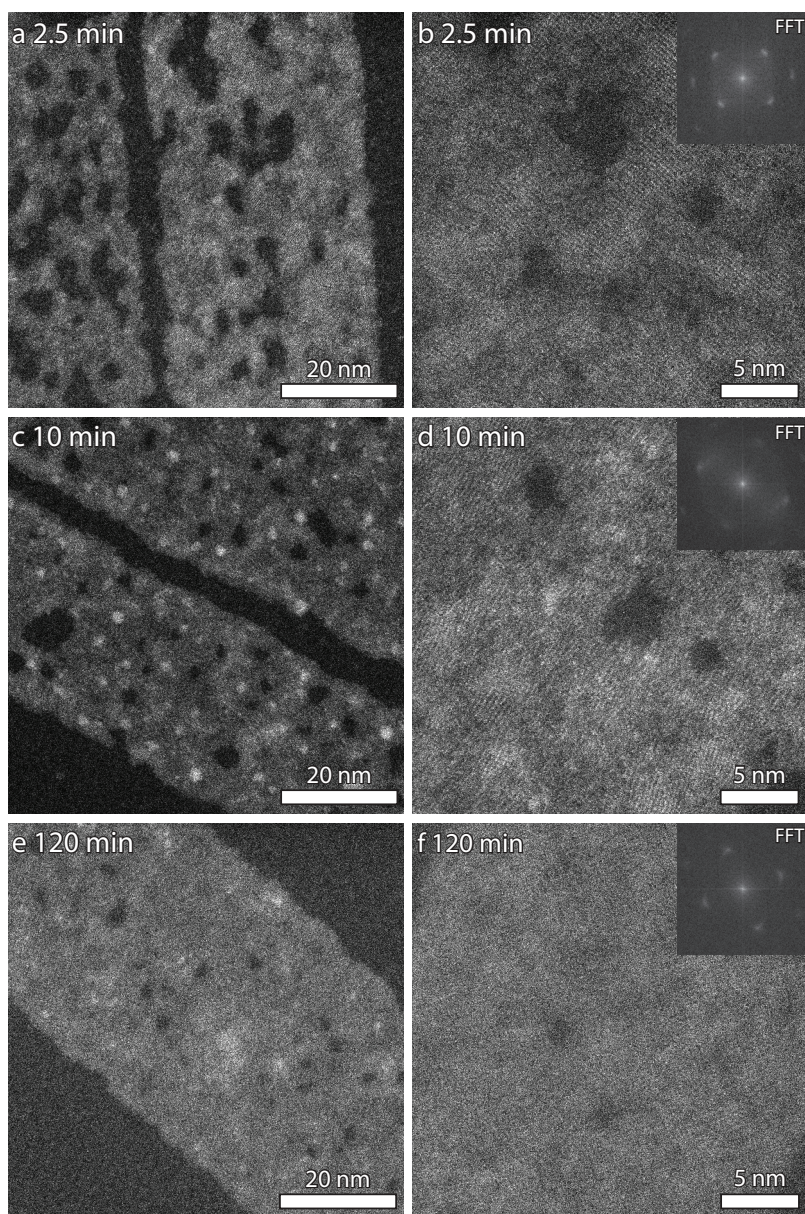


Figure 6.3 Structure and crystallinity of NSs during cation exchange. In (a) and (b) the NSs are shown with atomic resolution after 2.5 min of exchange. The sheets have large voids, connected by amorphous areas, that are still present after 10 min (c and d). After 120 min the Pb is completely exchanged, the voids have almost disappeared and the overall crystallinity of the NSs has improved (e and f).

eV (320 nm) when only ~ 1.2 nm thick, while they are around 2.8 eV (440 nm) when ~ 2 nm thick. Typically, the thinnest nanoplatelets have a very weak emission peak from their HH exciton-to-ground-state transition while there is no luminescence detected from the thickest nanoplatelets (~ 2 nm).²⁵ In addition to the band gap emission, some sub-band gap photoluminescence is observed, commonly referred to as trap emission. These charge-carrier traps are usually attributed to structural imperfections or uncoordinated (surface) atoms and a lot of research has focused on the prevention and repair of these imperfections in NCs.³⁴⁻³⁷ However, the direct study of these traps has been challenging on both an ensemble level and for individual NCs due to the heterogeneity of traps and the wide range of time scales involved in trap-related dynamics.^{38,39}

In a NS suspension, scattering by the large CdS sheets makes it difficult to extract quantitative information from the absorption spectra (Figure 6.4a). However, a clear transition is observed around 3.1 eV (400 nm) in all measurements. This is a large blueshift compared to the parent PbS NSs which showed a transition between 1.6 and 1.8 eV (indicated by the gray box).²¹ Unlike the parent PbS sheets, the exchanged CdS sheets show a broad sub-band gap luminescence transition when excited at 390 nm (Figure 6.4b). A low background of trap-emission emerges below 2 eV after 10 min of exchange (over 60% of the cations are Cd), when still more than 80% of the NSs are heavily damaged (Figure 6.3c and d). Furthermore, from 30 min onward there is an increase in trap luminescence with increasing reaction time. In the final CdS NSs (after 120–240 min at 100 °C) a broad luminescence feature is observed between 2.4 and 1.6 eV. Band-gap luminescence would be expected below 2.8 eV but is not observed in any measurement, even with an additional 120 min of annealing at 100 °C or a prolonged cation exchange at higher temperature. On the other hand, the intensity of the trap-luminescence does increase significantly (Figure S6.16).

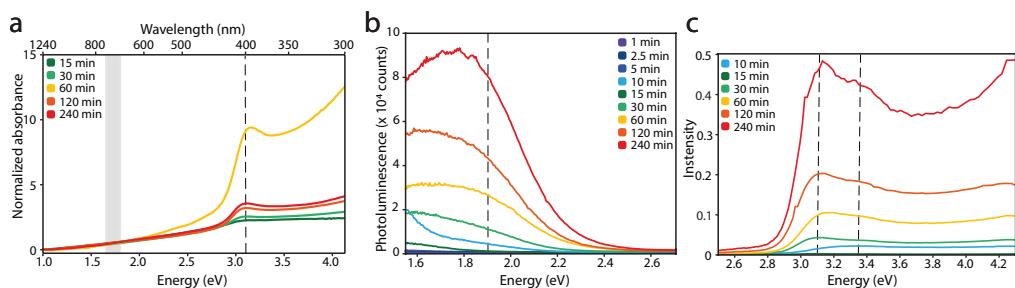


Figure 6.4 Absorption, photoluminescence, and photoluminescence excitation spectroscopy measurements were recorded for CdS NSs exchanged for 1 to 240 min at 100 °C. (a) Absorption measurements of the NSs when dispersed in hexane. Each sample displays considerable scattering at long wavelengths. For clarity, the measurements were normalized at 1.55 eV (800 nm). All CdS NSs have a transition around 3.1 eV (400 nm, indicated by the dashed line), which is a large shift when compared to the PbS sheets (1.8 eV, indicated by the gray box). (b) Photoluminescence spectra of all intermediate cation exchange samples excited at 390 nm. Initially no luminescence is observed, but after 10 min, a broad subgap emerges below 2.2 eV which increases over time. (c) The photoluminescence excitation spectra as monitored at 1.9 eV (650 nm), indicated by the dashed line in (b). The heavy-hole and light-hole exciton peaks are observed at 3.1 and 3.35 eV, respectively (indicated by the black dashed lines), while free carrier absorption starts at 3.8 eV.

To gain additional insight into the optical transitions of the CdS sheets we performed photoluminescence excitation spectroscopy for intermediate CdS/PbS structures and the final CdS NSs (Figure 6.4c). While monitoring the luminescence at 1.9 eV (650 nm), the spectra gradually show the (HH, CB) and (LH, CB) excitonic transitions and the onset of free carrier generation, typical for a 2D quantum well.²⁵ The typical heavy-hole and light-hole exciton peaks emerge at 3.1 eV and 3.35 eV respectively, and the absorption increases again after 3.8 eV. These excitonic transitions are at higher energy than those of the directly synthesized CdS platelets,²⁵ reflecting very strong confinement in the thickness direction. Moreover, the electron-hole binding energy is as high as 0.7 eV, due to the thinness of the sheets and low dielectric constant. These ultrathin CdS NSs (2.2 ± 0.4 nm) thus show strong quantum confinement and a large electron-hole binding energy. Based on the optical measurements we conclude that our CdS NSs have strong excitonic and band-to-band absorption, enhanced by a very high exciton binding energy. Emission spectroscopy shows that this only results in broad trap-emission with a large Stokes shift. To obtain excitonic photoluminescence, both structural improvement after cation exchange and improvement of the surface passivation are needed.

In summary, we have obtained colloidal CdS NSs by Cd²⁺-for-Pb²⁺ exchange in PbS NSs, with the latter having a deformed orthorhombic structure. These CdS NSs have an average thickness of 2.2 ± 0.4 nm and lateral dimensions of 205 nm by 30 nm with remarkably straight edges. The exchange process was monitored with ex situ analysis of the intermediate reaction products. The Cd²⁺-for-Pb²⁺ exchange initially progresses exponentially until saturation is achieved, similar to the case for the first Langmuir absorption isotherm. We interpreted this as the random adsorption of Cd²⁺ cations at appropriate surface sites being the rate-limiting step in the exchange, not the diffusion of cations into the ultrathin structure. In addition, EDX maps showed the continued homogeneous distribution of the Cd²⁺ ions, already from the earliest stages of the exchange. Thus, the exchange occurs via the large top and bottom facets of the NSs.

The NSs show significant damage from the early stages of cation exchange; both amorphous regions and large voids are observed within the still rectangular sheets. Upon extended cation exchange and continued annealing, these voids become less prominent in the ensemble, indicating that self-repair takes place in up to 40% of the NSs. The final CdS NSs remain planar, retaining the highly anisotropic shape with lateral dimensions similar to those of the parent PbS NSs.

While the original narrow band gap PbS NSs show no luminescence, the NSs begin to show excitonic absorption features typical for ultrathin CdS NSs after 10 min of exchange. They begin to show broad, weak luminescence centered at around 700 nm. The large redshift with respect to the band gap indicates that trap emission is the dominant radiative recombination mechanism. Upon probing the broad emission band with photoluminescence excitation spectroscopy, features of the heavy-hole and light-hole transitions are observed at 3.1 and 3.35 eV respectively, while the onset of free carrier absorption is at 3.8 eV. In conclusion, this study highlights the successful synthesis of colloidal, ultrathin, but planar CdS NSs via cation exchange. After which a self-repair mechanism results in more crystalline sheets showing trap luminescence.

References

- [1] Casavola, M.; van Huis, M. A.; Bals, S.; Lambert, K.; Hens, Z.; Vanmaekelbergh, D. Anisotropic Cation Exchange in PbSe/CdSe Core/Shell Nanocrystals of Different Geometry. *Chem. Mater.* 2011, 24 (2), 294-302. DOI: 10.1021/cm202796s.
- [2] Beberwyck, B. J.; Surendranath, Y.; Alivisatos, A. P. Cation Exchange: A Versatile Tool for Nanomaterials Synthesis. *J. Phys. Chem. C* 2013, 117 (39), 19759-19770. DOI: 10.1021/jp405989z.
- [3] Galle, T.; Khoshkhoo, M. S.; Martin-Garcia, B.; Meerbach, C.; Sayevich, V.; Koitzsch, A.; Lesnyak, V.; Eychmuller, A. Colloidal PbSe Nanoplatelets of Varied Thickness with Tunable Optical Properties. *Chem. Mater.* 2019, 31 (10), 3803-3811. DOI: 10.1021/acs.chemmater.9b01330.
- [4] Pietryga, J. M.; Werder, D. J.; Williams, D. J.; Casson, J. L.; Schaller, R. D.; Klimov, V. I.; Hollingsworth, J. A. Utilizing the Lability of Lead Selenide to Produce Heterostructured Nanocrystals with Bright, Stable Infrared Emission. *J. Am. Chem. Soc.* 2008, 130 (14), 4879-4885. DOI: 10.1021/ja710437r.
- [5] Costi, R.; Saunders, A. E.; Banin, U. Colloidal Hybrid Nanostructures: a New Type of Functional Materials. *Angew. Chem. Int. Ed.* 2010, 49 (29), 4878-4897. DOI: 10.1002/anie.200906010.
- [6] de Mello Donega, C. Synthesis and Properties of Colloidal Heteronanocrystals. *Chem. Soc. Rev.* 2011, 40 (3), 1512-1546. DOI: 10.1039/c0cs00055h.
- [7] Sahu, A.; Kang, M. S.; Kompch, A.; Notthoff, C.; Wills, A. W.; Deng, D.; Winterer, M.; Frisbie, C. D.; Norris, D. J. Electronic Impurity Doping in CdSe Nanocrystals. *Nano Lett.* 2012, 12 (5), 2587-2594. DOI: 10.1021/nl300880g.
- [8] Vlaskin, V. A.; Barrows, C. J.; Erickson, C. S.; Gamelin, D. R. Nanocrystal Diffusion Doping. *J. Am. Chem. Soc.* 2013, 135 (38), 14380-14389. DOI: 10.1021/ja4072207.
- [9] Barrows, C. J.; Chakraborty, P.; Kornowske, L. M.; Gamelin, D. R. Tuning Equilibrium Compositions in Colloidal Cd_{1-x}MnxSe Nanocrystals Using Diffusion Doping and Cation Exchange. *ACS Nano* 2016, 10 (1), 910-918. DOI: 10.1021/acsnano.5b07389.
- [10] Salzmänn, B. B. V.; Wit, J.; Li, C.; Arenas-Esteban, D.; Bals, S.; Meijerink, A.; Vanmaekelbergh, D. Two-Dimensional CdSe-PbSe Heterostructures and PbSe Nanoplatelets: Formation, Atomic Structure, and Optical Properties. *J. Phys. Chem. C* 2022, 126 (3), 1513-1522. DOI: 10.1021/acs.jpcc.1c09412.
- [11] Zhang, J.; Chernomordik, B. D.; Crisp, R. W.; Kroupa, D. M.; Luther, J. M.; Miller, E. M.; Gao, J.; Beard, M. C. Preparation of Cd/Pb Chalcogenide Heterostructured Janus Particles via Controllable Cation Exchange. *ACS Nano* 2015, 9 (7), 7151-7163. DOI: 10.1021/acsnano.5b01859.
- [12] Sadtler, B.; Demchenko, D. O.; Zheng, H.; Hughes, S. M.; Merkle, M. G.; Dahmen, U.; Wang, L. W.; Alivisatos, A. P. Selective Facet Reactivity During Cation Exchange in Cadmium Sulfide Nanorods. *J. Am. Chem. Soc.* 2009, 131 (14), 5285-5293. DOI: 10.1021/ja809854q.
- [13] Hewavitharana, I. K.; Brock, S. L. When Ligand Exchange Leads to Ion Exchange: Nanocrystal Facets Dictate the Outcome. *ACS Nano* 2017, 11 (11), 11217-11224. DOI: 10.1021/acsnano.7b05534.
- [14] Son, D. H.; Hughes, S. M.; Yin, Y.; Paul Alivisatos, A. Cation Exchange Reactions in Ionic Nanocrystals. *Science* 2004, 306 (5698), 1009-1012. DOI: 10.1126/science.1103755.
- [15] Bals, S.; Casavola, M.; van Huis, M. A.; Van Aert, S.; Batenburg, K. J.; Van Tendeloo, G.; Vanmaekelbergh, D. Three-Dimensional Atomic Imaging of Colloidal Core-Shell Nanocrystals. *Nano Lett.* 2011, 11 (8), 3420-3424. DOI: 10.1021/nl201826e.
- [16] De Trizio, L.; Manna, L. Forging Colloidal Nanostructures via Cation Exchange Reactions. *Chem. Rev.* 2016, 116 (18), 10852-10887. DOI: 10.1021/acs.chemrev.5b00739.
- [17] Jia, G.; Pang, Y.; Ning, J.; Banin, U.; Ji, B. Heavy-Metal-Free Colloidal Semiconductor Nanorods: Recent Advances and Future Perspectives. *Adv. Mater.* 2019, 31 (25), e1900781. DOI: 10.1002/adma.201900781.
- [18] Grodzińska, D.; Pietra, F.; van Huis, M. A.; Vanmaekelbergh, D.; de Mello Donega, C. Thermally Induced Atomic Reconstruction of PbSe/CdSe Core/Shell Quantum Dots into PbSe/CdSe Bi-hemisphere Hetero-nanocrystals. *J. Mater. Chem.* 2011, 21 (31). DOI: 10.1039/c0jm04458j.
- [19] Miszta, K.; Dorfs, D.; Genovese, A.; Kim, M. R.; Manna, L. Cation Exchange Reactions in Colloidal Branched Nanocrystals. *ACS Nano* 2011, 5 (9), 7176-7183. DOI: 10.1021/nn201988w.
- [20] Akkerman, Q. A.; Martín-García, B.; Buha, J.; Almeida, G.; Toso, S.; Marras, S.; Bonaccorso, F.; Petralanda, U.; Infante, I.; Manna, L. Ultrathin Orthorhombic PbS Nanosheets. *Chem. Mater.* 2019, 31 (19), 8145-8153. DOI: 10.1021/acs.chemmater.9b02914.
- [21] van der Sluijs, M. M.; Salzmänn, B. B. V.; Arenas Esteban, D.; Li, C.; Jannis, D.; Brafine, L. C.; Laning, T. D.; Reinders, J. W. C.; Hijmans, N. S. A.; Moes, J. R.; et al. Study of the Mechanism and Increasing Crystallinity in the Self-Templated Growth of Ultrathin PbS Nanosheets. *Chem. Mater.* 2023, 35 (7), 2988-2998. DOI: 10.1021/acs.chemmater.3c00300.
- [22] Montazeri, M.; Smith, L. M.; Jackson, H. E.; Yarrison-Rice, J. M.; Choi, Y.-J.; Park, J.-G. Raman Stress Mapping of CdS Nanosheets. *Appl. Phys. Lett.* 2009, 95 (8). DOI: 10.1063/1.3211121.

- [23] Kim, W. D.; Yoon, D.-E.; Kim, D.; Koh, S.; Bae, W. K.; Chae, W.-S.; Lee, D. C. Stacking of Colloidal CdSe Nanoplatelets into Twisted Ribbon Superstructures: Origin of Twisting and Its Implication in Optical Properties. *J. Phys. Chem. C* 2019, 123 (14), 9445-9453. DOI: 10.1021/acs.jpcc.8b09987.
- [24] Guillemeney, L.; Lermusiaux, L.; Landaburu, G.; Wagnon, B.; Abecassis, B. Curvature and Self-Assembly of Semi-Conducting Nanoplatelets. *Commun. Chem.* 2022, 5 (1), 7. DOI: 10.1038/s42004-021-00621-z.
- [25] Ithurria, S.; Tessier, M. D.; Mahler, B.; Lobo, R. P.; Dubertret, B.; Efron, A. L. Colloidal Nanoplatelets with Two-Dimensional Electronic Structure. *Nat. Mater.* 2011, 10 (12), 936-941. DOI: 10.1038/nmat3145.
- [26] Hutter, E. M.; Bladt, E.; Goris, B.; Pietra, F.; van der Bok, J. C.; Boneschanscher, M. P.; de Mello Donega, C.; Bals, S.; Vanmaekelbergh, D. Conformal and Atomic Characterization of Ultrathin CdSe Platelets with a Helical Shape. *Nano Lett.* 2014, 14 (11), 6257-6262. DOI: 10.1021/nl5025744.
- [27] Dufour, M.; Qu, J.; Greboval, C.; Methivier, C.; Lhuillier, E.; Ithurria, S. Halide Ligands To Release Strain in Cadmium Chalcogenide Nanoplatelets and Achieve High Brightness. *ACS Nano* 2019, 13 (5), 5326-5334. DOI: 10.1021/acsnano.8b09794.
- [28] Diroll, B. T.; Guzelurk, B.; Po, H.; Dabard, C.; Fu, N.; Makke, L.; Lhuillier, E.; Ithurria, S. 2D II-VI Semiconductor Nanoplatelets: From Material Synthesis to Optoelectronic Integration. *Chem. Rev.* 2023, 123 (7), 3543-3624. DOI: 10.1021/acs.chemrev.2c00436.
- [29] Niles, D. W.; Hochst, H. Band Offsets and Interfacial Properties of Cubic CdS Grown by Molecular-Beam Epitaxy on CdTe(110). *Phys. Rev. B* 1990, 41 (18), 12710-12719. DOI: 10.1103/physrevb.41.12710.
- [30] Delerue, C.; Lannoo, M. Nanostructures: Theory and Modelling; Springer Berlin Heidelberg, 2004. DOI: 10.1007/978-3-662-08903-3.
- [31] Antanovich, A.; Achtstein, A. W.; Matsukovich, A.; Prudnikau, A.; Bhaskar, P.; Gurin, V.; Molinari, M.; Artemyev, M. A Strain-Induced Exciton Transition Energy Shift in CdSe Nanoplatelets: The Impact of an Organic Ligand Shell. *Nanoscale* 2017, 9 (45), 18042-18053. DOI: 10.1039/c7nr05065h.
- [32] Galle, T.; Spittel, D.; Weiss, N.; Shamraienko, V.; Decker, H.; Georgi, M.; Hubner, R.; Metzkw, N.; Steinbach, C.; Schwarz, D.; et al. Simultaneous Ligand and Cation Exchange of Colloidal CdSe Nanoplatelets Toward PbSe Nanoplatelets for Application in Photodetectors. *J. Phys. Chem. Lett.* 2021, 5214-5220. DOI: 10.1021/acs.jpcllett.1c01362.
- [33] Li, C.; Tardajos, A. P.; Wang, D.; Choukroun, D.; Van Daele, K.; Breugelmans, T.; Bals, S. A Simple Method to Clean Ligand Contamination on TEM Grids. *Ultramicroscopy* 2021, 221, 113195. DOI: 10.1016/j.ultramic.2020.113195.
- [34] Hanifi, D. A.; Bronstein, N. D.; Koscher, B. A.; Nett, Z.; Swabeck, J. K.; Takano, K.; Schwartzberg, A. M.; Maserati, L.; Vandewal, K.; van de Burgt, Y.; et al. Redefining Near-Unity Luminescence in Quantum Dots with Photothermal Threshold Quantum Yield. *Science* 2019, 363 (6432), 1199-1202. DOI: 10.1126/science.aat3803.
- [35] van der Stam, W.; Grimaldi, G.; Geuchies, J. J.; Gudjonsdottir, S.; van Uffelen, P. T.; van Overeem, M.; Brynjarsson, B.; Kirkwood, N.; Houtepen, A. J. Electrochemical Modulation of the Photophysics of Surface-Localized Trap States in Core/Shell/(Shell) Quantum Dot Films. *Chem. Mater.* 2019, 31 (20), 8484-8493. DOI: 10.1021/acs.chemmater.9b02908.
- [36] Hartley, C. L.; Kessler, M. L.; Dempsey, J. L. Molecular-Level Insight into Semiconductor Nanocrystal Surfaces. *J. Am. Chem. Soc.* 2021, 143 (3), 1251-1266. DOI: 10.1021/jacs.0c10658.
- [37] Liu, X.; Fu, T.; Liu, J.; Wang, Y.; Jia, Y.; Wang, C.; Li, X.; Zhang, X.; Liu, Y. Solution Annealing Induces Surface Chemical Reconstruction for High-Efficiency PbS Quantum Dot Solar Cells. *ACS Appl. Mater. Interfaces* 2022, 14 (12), 14274-14283. DOI: 10.1021/acsam.2c01196.
- [38] Hinterting, S. O. M.; Salzmann, B. B. V.; Vonk, S. J. W.; Vanmaekelbergh, D.; Weckhuysen, B. M.; Hutter, E. M.; Rabouw, F. T. Single Trap States in Single CdSe Nanoplatelets. *ACS Nano* 2021, 15 (4), 7216-7225. DOI: 10.1021/acsnano.1c00481.
- [39] Rabouw, F. T.; van der Bok, J. C.; Spinicelli, P.; Mahler, B.; Nasilowski, M.; Pedetti, S.; Dubertret, B.; Vanmaekelbergh, D. Temporary Charge Carrier Separation Dominates the Photoluminescence Decay Dynamics of Colloidal CdSe Nanoplatelets. *Nano Lett.* 2016, 16 (3), 2047-2053. DOI: 10.1021/acs.nanolett.6b00053.

S6 Supporting Information

S6.1 Experimental methods and characterization

Chemicals

Acetonitrile (ACN, anhydrous, 99.8%), 1-butanol (BuOH) 99.8%, cadmium acetate dihydrate ($\text{Cd}(\text{Ac})_2 \cdot 3\text{H}_2\text{O}$), lead(II) thiocyanate ($\text{Pb}(\text{SCN})_2$ 99.5%), methanol (MeOH, 99.8%), 1-octadecene (ODE, 90%), oleic acid (OA, 90%), oleylamine (OLAM, 99%), selenium powder (Se mesh, 99.99%) and tetrachloroethylene (TCE) were purchased from Sigma-Aldrich. Toluene (anhydrous, 99.8%) was purchased from Alfa Aesar.

Lead sulfide nanosheet synthesis

Lead sulfide (PbS) nanosheets (NSs) were prepared following a previously reported synthesis procedure by Akkerman et al.¹ In a typical synthesis, 32.3 mg (0.1 mmol) $\text{Pb}(\text{SCN})_2$ was added to a 25 mL three-neck flask with 223.8 mg (0.250 mL) OA, 101.6 mg (0.125 mL) OLAM and 7.9 g (10 mL) ODE. To dissolve the $\text{Pb}(\text{SCN})_2$ the flask was capped with a Vigreux, two septa and heated in air to 110 °C for 30 minutes (oxygen is necessary for the decomposition). Then, the temperature was quickly raised to 165 °C at a rate of ~15 °C per minute. Around 155 °C the transparent reaction mixture turns light brown, and when the temperature reaches 165 °C the flask is quickly cooled with a water bath. The NSs were washed by centrifugation at 2750 RPM (840 RCF), the clear supernatant was removed, and the precipitate was redispersed in 5 mL toluene. As an additional washing step, 5 mL of acetonitrile was added before centrifuging again at 2750 RPM. The supernatant was removed and the precipitate was redispersed in 5 mL toluene.² See [Figure S6.1](#) and [S6.2](#) for the characterization of the PbS NSs.

Cation exchange of the lead sulfide nanosheets to cadmium sulfide nanosheets

A 0.35 M solution of $\text{Cd}(\text{OA})_2$ was prepared following a procedure by Casavola et al.,³ which results in an excess of OA remaining in the precursor. From the PbS NSs dispersion, 2 mL was dried in vacuum and the sheets were redispersed in 5 mL ODE by sonication. In a N₂ filled glovebox, an aluminium block with a reference vial containing 7 mL ODE and a thermometer was heated to the desired reaction temperature (usually 100 °C). When the temperature of the block had stabilized, a stirring bar and 2 mL of a 0.35 M $\text{Cd}(\text{OA})_2$ solution was added to the prepared PbS NSs. The experiment time starts when the vial is placed in the pre-heated block, where the PbS NSs were kept for the duration of the reaction (1, 2.5, 10, 15, 30, 60, 120 or 240 minutes) and then allowed to cool to room temperature. At longer reaction times, the initially dark brown dispersion changes color to light brown or even orange ([Figure S6.3](#)). It is important to note that it takes about 3 minutes until the dispersion reaches 90 °C, and another 10 minutes to reach 100 °C ([Figure S6.4](#) shows a temperature trace).

In addition to the standard cation exchange procedure discussed above, more experiments were performed with varied reaction parameters. An important additional experiment, consisted of adding 0.25 mL 0.35 M $\text{Cd}(\text{OA})_2$ after 2 hours at 100 °C, followed by a temperature increase to 130 °C for one hour. Then, another 0.25 mL $\text{Cd}(\text{OA})_2$ was added before another temperature increase to 150 °C for the final hour. The resulting dispersion has a distinct yellow colour ([Figure S6.3](#)). When discussed, the results from this cation exchange procedure will be referred to as “240 min high temperature” (240 min high T). All through these experiments, it

is important to note that occasionally formed by-products of the PbS NSs synthesis are rock salt PbS cubes (~16.7 nm) and thicker 2D “bones”. As these side-products undergo the cation exchange procedure, they retain the majority of their Pb center while surrounded completely exchanged NSs (Figure S6.17).

As the dispersion had cooled to room temperature, the vial was centrifuged at 2750 RPM for 10 minutes. The clear supernatant was removed by pipet and the precipitate was redispersed in 1 mL toluene. Then, 1 ml methanol and 2 mL butanol were added as an antisolvent and the dispersion was again centrifuged at 2750 RPM for 10 minutes. The precipitate was redispersed in 1 mL of toluene. This washing step was repeated when needed.

Characterization

TEM samples were prepared by dropcasting a dilute dispersion of NCs on carbon-coated copper formvar TEM grids. To induce stacking of the sheets MeOH/BuOH (1:2) was added to the dispersion before dropcasting. An edge-up, stacked orientation of the sheets was achieved which allows for imaging in the lateral direction of the PbS sheets. To reduce hydrocarbon contamination during imaging, the TEM sample was treated with EtOH and activated carbon following a previously published procedure.⁴ BF-TEM imaging was performed on a Thermo Fisher Talos L120C, or on a Fei Talos F200X operating at respectively 120 and 200 keV. Low-resolution HAADF-STEM images were acquired on a Fei Talos F200X operating at 200 keV. Atomically resolved high-resolution HAADF-STEM imaging was performed on a double aberration-corrected Thermo Fisher Spectra 300, operating at an accelerating voltage of 300 keV.

UV/Vis absorption spectra were measured on a PerkinElmer 950 UV/Vis/NIR spectrophotometer with quartz cuvettes. The samples for these measurements were prepared by drying the NSs in vacuum, after which they were redispersed in 2 mL hexane. Photoluminescence measurements were performed on an Edinburgh Instruments FLS920 spectrometer equipped with TMS300 monochromators and a 450 W Xe lamp. To all samples dispersed in 1 mL of toluene, we added an additional mL of toluene before transferring the sample to a quartz cuvette. With an excitation wavelength of 390 nm, the measurements were performed from 420 to 800 nm in steps of 2 nm with a dwell time of 1 second, an excitation slit width of 10 nm and emission slit width of 5 nm. A 416 nm longpass filter was placed in the emission path. Photoluminescence excitation measurements were performed with the same setup without the filter, by monitoring the emission at 650 nm upon excitation from 260 to 500 nm. A step size of 2 nm, dwell time of 1 second and 10 nm slit width were used. The recorded emission spectra were corrected for the spectral responsivity of the detectors and monochromators.

Proton nuclear magnetic resonance (¹H-NMR) measurements were performed using an Agilent MRF400 equipped with a OneNMR probe and Optima Tune system. Spectra were recorded according to the following parameters: 400 MHz, CDCl₃, 25 °C. In short, 0.6 mL of the CdS NSs dispersion was dried and redispersed in 0.6 mL CDCl₃. The samples were then measured with a long relaxation delay (25 s) to allow complete relaxation.^{5,6}

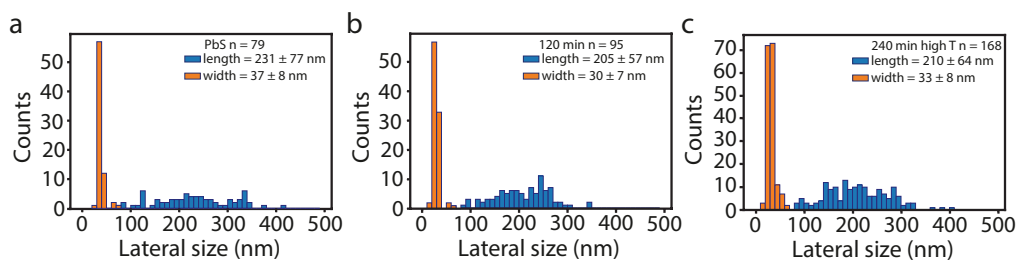


Figure S6.1 The lateral dimensions of the NSs were determined from HAADF-STEM images for the parent PbS NSs (a) and after undergoing cation exchange (b and c). The histograms have a bin size of 10 nm. (a) The parent PbS NSs have an average length of 231 ± 77 nm and width of 37 ± 8 nm. As these PbS NSs undergo cation exchange for 120 minutes at 100°C (b), or even for a prolonged reaction at higher temperature (c and see supporting information S6.1) the average length decreases to 205 ± 57 and 210 ± 64 nm. This decrease is predominantly due to a decline in the number of NSs longer than 300 nm. In addition, a slight decrease in width is observed as well, although still within the reported NS dimensions.

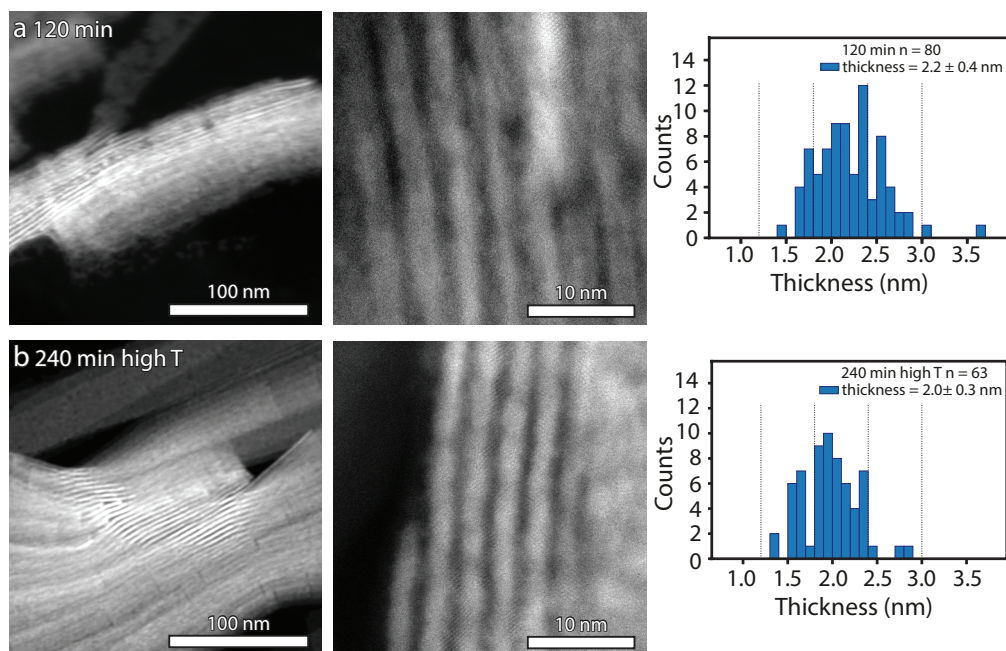


Figure S6.2 The thickness of the parent PbS NSs was previously reported to be a 1:1 population of 1.2 and 1.8 nm (4 or 6 orthorhombic monolayers respectively).² After cation exchange, both with the 120 minutes and the 240 min high temperature procedure, the average thickness has increased towards 2.2 ± 0.4 nm (a) and 2.0 ± 0.3 nm (in b). In TEM images it is clearly observed that both thicker and thinner areas are present; for characterization we measured the thicker areas of the NSs.



Figure S6.3 Pictures of the PbS NSs before (a) and after cation exchange (b and c). The initially dark brown dispersion turns light brown or orange, or even yellow in case of prolonged reaction times at higher temperatures. After purification, these colors are retained (c).

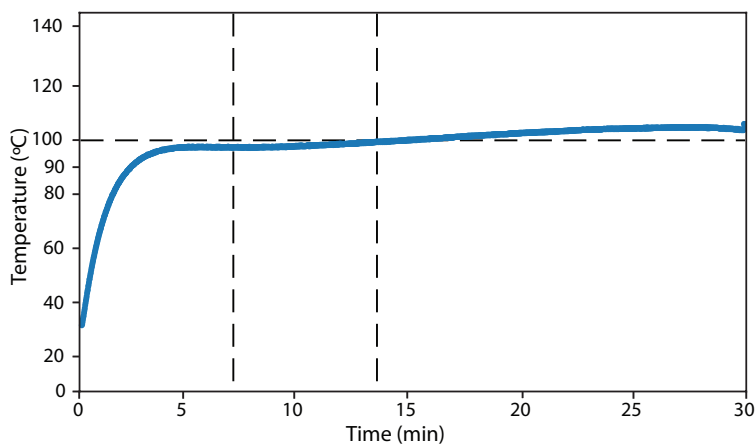


Figure S6.4 The temperature trace of a vial containing 7 mL ODE upon placement in a preheated (100 °C) aluminium block at time 0. It takes about 3 minutes for the solution to reach 90 °C, but another 10 minutes to fully reach 100 °C.

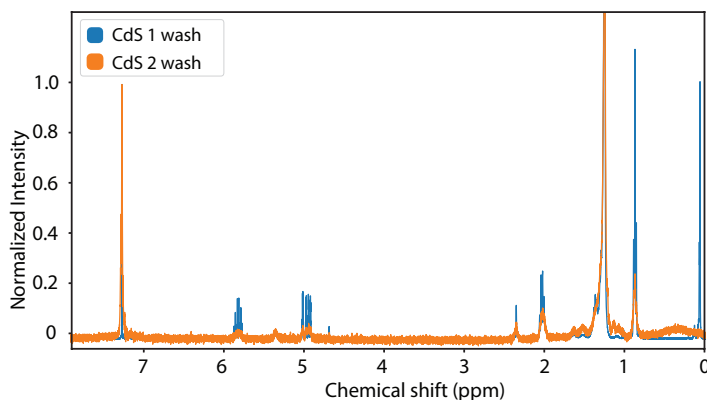


Figure S6.5 $^1\text{H-NMR}$ spectra of exchanged CdS NSs (120 min) after 1 and 2 rounds of purification (Supporting information S6.1). Table S6.1 gives an overview of each peak. ODE is still present in the dispersion after 1 washing step (the sharp resonances at 5.8 and 4.9 ppm). The small 5.3 ppm resonance is attributed to the presence of OA. The relatively sharp peak does not show broadening due to binding to the surface of the NSs, as was previously observed both in 3D and 2D materials.⁷⁻⁹ After the second washing step both the OA and ODE features decrease.

Table S6.1 List of the resonances observed in Figure S6.5 and attributed to the protons present in the CdS dispersion. Note that thiocyanate, the ligand on the parent PbS NSs does not contain any protons and therefore cannot be characterized with $^1\text{H-NMR}$.

Chemical shift (ppm)	Corresponds to	Group
0.9	OA, ODE	-CH ₃
1.3	OA, ODE	-CH ₂
2.0	OA, ODE	-CH ₂ , -NH ₂
2.3	OA	O=C-CH ₃
4.9	ODE	=CH ₂
5.3	OA	-HC=CH-
5.8	ODE	-CH=CH ₂
7.3	CDCl ₃	-

S6.2 Crystal structure of the CdS NSs

Table S6.2 The interplanar distances corresponding to the peak positions in Figure S6.7.

Crystal structure	Compound	ICSD #	a (Å)	b (Å)	c (Å)
Deformed orthorhombic	PbS	14945	11.9	4.22	4.22
Orthorhombic	CdS	600773	3.471	4.873	3.399
Rock salt	CdS	52825	5.3	5.3	5.3
Wurzite	CdS	154186	4.1365	4.1365	6.7160
Zinc blende	CdS	81925	5.830	5.830	5.830

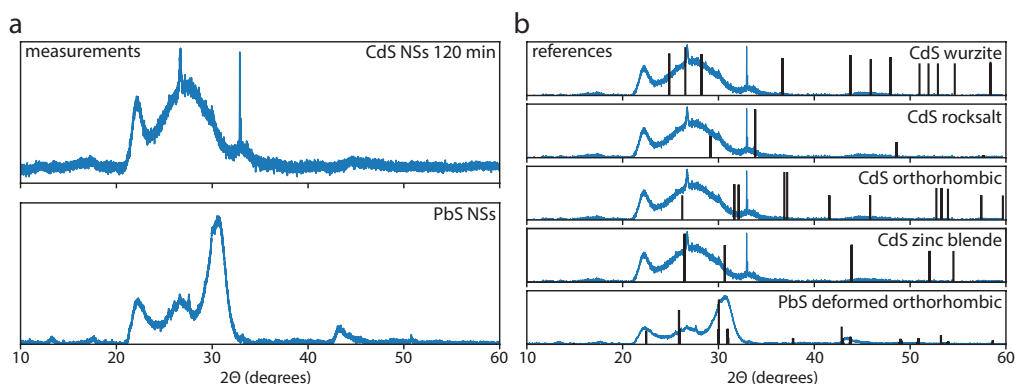


Figure S6.6 (a) For XRD measurements, the PbS NSs (bottom) and CdS NSs (top) dispersions were drop-casted on a silicon wafer. The parent PbS NSs pattern has broad peaks between 20° and 35°, and the CdS NSs pattern has very similar peaks that are further broadened and shifted to slightly higher degrees. (b) When comparing the XRD measurements to reference data of the deformed orthorhombic crystal structure (ICSD: 14945), the peak position of the PbS NSs fits quite well. However, the relative intensity of the experimental peaks does not match, which could be due to some preferred orientation of the NSs. We compare the CdS NSs to potential crystal structure candidates: being zinc blende (ICSD: 81925), orthorhombic (ICSD: 600773), rock salt (ICSD: 528255) and wurzite (ICSD: 154186), but no pattern fits completely. Although wurzite and zinc blende result in better fits than the other structures. Specifically, the reflection at 22° only corresponds exclusively to the deformed orthorhombic PbS crystal structure. A possible explanation could be residual PbS, but the intensity is high when compared to EDX measurements (Table S6.5 residual Pb of only ~5%).

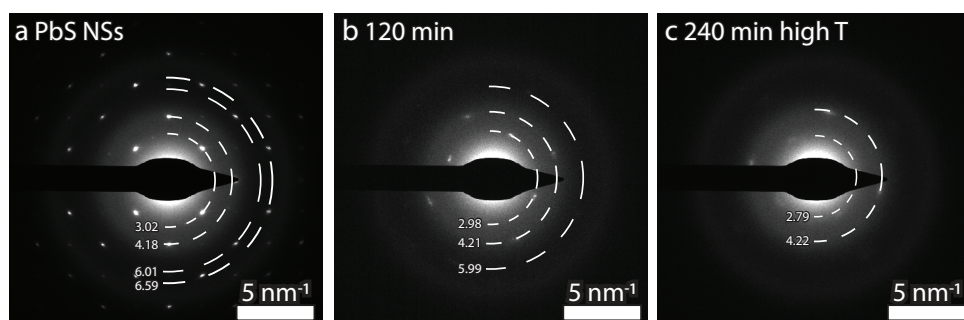


Figure S6.7 The SAED patterns of the single NSs in Figure 6.1 were azimuthally integrated with CrystBox software.⁵ In all diffractograms each ring has been labelled with the peak position, $2\pi/d$ in nm^{-1} . The interplanar distances corresponding to these values are listed in Table S6.3.

Table S6.3 The interplanar distances corresponding to the peak positions in Figure S6.7.

PbS (Å)	CdS 120 min (Å)	CdS 240 min high T (Å)
3.31	3.35	3.59
2.39	2.38	2.37
1.66	1.67	-
1.52	-	-

Due to the 2D ultrathin nature of the NSs studied here, many of the reflections ordinarily observed in XRD and SAED are lacking. As we only observe 2 or 3 rings clearly in SAED it has been challenging to assign a crystal structure to the CdS NSs. In **Table S6.4** we have indicated potential lattice spacings in bold (within 0.07 \AA) for each potential crystal structure of the CdS NSs (b and c in **Figure S6.7**). The deformed orthorhombic crystal structure of the parent PbS NSs overlaps with the 2.38 and 1.67 lattice spacings but is lacking the 3.35. All other candidates have lattice spacings similar to the CdS NSs, although the orthorhombic and wurzite structure have the most overlap. We therefore cannot definitively assign a crystal structure to the CdS NSs. In view of the fact that the CdS sheets are very thin, and the parent PbS sheets have a deformed orthorhombic crystal structure it is not unthinkable that the strain of the ligands induces deformation from a conventional structure.

Table S6.4 The d-spacings of the potential crystal structures of the NSs observed in Figure 6.1, Figure S6.7. We have selected the potential lattice spacings observed in the CdS samples from Table S6.3 within 0.07, to compensate for the manual calibration of the Crystbox software.

CdS NSs SAED (Å)	Deformed orthorhombic (Å)	Orthorhombic (Å)	Wurzite (Å)	Zinc blende (Å)	Rock salt (Å)
3.35	3.96	3.40 (001)	3.58 (100)	3.37 (111)	3.06
2.38	3.44	2.82	3.36 (002)	2.92	2.65
1.67	2.97	2.79	3.16	2.06	1.87
-	2.88	2.44	2.45 (012)	1.76	1.6 (311)
-	2.66	2.43 (101)	2.06	1.68 (222)	-
-	2.43 (410)	2.17	1.98	-	-
-	2.38 (311)	1.74	1.90	-	-
-	2.11	1.72 (121)	1.79	-	-
-	1.65 (611)	1.70 (002)	1.76	-	-
-	1.57 (701)	1.60	1.73	-	-
-	-	1.55	1.68 (004)	-	-
-	-	-	1.58	-	-

S6.3 Compositional analysis with EDX

The compositional analysis of the cation exchange at different stages has been performed by Energy dispersive X-ray Spectroscopy (EDX) analysis. EDX spectra were acquired for samples deposited on a TEM grid prepared as discussed in [supporting information S6.1](#). [Figure S6.8](#) shows the representative spectra of PbS NSs and exchanged CdS NSs (240 min high T).

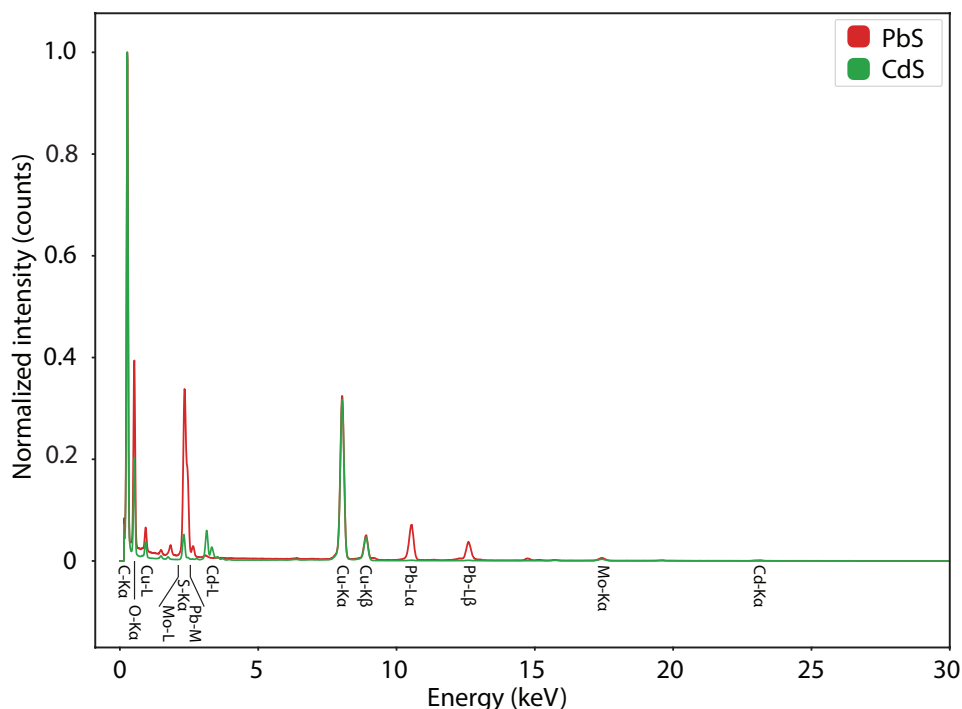


Figure S6.8 Representative bulk EDX measurements of the parent PbS NSs and exchanged CdS NSs on copper formvar-carbon TEM grids. To quantify the elements the S-K α lines, the Pb-L α lines and Cd-L α lines were used, as these have limited overlap with other elements. In some measurements, a small amount of molybdenum was detected, which is possibly due to some parts of the microscope.

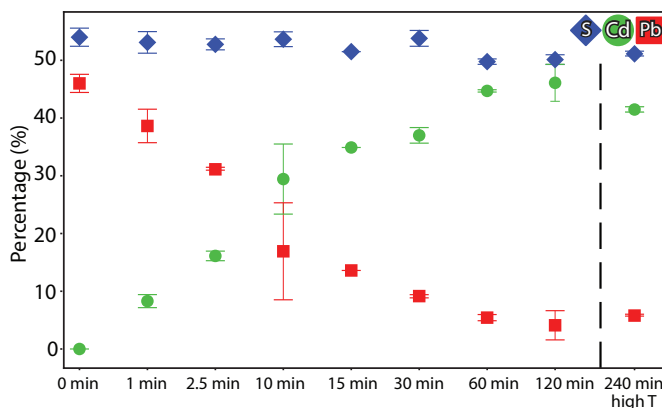
In [Table S6.5](#) we report the quantification of the bulk EDX measurements. Each individual measurement has an uncertainty of $\pm 5\%$, but in the table we report the average percentage of each element and the standard deviation based on measuring at least 3 different areas on the TEM grids (except for the 15 minutes sample). In the last column of the table we report the percentage of cation exchange (% CE), determined as the percentage of cadmium over the total fraction of cations in the sheets at that stage.

Table S6.5 The average bulk EDX results for all experiments performed at 100 °C.

Bulk EDX measurements 100°C	% Cd	% Pb	% S	% CE (% Cd of cations)
0 min (n=3)	0	46 ± 1.57	54 ± 1.57	0
1 min (n=3)	8.29 ± 1.13	38.63 ± 2.9	53.1 ± 1.87	17.7
2.5 min (n=3)	16.12 ± 0.83	31.12 ± 0.15	52.76 ± 0.95	35.1
10 min (n=6)	29.43 ± 6.07	16.92 ± 8.4	53.65 ± 1.28	63.5
15 min (n=1)	34.9	13.6	51.5	72
30 min (n=3)	37 ± 1.35	9.16 ± 0.13	53.8 ± 1.37	80.2
60 min (n=3)	44.7 ± 0.2	5.43 ± 0.54	49.77 ± 0.47	89.2
120 min (n=6)	46.1 ± 3.2	4.1 ± 2.53	50.12 ± 0.84	91.8
-	-	-	-	-
240 min high T (n=3)	42.03 ± 0.49	6.09 ± 0.16	51.83 ± 0.4	87.3

Table S6.6 The average bulk EDX results for additional low temperature cation exchange experiments. At lower temperatures (room temperature or 50 °C for 120 minutes) the cation exchange proceeds at a slower rate and does not result in complete exchange.

Bulk EDX measurements	% Cd	% Pb	% S	% CE
Room temperature 120 min (n=3)	5.55 ± 0.38	38.23 ± 0.86	56.23 ± 0.55	12.7
50 °C 120 min (n=3)	7.18 ± 0.14	35.1 ± 0.62	57.7 ± 0.56	17

**Figure S6.9** The percentages of sulfur, lead and cadmium as reported in Table S6.5 are plotted over time. The PbS NSs initially contain 54% sulfur and 46% lead and after 120 minutes at 100 °C a complete Cd²⁺-for-Pb²⁺ is achieved. After 60 minutes of cation exchange a small decrease in sulfur is observed (from ~55% to 50%).

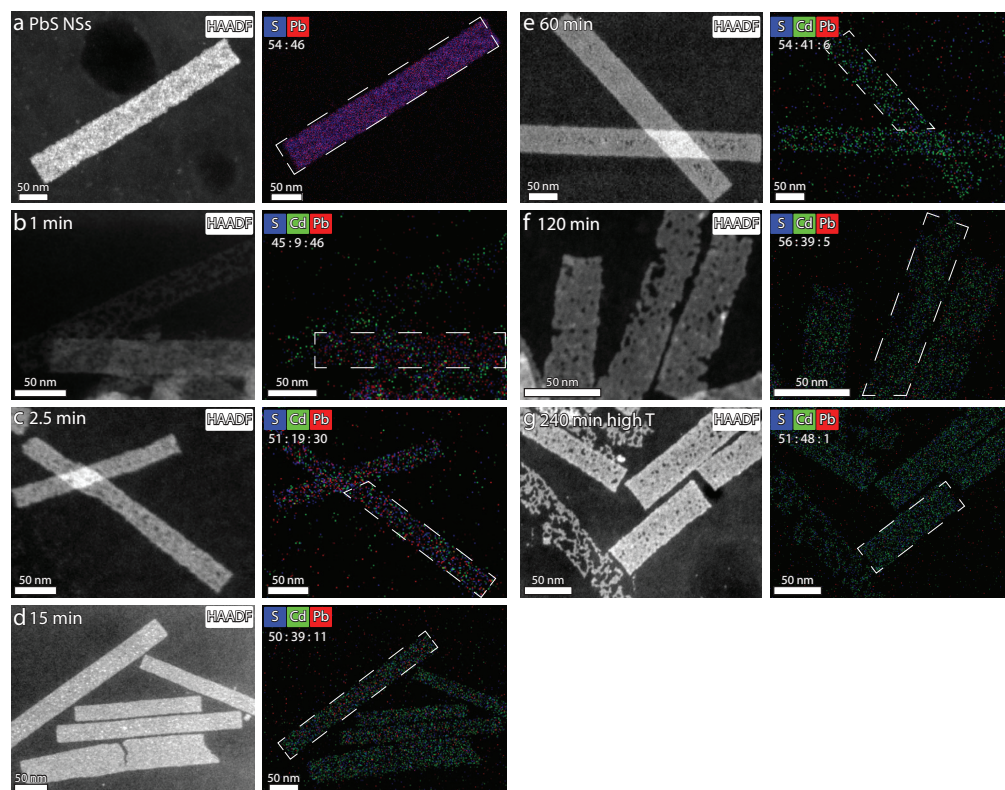


Figure S6.10 HAADF-STEM images (left) and their corresponding EDX maps (right). The single NSs as indicated by the white boxes are quantified and the elemental contents are reported in the top left of each map. These single NSs follow the same trend as the bulk EDX measurements reported in Table S5. Note that this technique provides information about single (or a few) NSs, but does not contain ensemble information. During the cation exchange, each map (b-g) shows a homogeneous distribution of cadmium and lead within the sheets. Late in the exchange (f-g), the remaining lead ions are primarily present in the background of the maps. We observe both intact and damaged NSs in the HAADF-STEM images, we will discuss this further below.

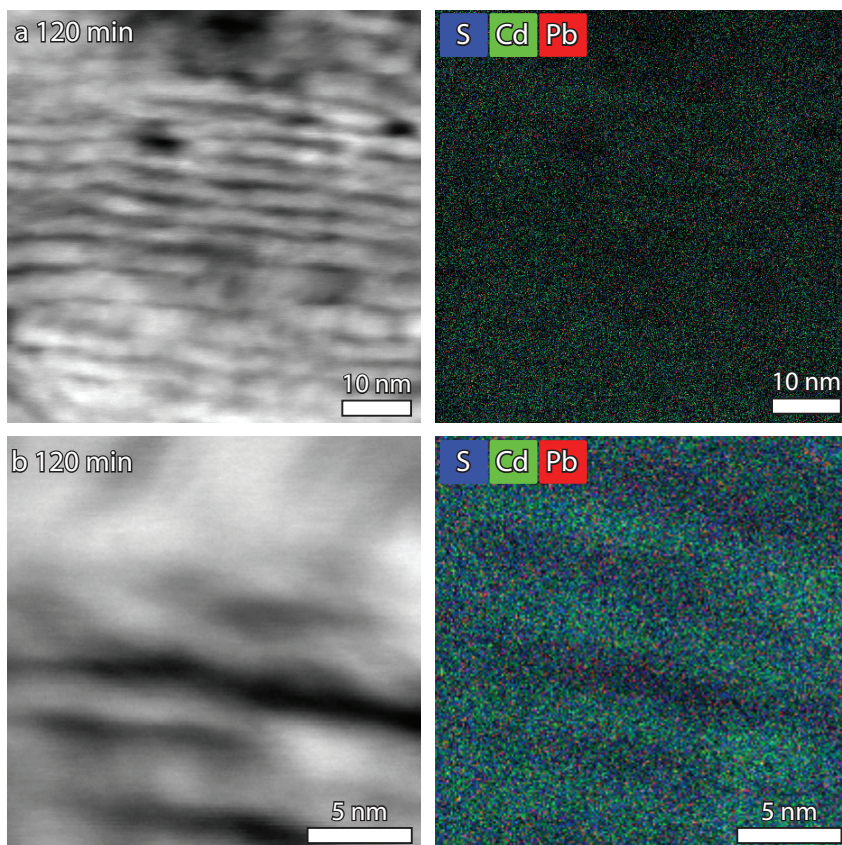


Figure S6.11 HAADF-STEM images of stacked CdS NSs at a 10 nm (a) and a 5 nm scale (b). The corresponding EDX maps were measured until hydrocarbon contamination resulted in image drift. They have a low signal, making the stacked sheets difficult to discern, but we tentatively conclude that the residual lead is randomly distributed in the maps.

S6.4 Model for adsorption to a surface

When modelling the kinetic process of reactions, a conventional approach is to simplify the calculations to the slowest step, as that rate is the bottleneck for the overall rate.¹⁰ This simplification allows for the description of heterogeneous processes by well-known equations, originally developed for homogeneous systems. The PbS NSs are very thin, consisting of only 4 or 6 monolayers (1.2 to 1.8 nm). Thus, the number of readily available surface atoms in a NS is more than 50% (4 MLs) or more than 33% (6 MLs). The entire surface of the NSs is readily accessible when they are dispersed in a solvent, meaning that only two or four additional monolayers need to be traversed by diffusion. Therefore, we consider the rate-limiting step in the cation exchange to be the adsorption of the cadmium ions onto specific surface sites of the sheets. Labelling the fraction of sites on the surface available for Cd^{2+} adsorption as $\theta(t)$, the random adsorption on these sites can be described by:

$$\frac{d\theta}{dt} = k(1 - \theta) \quad (\text{S6.1})$$

Resulting in:

$$\theta(t) = 1 - e^{-kt} \quad (\text{S6.2})$$

At 0% exchange, all the potential sites on the surface are still free ($\theta = 0$), while at 100% exchange (46% cadmium in the sheets) every potential site is occupied by a Cd^{2+} adsorbate ($\theta = 1$). It is a molecular adsorption process at a limited number of atomic positions. In **Figure S6.12** we plot the fractions of cadmium and lead on a linear time scale, and fit the datapoints with the above equation. The exchange follows this trend quite well, with an initial high reaction rate that decreases after 15 minutes and saturates around 1 hour.

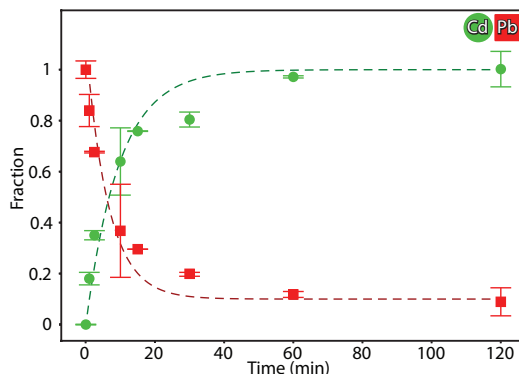


Figure S6.12 The fractions of cations as determined with bulk EDX measurements are plotted on a linear timescale. As the lead atoms in the PbS NSs are replaced with cadmium, the original fraction of 1 (46%) fully reduces to 0.09 (4.1%). The dark green and dark red dashed lines show the fit of the datapoints. The cadmium trend was fit with the first Langmuir isotherm: $\theta(t) = 1 - e^{-kt}$ and the lead trend with its reverse: $\theta(t) = e^{-kt} + 0.09$ (with 0.09 being the residual lead in the sample).

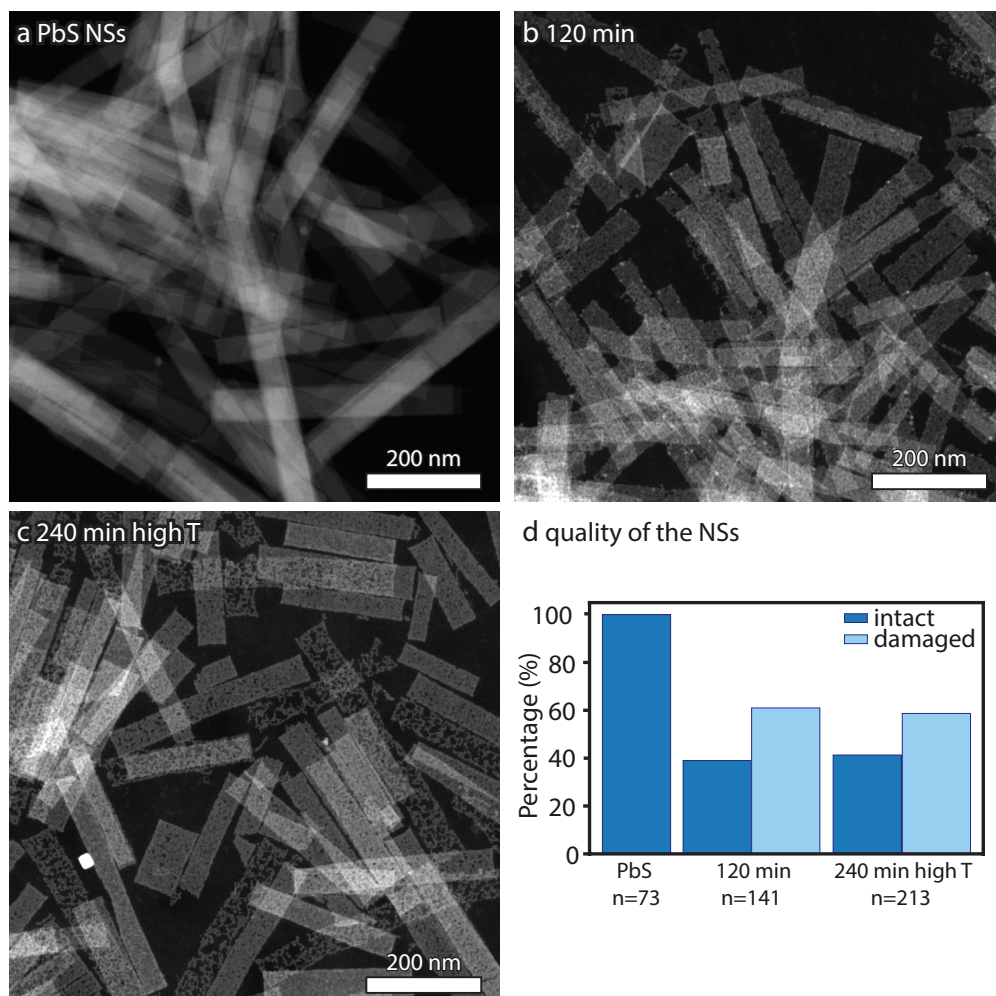


Figure S6.13 The parent PbS NSs were recently shown to display some small scale defects,¹ but during the cation exchange part of the CdS NSs are noticeably damaged. We deem the parent PbS NSs to be intact (a), while after 120 minutes of cation exchange ~60% of the remarkably rectangular NSs has large holes (b). After additional time at higher temperature (240 min high T), the damaged NSs still comprise ~60% of the population (c). (d) A histogram showing the percentages of the intact and damaged sheets.

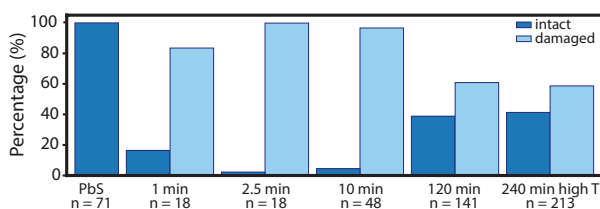


Figure S6.14 To study the quality of the NSs throughout the cation exchange we characterized the CdS NSs with HAADF-STEM. They are characterized as either intact or damaged i.e. containing large holes within the rectangular sheet. Due to clustering the 1 and 2.5 minute samples only a few NSs could be characterized, but the majority is damaged (>80%). In the 10 minute sample a larger population could be characterized and more than 90% of the NSs are damaged. An additional 110 minutes of cation exchange brings the percentage of damaged NSs down to 61% with no significant improvement in the 240 minutes high temperature experiment (59%). Thus, the initial PbS NSs quickly deteriorate resulting in damage in the majority of the NSs, although later in the cation exchange these holes appear to repair resulting in a lower degree of damage.

Table S6.7 The experimental parameters of the samples characterised in Figure S6.16.

Experiment	Initial Cd(OA) ₂	100 °C	Additional reactant	130 °C	150 °C
CdS 120 min	2 mL 0.35 M	2 hours	-	-	-
CdS 240 min high T	2 mL 0.35 M	2 hours	2x 0.25 mL 0.35 M	1 hour	1 hour
CdS 240 min high T with OA	2 mL 0.35 M	2 hours	2x 0.25 mL OA	1 hour	1 hour
CdS 4 mL 0.1 M	4 mL 0.1 M	2 hours	-	1 hour	1 hour
CdS 4 mL 0.35 M	4 mL 0.35 M	2 hours	-	1 hour	1 hour

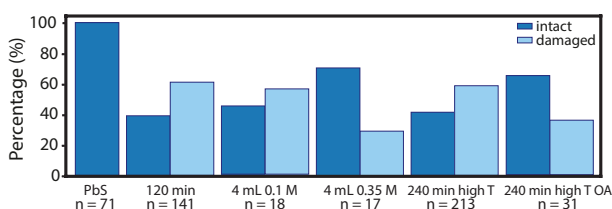


Figure S6.15 The CdS NSs of the additional experiments described in Table S6.7 were characterized with HAADF-STEM. Here, we doubled the amount of cadmium precursor added and we varied the concentration of the precursor. The 4 mL 0.1 M precursor improved the number of intact NSs slightly when compared to the 120 min sample (~55%), but 4 mL 0.35 M precursor improved the yield of intact NSs significantly to ~70%. Further experiments at a higher temperature with additional OA appear to also improve the quality of the NSs (~65% intact). Again, we could only characterize a few NSs, and therefore these conclusions can only be tentatively drawn.

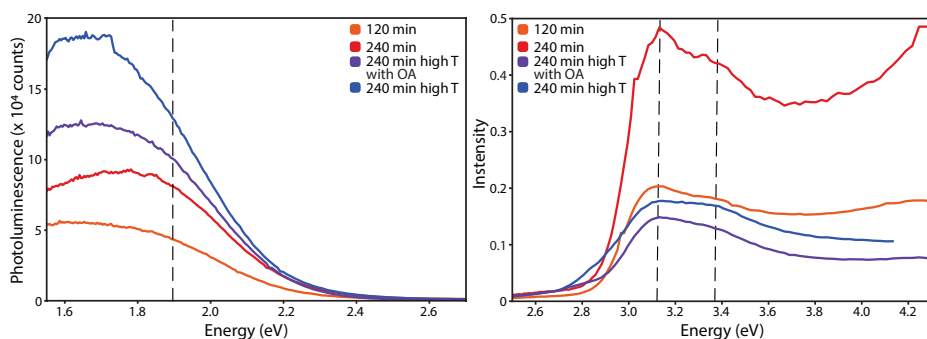


Figure S6.16 Photoluminescence emission and excitation measurements of completely exchanged CdS NSs. (a) We compare the emission of the CdS sheets after 120 and 240 minute experiments at 100°C and the 240 min high T experiment. When excited at 390 nm all samples show a broad sub-bandgap photoluminescence peak below 2.2 eV. With a prolonged reaction at higher temperature the sub-bandgap luminescence increases, potentially due to improved quality of the NSs upon annealing or as a result of the additional precursor. (b) The excitation spectra of the CdS NSs as monitored at 1.9 eV (650 nm) show the heavy-hole and light-hole exciton peaks at 3.1 eV and 3.35 eV respectively (indicated by the black dashed lines), while free carrier absorption sets on at 3.8 eV.

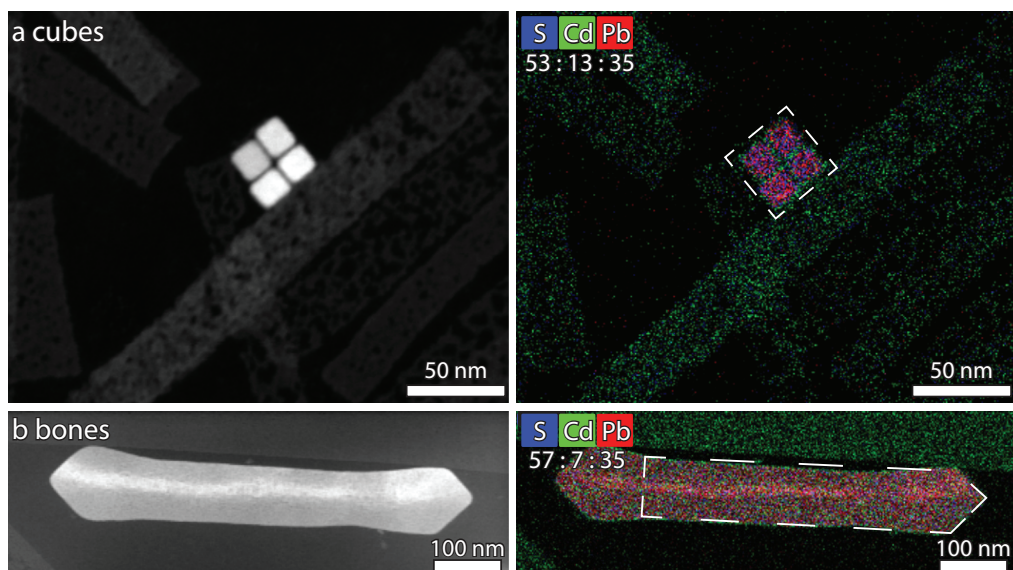


Figure S6.17 (a) As a by-product of the PbS NSs synthesis, rock salt PbS cubes can form with an average size of 16.7 nm. (b) Another by-product of the PbS NSs synthesis which can form are the “bones”. These bones tend to form when the initial synthesis is prolonged at 165°C. After these by-products undergo a cation exchange procedure, they are surrounded by CdS NSs containing up to 43% cadmium. However, the cubes still have a PbS core with a thin shell of CdS (between 3 and 4 nm thick) while the bones show homogeneous incorporation in the analyzed zone axis. Quantification of the areas indicated by the white boxes in the EDX maps shows that the cubes only contain 12.9% Cd, and the bone only contains 7.4% Cd.

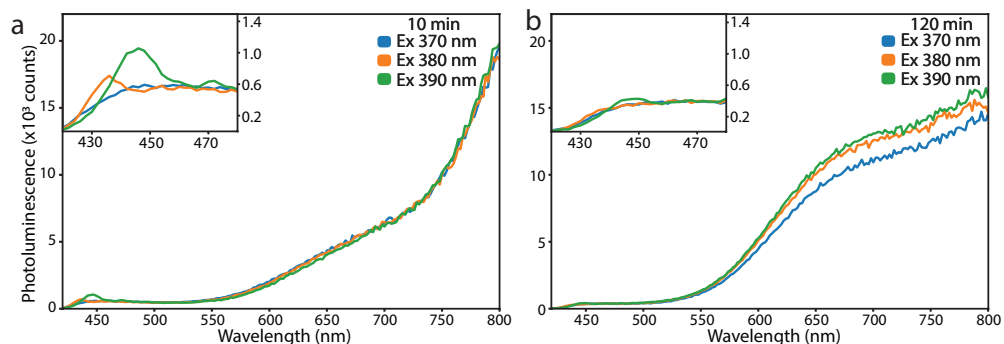


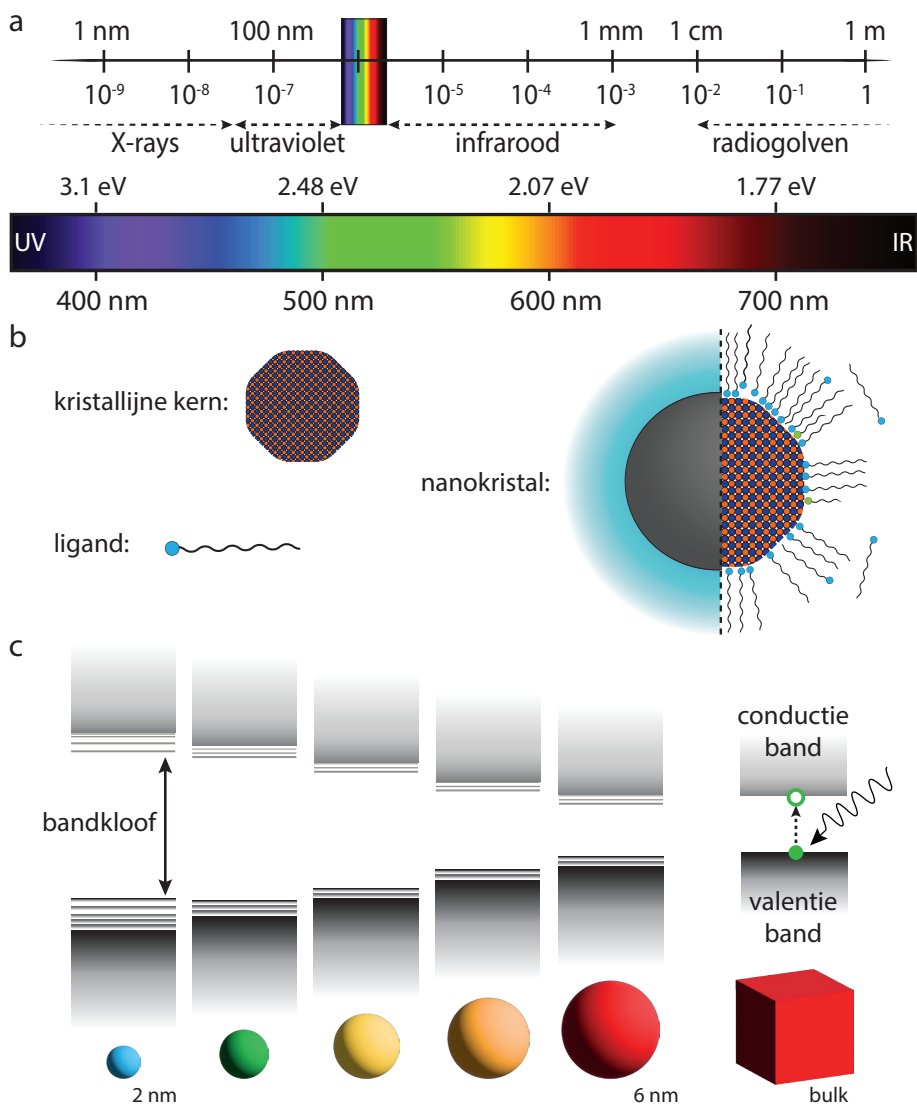
Figure S6.18 In the photoluminescence measurements a Raman scattering feature is observed around 446 nm. For both 10 minutes and 120 minutes of exchange, an inset is shown of the 420 to 480 nm area showing that this scattering depends upon the excitation wavelength and is less pronounced at longer reaction times.

References

- [1] Akkerman, Q. A.; Martín-García, B.; Buha, J.; Almeida, G.; Toso, S.; Marras, S.; Bonaccorso, F.; Petralanda, U.; Infante, I.; Manna, L. Ultrathin Orthorhombic PbS Nanosheets. *Chem. Mater.* **2019**, *31* (19), 8145-8153. DOI: 10.1021/acs.chemmater.9b02914.
- [2] van der Sluijs, M. M.; Salzmann, B. B. V.; Arenas Esteban, D.; Li, C.; Jannis, D.; Brafine, L. C.; Laning, T. D.; Reinders, J. W. C.; Hijmans, N. S. A.; Moes, J. R.; et al. Study of the Mechanism and Increasing Crystallinity in the Self-Templated Growth of Ultrathin PbS Nanosheets. *Chem. Mater.* **2023**, *35* (7), 2988-2998. DOI: 10.1021/acs.chemmater.3c00300.
- [3] Casavola, M.; van Huis, M. A.; Bals, S.; Lambert, K.; Hens, Z.; Vanmaekelbergh, D. Anisotropic Cation Exchange in PbSe/CdSe Core/Shell Nanocrystals of Different Geometry. *Chem. Mater.* **2011**, *24* (2), 294-302. DOI: 10.1021/cm202796s.
- [4] Li, C.; Tardajos, A. P.; Wang, D.; Choukroun, D.; Van Daele, K.; Breugelmans, T.; Bals, S. A Simple Method to Clean Ligand Contamination on TEM Grids. *Ultramicroscopy* **2021**, *221*, 113195. DOI: 10.1016/j.ultramic.2020.113195.
- [5] Anderson, N. C.; Hendricks, M. P.; Choi, J. J.; Owen, J. S. Ligand Exchange and the Stoichiometry of Metal Chalcogenide Nanocrystals: Spectroscopic Observation of Facile Metal-Carboxylate Displacement and Binding. *J. Am. Chem. Soc.* **2013**, *135* (49), 18536-18548. DOI: 10.1021/ja4086758.
- [6] Moreels, I.; Fritzing, B.; Martins, J. C.; Hens, Z. Surface Chemistry of Colloidal PbSe Nanocrystals. *J. Am. Chem. Soc.* **2008**, *130* (45), 15081-15086. DOI: 10.1021/ja803994m.
- [7] Moreels, I.; Lambert, K.; De Muynck, D.; Vanhaecke, F.; Poelman, D.; Martins, J. C.; Allan, G.; Hens, Z. Composition and Size-Dependent Extinction Coefficient of Colloidal PbSe Quantum Dots. *Chem. Mater.* **2007**, *19* (25), 6101-6106. DOI: 10.1021/cm071410q.
- [8] De Roo, J.; Yazdani, N.; Drijvers, E.; Lauria, A.; Maes, J.; Owen, J. S.; Van Driessche, I.; Niederberger, M.; Wood, V.; Martins, J. C.; et al. Probing Solvent-Ligand Interactions in Colloidal Nanocrystals by the NMR Line Broadening. *Chem. Mater.* **2018**, *30* (15), 5485-5492. DOI: 10.1021/acs.chemmater.8b02523.
- [9] Singh, S.; Leemans, J.; Zaccaria, F.; Infante, I.; Hens, Z. Ligand Adsorption Energy and the Postpurification Surface Chemistry of Colloidal Metal Chalcogenide Nanocrystals. *Chem. Mater.* **2021**, *33* (8), 2796-2803. DOI: 10.1021/acs.chemmater.0c04761.
- [10] Zagorodni, A. *Ion Exchange Materials Properties and Applications*; Elsevier, 2007.

The background features a collection of colorful geometric shapes: squares and rectangles in shades of blue, orange, green, purple, red, and yellow, scattered across the white page. At the top, there are two horizontal blue lines of different lengths. The word 'APPENDIX' is centered in a bold, blue, sans-serif font.

APPENDIX



Figuur 7.1 (a) Schematisch overzicht van een deel van het elektromagnetische spectrum dat loopt van golven met een grote van meters tot golven van een nanometer groot. De ogen van een mens zijn alleen gevoelig voor licht in het zichtbare gedeelte tussen de 380 (hoge energie, violet) en 760 nm (lage energie, rood), de regenboog. (b) Schematische tekening van een colloïdaal nanokristal, een hybride systeem dat bestaat uit een anorganische kristallijne kern die bedekt is met liganden en daardoor kan worden gestabiliseerd in een oplosmiddel. We spreken dan van een dispersie van nanokristallen. (c) Schematische weergave van de bandstructuur van een bulk halfgeleider (rechts) en de bandenstructuur van steeds kleiner wordende nanokristallen (links). Naarmate de nanokristallen kleiner worden, worden ze steeds meer opgesloten en wordt de bandkloof groter terwijl discrete energieniveaus ontstaan aan de randen van de banden.

Het licht dat we iedere dag zien bestaat uit fotonen, dit zijn lichtdeeltjes met verschillende energieën en golflengtes. Van het hele spectrum noemen we slechts het kleine deel van het spectrum waar het menselijk oog gevoelig voor is het zichtbare licht. Wij ervaren zichtbaar licht als wit, maar in werkelijkheid is het een combinatie van kleuren en golflengten tussen 380 nm (violet) en 660 nm (rood). Pas wanneer dit licht wordt gebroken, bijvoorbeeld door een prisma, regendruppels of op de achterkant van een DVD, kunnen we deze verschillende kleuren van de regenboog ook daadwerkelijk zien. In **Figuur 7.1a** staat het volledige spectrum schematisch gerangschikt.¹

De kleur van de voorwerpen om ons heen wordt bepaald door het deel van het spectrum dat door het object wordt gereflecteerd, de overige kleuren worden geabsorbeerd. Als bijvoorbeeld alle fotonen van het zichtbare spectrum worden geabsorbeerd zien we een voorwerp als zwart, maar wanneer het al die fotonen reflecteert zien we het als wit. De mix van geabsorbeerd en gereflecteerd licht resulteert in alle kleuren tussen deze twee uitersten in. Welke fotonen door een materiaal worden geabsorbeerd wordt bepaald door het energieverschil tussen de grondtoestand en de geëxciteerde toestand. In het geval van halfgeleiders noemen we dit energieverschil ook wel de bandkloof energie (bandgap). Alle fotonen met een lagere energie dan de bandkloof wordt gereflecteerd of doorgelaten, terwijl fotonen met een energie gelijk aan of hoger dan de bandkloof worden geabsorbeerd.

Net onder en boven het zichtbare licht liggen het (nabij) infrarood (NIR, lagere energie) en het ultraviolet (UV, hogere energie). De ogen van mensen zijn hier minder gevoelig, maar dieren kunnen vaak wel in één van deze gebieden zien (goudvissen zijn zelfs gevoelig voor beide gebieden²). Ook technologische toepassingen maken gebruik van het UV en NIR, denk bijvoorbeeld aan medisch onderzoek, nachtbrillen en het schoonmaken van oppervlakken. Voor deze toepassingen is UV/NIR gevoelig materiaal nodig en halfgeleider nanomaterialen zijn hier een snel groeiende klasse omdat de optische resonanties goed kunnen worden aangepast.

Normaal gesproken zijn de eigenschappen van een materiaal onafhankelijk van zijn grootte. Door een witte papieren pagina kleiner te knippen verandert deze bijvoorbeeld niet van kleur. Echter, wanneer sommige materialen klein genoeg zijn, kleiner dan 100 nanometer, kunnen hun eigenschappen grootteafhankelijk worden. Eén nanometer is 0.000000001 of 10^{-9} meter, voor context: een rode bloedcel heeft een gemiddelde grootte van 7500 nm (0.0000075 of 7.5×10^{-6} meter) en een DVD is 1200000 nm dik (0.0012 of 1.2×10^{-3} meter). Objecten van slechts honderden nanometers groot zijn dus veel kleiner dan wat we met het blote oog kunnen zien.

Een kristal dat we vaak in het dagelijks leven tegenkomen is tafelzout. De witte kristallijne vlokken versterken niet alleen de smaak van eten maar volgen ook de wetenschappelijke definitie van een kristal: ze zijn opgebouwd uit periodiek geordende atomen, ionen of moleculen. Kristallen kunnen verschillende geometrische structuren hebben, maar we kunnen deze structuur altijd beschrijven met behulp van een eenheidscel die zich door het hele kristal heen herhaalt.³ Het kost energie om een kristal te splijten en daarmee de bindingen tussen atomen in het kristalrooster te breken om nieuwe oppervlakken te vormen. Deze oppervlakken noemen we facetten en het type facet dat wordt gevormd is afhankelijk van de kristalstructuur en de richting waarin de eenheidscel wordt gespleten. De gevormde facetten beïnvloeden de chemische en fysische eigenschappen van het kristal, maar adsorptie van moleculen op het oppervlak kan de relatieve stabiliteit van de facetten drastisch veranderen.⁴

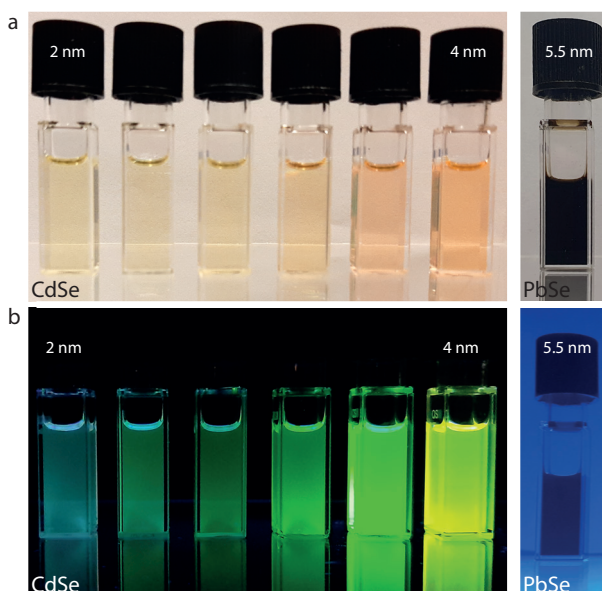
In deze thesis hebben we colloïdale nanokristallen bestudeerd, deze bestaan uit een anorganische kristallijne kern die bedekt is met een geadsorbeerde laag van (organische) liganden (**Figuur 7.1b**). Terwijl de kristallijne kern de optische en elektronische eigenschappen van de nanokristallen bepaalt interageren de liganden met het oplosmiddel. Daarmee bepalen de liganden of de nanokristallen in het oplosmiddel blijven bewegen (we noemen dit een dispersie) of naar de bodem zakken. De combinatie van de kristallijne kern en de liganden bepaalt de overkoepelende eigenschappen van de nanokristallen. Eigenlijk moeten we ze daarom beschouwen als een hybride systeem. Specifiek hebben we hier nanokristallen bestudeerd die bestaan uit halfgeleider materialen van groep II en IV van het periodiek systeem (CdS, PbSe en PbS).

Op grote schaal, we noemen dit ook wel in bulk, bestaan deze materialen uit heel veel atomen (meer dan $\sim 10^7$). De overlappende golf functies van de valentie elektronen vormen de bindingen tussen deze atomen, deze vormen bindende en anti-bindende energieniveaus. Het grote aantal atomen zorgt ervoor dat twee energiebanden ontstaan met een schijnbaar ononderbroken dichtheid van energieniveaus (**Figuur 7.1c** rechts). De onderste energieband bevat nog steeds elektronen en noemen we de valentieband (VB), terwijl de bovenste lege energieband de conductieband (CB) wordt genoemd. In het gebied daartussenin zijn geen energieniveaus beschikbaar, we noemen dit de bandkloof (bandgap, E_g).⁵ Zolang er geen elektronen aanwezig zijn in de CB is de elektrische geleiding van een materiaal erg laag, het is dan een isolator. Echter, wanneer er elektronen in de CB aanwezig zijn kan het materiaal wel geleiden. Halfgeleiders zitten tussen deze twee extremen in; de bandkloof van deze materialen is zo klein dat elektronen hem kunnen overbruggen door absorptie van energie. In bulk halfgeleiders kunnen bijvoorbeeld door middel van warmte of licht elektronen van de VB naar de CB worden geëxciteerd als de geabsorbeerde energie in ieder geval gelijk is aan de bandkloof (**Figuur 7.1c**). Het geëxciteerde elektron (e^-) laat een gat achter in de VB (h^+), samen vormen deze een elektron-gat paar, een exciton. Na verloop van tijd zal het elektron terugvallen naar de VB, recombinatie. De geabsorbeerde energie wordt daarbij weer vrijgegeven door bijvoorbeeld uitzending van een foton met een energie (een kleur) die overeenkomt met de bandkloof.

Halfgeleiders die kleiner zijn dan ~ 100 nm bestaan uit minder dan $\sim 10^7$ atomen. Op deze schaal begint de grootte van de halfgeleider de fysische en chemische eigenschappen te beïnvloeden. Twee fundamentele effecten kunnen hiervoor worden aangewezen, allereerst de toename van het aantal atomen aan het oppervlak in verhouding tot het aantal interne atomen. Oppervlak atomen zijn omringd met minder naburige atomen dan de interne atomen waardoor ze onverzadigde chemische bindingen hebben. Het tweede effect is de afgenomen hoeveelheid atomen waardoor er minder orbitalen beschikbaar zijn om de CB en VB te vormen terwijl het nanokristal de grootte van de exciton Bohr radius (a_0) benadert. Deze materiaal afhankelijke radius beschrijft het volume van het elektron-gat exciton in het bulk materiaal. In bulk kunnen de kinetische energie en aantrekkingskracht van elektron en gat deze radius bepalen, meestal ligt deze tussen de 2 en 50 nm. Nanokristallen die ongeveer twee keer zo groot zijn als deze Bohr radius beginnen deze excitonen in te perken, ze kunnen zich niet meer volledig uitspreiden. Het gevolg is een grotere bandkloof, terwijl er door het lagere aantal atomen minder bindingen en energieniveaus worden gevormd en de banden meer discreet worden (**Figuur 7.1c**, links).⁶ Naast de grootte heeft ook de vorm van het nanokristal invloed op de bandenstructuur. In een bolvormig nanokristal wordt een exciton van 3 kanten ingesloten (zoals we hebben bestudeerd in **hoofdstuk 4**), maar in een staafvormig nanokristal kunnen de excitons zich in de lengte nog steeds vrij bewegen. Twee-dimensionale rechthoekige nanokristallen (zoals we hebben

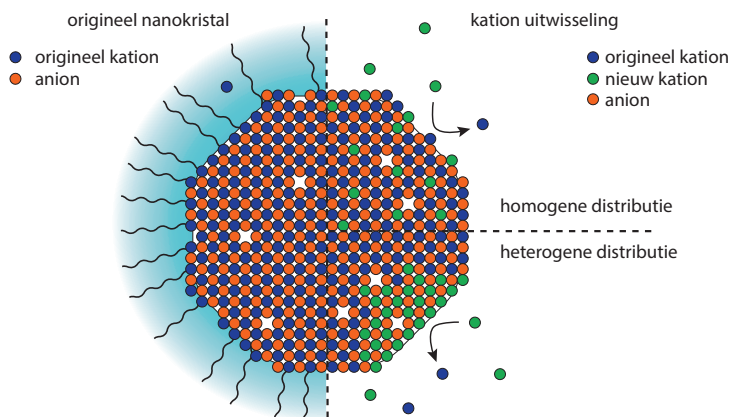
bestudeerd in **hoofdstuk 5** en **6**) hebben nog slechts 1 richting, de dikte, waarin de excitons worden ingesloten.

De directe relatie tussen de grootte van de nanokristallen en de bandkloof zorgt ervoor dat de optische eigenschappen van halfgeleider nanokristallen kunnen worden gecontroleerd over een groot gebied van energieën (golflengtes).⁷ De exciton Bohr radius en bandkloof van het materiaal bepalen echter het gebied waarin deze eigenschappen kunnen worden aangepast. Veel wetenschappelijk onderzoek is er bijvoorbeeld gedaan naar nanokristallen bestaande uit cadmium en selenium (CdSe). Bulk CdSe heeft een bandkloof van 1.74 eV (712 nm), al het licht met een energie hoger dan de bandkloof wordt daardoor geabsorbeerd terwijl rood licht wordt gereflecteerd. Bulk CdSe heeft hierdoor een rode kleur. De exciton Bohr radius is slechts 6 nm,⁶ en inperking van de excitonen begint dus al bij nanokristallen van ~ 12 nm. In **Figuur 7.1c** laten we schematisch zien hoe de bandkloof van steeds kleinere CdSe nanokristallen toeneemt. Hierdoor verschuift ook de absorptie en emissie van de nanokristallen van rood (lagere energie) naar hogere energie (lagere golflengte, blauw). In de praktijk is de kleur van een verdunning van CdSe nanokristallen minder duidelijk in daglicht (**Figuur 7.2a**) maar wanneer verlicht met een UV lamp is de kleur van de emissie duidelijk te zien (**Figuur 7.2b**). Bulk loodselenide (PbSe) heeft een veel kleinere bulk bandkloof van 0.27 eV (4592 nm) en een exciton Bohr radius van 46 nm.⁸ Hierdoor wordt bij alle PbSe nanokristallen al het zichtbare licht geabsorbeerd en ziet een dispersie van PbSe er zwart uit (**Figuur 7.2b**). Hetzelfde principe gaat echter wel op, ook in het NIR kunnen de optische eigenschappen van PbSe nanokristallen worden aangepast maar het is met het menselijk oog niet te zien.



Figuur 7.2 (a) Foto's van CdSe en PbSe nanokristallen in dispersie. Zowel bij daglicht (a) als onder excitatie met een UV-lamp in het donker (b). De CdSe nanokristallen laten in beide gevallen een mooie variatie in kleuren zien. Voor PbSe ligt de bandkloof in het NIR, al het zichtbare licht wordt daardoor geabsorbeerd en de dispersie ziet er voor ons in beide gevallen zwart uit. Dit figuur is gemaakt met de input van Relinde Moes en Elleke van Harten.

Na het synthetiseren (het maken) van de nanokristallen is het mogelijk om de kristallijne kern verder aan te passen met bijvoorbeeld een kation uitwisselingsreactie. Alle colloïdale nanokristallen die we hier hebben bestudeerd bestaan uit grote anionen (S^{2-} , Se^{2-}) en kleine kationen (Pb^{2+} , Cd^{2+}). In een uitwisselingsreactie kunnen de kationen van de originele nanokristallen worden vervangen door een nieuw kation (Figuur 7.3). Het geeft ons de mogelijkheid om nanokristallen te vormen die niet direct kunnen worden gesynthetiseerd. Voor uitwisselingsreacties in bulk zijn (vaak) hoge temperaturen en hoge druk nodig. De kleine afmetingen en het overvloed aan oppervlakken dicht bij het oplosmiddel maken nanokristallen echter uitermate geschikt voor dit soort reacties. Door een precursor van nieuwe kationen aan de dispersie toe te voegen kan bij lage temperaturen een AX nanokristal worden omgezet naar BX. Of er een uitwisseling plaatsvindt wordt vervolgens bepaald door de vrije energie van de reactie. Deze energie is afhankelijk van bijvoorbeeld de kationen zelf, hun relatieve stabiliteit in het nanokristal en in de oplossing en de stabiliteit van de nanokristallen. Vervolgens is er een reeks van inherent gekoppelde elementaire kinetische en thermodynamische stappen die moeten worden doorlopen zodat de kationen kunnen uitwisselen.^{7,9,10,11,12} Bij de uitwisseling blijven de anionen en hun ordening behouden, deze functioneren zelfs als een raamwerk waardoor tijdens de uitwisseling ook vaak de grootte en de vorm van de originele nanokristallen behouden kan blijven.⁹ De originele nanokristallen kunnen volledig worden uitgewisseld (BX),^{13,14} slechts gedeeltelijk worden vervangen ($A_{1-x}B_xX$) of er kunnen heterostructuren worden gevormd met atomair scherpe raakvlakken.¹⁵⁻¹⁷ In hoofdstuk 6 bestuderen we de post-synthetische kation uitwisseling van PbS nanoplaatjes naar CdS nanoplaatjes. Juist door de rechthoekige vorm van deze nanokristallen kunnen we de kationuitwisseling bestuderen in specifieke richtingen. De rechthoekige vorm van deze nanokristallen geeft ons de mogelijkheid om deze uitwisseling te bestuderen in specifieke richtingen. Met samples gemaakt op verschillende momenten tijdens de reactie kunnen we deze ex situ bestuderen en daarmee de kationuitwisseling volgen.

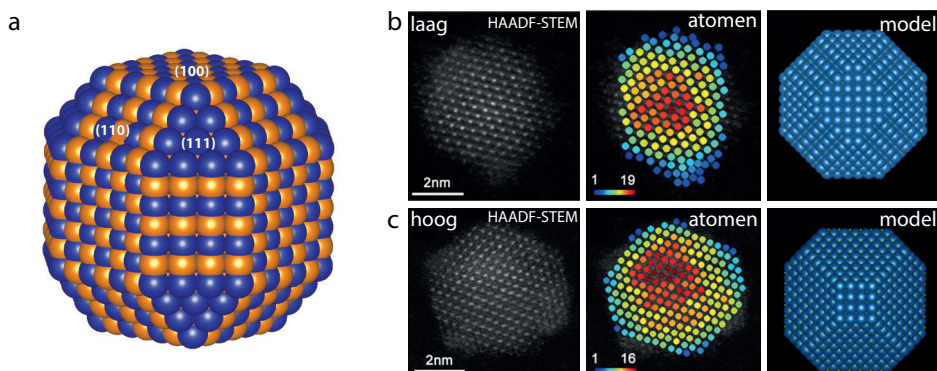


Figuur 7.3 Schematische afbeelding van een origineel nanokristal zoals gesynthetiseerd (links), bestaande uit de ligand lag en de anorganische kristallijne kern bestaande uit kationen (blauw) en anionen (oranje). Het aantal defecten en missende ionen in de afbeelding is slechts om aan te geven dat alle kristallen defecten bevatten. Rechts laten we schematisch twee manieren zien waarop de kation uitwisseling plaats kan vinden. Boven gebeurt dit via een homogene distributie terwijl onder een heteroogeen bewegend front zich door het nanokristal beweegt. Figuur aangepast van Maarten Bransen.

Het oppervlak van de anorganische kristallijne kern van de halfgeleider nanokristallen bestaat uit metaal kationen (Pb^{2+} , Cd^{2+}) en anionen (S^{2-} , Se^{2-}) met ongebonden elektronen. Door bindingen te vormen met (organische) liganden passiveren deze het oppervlak, ze vormen er een laag of schil om het nanokristal heen die vervolgens de interactie met het oplosmiddel bepaalt. Deze liganden zijn amfifilisch, net als zeepmoleculen hebben ze een polaire kop en een apolaire koolwaterstof staart (**Figuur 7.1b**). De polaire kop (bijvoorbeeld N, O, S, P) vormt een binding met de ongedeelde elektronen van de ionen op het oppervlak terwijl de apolaire staart bij een gunstige interactie het oplosmiddel in steekt waardoor de dispersie wordt gestabiliseerd. Zowel anionen als kationen kunnen bindingen vormen met liganden, maar het aantal opties voor anionen is beperkt (bijvoorbeeld fosfines). Voor de metalen kationen zijn er veel meer geschikte liganden, bijvoorbeeld organische alkylamines, vetzuren, alkylthiols of zelfs anorganische ionen als S^{2-} en OH^- .⁷

Liganden spelen al tijdens de synthese van nanokristallen een belangrijke rol. Bulk kristallen vormen (meestal) een thermodynamisch stabiele fase, maar door liganden kan de oppervlak energie van (specifieke) facetten verlagen en de groei van deze facetten vertragen. Nanokristallen met metastabiele kristalstructuren en vormen worden hierdoor mogelijk. Bijvoorbeeld in het geval van PbSe nanokristallen met een kubische keukenzoutstructuur, in theorie heeft een kubus van {100} facetten de laagste oppervlak energie.¹⁸ In de praktijk kunnen facetten met een hogere oppervlak energie door middel van liganden, bijvoorbeeld oliezuur, worden gestabiliseerd. Hierdoor kunnen nanokristallen worden gevormd met een afgevlakte kubus-octaëdrische vorm (**Figuur 7.4a**).

Een binding tussen een ligand en het oppervlak van een nanokristal klinkt definitief. Echter, met behulp van NMR is aangetoond dat liganden reversibel binden, ze binden aan het oppervlak maar gaan ook weer van het oppervlak af voordat ze opnieuw binden. Hoe lang de liganden daadwerkelijk op het oppervlak spenderen is afhankelijk van de bindingssterkte.^{19,20} Zwakker gebonden liganden blijven korter aan het oppervlak gebonden (≥ 0.05 milliseconde), terwijl sterker gebonden liganden langer op het oppervlak blijven (seconden).⁷ Het betekent dat de liganddichtheid ook na de synthese kan variëren, waarmee ook nog steeds de facetgrootte en vorm van de nanokristallen kan veranderen. Voor nanokristallen met veel liganden (een hoge liganddichtheid) worden de hoog energetische facetten gestabiliseerd en daardoor groter, terwijl bij een lage liganddichtheid de laag energetische facetten duidelijker aanwezig zijn (**Figuur 7.4b en c**).²¹ Voor het onderzoek besproken in **hoofdstuk 3 en 4** is het goed om te onthouden dat een PbSe nanokristal met een diameter van ongeveer 6.5 ± 0.3 nm en gemiddeld ~ 505 liganden per facet een ligand dichtheid heeft tussen de $3.7\text{-}5.0$ nm⁻² op de {111} facetten, $2.0\text{-}4.3$ nm⁻² op de {110} facetten, en $0\text{-}1.0$ nm⁻² op de {100} facetten.²² De lagere oppervlak energie van {100} facetten met liganden resulteert dus ook in een lagere liganddichtheid en daardoor in meer reactieve facetten. Doordat het aantal gebonden liganden op het oppervlak kan blijven variëren kunnen colloïdale nanokristallen dus niet worden gedefinieerd als een specifiek systeem met een chemische formule zoals dit voor moleculen wel kan. Nanokristallen moeten we dus beschouwen als dynamische structuren met partij-tot-partij variaties, een grillige ligand laag en samenstellingen en vormen die afhankelijk zijn van de ligand concentratie. Gecontroleerd werken met dispersies van colloïdale nanokristallen is hierdoor een uitdaging, zeker over lange tijd.



Figuur 7.4 (a) Schematische weergave van een PbSe keukenzoutstructuur nanokristal van ongeveer 6 nm groot in aanwezigheid van liganden. De liganden stabiliseren ook de facetten met een hogere oppervlak energie ($\{110\}$, $\{111\}$) zodoende krijgen de nanokristallen een afgevlakte kubus-octaëdrische vorm. In (b) en (c) laten we een ex situ studie van de nanokristallen zien met HAADF-STEM waarbij de atomen in de kolommen werden geteld voor een nanokristal met lage en hoge liganddichtheid.²¹ In het middelste paneel is dit weergegeven met kleuren, blauw is slechts 1 atoom, rood 16 of 19 atomen. In het rechter paneel laten we het schematische model zien van de data uit verschillende nanokristallen die op deze manier werden gekarakteriseerd. Let op de toegenomen grootte van de $\{111\}$ facetten bij nanokristallen met een hoge liganddichtheid.

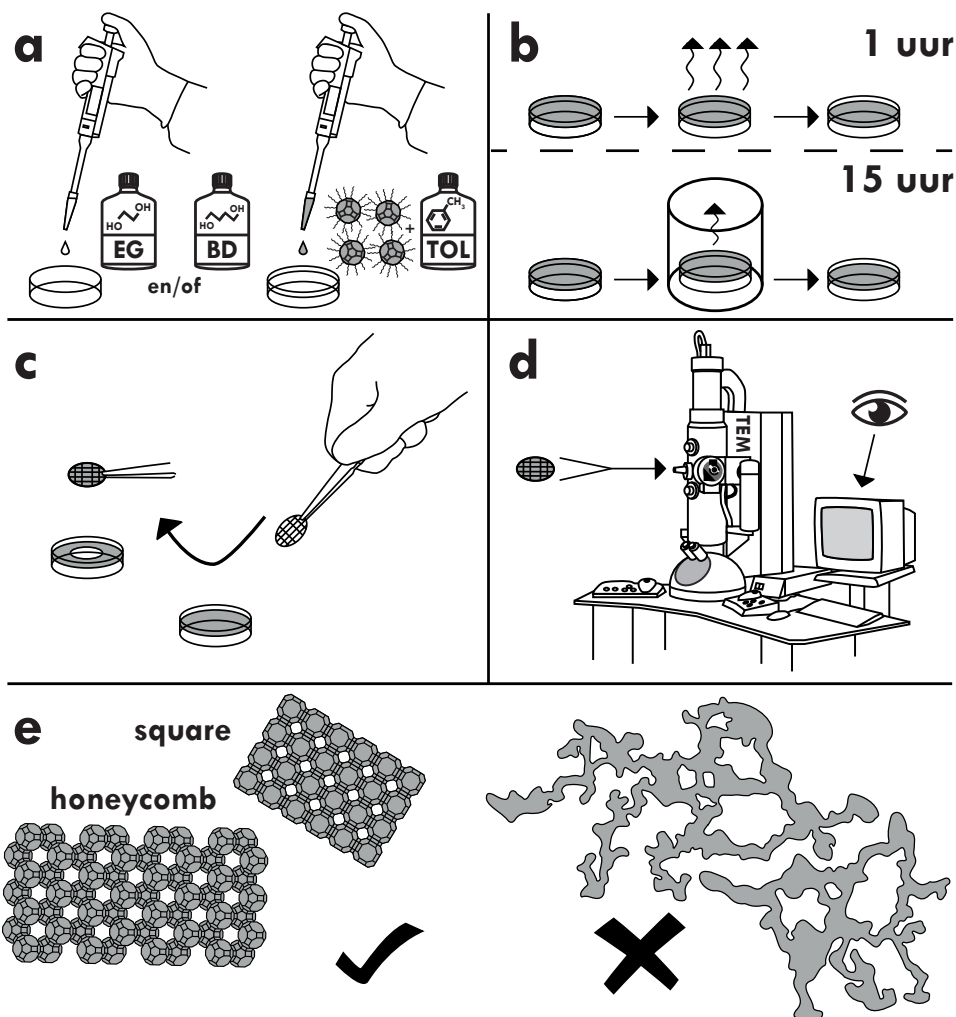
Tot nu toe hebben we voornamelijk nanokristallen besproken die in een oplosmiddel zijn gestabiliseerd door middel van hun liganden, een dispersie. Voor het toepassen van de grootte-afhankelijke optische en elektronische eigenschappen van de nanokristallen in applicaties (bijvoorbeeld in zonnecellen, detectoren en tv-schermen), moeten de nanokristallen kunnen worden gebruikt als elektronische componenten. Deze componenten (zoals circuits, transistors, displays, diodes etc.) worden momenteel vaak gemaakt van halfgeleider silicium kristallen door middel van een “top-down” proces. In zo’n proces begin je met een groter kristal waar je vervolgens, stukje bij beetje materiaal weghaalt op de plekken waar je dit niet wilt hebben. Denk bijvoorbeeld aan hoe een marmeren beeld wordt uitgebeiteld. Meestal worden de elektronische componenten opgebouwd uit 2D materialen, dunne lagen, ook wel “thin films” genoemd. Met nanokristallen kunnen we dezelfde dunne lagen opbouwen door een “bottom-up” procedure waarbij de losse nanokristallen één geheel gaan vormen. Denk bijvoorbeeld aan een legoset, die blokje voor blokje in elkaar wordt gezet om uiteindelijk een kasteel te bouwen. De eigenschappen van deze legoblokjes, de nanokristallen, kunnen worden aangepast door middel van de grootte en vorm van de nanokristallen terwijl met behulp van kation uitwisseling heterostructuren kunnen worden gevormd. De eigenschappen van de nanokristallen en daarmee van deze “bottom-up” gefabriceerde thin films kunnen dus nauwkeurig worden afgestemd op een manier die voor traditionele bulk halfgeleiders niet mogelijk is.²³

Om thin films te maken uit nanokristallen kan een dispersie op een onderlaag, een support, worden gedrupt, gespincoat of geprint. In ieder van deze technieken is het oplosmiddel de drager om de nanokristallen gelijkmatig over de support uit te spreiden. Wanneer vervolgens het oplosmiddel verdampt aggregeren en zelf-organiseren de nanokristallen totdat ze samen de dunne laag vormen. Hierdoor worden de liganden gebonden aan het oppervlak van

de nanokristallen ook een onderdeel van de gevormde dunne laag. De liganden hebben een grote invloed op de interacties tussen de nanokristallen en de uiteindelijke structuur van de film. In een goed oplosmiddel strekken de liganden zich volledig uit, waardoor de attractieve interacties tussen de kernen volledig worden afgeschermd. De nanokristallen gedragen zich hierdoor als harde bollen, die zich in de thin film het meest efficiënt kunnen ordenen als de dichtste bolstapel in een kubisch vlakgecentreerde structuur (fcc). In het geval van een minder ideaal oplosmiddel strekken de liganden zich minder uit en worden de interacties tussen de kernen niet meer volledig afgeschermd. We spreken dan van een zachte bol interactie, waarbij de attractie tussen de kernen de gevormde structuren begint te beïnvloeden. Er worden dan eerder kubisch ruimte gecentreerde (bcc) structuren gevormd.^{24,25} Ook de snelheid waarmee het oplosmiddel verdampt en de uniformiteit van de nanokristallen spelen een grote rol voor de gevormde structuur. Slecht geordende, polykristallijne en amorf structuren vormen zich wanneer er sprake is van snelle verdamping en polydisperse nanokristallen. In het geval van langzame verdamping van een dispersie van uniforme nanokristallen kunnen deze films vormen met ordening over lange afstanden; superstructuren.^{23,26}

De liganden op het oppervlak van de nanokristallen worden ook een onderdeel van de thin films waar ze de nanokristallen nog steeds gescheiden houden en een barrière zijn voor de geleiding van de elektronen. De nanokristallen kunnen hierdoor slechts zwak kwantum-mechanisch koppelen en ze behouden hierdoor hun eigen gelocaliseerde bandenstructuur.²⁷ Elektronen kunnen zich alleen door de film verplaatsen door van het ene naar het andere nanokristal te “springen”. De snelheid van de geleiding (de mobiliteit) is hierdoor laag, meestal niet hoger dan $1 \text{ cm}^2/(\text{V s})$.²⁸⁻³⁰ Ter vergelijking, in een silicium kristal kan de mobiliteit wel tot $10^5 \text{ cm}^2/(\text{V s})$ bedragen.³¹ Door de lange organische liganden uit te wisselen voor kortere liganden of compacte anorganische moleculen kan de mobiliteit worden verhoogd. De isolerende laag wordt dan dunner en de nanokristallen kunnen dichter bij elkaar komen. De bandenstructuren van naburige nanokristallen beginnen te overlappen en een nieuwe bandenstructuur ontstaat. Hoe de nanokristallen zijn geordend beïnvloedt de manier waarop de nieuwe bandenstructuur zich vormt. De mobiliteit kan door het uitwisselen van de liganden worden verbeterd tot ongeveer $20 \text{ cm}^2/(\text{V s})$.³¹⁻³⁶

Met een kristallijne koppeling van de nanokristallen (een doorlopend kristal zonder liganden) kan de mobiliteit nog meer verbeteren, in elk geval in theorie. De legoblokjes bestaan dan alleen nog uit de anorganische kernen direct verbonden met een kristallijne “nek”. Een manier om nanokristallen te koppelen met behoud van hun ordening is “oriented attachment”, georiënteerde aanhechting. Het is een intrigerend “niet-klassiek” mechanisme voor kristalgroei dat in de natuur bijvoorbeeld plaatsvindt bij de vorming van biomineralen.³⁷⁻³⁹ Daar worden lading-gestabiliseerde kristallen gedestabiliseerd, waardoor de attractie tussen de facetten van naburige kristallen toeneemt en deze naar elkaar toe draaien. Van facet naar facet kunnen uiteindelijk covalente bindingen worden gevormd. Twee facetten met hoge oppervlak energie kunnen zo worden geëlimineerd terwijl de nanokristallen een groter kristal met een lagere oppervlak energie vormen.



Figuur 7.5 De Ikea handleiding voor een zelf-organisatie en oriented attachment experiment. Voor deze experimenten is het van belang om vrij van zuurstof en andere onzuiverheden te werken, al deze experimenten zijn daarom in een glovebox onder stikstof gedaan. In een petrischaaltje pipetteren we de vloeibare support, ethyleen glycol of een mengsel met 1,4-butaandiol, waar we vervolgens de PbSe nanokristal dispersie in toluene bovenop pipetteren (a). Voor de vorming van square superlattices verdampt de toluene in een uur, waarna de gevormde superstructuur op de support blijft drijven (b boven). Voor de vorming van een honeycomb superlattice is een tragere verdamping over 15 uur gunstig, het petrischaaltje wordt dan afgedekt met een bekglas om verdamping te vertragen (b onder). Na het vormen van de superlattice kan deze met een scheppende of stampende beweging worden overgebracht op een TEM grid voor verdere ex situ karakterisatie (c en d). Bij een succesvol experiment vormen we een square of honeycomb geordende superstructuur, terwijl gesmolten ongeordende structuren vormen bij te snelle ongecontroleerde attachment, te snelle verdamping of verontreiniging (e). Figuur aangepast van Carlo van Overbeek.

In het laboratorium wordt oriented attachment onderzocht als een methode om zelf-geordende superstructuren van nanokristallen om te zetten in twee en drie dimensionale superstructuren (in twee dimensionale superlattices). Deze superstructuren hebben vervolgens niet alleen een periodieke structuur van nanokristallen maar ook van gaten (**Figuur 7.5e**). Het meeste onderzoek naar oriented attachment is gedaan met behulp van lood-gebaseerde nanokristallen (PbSe, PbS and PbTe).^{24,25,40-51} Deze nanokristallen hebben een keuzenzoutstructuur en een afgevlakte kubus-octaëdrische vorm, hun oppervlak bestaat uit zes chemisch identieke stoichiometrische {100} facetten, acht {110} en acht {111} facetten (**Figuur 7.4a**). In het lab wordt een experiment voor de studie van zelf-organisatie en oriented attachment gedaan in de zuurstofvrije omgeving van een glovebox. Daar wordt in een petrischaaltje een dispersie van nanokristallen op het oppervlak van een niet mengbare vloeistof zoals ethyleen glycol gedruppeld (**Figuur 7.5a**). Voor 2D superstructuren doen we dit met lage concentraties maar voor 3D superstructuren worden dispersies met een hoge concentratie gebruikt. De dispersie spreidt zich uit over het oppervlak en blijft bovenop de vloeistof liggen terwijl het oplosmiddel (meestal toluene) verdampt. De nanokristallen worden dan in een steeds dunnere laag dichters naar elkaar geduwd (**Figuur 7.5b**), en ze organiseren zichzelf in een structuur die bovenop de ethyleen glycol blijft drijven. Bij een succesvol experiment organiseren de nanokristallen zichzelf als harde bollen in een fcc structuur bij langzame verdamping en als zachte bollen bij snelle verdamping. Wanneer vervolgens de facet-facet attractie toeneemt kunnen deze naar elkaar toe draaien en kunnen tussen naburige kristallijne nekken worden gevormd.

Bij PbSe nanokristallen zijn de liganden slechts zwak gebonden aan de {100} facetten terwijl daar ook minder liganden gebonden zijn dan op de hoog energetische facetten. Deze laag energetische facetten verliezen daardoor als eerste hun liganden.^{18,22} Attractie tussen de stoichiometrische {100} facetten neemt toe en onomkeerbare epitaxiale verbindingen kunnen gevormd worden met de kale {100} facetten van naburige nanokristallen (**Figuur 7.5b**). Een sample kan vervolgens worden genomen van de gevormde superstructuur (**Figuur 7.5c**), dat met behulp van ex situ technieken zoals TEM kan worden gekarakteriseerd (**Figuur 7.5d en e**).

In een gecontroleerd proces kan met behulp van oriented attachment een superlattice worden gemaakt waarin niet alleen de nanokristallen geordend zijn maar ook de gaten in de structuur. De specifieke geometrische ordening van een 2D materiaal, zoals “square” (met ook een vierkante periodiciteit van gaten) en “honeycomb” (hexagonale periodiciteit van gaten) wordt voornamelijk bepaald tijdens de verdamping van de dispersie. Vervolgens wordt met oriented attachment de structuur vastgezet. In het ideale geval wordt er een kristallijne nek gevormd tussen de twee kristallen,^{52,53} waarna de elektronische koppeling tussen de nanokristallen nog slechts gelimiteerd is door de breedte van de nek.

De bandenstructuren van de square en honeycomb superlattices zijn interessant voor potentiële toepassingen. In het bijzonder combineren de honeycomb superlattices de bandkloof van een conventionele halfgeleider met een vergelijkbare bandenstructuur als grafeen: Dirac-type banden die resulteren in een mobiliteit die hoger kan zijn dan voor silicium.^{54,55} Het controleren van oriented attachment is (nog steeds) een grote uitdaging, slechts enkele onderzoeksgroepen (en PhD studenten) hebben het lef en doorzettingsvermogen gehad om bij te dragen aan het onderzoek in dit veld. In de literatuur kunnen we de belangrijkste bijdragen van onderzoeksgroepen over oriented attachment van lood-gebaseerde nanokristallen ruwweg op twee handen tellen. In **hoofdstuk 3** bespreken we het onderzoek naar zelf-organisatie en oriented attachment tot 2020. Onder andere de onderzoeksgroepen van Daniel Vanmaekelbergh, Matt

Law, Tobias Hanrath, Zeger Hens, Paul Alivisatos en William Tisdale hebben grote bijdragen geleverd aan ons begrip van zelf-organisatie en oriented attachment van PbX superlattices in zowel twee als drie dimensies.^{24,25,40-47,56-58}

In **hoofdstuk 4** bestuderen we specifiek hoe oriented attachment plaatsvindt in een monolaag nanokristallen op een vloeistof. Daar laten we zien dat het voor het vormen van grote superstructuren gunstig is om de twee processen, zelf-organisatie en oriented attachment, zoveel mogelijk van elkaar te scheiden. Insluiting van oplosmiddel in de ligandlaag bleek belangrijk te zijn door middel van langzame verdamping in een afgedekt petrischaaltje. De nanokristallen kunnen zich dan tijdens de zelf-organisatie als harde bollen organiseren in een dubbele hexagonale laag, voordat oriented attachment de nanokristallen irreversibel aan elkaar koppelt om een honeycomb structuur te vormen.

Referenties

- [1] *Electromagnetic (EM) Spectrum*. UCAR Center for Education, 2023. www.scied.ucar.edu/learning-zone/earth-system/electromagnetic-spectrum (accessed on 23-04-2024).
- [2] Palacios, A. G.; Varela, F. J.; Srivastava, R.; Goldsmith, T. H. Spectral Sensitivity of Cones in the Goldfish, *Carassius Auratus*. *Vision Research* **1998**, *38* (14), 2135-2146. DOI: 10.1016/s0042-6989(97)00411-2.
- [3] Atkins, P. W.; Overton, T. L.; Rourke, J. P.; Weller, M. T.; Armstrong, F. A. *Shriver and Atkins' Inorganic Chemistry*; Oxford University Press, 2010.
- [4] Houtepen, A. J.; Koole, R.; Vanmaekelbergh, D.; Meeldijk, J.; Hickey, S. G. The Hidden Role of Acetate in the PbSe Nanocrystal Synthesis. *J. Am. Chem. Soc.* **2006**, *128* (21), 6792-6793. DOI: 10.1021/ja061644w.
- [5] Filler, M. Semiconductors, Principles. In *Encyclopedia of Applied Electrochemistry*, Ota, K. I., Kreysa, G., & Savinell, R. F. Ed.; Springer, 2014; pp 1953-1958.
- [6] Wise, F. W. Lead Salt Quantum Dots: the Limit of Strong Quantum Confinement. *Acc. Chem. Res.* **2000**, *33* (11), 773-780. DOI: 10.1021/ar970220q.
- [7] de Mello Donegá, C. *Nanoparticles: Workhorses of Nanoscience*; 2014. DOI: 10.1007/978-3-662-44823-6.
- [8] Murphy, J. E.; Beard, M. C.; Norman, A. G.; Ahrenkiel, S. P.; Johnson, J. C.; Yu, P.; Micic, O. I.; Ellingson, R. J.; Nozik, A. J. PbTe Colloidal Nanocrystals: Synthesis, Characterization, and Multiple Exciton Generation. *J. Am. Chem. Soc.* **2006**, *128* (10), 3241-3247. DOI: 10.1021/ja0574973.
- [9] Gupta, S.; Kershaw, S. V.; Rogach, A. L. 25th Anniversary Article: Ion Exchange in Colloidal Nanocrystals. *Adv. Mater.* **2013**, *25* (48), 6923-6943. DOI: 10.1002/adma.201302400.
- [10] Beberwyck, B. J.; Surendranath, Y.; Alivisatos, A. P. Cation Exchange: A Versatile Tool for Nanomaterials Synthesis. *J. Phys. Chem. C* **2013**, *117* (39), 19759-19770. DOI: 10.1021/jp405989z.
- [11] Rivest, J. B.; Jain, P. K. Cation exchange on the nanoscale: an emerging technique for new material synthesis, device fabrication, and chemical sensing. *Chem. Soc. Rev.* **2013**, *42* (1), 89-96. DOI: 10.1039/c2cs35241a.
- [12] De Trizio, L.; Manna, L. Forging Colloidal Nanostructures via Cation Exchange Reactions. *Chem. Rev.* **2016**, *116* (18), 10852-10887. DOI: 10.1021/acs.chemrev.5b00739.
- [13] Casavola, M.; van Huis, M. A.; Bals, S.; Lambert, K.; Hens, Z.; Vanmaekelbergh, D. Anisotropic Cation Exchange in PbSe/CdSe Core/Shell Nanocrystals of Different Geometry. *Chem. Mater.* **2011**, *24* (2), 294-302. DOI: 10.1021/cm202796s.
- [14] Galle, T.; Khoshkhoo, M. S.; Martin-Garcia, B.; Meerbach, C.; Sayevich, V.; Koitzsch, A.; Lesnyak, V.; Eychmuller, A. Colloidal PbSe Nanoplatelets of Varied Thickness with Tunable Optical Properties. *Chem. Mater.* **2019**, *31* (10), 3803-3811. DOI: 10.1021/acs.chemmater.9b01330.
- [15] Pietryga, J. M.; Werder, D. J.; Williams, D. J.; Casson, J. L.; Schaller, R. D.; Klimov, V. I.; Hollingsworth, J. A. Utilizing the Lability of Lead Selenide to Produce Heterostructured Nanocrystals with Bright, Stable Infrared Emission. *J. Am. Chem. Soc.* **2008**, *130* (14), 4879-4885. DOI: 10.1021/ja710437r.
- [16] Costi, R.; Saunders, A. E.; Banin, U. Colloidal Hybrid Nanostructures: a New Type of Functional Materials. *Angew. Chem. Int. Ed.* **2010**, *49* (29), 4878-4897. DOI: 10.1002/anie.200906010.
- [17] de Mello Donega, C. Synthesis and Properties of Colloidal Heteronanocrystals. *Chem. Soc. Rev.* **2011**, *40* (3), 1512-1546. DOI: 10.1039/c0cs00055h.
- [18] Fang, C.; van Huis, M. A.; Vanmaekelbergh, D.; Zandbergen, H. W. Energetics of Polar and Nonpolar Facets of PbSe Nanocrystals from Theory and Experiment. *ACS Nano* **2010**, *4* (1), 211-218. DOI: 10.1021/nn9013406.
- [19] Anderson, N. C.; Hendricks, M. P.; Choi, J. J.; Owen, J. S. Ligand Exchange and the Stoichiometry of Metal Chalcogenide Nanocrystals: Spectroscopic Observation of Facile Metal-Carboxylate Displacement and Binding. *J. Am. Chem. Soc.* **2013**, *135* (49), 18536-18548. DOI: 10.1021/ja4086758.
- [20] Moreels, I.; Justo, Y.; De Geyter, B.; Hastraete, K.; Martins, J. C.; Hens, Z. Size-Tunable, Bright, and Stable PbS Quantum Dots: a Surface Chemistry Study. *ACS Nano* **2011**, *5* (3), 2004-2012. DOI: 10.1021/nn103050w.
- [21] Peters, J. L.; van den Bos, K. H. W.; Van Aert, S.; Goris, B.; Bals, S.; Vanmaekelbergh, D. Ligand-Induced Shape Transformation of PbSe Nanocrystals. *Chem. Mater.* **2017**, *29* (9), 4122-4128. DOI: 10.1021/acs.chemmater.7b01103.
- [22] Abelson, A.; Qian, C.; Salk, T.; Luan, Z.; Fu, K.; Zheng, J. G.; Wardini, J. L.; Law, M. Collective Topo-Epitaxy in the Self-Assembly of a 3D Quantum Dot Superlattice. *Nat. Mater.* **2020**, *19* (1), 49-55. DOI: 10.1038/s41563-019-0485-2.
- [23] Kagan, C. R.; Lifshitz, E.; Sargent, E. H.; Talapin, D. V. Building Devices from Colloidal Quantum Dots. *Science* **2016**, *353* (6302). DOI: 10.1126/science.aac5523.
- [24] Bian, K.; Choi, J. J.; Kaushik, A.; Clancy, P.; Smilgies, D. M.; Hanrath, T. Shape-Anisotropy Driven Symmetry Transformations in Nanocrystal Superlattice Polymorphs. *ACS Nano* **2011**, *5* (4), 2815-2823. DOI: 10.1021/nn103303q.
- [25] Choi, J. J.; Bealing, C. R.; Bian, K.; Hughes, K. J.; Zhang, W.; Smilgies, D. M.; Hennig, R. G.; Engstrom, J. R.; Hanrath, T. Controlling Nanocrystal Superlattice Symmetry and Shape-Anisotropic Interactions through Variable Ligand Surface Coverage. *J. Am. Chem. Soc.* **2011**, *133* (9), 3131-3138. DOI: 10.1021/ja110454b.

- [26] Murray, C. B.; Kagan, C. R.; Bawendi, M. G. Self-Organization of CdSe Nanocrystallites into Three-Dimensional Quantum Dot Superlattices. *Science* **1995**, *270* (5240), 1335-1338. DOI: 10.1126/science.270.5240.1335.
- [27] Araujo, J. J.; Brozek, C. K.; Kroupa, D.; Gamelin, D. R. Degenerately n-Doped Colloidal PbSe Quantum Dots: Band Assignments and Electrostatic Effects. *Nano Lett.* **2018**, 3893-3900. DOI: 10.1021/acs.nanolett.8b01235.
- [28] Roest, A. L.; Houtepen, A. J.; Kelly, J. J.; Vanmaekelbergh, D. Electron-Conducting Quantum-Dot Solids with Ionic Charge Compensation. *Faraday Discuss.* **2004**, *125*, 55-62. DOI: 10.1039/b302839a.
- [29] Chandler, R. E.; Houtepen, A. J.; Nelson, J.; Vanmaekelbergh, D. Electron Transport in Quantum Dot Solids: Monte Carlo Simulations of the Effects of Shell Filling, Coulomb Repulsions, and Site Disorder. *Phys. Rev. B* **2007**, *75* (8). DOI: 10.1103/PhysRevB.75.085325.
- [30] Houtepen, A. J.; Kockmann, D.; Vanmaekelbergh, D. Reappraisal of Variable-Range Hopping in Quantum-Dot Solids. *Nano Lett.* **2008**, *8* (10), 3516-3520. DOI: 10.1021/nl8020347.
- [31] Kasap, S. O. Principles of Electronic Materials and Devices; 2006. ISBN: 0078028183.
- [32] Yu, D.; Wang, C. J.; Guyot-Sionnest, P. n-Type Conducting CdSe Nanocrystal Solids. *Science* **2003**, *300* (5623), 1277-1280.
- [33] Lee, J.-S.; Kovalenko, M. V.; Huang, J.; Chung, D. S.; Talapin, D. V. Band-Like Transport, High Electron Mobility and High Photoconductivity in All-Inorganic Nanocrystal Arrays. *Nature Nanotechnology* **2011**, *6* (6), 348-352. DOI: 10.1038/nnano.2011.46.
- [34] Oh, S. J.; Wang, Z.; Berry, N. E.; Choi, J. H.; Zhao, T.; Gauling, E. A.; Paik, T.; Lai, Y.; Murray, C. B.; Kagan, C. R. Engineering Charge Injection and Charge Transport for High Performance PbSe Nanocrystal Thin Film Devices and Circuits. *Nano Lett.* **2014**, *14* (11), 6210-6216. DOI: 10.1021/nl502491d.
- [35] Sandeep, C. S.; Azpiroz, J. M.; Evers, W. H.; Boehme, S. C.; Moreels, I.; Kinge, S.; Siebbeles, L. D.; Infante, I.; Houtepen, A. J. Epitaxially Connected PbSe Quantum-Dot Films: Controlled Neck Formation and Optoelectronic Properties. *ACS Nano* **2014**, *8* (11), 11499-11511. DOI: 10.1021/nn504679k.
- [36] Lan, X. Z.; Chen, M. L.; Hudson, M. H.; Kamysbayev, V.; Wang, Y. Y.; Guyot-Sionnest, P.; Talapin, D. V. Quantum Dot Solids Showing State-Resolved Band-Like Transport. *Nat. Mater.* **2020**, *19* (3), 323-329. DOI: 10.1038/s41563-019-0582-2.
- [37] Alivisatos, A. P. Biomineralization. Naturally aligned nanocrystals. *Science* **2000**, *289* (5480), 736-737. DOI: 10.1126/science.289.5480.736.
- [38] Niederberger, M.; Colfen, H. Oriented Attachment and Mesocrystals: Non-Classical Crystallization Mechanisms Based on Nanoparticle Assembly. *Phys. Chem. Phys.* **2006**, *8* (28), 3271-3287. DOI: 10.1039/b604589h.
- [39] Chen, J. D.; Wang, Y. J.; Wei, K.; Zhang, S. H.; Shi, X. T. Self-Organization of Hydroxyapatite Nanorods Through Oriented Attachment. *Biomaterials* **2007**, *28* (14), 2275-2280. DOI: 10.1016/j.biomaterials.2007.01.033.
- [40] Evers, W. H.; De Nijs, B.; Fillion, L.; Castillo, S.; Dijkstra, M.; Vanmaekelbergh, D. Entropy-Driven Formation of Binary Semiconductor-Nanocrystal Superlattices. *Nano Lett.* **2010**, *10* (10), 4235-4241. DOI: 10.1021/nl102705p.
- [41] Choi, J. J.; Bian, K.; Baumgardner, W. J.; Smilgies, D. M.; Hanrath, T. Interface-Induced Nucleation, Orientational Alignment and Symmetry Transformations in Nanocube Superlattices. *Nano Lett.* **2012**, *12* (9), 4791-4798. DOI: 10.1021/nl3026289.
- [42] Evers, W. H.; Goris, B.; Bals, S.; Casavola, M.; de Graaf, J.; van Roij, R.; Dijkstra, M.; Vanmaekelbergh, D. Low-Dimensional Semiconductor Superlattices Formed by Geometric Control over Nanocrystal Attachment. *Nano Lett.* **2013**, *13* (6), 2317-2323. DOI: 10.1021/nl303322k.
- [43] Walravens, W.; De Roo, J.; Drijvers, E.; Ten Brinck, S.; Solano, E.; Dendooven, J.; Detavernier, C.; Infante, I.; Hens, Z. Chemically Triggered Formation of Two-Dimensional Epitaxial Quantum Dot Superlattices. *ACS Nano* **2016**, *10* (7), 6861-6870. DOI: 10.1021/acsnano.6b02562.
- [44] Weidman, M. C.; Smilgies, D. M.; Tisdale, W. A. Kinetics of the Self-Assembly of Nanocrystal Superlattices Measured by Real-Time In Situ X-Ray Scattering. *Nat. Mater.* **2016**, *15* (7), 775-781. DOI: 10.1038/nmat4600.
- [45] Ondry, J. C.; Hauwiller, M. R.; Alivisatos, A. P. Dynamics and Removal Pathway of Edge Dislocations in Imperfectly Attached PbTe Nanocrystal Pairs: Toward Design Rules for Oriented Attachment. *ACS Nano* **2018**, *12* (4), 3178-3189. DOI: 10.1021/acsnano.8b00638.
- [46] van Overbeek, C.; Peters, J. L.; van Rossum, S. A. P.; Smits, M.; van Huis, M. A.; Vanmaekelbergh, D. Interfacial Self-Assembly and Oriented Attachment in the Family of PbX (X = S, Se, Te) Nanocrystals. *J. Phys. Chem. C* **2018**, *122* (23), 12464-12473. DOI: 10.1021/acs.jpcc.8b01876.
- [47] McCray, A. R. C.; Savitzky, B. H.; Whitham, K.; Hanrath, T.; Kourkoutis, L. F. Orientational Disorder in Epitaxially Connected Quantum Dot Solids. *ACS Nano* **2019**. DOI: 10.1021/acsnano.9b04951.
- [48] Cimada da Silva, J.; Balazs, D. M.; Dunbar, T. A.; Hanrath, T. Fundamental Processes and Practical Considerations of Lead Chalcogenide Mesocrystals Formed via Self-Assembly and Directed Attachment of Nanocrystals at a Fluid Interface. *Chem. Mater.* **2021**. DOI: 10.1021/acs.chemmater.1c02910.
- [49] van der Sluijs, M. M.; Sanders, D.; Jansen, K. J.; Soligno, G.; Vanmaekelbergh, D.; Peters, J. L. On the Formation of Honeycomb Superlattices from PbSe Quantum Dots: The Role of Solvent-Mediated Repulsion and Facet-to-Facet Attraction in NC Self-Assembly and Alignment. *J. Phys. Chem. C* **2022**. DOI: 10.1021/acs.jpcc.1c07430.

- [50] Hoglund, E. R.; Kim, G.; Kavrik, M. S.; Law, M.; Hachtel, J. A. Structural and Temperature Dependence of Emergent Electronic States in PbSe Quantum Dot Superlattices. *Microsc. Microanal.* **2023**, *29*, 361. DOI: 10.1093/micmic/ozad067.168.
- [51] Pinna, J.; Mehrabi Koushki, R.; Gavhane, D. S.; Ahmadi, M.; Mutalik, S.; Zohaib, M.; Protesescu, L.; Kooi, B. J.; Portale, G.; Loi, M. A. Approaching Bulk Mobility in PbSe Colloidal Quantum Dots 3D Superlattices. *Adv. Mater.* **2023**, *35* (8), e2207364. DOI: 10.1002/adma.202207364.
- [52] Geuchies, J. J.; van Overbeek, C.; Evers, W. H.; Goris, B.; de Backer, A.; Gantapara, A. P.; Rabouw, F. T.; Hilhorst, J.; Peters, J. L.; Konovalov, O.; et al. In Situ Study of the Formation Mechanism of Two-Dimensional Superlattices from PbSe Nanocrystals. *Nat. Mater.* **2016**, *15* (12), 1248-1254. DOI: 10.1038/nmat4746.
- [53] Wang, Y.; Peng, X. X.; Abelson, A.; Zhang, B. K.; Qian, C.; Ercius, P.; Wang, L. W.; Law, M.; Zheng, H. M. In situ TEM observation of Neck Formation During Oriented Attachment of PbSe Nanocrystals. *Nano Research* **2019**, *12* (10), 2549-2553. DOI: 10.1007/s12274-019-2483-8.
- [54] Kalesaki, E.; Delerue, C.; Morais Smith, C.; Beugeling, W.; Allan, G.; Vanmaekelbergh, D. Dirac Cones, Topological Edge States, and Nontrivial Flat Bands in Two-Dimensional Semiconductors with a Honeycomb Nanogeometry. *Phys. Rev. X* **2014**, *4* (1), 011010. DOI: 10.1103/PhysRevX.4.011010.
- [55] Beugeling, W.; Kalesaki, E.; Delerue, C.; Niquet, Y. M.; Vanmaekelbergh, D.; Morais Smith, C. Topological States in Multi-Orbital HgTe Honeycomb Lattices. *Nat. Commun.* **2015**, *6*, 6316. DOI: 10.1038/ncomms7316.
- [56] Weidman, M. C.; Nguyen, Q.; Smilgies, D. M.; Tisdale, W. A. Impact of Size Dispersity, Ligand Coverage, and Ligand Length on the Structure of PbS Nanocrystal Superlattices. *Chem. Mater.* **2018**, *30* (3), 807-816. DOI: 10.1021/acs.chemmater.7b04322.
- [57] Walravens, W. Epitaxial quantum dot superlattices forcing connections to improve processing and properties. **2019**.
- [58] Geuchies, J. J.; Soligno, G.; Geraffy, E.; Hendrikx, C. P.; van Overbeek, C. V.; Montanarella, F.; Slot, M. R.; Konovalov, O. V.; Petukhov, A. V.; Vanmaekelbergh, D. Unravelling Three-Dimensional Adsorption Geometries of PbSe Nanocrystal Monolayers at a Liquid-Air Interface. *Commun. Chem.* **2020**, *3* (1). DOI: 10.1038/s42004-020-0275-4.

List of Publications

This thesis is based on the following publications

Oriented Attachment: From Natural Crystal Growth to a Materials Engineering Tool

Bastiaan B.V. Salzmänn*, Maaïke M. van der Sluijs*, Giuseppe Soligno and Daniel Vanmaekelbergh, *Accounts of Chemical Research* **2021**, 54 (4), 787-797.

*These authors contributed equally

On the Formation of Honeycomb Superlattices from PbSe Quantum Dots: The Role of Solvent-Mediated Repulsion and Facet-to-Facet Attraction in NC Self-Assembly and Alignment
Maaïke M. van der Sluijs, Dinja Sanders, Kevin J. Jansen, Giuseppe Soligno, Daniel Vanmaekelbergh and Joep L. Peters, *Journal of Physical Chemistry C* **2022**, 126 (2), 986-996.

Study of the Mechanism and Increasing Crystallinity in the Self-Templated Growth of Ultrathin PbS Nanosheets

Maaïke M. van der Sluijs, Bastiaan B.V. Salzmänn, Daniel Arenas Esteban, Chen Li, Daen Jannis, Laura C. Brafine, Tim D. Laning, Joost W. C. Reinders, Natalie S. A. Hijmans, Jesper R. Moes, Johan Verbeeck, Sara Bals and Daniel Vanmaekelbergh, *Chemistry of Materials* **2023**, 35 (7), 2988-2998.

Cation Exchange and Spontaneous Crystal Repair Resulting in Ultrathin, Planar CdS Nanosheets

Maaïke M. van der Sluijs, Jara F. Vliem, Jur W. de Wit, Jeppe J. Rietveld, Johannes D. Meeldijk, and Daniel A. M. Vanmaekelbergh, *Chemistry of Materials* **2023**, 35 (19), 8301-8308.

Other publications

Electronic properties of atomically coherent square PbSe nanocrystal superlattice resolved by Scanning Tunneling Spectroscopy

Pierre Capiod, Maaïke van der Sluijs, Jeroen de Boer, Christophe Delerue, Ingmar Swart and Daniel Vanmaekelbergh, *Nanotechnology* **2021**, 32 (32), 325706.

In Situ Optical and X-ray Spectroscopy Reveals Evolution toward Mature CdSe Nanoplatelets by Synergetic Action of Myristate and Acetate Ligands

Johanna C. van der Bok, P. Tim Prins, Federico Montanarella, D. Nicolette Maaskant, Floor A. Brzesowsky, Maaïke M. van der Sluijs, Bastiaan B. V. Salzmänn, Freddy T. Rabouw, Andrei V. Petukhov, Celso De Mello Donega, Daniel Vanmaekelbergh, and Andries Meijerink, *Journal of the American Chemical Society*, **2022**, 144 (18), 8096-8105.

Growth and Self-Assembly of CsPbBr₃ Nanocrystals in the TOPO/PbBr₂ Synthesis as Seen with X-ray Scattering

Federico Montanarella, Quinten A. Akkerman, Dennis Bonatz, Maaïke M. van der Sluijs, Johanna C. van der Bok, P. Tim Prins, Marcel Aebli, Alf Mews, Daniel Vanmaekelbergh, and Maksym V. Kovalenko* *Nano Letters* **2023**, 23 (2), 667-676.

About the author

Maike Marina van der Sluijs was born on the 2nd of March 1990 in Utrecht. In 2009 she graduated from the Werkplaats in Bilthoven. Initially, she studied Theatre-, Film-, and Television Studies (TFT) at Utrecht University, during which she became a co-editor-in-chief at BLIK Journal for Audio Visual Culture. After TFT, she went on to obtain a bachelor's degree in Chemistry at the UU. She then enrolled in the Master's program: Nanomaterials: Chemistry and Physics at Utrecht University. Maike did her Master thesis research at Condensed Matter and Interfaces (CMI) under the supervision of Federico Montanarella and Daniel Vanmaekelbergh, where she studied the synthesis and self-assembly of CdSe two-dimensional nanoplatelets in spherical supraparticles. Then she proceeded to a half-year research internship at the group of Daniel Gamelin at the University of Washington, where she worked on the synthesis and optical characterization of colloidal nanomaterials.

After obtaining her Master's degree in 2017, Maike started as PhD researcher in the CMI group in November of that year. Under the supervision of Daniel Vanmaekelbergh she worked on the synthesis and self-assembly of lead selenide nanocrystals into square and hexagonally ordered superstructures. In addition, she also worked on the synthesis and cation exchange of lead sulphide two-dimensional nanosheets. During this time she supervised 2 Master students, 2 bachelor students and several second-year research projects. Most of the primary findings of this research are described in this thesis and have been published in peer-reviewed scientific journals.

